Rhodium Complexes and Particles on Carbon Nanofibres

Surface Chemistry of Carbon Nanofibres and Catalytic Properties of Supported Rhodium Species

Cover lay-out by Jan den Boesterd, Audio-Visual service department, Faculty of Chemistry, Utrecht University

This thesis was printed by ponsen & looijen bv, Wageningen

ISBN 90-393-2900-1

Rhodium Complexes and Particles on Carbon Nanofibres

Surface Chemistry of Carbon Nanofibres and Catalytic Properties of Supported Rhodium Species

Rhodium complexen en deeltjes op kooldraden

Oppervlaktechemie van kooldraden en katalytische eigenschappen van de gedragen rhodium verbindingen

(met een samenvatting in het Nederlands)

Proefschrift

ter verkrijging van de graad van doctor aan de Universiteit Utrecht op gezag van de Rector Magnificus, Prof. Dr. W.H. Gispen, ingevolge het besluit van het College voor Promoties in het openbaar te verdedigen op woensdag 16 januari 2002 des middags te 4:15 uur

door

Tijmen George Ros

geboren op 29 mei 1972, te Nieuwerkerk aan den IJssel

Promotoren

Prof. Dr. Ir. D.C. Koningsberger
Prof. Dr. Ir. J.W. Geus

Co-promotor

Dr. A.J. van Dillen

Allen verbonden aan de Sectie Anorganische Chemie en Katalyse, Debye instituut, Faculteit Scheikunde, Universiteit Utrecht

Het in dit proefschrift beschreven onderzoek werd mede mogelijk gemaakt met financiële steun van het gebied Chemische Wetenschappen (CW) van de Nederlandse Organisatie voor Wetenschappelijk Onderzoek (NWO).

If we knew what we were doing,
it wouldn't be called research,
would it?

(Albert Einstein)

Contents

Chapter 1	Introduction	1
Chapter 2	Surface Structure of Untreated Parallel and Fishbone Carbon Nanofibres: an Infrared Study	13
Chapter 3	Surface Oxidation of Carbon Nanofibres	29
Chapter 4	Rhodium Complexes with (N-phenyl) Anthranilic Acid Ligands as Catalysts for Hydrogenation	59
Chapter 5	Modification of Carbon Nanofibres for Immobilisation of Metal Complexes. A Case Study with Rhodium-Anthranilic Acid	79
Chapter 6	Preparation and Activity of Small Rhodium Metal Particles on Fishbone Carbon Nanofibres	109
Chapter 7	Summary	143
	Samenvatting	147
	Samenvatting voor leken	151
	Dankwoord	161
	List of Publications	165
	Curriculum Vitae	167

1
Introduction

The research described in this thesis deals with carbon nanofibres (CNFs) as support for rhodium complexes and rhodium metal particles. The study has been carried out because of the high potential of CNFs as a catalyst support material. A strong incentive for their use is the replacement of activated carbon, whose properties are often difficult to control. Furthermore, the highly structured carbon nanofibres can play an important role in gaining a more fundamental understanding of processes and interactions occurring at carbon surfaces.

History of carbon nanofibres

Carbon nanofibres have already been known for a long time. In 1889, Hughes and Chambers[1] reported their growth from carbon-containing gases by using a metal crucible as catalyst. Until the 1980s, the growth of carbon nanofibres was merely considered to be a serious problem. They are formed in a temperature range, where many important reactions, such as Fischer-Tropsch synthesis and steam-methane reforming, are carried out. The metal catalysts used in these reactions also catalyse carbon nanofibre growth. Due to their high mechanical strength and the mechanism of growth CNFs are not only capable of completely destroying the catalyst, the fibres can also penetrate reactor walls and damage reactors severely.[2]

The first studies on carbon nanofibres were devoted to the elucidation of the mechanism of growth with the objective to prevent the unwelcome appearance of these fibres during the above-mentioned reactions. Researchers tried, for

instance, to use copper metal alloys with iron or nickel and to utilise very small metal particles to suppress fibre growth.[3] In the 1980s, it was realised that carbon nanofibres are a unique material with properties suitable for many applications. The interest in carbon nanofibres further increased considerably with the discovery of the related carbon nanotubes in 1991.[4] The research shifted from preventing carbon nanofibre growth to controlling the growth and therewith the properties of the resulting fibres: surface structure (basal versus edge planes of graphite), diameter and length, mechanical strength, and texture of the clusters of fibres. It is, for instance, possible to obtain entangled fibres that form strong macroscopic bodies. These bodies are a promising catalyst support material. Hoogenraad *et al.*[5-7] executed one of the first extensive studies on controlling the morphology of clusters of carbon nanofibres on a macroscopic scale for their use as catalyst support. In conclusion, carbon nanofibres were first treated as an enemy, but they slowly have become a friend as well.

Mechamism of growth and structure of carbon nanofibres

The last two decades a number of research groups have studied the mechanism of growth of carbon nanofibres. Although a general picture has emerged from the research effort, there are still uncertainties about many growth details. De Jong and Geus[2] have recently reviewed the growth of carbon nanofibres. In general, the most important metals that catalyse the growth of CNFs are iron, cobalt and nickel. These metals can dissolve carbon atoms and/or form (meta-stable) metal carbides. The size of the metal particles used is about 10-50 nm for supported particles and typically 100 nm for unsupported metal particles, although (roughened) metal surfaces have been known to catalyse CNF growth as well. The gases most commonly used are methane, carbon monoxide, synthesis gas (H_2/CO), ethyne, and ethene. The growth temperatures utilised range from 400°C to 900°C. Fibres with diameters of 10-100 nm and lengths of 0.1 to more than 1000 μm can be obtained.

The CNF growth process can be divided into an initiation, propagation, and termination step. Figure 1.1 shows a schematic representation of the mechanism of growth. Small supported metal particles are exposed to a carbon-containing gas at elevated temperatures. The gases indicated in Figure 1.1 are synthesis gas and methane, because these gases have been employed in the research described in this thesis. The carbon-containing gas decomposes on the exposed metal surface under the formation of carbon and hydrogen, water and/or carbon dioxide. The carbon thus formed dissolves in the metal phase and diffuses through the particle to the interface, where nucleation of graphite has initiated. Growth of the graphite layers or nucleation of other graphite layers continues at the interface of the initial nucleation. The metal particle is usually lifted from the support and the growth process continues until encapsulation of the metal particle by graphite layers terminates the growth. The rate of the growth process is diffusion-controlled and the growth is probably driven by a concentration

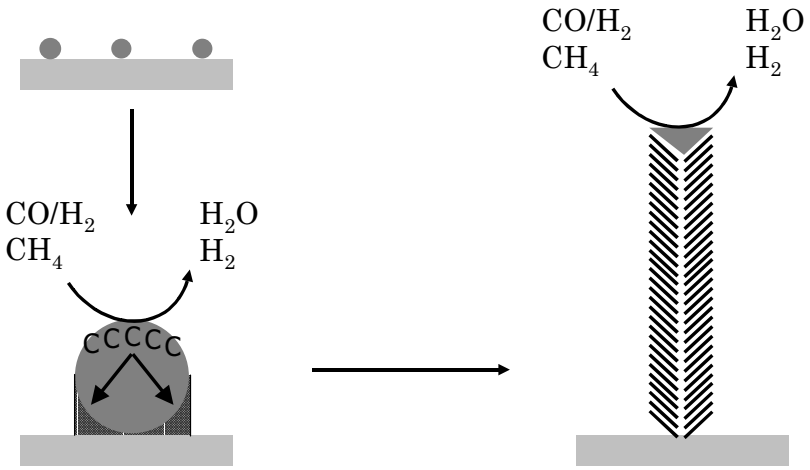

Figure 1.1 Schematic representation of the mechanism of growth of carbon nanofibres (a fishbone fibre is depicted).

gradient of dissolved carbon within the metal particle. During the first stages of growth of graphitic layers, the metal particle becomes pear-shaped and the tip of the particle points towards the newly formed fibre. The diameter of the fibre roughly equals the diameter of the particle. The steady-state growth process is a delicate balance between dissociative adsorption of the gas molecules, carbon diffusion through the particle, and crystallisation of graphitic layers.

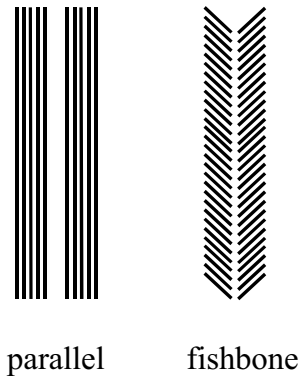

Figure 1.2 Cross-section of the graphitic layers of parallel and fishbone carbon nanofibres.

Generally, two types of fibre can be distinguished. Parallel fibres consist of coaxial cylindrical sheets of graphitic carbon. Figure 1.2 shows a cross-section of the graphitic layers of a parallel CNF. The graphitic layers are oriented parallel to the fibre axis and the fibre has a hollow core. The surface of a parallel fibre consists of graphitic basal planes. With fishbone carbon nanofibres the graphitic layers are cone shaped and stacked on top of each other. The cross-section in

Figure 1.2 shows that now the graphitic layers are oriented at an angle to the fibre axis. In the core of the fibre most probably disordered graphitic layers are located. The surface of fishbone fibres is composed of the edges of graphitic layers.

The general picture sketched above still raises many questions. There is, for instance, much debate about the initiation of growth. The formation of a (sub)surface carbide at the surface of the metal particle that is exposed to the gas phase is more or less accepted. However, evidence from magnetic measurements creates doubt about the presence of a (metastable) bulk carbide. According to Hoogenraad[5] and Teunissen,[8] intermediate reaction of at least a fraction of a metal particle to a metastable bulk carbide is a prerequisite for nucleation. Under certain conditions, the metal carbide decomposes into metal and a graphitic envelope, and the metal can be squeezed out of this envelope, initiating the growth process. Whether bulk carbide or merely dissolved carbon atoms are present during steady-state growth is still under debate. The nucleation of graphitic layers is also dependent on the size of the metal particles and the growth conditions.[5] It is, furthermore, uncertain how and why the metal particles change shape during the first stages of growth. A likely explanation is the deformation of the metal particles by the very strong graphitic layers, but many other explanations have been given as well. The change of shape has been related to liquid-like properties of the metal under the conditions used,[9-11] to erosion of the particle,[12] to change of shape during the escape of the metal particle from the graphitic envelope,[5] to reconstruction of the particle in order to expose the most active crystallographic faces,[13, 14] and to differences in growth rate at different points in the particle.[15] Several authors have indicated that the crystallographic orientation of the various faces of the metal particle is important for optimal growth.[13, 14, 16] Also, it was pointed out that the crystallographic faces can reconstruct during precipitation of carbon. With nickel different faces are needed for dissociative adsorption of gas molecules and nucleation of graphite. The exact role of the different crystallographic metal surfaces on nanofibre growth, however, still has to be clarified. Another question that deserves attention is the explanation of the growth of either parallel or fishbone fibres. Although literature[8, 15] has provided some clues, much more research should be executed. Finally, no clarification has been given what factors cause encapsulation, stopping the growth of fibres, to happen. Encapsulation of the metal growth particles probably occurs by the statistically governed nucleation of graphitic layers on the metal-gas interface. As yet the kinetics of the nucleation of graphitic layers on different crystallographic metal surfaces is not known.

The fibres used in this thesis all were grown from the same nickel-on-alumina catalyst. By using synthesis gas and a growth temperature of 600°C, parallel fibres result, whereas with methane at 570°C fishbone fibres grow. These conditions are the standard conditions used in our laboratory for the growth of

these types of fibres. The fibres obtained are described in more detail in Chapter 2.

Carbon nanofibres as catalyst support

Carbon nanofibres have properties that make them very suitable as catalyst support material. First, CNFs have a high surface area, which is indispensable for the stabilisation of small metal particles at significant metal loadings. The surface area of the fishbone fibres used in this study amounts to about 100 m^2/g, while that of the parallel fibres is approximately 160 m^2/g. CNFs are also mechanically strong. The bulk crushing strength (BCS) of the bodies of entangled carbon nanofibres is a good measure of the mechanical strength required for catalyst bodies to be employed in industrial reactors. With the strong macrobodies of fishbone fibres the BCS is about 0.90 MPa.[5, 8] This value is comparable to that of commercially available support materials. Hoogenraad *et al.*[5, 7] also showed that prolonged ultrasonic treatment in the liquid phase hardly affects the particle size distribution of CNFs, whereas treatment of a typical activated carbon produced a significant amount of fines. The agglomerates of nanofibres have a high porosity with only mesopores and macropores present in between the fibres. Therefore, less problems with diffusion of reactants and products to and from the catalytically active sites are expected than with microporous materials. As-synthesised nanofibres are hydrophobic. However, oxygen-containing groups can be introduced on the surface of the fibres by oxidation. This renders the fibres more hydrophilic. With well-controlled oxidation treatments the extent of hydrophobicity may be fine-tuned for different applications. In addition, CNFs are inert and can be used in strongly acidic or basic media.

The mechanical strength and the absence of micropores of carbon nanofibres make this material especially suitable as catalyst support for liquid-phase reactions. The skeins of fibres can withstand the forces executed by stirring of the reaction medium and the mesoporous macrostructure decreases the chance of encountering diffusion limitation during catalytic reaction in the liquid phase. Also, the ability to control the hydrophobicity and therewith the wetting properties of the fibres by apolar or polar liquids is an important advantage over classical oxidic catalyst support materials.

Carbon nanofibres have more advantages. The atomic structure of the fibres is well defined, in contrast to that of activated carbon. As already mentioned, two distinct structures (fishbone and parallel) can be distinguished. Furthermore, the fibres are only polluted by the original growth catalyst. Because of the synthesis procedure of activated carbon, this material is polluted with many heteroatoms, such as metals, sulphur, nitrogen and oxygen. Carbon nanotubes, that are obtained by arc discharge techniques, are polluted with other forms of carbon, such as amorphous carbon, carbon onions and fullerenes, which are difficult to remove. Due to the high purity and the well-defined structure, it is expected that

catalyst preparation with CNFs as the support is much more reproducible than with activated carbon and that the influence of the atomic surface structure of the fibres on the catalytic activity can be studied as well.

An important prerequisite for the use of carbon nanofibres as catalyst support material is low cost of production. Recent production-cost estimates have shown that CNFs may be obtained for a price less than 10 US$/kg when grown in a fluidised-bed in large volumes.[2] At this price level carbon nanofibres can even compete with activated carbon as a support for precious metal catalysts. An additional important advantage is that the CNF support can be virtually completely combusted after deactivation of the catalyst to recover the precious metal component.

The inertness and hydrophobicity of CNFs is a drawback for the use of these fibres as catalyst support material. Due to these properties, the application and anchoring of the active phase is difficult to achieve. One option for catalyst synthesis would be the use of organic catalyst precursor solutions. However, the original growth catalyst is still contaminating the fibres. Immersion in acid easily removes the metal of the growth catalyst. The removal of the oxidic alumina support used in this study, on the contrary, requires a more severe treatment. Most of the alumina can be removed, for instance, by boiling in nitric acid or a mixture of nitric and sulphuric acid. Such treatments also bring about the surface oxidation of CNFs. Thus, treatment of carbon nanofibres in concentrated acid solutions at elevated temperatures serves two purposes: removal of the metal and the support of the original growth catalyst and surface oxidation of the carbon nanofibres. The surface oxidation of CNFs is an important pre-treatment step for use of the fibres as catalyst support. The increased hydrophilicity of surface-oxidised CNFs causes a better wetting with aqueous catalyst precursor solutions and a whole range of techniques, such as impregnation, ion exchange and deposition-precipitation from a homogeneous solution, can be carried out with aqueous solutions to deposit the active phase. Because surface oxidation introduces carboxylic groups on the fibres, ion exchange techniques are very well possible. The oxidic surface groups not only act as anchoring sites for catalyst precursor complexes, but also for the final metal particles. Furthermore, the oxygen-containing surface groups can also bring about different activities and/or selectivities. Finally, oxygen-containing surface groups, for instance, carboxylic groups, can be used as anchoring sites for the immobilisation of metal-ligand systems as well.

Now that surface oxidation of carbon nanofibres has been identified as an essential step in the application of CNFs as catalyst support, two important catalyst preparation routes can be distinguished. The first and most difficult route consists of the immobilisation of catalytically active metal complexes on nanofibres by organic derivatisation reactions. The second route is the

preparation of small supported metal particles on CNFs. Both routes will be dealt with in this thesis.

Table 1.1 Advantages and disadvantages of homogeneous and heterogeneous catalysts.

	Homogeneous	Heterogeneous
Metal efficiency	++	+/-
Selectivity	++	+/-
Reproducibility	++	+/-
Sensitivity	+/-	+/-
Separation	--	++
Thermal stability	--	+

Immobilisation of metal complexes on carbon nanofibres

With immobilisation of homogeneous catalysts onto solid supports the objective is to combine the advantages of homogeneous and heterogeneous catalysts. In order to appreciate the interest in immobilised metal complex catalysts, it is useful to consider the advantages and disadvantages of homogeneous and heterogeneous catalysts, which are schematically summarised in Table 1.1.[17] In a heterogeneous system the reaction takes place on the surface of the catalytically active material. Depending upon the particle size the fraction of surface atoms may be quite low. In contrast, with homogeneous catalysts all metal atoms are in principle available as catalytic centres as they are isolated by the surrounding ligands. Therefore, the metal efficiency of homogeneous catalysts is much higher than that of heterogeneous catalysts. More importantly, homogeneous catalysts are generally much more selective than heterogeneous catalysts. A metal complex usually has only one active site and, therefore, it is easier to tune the selectivity by changes in the surrounding ligands than with heterogeneous catalysts that may have more active sites in the form of different crystallographic surfaces and different surface defects. Furthermore, the active site of a homogeneous catalyst can easily be reproduced, whereas the presence of specific active surface sites with heterogeneous catalysts is extremely difficult to control. In addition, homogeneous catalysts are frequently sensitive to water and oxygen, but not so sensitive to elements that poison many heterogeneous catalysts, such as sulphur or nitrogen. However, the single most important disadvantage of homogeneous catalysts is the problem of separating the catalyst from the reaction products. Often an efficient distillation or ion exchange process is needed. Homogeneous catalysts are usually expensive and small catalyst losses may render a process uneconomic. Furthermore, in many cases contamination of the reaction product with catalyst is unacceptable, for instance, in the food

industry. Another disadvantage of homogeneous catalysts is their low thermal stability compared to heterogeneous catalysts.

The problem of separating homogeneous metal complexes from the reaction products has hindered the application of such catalysts in industrial processes. The idea behind immobilisation of a homogeneous complex onto a solid support is to make available an efficient and selective catalyst that can easily be removed from the reaction mixture. Furthermore, the catalyst could become more robust and less sensitive towards water and oxygen. The application of immobilised catalysts could be envisaged in the area of production of fine chemicals, where selectivity is the key factor, or, for instance, in polymerisation reactions, where the properties of the catalyst can determine the final properties of the polymer.

A number of immobilisation methods can be distinguished, such as encapsulation or entrapment, supported liquid phase, and immobilisation by covalent bonding. As yet the immobilisation by covalent bonding of metal complexes onto carbon nanofibres or carbon nanotubes has, to our best knowledge, not been explored. Some reports describe the impregnation or adsorption of homogeneous catalysts on these new carbon materials.[18-20] Furthermore, only a few articles have been published about the immobilisation by covalent bonding of metal complexes to carbon in general. Kagan *et al.*[21] synthesised a chiral rhodium catalyst on partially graphitised carbon, while McCabe and Orchin[22] attached cobalt and tin complexes to bituminous coal. The inertness of CNFs and, to a lesser extent, carbon in general makes immobilisation with these materials much more difficult than with polymers or oxidic supports, such as silica and alumina. The derivatisation of carbon nanofibres is not straightforward. Although it has been recognised that many standard organic reactions can be executed on carbon materials, it has also been shown that the inertness of CNFs or nanotubes requires special treatments. [23, 24] Thus, the relative inertness with respect to polymeric or oxidic carriers and the lack of knowledge about the surface chemistry of carbon nanofibres has prevented the use of these carriers as support for immobilised metal complexes. However, in our opinion, the availability of the fibres plays a role as well. Whereas carbon nanotubes are mainly studied by physicists and physical chemists and carbon nanofibres are synthesised by inorganic chemists, organic chemists have mostly explored the research into immobilisation of homogeneous catalysts. The immobilisation of metal complexes onto CNFs is a typical example of research that resides at the boundary of several disciplines. On the one hand, a thorough knowledge of carbon nanofibre growth and surface chemistry is needed with all the accompanying characterisation techniques. On the other hand, an in-depth familiarity with the synthesis and characterisation of homogeneous catalysts is required. This calls for cross-boundary, interdisciplinary research, which is very difficult to execute. Different perspectives of view play a role as well. Whereas the carbon nanofibre specialist tends to approach immobilisation with the CNFs as a starting point, the expert in metal complexes addresses the

research question with the homogeneous catalyst as the start. It is clear that both approaches initially will lead to different 'ends'. Balancing on the edge between two disciplines, it was chosen to consider carbon nanofibres as the starting point and to construct an immobilised metal complex catalyst from this perspective. Furthermore, the first 15 years of research into immobilisation have taught that simply immobilising a successful homogeneously active metal complex catalyst to a functionalised support mostly yields an inferior version of that catalyst.[17] An alternative approach could be to purposely change the electronic and steric features of the complex by immobilisation and, by doing so, design bound catalysts that do not have homogeneous analogues. This concept is dealt with in more detail in Chapter 5.

Small metal particles on carbon nanofibres

As yet the use of carbon nanofibres or carbon nanotubes as catalyst support has not been examined in-depth. Impregnation onto fibres that are not oxidised is a common method, but several others use oxidised CNFs or nanotubes. Hoogenraad *et al.*[5-7, 25, 26] extensively studied the use of Pd/CNFs for the hydrogenation of nitrobenzene to aniline. The smallest Pd particles were obtained when fibres that were pre-oxidised with HNO_3 were ion-exchanged with a positively charged Pd-ammonia complex under the exclusion of air. With parallel fibres a maximal loading of 3 wt% was obtained, while with fishbone fibres only 1.5 wt% Pd could be exchanged.[6] On parallel fibres Pd particles of about 1.5 nm were obtained.[26] The Pd/CNFs catalyst turned out to be more active than a Pd-on-activated carbon catalyst of a higher metal loading.[5] However, no explanation for this observation could be given.

Baker and co-workers studied the activity of several metals on CNFs. Fe or FeCu precursors were impregnated on HCl-treated CNFs, ultimately resulting in particles of an average size of 12 nm at 5 wt% loading.[27] In spite of the relatively large size of the metal crystallites, the activity of these catalysts was considerably higher in the hydrogenation of ethylene than Fe(Cu) on activated carbon or alumina. The authors pointed out the possible relationship between the enhanced activity and a unique metal-support interaction between the metal particles and the basal planes of the fibres. In later publications,[28-30] Ni was impregnated on CNFs, resulting in 6-8 nm sized particles. Again, an activity improvement compared to nickel metal on classical supports was obtained in the hydrogenation of 1-butene and 1,3-butadiene.[28] Furthermore, differently structured fishbone type carbon nanofibres displayed different activities and selectivities.[29] Preferential blocking of either the armchair or the zigzag graphitic edge faces with P or B, respectively, indicated that the effects could be ascribed to the catalytic action of Ni residing on the zigzag faces.[30] Similar effects were found when the hydrogenation of crotonaldehyde on Ni/CNF was studied.[31] The nanofibre-supported catalysts were more active than Ni/Al_2O_3. Moreover, when alumina or 'ribbon' type CNFs were used as the support selective hydrogenation

of the double bond took place, whereas with 'platelet' type CNFs the aldehyde functional group was converted. The results were related to the way of adsorption of crotonaldehyde on nickel particles on the zigzag faces, which supposedly have a special atomic arrangement.

Other researchers found surprising selectivities in selective hydrogenation reactions as well. Ledoux and co-workers.[32] impregnated Pd on acid-treated CNFs and obtained 3-5 nm sized particles at 5 wt% loading. A very high activity and a 98 % selectivity towards the aldehyde was found with the hydrogenation of cinnamaldehyde at atmospheric pressure and 80°C. Planeix *et al.*,[33] on the contrary, observed a selectivity towards cinnamyl alcohol of 92 % with 3-7 nm sized Ru particles on non-purified nanotubes (0.2 wt% loading).

Finally, it is worth to mention the work of Ang *et al.*[34] and of Prinsloo and co-workers.[35] Ang deposited 2 nm sized Pd particles on HNO_3/H_2SO_4-oxidised carbon nanotubes by using an electroless plating technique. He reported that the tubes were densely coated with particles, indicating a high metal loading. Prinsloo used the deposition-precipitation method to obtain HNO_3-oxidised carbon nanofibres densely coated with cobalt particles of 7 nm diameter.

The improved activities and selectivities found with metal-on-CNF catalysts are striking. Probably the properties of the fibre support are unique and influence the performance of the catalyst significantly. In order to shed more light on this phenomenon more studies should be directed to investigating metal-support interactions. One of the techniques that could be used is XAFS spectroscopy. However, in order to do so, very small and uniform metal particles have to be synthesised on CNFs. The size of the metal particles obtained by most authors is too large for this purpose. Accordingly, there is a challenge to synthesise extremely small metal particles on CNFs. Of course, the synthesis of metal particles of such a small size and the investigation of their catalytic activity is already very worthwhile by itself.

Outline of this thesis

Above, we have identified the prerequisites for the use of carbon nanofibres as a catalyst support material and the various routes of catalyst preparation that can be taken. These subjects are investigated in this thesis. **Chapter 2** describes an infrared study on the surface structure of untreated parallel and fishbone carbon nanofibres. It is shown that IR spectroscopy is an excellent tool to obtain information about CH species and therewith about defects on the surface of the fibres. The results of this study also provide clues about the surface reactivity of the fibres. The surface oxidation of parallel and fishbone carbon nanofibres is studied in **Chapter 3**. The fibres are subjected to several gas-phase and liquid-phase oxidation treatments and, together with other techniques, studied with infrared spectroscopy, thermogravimetric analysis and XPS. Based on the results obtained a mechanism of oxidation is proposed. Furthermore, more knowledge about the nature and the amount of oxygen-containing surface groups is

gathered. Additionally, the effect of surface oxidation on the wetting properties of CNFs is investigated. **Chapter 4** deals with the synthesis, characterisation and activity in the liquid-phase hydrogenation of cyclohexene of homogeneous rhodium complexes with (N-phenyl) anthranilic acid. The interaction of the ligands with Rh is studied with IR spectroscopy. Furthermore, additional data obtained with other techniques give more information about the structure and the homogeneity of the complexes. The immobilisation of rhodium-anthranilic acid onto carbon nanofibres is described in **Chapter 5**. The immobilisation of Rh/anthranilic acid onto fishbone carbon nanofibres is executed via (i) surface oxidation of the fibres, (ii) conversion of the carboxyl groups into acid chloride groups, (iii) attachment of anthranilic acid, and (iv) complexation of rhodium(III). The final Rh(III) complex is also reduced with $NaBH_4$ to obtain a Rh(I) complex. The immobilisation process is followed and the final complex is characterised by IR, XPS, XAFS spectroscopy, and by molecular modelling. The results on the preparation and activity of small rhodium metal particles on fishbone carbon nanofibres are presented in **Chapter 6**. The particles are deposited on the fibres by several impregnation and ion exchange techniques using $RhCl_3 \cdot 2H_2O$ as the precursor salt. Furthermore, the influence of calcination and reduction procedures on the final metal particle size is studied. It is also investigated which fibre pre-treatment methods are needed for optimal interaction of the catalyst precursor with the nanofibres. The catalysts are characterised with transmission electron microscopy and with XAFS spectroscopy. The activity of the Rh/CNF catalysts in the liquid-phase hydrogenation of cyclohexene is tested. Finally, in **Chapter 7** all results are summarised and some concluding remarks are presented.

References

1 T.V. Hughes and C.R. Chambers, *U.S. Patent* **405,480** (1889)

2 K.P. de Jong and J.W. Geus, *Catal. Rev.-Sci. Eng.* **42-4** (2000), 481

3 W. Teunissen and M.S. Hoogenraad in HeteroGEneoUS Catalysis, Preparation, Characterisation and Application (Eds. K.P. de Jong and A.J. van Dillen), Publicard, Utrecht, 1998, p. 137

4 S. Iijima, *Nature* **354** (1991), 56

5 M.S. Hoogenraad, PhD Thesis (1995), Utrecht University, The Netherlands

6 M.S. Hoogenraad, M.F. Onwezen, A.J. van Dillen, and J.W. Geus, *Stud. Surf. Sci. Catal.* **101** (1995), 1331

7 J.W. Geus, M.S. Hoogenraad, and A.J. van Dillen in Synthesis and Properties of Advanced Catalytic Materials (Eds. E. Iglesia, P.W. Lednor, D.A. Nagaki, and L.T. Thompson), Materials Research Society Pittsburgh, Pittsburgh, 1995, p. 87

8 W. Teunissen, PhD Thesis (2000), Utrecht University, The Netherlands

9 R.T.K. Baker and P.S. Harris, *Chem. and Phys. Carbon* **14** (1978), 83

10 R.T.K. Baker in Carbon Fibers Filaments and Composites (Eds. J.L. Figueiredo, C.A. Bernardo, R.T.K. Baker, and K.J. Hüttinger), NATO ASI series C Vol. 177, Kluwer Academic Publishers, Dordrecht, 1990, p. 405
11 A. Sacco in Carbon Fibers Filaments and Composites (Eds. J.L. Figueiredo, C.A. Bernardo, R.T.K. Baker, and K.J. Hüttinger), NATO ASI series C Vol. 177, Kluwer Academic Publishers, Dordrecht, 1990, p. 459
12 E. Boellaard, P.K. de Bokx, A.J.H.M. Kock, and J.W. Geus, *J. Catal.* **96** (1985), 481
13 I. Alstrup, *J. Catal.* **115** (1989), 241
14 R.T. Yang and J.P. Chen, *J. Catal.* **115** (1989), 52
15 J.W. Snoeck, G.F. Froment, and M. Fowlest, *J. Catal.* **169** (1997), 240
16 M. Audier, A. Oberlin and M. Coulon, *J. Cryst. Growth* **55** (1981), 549
17 F.R. Hartley, Supported Metal Complexes, D. Reidel publishing company, Dordrecht, 1985
18 A.A. Keterling, A.S. Lisitsyn, V.A. Likholobov, A.A. Gall', and A.S Trachum, *Kinet. Catal. (Eng. Trans.)* **31-6** (1990), 1273
19 Yu. Yu. Volodin, A.T. Teleshev, V.V. Morozova, A.V. Tolkachev, Yu. S. Mardashev, and E.E. Nifantyev, *Russ. Chem. Bull.* **48-5** (1999), 899
20 Y. Zhang, H.-B. Zhang, G.-D. Lin, P. Chen, Y.-Z. Yuan, and K.R. Tsai, *Appl. Catal., A* **187** (1999), 213
21 H.B. Kagan, T. Yamagishi, J.C. Motte, and R. Setton, *Isr. J. Chem* **17** (1978), 274
22 M.V. McCabe and M. Orchin, *Fuel* **55** (1976), 266
23 J. Chen, M.A. Hamon, H. Hu, Y. Chen, A.M. Rao, P.C. Eklund, and R.C. Haddon, *Science* **282** (1998), 95
24 M.A. Hamon, J. Chen, H. Hu, Y. Chen, M.E. Itkis, A.M. Rao, P.C. Eklund, and R.C. Haddon, *Adv. Mater.* **11-10** (1999), 834
25 M.S. Hoogenraad, R.A.G.M.M. van Leeuwarden, G.J.B. van Breda Vriesman, A.Broersma, A.J. van Dillen, and J.W. Geus in Preparation of Catalysts VI (Eds. G. Poncelet *et al.*), Elsevier, Amsterdam, 1995, p. 263
26 B.L. Mojet, M.S. Hoogenraad, A.J. van Dillen, J.W. Geus, and D.C. Koningsberger, *J. Chem. Soc., Faraday Trans.* **93-24** (1997), 4371
27 N.M. Rodriguez, M.-S. Kim, and R.T.K. Baker, *J. Phys. Chem.* **98** (1994), 13108
28 A. Chambers, T. Nemes, N.M. Rodriguez, and R.T.K. Baker, *J. Phys. Chem. B* **102** (1998), 2251
29 C. Park and R.T.K. Baker, *J. Phys. Chem. B* **102** (1998), 5168
30 C. Park and R.T.K. Baker, *J. Phys. Chem. B* **103** (1999), 2453
31 F. Salman, C. Park, and R.T.K. Baker, *Catalysis Today* **53** (1999), 385
32 C. Pham-Huu, N. Keller, L.J. Charbonniere, R. Ziessel, and M.J. Ledoux, *Chem. Commun.* (2000), 1871
33 J.M. Planeix, N. Coustel, B. Coq, V. Brotons, P.S. Kumbhar, R. Dutartre, P. Geneste, P. Bernier, and P.M. Ajayan, *J. Am. Chem. Soc.* **116** (1994), 7935
34 L.-M. Ang, T.S. Andy Hor, G.-Q. Xu, C.-H. Tung, S. Zhao, and J.L.S. Wang, *Chem. Mater.* **11** (1999), 2115
35 M. Keyser and F.F. Prinsloo, *J. Mol. Catal.*, submitted

2

Surface Structure of Untreated Parallel and Fishbone Carbon Nanofibres: an Infrared Study

Abstract

The surface structure of untreated parallel and fishbone carbon nanofibres has been studied with transmission infrared spectroscopy. From a comparison of the spectra of the nanofibres and two graphites it can be concluded that both parallel and fishbone carbon nanofibres have a defect-rich graphitic surface structure. These defects bring about the presence of CH_2/CH_3 groups as well as aromatic C-H groups on both types of fibre. Moreover, on the fishbone carbon nanofibres some surface oxides are formed at the defect sites. Not much difference between parallel and fishbone carbon nanofibres is found, suggesting that the surface reactivity of parallel and fishbone carbon nanofibres is about the same.

2.1 Introduction

Carbon nanofibres (CNFs) that are obtained by catalytic decomposition of carbon-containing gases on small metal particles are a promising catalyst support material for liquid-phase reactions. The fibres are mechanically strong and can withstand the forces involved in vigorous agitation of the reaction medium. Furthermore, the skeins of fibres possess a mesoporeus macrostructure, which decreases the possibility to encounter diffusion limitation during catalytic reactions in the liquid phase. The structure of the CNFs can be tuned by changing the growth conditions and their hydrophobicity can be controlled by surface oxidation. Moreover, carbon nanofibres are very pure. They contain no other types of carbon, such as carbon onions, fullerenes or amorphous carbon, and no heteroatoms, such as sulphur, are incorporated during synthesis. They are chemically inert and can be used in strongly acidic or basic liquids. When grown in a fluidised bed reactor, carbon nanofibres can be obtained at low cost, making application as a catalyst support material possible.[1] Finally, after deactivation of the catalyst CNFs can be readily combusted to recover the precious metal component of spent catalysts, without leaving ash residues.

The mechanism of growth of CNFs has been studied extensively.[1-10] By changing the growth conditions or the metal, carbon nanofibres of a different structure can be obtained. Fishbone as well as parallel types of CNFs can be distinguished. With fishbone nanofibres the graphitic planes are oriented at an angle to the fibre axis, whereas with fibres of the parallel type the graphitic layers are oriented parallel to the axis.[3] Due to the different structure, the surface structure of parallel and fishbone carbon nanofibres have to differ as well. With the parallel fibres the surface consists of basal graphitic planes, whereas with fishbone fibres the edges of the graphitic layers are exposed. Consequently, one can assume that with parallel CNFs no hydrogen is present on the surface as it consists of closed graphene layers. With fishbone fibres, on the other hand, the graphitic edges could very well be terminated by hydrogen.

For the use of carbon nanofibres as a catalyst support it is important to be able to modify their surface, for instance, by the introduction of oxygen containing surface groups. A better interaction of the fibres with catalyst precursor complexes can thus be achieved. It is also viable to use these surface oxides as anchoring sites for the immobilisation of larger molecules and metal-ligand systems. Finally, the hydrophobic or hydrophilic character of the carbon nanofibres can be controlled by surface modification. The difference in surface structure of parallel and fishbone carbon nanofibres may induce a different surface reactivity. For instance, it can be expected that fishbone fibres, which terminate with the more reactive graphitic edges, are more liable to surface oxidation than parallel CNFs. As a first step towards an understanding of the surface reactivity and the mechanism of surface modification of carbon

nanofibres, it is, therefore, important to gain knowledge about the surface structure of the fibres.

Teunissen and co-workers[6] performed Electron Energy Loss Spectroscopy (EELS) measurements and concluded that with parallel carbon nanofibres no hydrogen was present at the edges of the fibres, which indicates that the outer layers consist of closed graphene planes. With fishbone CNFs, on the other hand, the edges of the fibres were terminated with carbon-hydrogen bonds. These bonds were thought to belong to aliphatic CH_2 groups, while no conclusions could be drawn concerning the presence or absence of aromatic C-H groups. These findings correlate well with the assumed surface structure of the different fibres.

The EELS study performed by Teunissen *et al.*[6] has given very valuable information about the surface structure of parallel and fishbone carbon nanofibres. However, the study did not take into account the possible connection between the presence of defects and carbon-hydrogen bonds. Accordingly, their EELS measurements were performed on small, perfectly ordered regions of parallel fibres. The volume of carbon nanofibres analysed was, furthermore, very small.

The presence of defects is very likely since the graphitic ordering within carbon nanofibres is less than in well-crystallised graphite.[1, 10] The d(002) spacing of the CNFs being larger than that of graphite reflects the lower ordering. Synthetic graphite can be made by decomposition of gaseous hydrocarbons at hot surfaces. Anderson[11] found that in the early stages of graphitisation the interlayer spacing is higher than the ideal 0.336 nm. Boehm[12] also noted that the distance between the graphitic layers in microcrystalline carbon is larger than in graphite. The decreased graphitic ordering of CNFs is most probably the origin of defects in their structure. Hydrogen may well be localised at these defect sites. It is, therefore, possible that parallel carbon nanofibres contain carbon-hydrogen species too.

In this investigation, we have studied the surface structure of parallel and fishbone carbon nanofibres with infrared spectroscopy. With IR spectroscopy a larger part of the surface of CNFs is analysed than with EELS. Therefore, it is possible to get an 'overall' impression of the surface structure of carbon nanofibres. Although the strong absorption of light by carbon nanofibres makes infrared spectroscopic analysis very difficult, this study teaches that IR spectroscopy is a suitable technique to investigate carbon nanofibres. A comparison of spectra of graphite and CNFs shows that the carbon nanofibres have a defect-rich structure and that carbon-hydrogen bonds are present on parallel as well as fishbone fibres.

2.2 Experimental

2.2.1 Growth of carbon nanofibres

Carbon nanofibres of the parallel and the fishbone type were produced by catalytic decomposition of CO/H_2 or CH_4 on Ni/Al_2O_3 catalysts, respectively.[3-6]

The Ni/Al_2O_3 catalysts with 20 or 30 wt% nickel metal loading were synthesised by the deposition-precipitation technique.[13] Alumina (Alon-C, Degussa) was suspended in an acidified aqueous solution of nickel nitrate (Acros, 99 %) and diluted ammonia was injected within two hours at room temperature under vigorous stirring until the pH had reached a value of 8.5. After overnight stirring, the suspension was filtered, washed, and dried at 120°C. Finally, the catalyst was calcined at 600°C in stagnant air for three hours.

Parallel carbon nanofibres were synthesised in small quantities in a fully automated micro-flow system. Fishbone carbon nanofibres, on the other hand, were grown on a larger scale in a manually operated set-up. Therefore, somewhat different synthesis conditions were employed.

For the growth of parallel carbon nanofibres, 100 mg of the 20 wt% Ni/Al_2O_3 catalyst was reduced at 700°C in 20 % H_2/Ar (flow rate 100 ml/min) in the micro-flow reactor for two hours. After reduction, the temperature was decreased to 600°C and synthesis gas (20 % CO and 7 % H_2 in Ar, flow rate 100 ml/min) was passed through the reactor during 10 hrs. After reaction, about 0.5 g of parallel CNFs were collected.

For the production of fishbone CNFs, 0.5 g of the 30 wt% Ni/Al_2O_3 catalyst was reduced at 600°C in 14 % H_2/N_2 (flow rate 350 ml/min) in a vertical tubular reactor (diameter 3 cm) for two hours. After having decreased the temperature to 570°C, methane (50 % in N_2, flow rate 450 ml/min) was passed through the catalyst bed for 6.5 hours. The yield of fibres amounted to approximately 12 g.

2.2.2 Characterisation of carbon nanofibres

The parallel and fishbone carbon nanofibres were characterised by transmission electron microscopy (TEM), nitrogen physisorption, X-ray diffraction (XRD), thermogravimetric analysis (TGA), and infrared spectroscopy (IR).

TEM samples were prepared by dispersing ground nanofibres in ethanol by ultrasound and drying a drop on a copper grid covered by a holey carbon film. They were imaged in a Philips CM-200 electron microscope operating at 200 kV.

CNF samples were de-gassed at 120°C in vacuum for at least 16 hours and nitrogen adsorption-desorption isotherms were measured at –196°C on a Micromeretics ASAP 2400 apparatus. Specific surface areas and pore volumes were calculated from the data obtained.

Powder XRD measurements were performed using an ENRAF-NONIUS X-ray diffraction system equipped with a curved position-sensitive INEL detector operating up to a width of 120°2θ. The applied radiation was Co K_α (λ = 1.78897 Å).

TGA analyses were carried out on a Netzsch STA-429 thermobalance. The gases evolved during analysis were monitored by a Fisons Thermolab quadropole mass spectrometer, using a capillary situated directly above the sample cup. Samples of 20-100 mg were heated in 60 ml/min Ar at a rate of 300°C/h to 850°C.

Diffuse reflectance infrared (DRIFT) was executed on a Perkin Elmer 1600 spectrometer equipped with a Spectra-Tech DRIFT accessory. Two hundred and fifty-six scans were co-added at a resolution of 2 cm^{-1} and a strong apodisation. Dilutions of 1 % (m/m) powdered sample in KBr were used. Transmission infrared spectra were recorded on a Perkin Elmer 2000 spectrometer equipped with an air dryer for removal of water vapour and carbon dioxide. One hundred scans were co-added at a resolution of 8 cm^{-1} and a boxcar apodisation. Samples were prepared by thoroughly mixing a small amount of ground nanofibres with pre-dried KBr. Tablets were pressed at 4 tons/cm^2 in vacuum for two minutes. The concentration of the nanofibres ranged from 0.1 to 1 ‰ (m/m). All transmission spectra were baseline corrected.

2.3 Results

Transmission electron microscopy

Figure 2.1 shows high resolution TEM micrographs of a parallel and a fishbone nanofibre. The graphitic layers are clearly visible. The images show that parallel and fishbone CNFs had been synthesised indeed. With the parallel fibres, perfect graphitic regions are alternated with defect regions. In Figure 2.1A some defects can be distinguished. Other images demonstrate that regions exist where the planes are bend, broken or interrupted. The micrograph of the fishbone fibre (Figure 2.1B) shows that the graphitic layers are oriented at an angle to the outer surface of the fibre (i.e., the axis of the fibre). Many planes are bend and careful examination establishes that planes merge, split and end. Moreover, the angle of the planes with respect to the fibre axis varies from almost parallel to more than 45°. From an image of fishbone fibres at lower magnification (see Figure 2.2), it can be made out that the fibres themselves are bend as well.

Macrostructure

The growth of parallel carbon nanofibres from CO/H_2 at 600°C results in a relatively open macroscopic structure of a low mechanical strength and density.[3, 4] The aggregates appear powdery and can easily be broken. The results of the analysis of the N_2-physisorption data and the observed fibre diameters with TEM are presented in Table 2.1. A specific surface area of 158 m^2/g and a pore volume

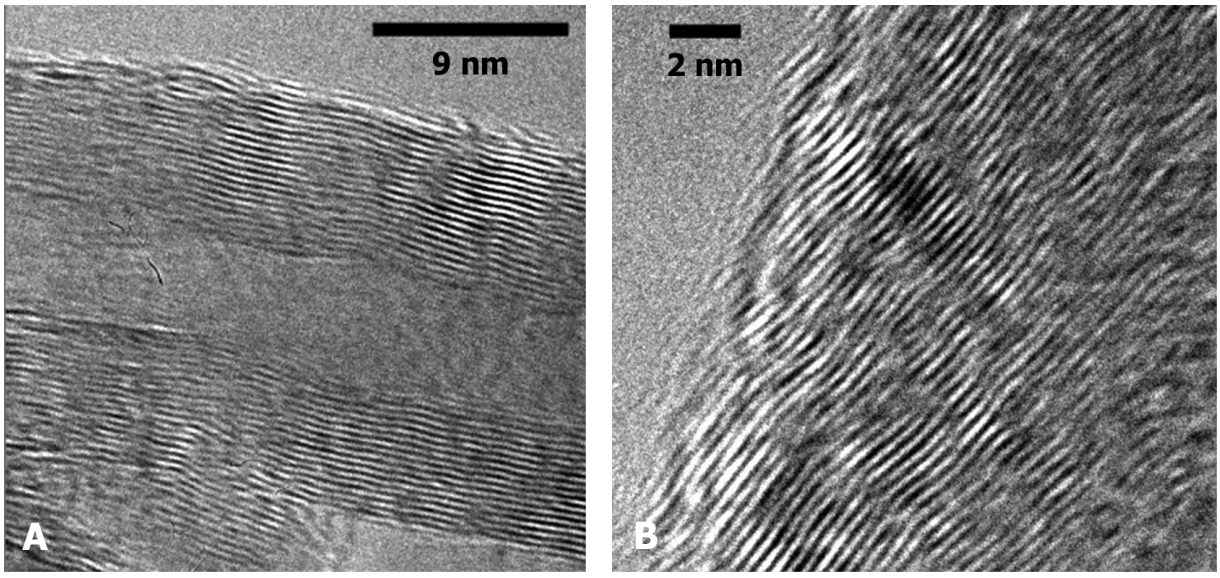

Figure 2.1 High resolution TEM micrographs of A) a parallel and B) a fishbone carbon nanofibre.

of 1.16 ml/g are obtained. No micropores are present. The diameter of the fibres varies between 15 and 20 nm. The fishbone carbon nanofibres, grown from CH_4 at 570°C, exhibit a strongly interwoven structure. This results in mechanically strong macroscopic bodies of a higher density than that of parallel nanofibres. A specific surface area of 103 m^2/g and a pore volume of 0.31 ml/g are found, again

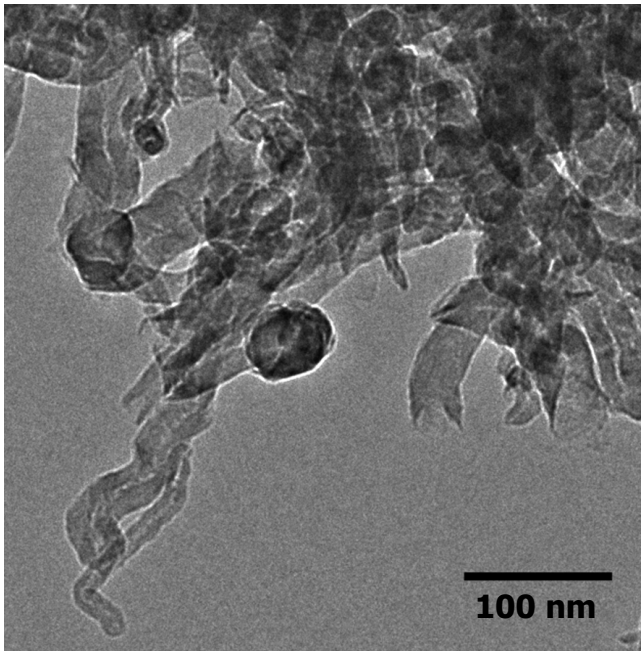

Figure 2.2 Transmission electron microscopy image of fishbone carbon nanofibres.

with no micropores present (see Table 2.1). The diameter of the fishbone fibres ranges from 20 to 90 nm. For both types of fibre a d(002) spacing of 0.344 nm is found with XRD. The width of the XRD peak is large compared to that of graphite.

Table 2.1 N_2-physisorption data and diameters of parallel and fishbone carbon nanofibres.

	BET surface area (m^2/g)	Pore vol. (ml/g)	Micropore vol. (ml/g)	Diameter (nm)
Parallel	158	1.16	0.00	15-20
Fishbone	103	0.31	0.00	20-90

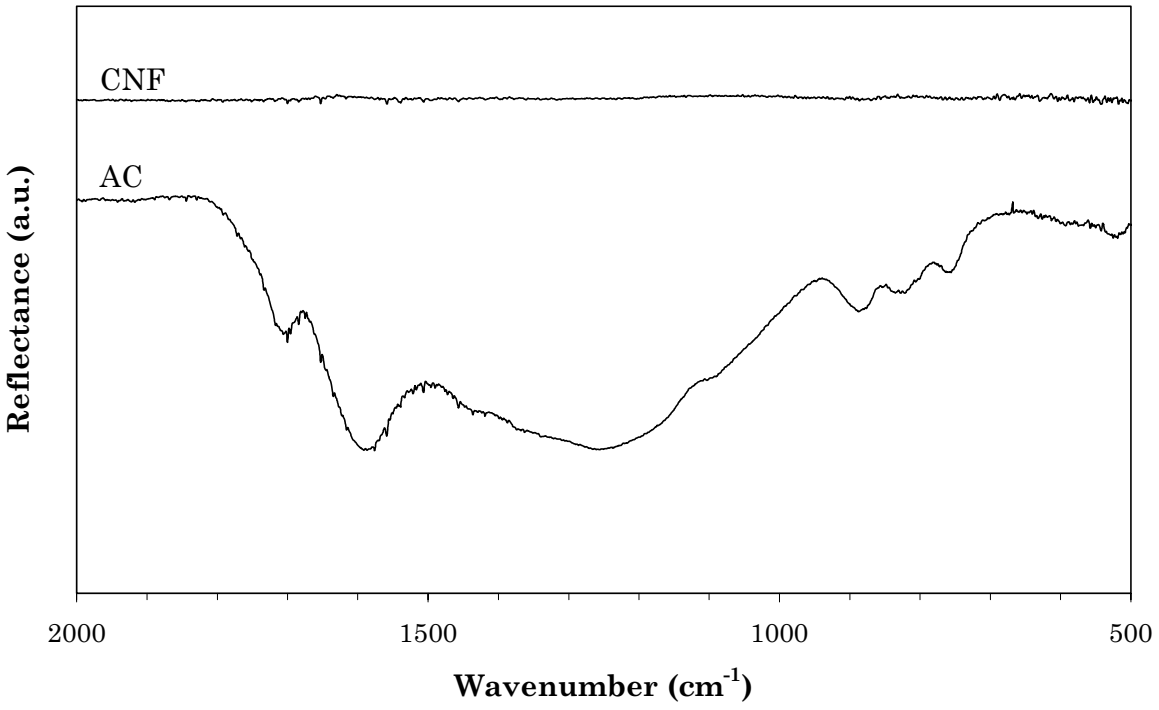

Figure 2.3 DRIFT spectra of parallel carbon nanofibres (CNF) and a DARCO KBB activated carbon (AC).

It must be noted that Al_2O_3, originating from the growth catalyst, is still present in the nanofibre samples. It was ascertained that the presence of Al_2O_3 did not interfere with the infrared study of the CNFs. The Al_2O_3 was not

removed, since the prolonged treatment with concentrated acids, needed for removal of the Al_2O_3, would modify the surface of the nanofibres as well.

Infrared nanofibres

In Figure 2.3 DRIFT spectra of parallel CNFs and a Darco KBB activated carbon are displayed. Whereas the activated carbon exhibits clearly distinguishable infrared bands, the spectrum of the parallel fibres shows only one straight line. These findings illustrate that although DRIFT spectroscopy is a surface-sensitive technique, it is not suitable for obtaining spectra of carbon nanofibres. Remarkable is the difference between the CNFs and the activated carbon. It is clear that the former absorbs much more infrared light than the latter. In other words, carbon nanofibres are highly opaque.

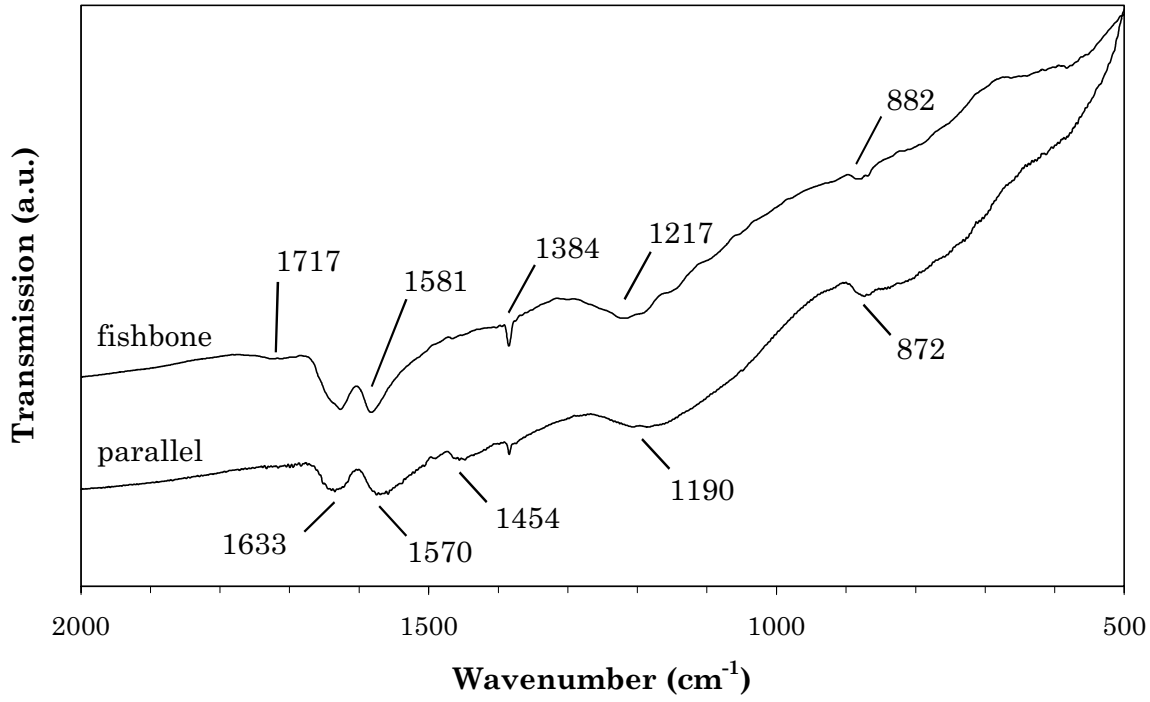

Figure 2.4 IR spectra of untreated parallel and fishbone carbon nanofibres. 2000-500 cm^{-1} range.

In order to get better infrared spectra of carbon nanofibres, transmission IR was applied. The strong IR absorbance of the fibres necessitated a very low sample concentration. To allow comparison, transmission levels of all spectra were kept approximately the same. It was established that, within the transmission window used, the intensity of the bands did not depend upon the transmission level of the spectra. Figure 2.4 shows spectra of parallel and fishbone nanofibres in the 2000-500 cm^{-1} range. Table 2.2 summarises all infrared band assignments. As a significant water contamination due to the low

sample concentrations was likely, the band at 1633 cm^{-1} can be discounted as being due to adsorbed water.[14, 15] This is supported by the observation that the band disappeared when the KBr-fibre mixture was dried at 80°C for several days before the tablet was pressed. The water is most probably exclusively adsorbed onto the KBr as the fibres are hydrophobic and no H_2O evolved during TGA analysis with a fibre sample. The sharp peak at 1384 cm^{-1} can also be discounted as being due to traces of nitrate, formed from NO_x taken up from the air.[16, 17] Both the 1384 and the 1633 cm^{-1} band are present in the KBr backgrounds too.

Table 2.2 Assignments of infrared absorptions found for carbon nanofibres and graphite.

Wavenumber (cm^{-1})	Assignment	Reference
3012	aromatic C-H stretching	18
2947	CH_2/CH_3 stretching	18
2917	CH_2/CH_3 stretching	18
2846	CH_2/CH_3 stretching	18
1717 – 1712	C=O stretching	14, 18, 20, 21
1633	adsorbed water	14, 15
1580 – 1570	aromatic ring stretching	14, 15, 18, 19
1454	CH_2/CH_3 bending	18, 24
1384	nitrate	16, 17
1217-1188	C-C stretching	14, 15
880 – 870	isolated aromatic C-H out-of-plane bending	18

The bands at about 1580 and 1200 cm^{-1} can be assigned to carbon skeleton vibrations.[14, 15, 18, 19] The higher wavenumber absorption is associated with an aromatic ring stretching mode, found at slightly higher wavenumbers in carbon blacks by Prest *et al.*[14] (1595 cm^{-1}) and in coal samples by Painter *et al.*[18] (1600 cm^{-1}). For parallel carbon nanofibres, however, Shaffer *et al.*[15] observed this band at 1550 cm^{-1} while Mawhinney and co-authors[19] detected this band at 1581 cm^{-1} for single-walled carbon nanotubes. The lower wavenumber absorption at about 1200 cm^{-1} is related to C-C stretching vibrations.[14] Prest[14] and Shaffer[15] observed this band at 1245 cm^{-1} and at about 1200 cm^{-1}, respectively.

The band at 880-870 cm^{-1}, present in both types of fibre, can be assigned to isolated aromatic C-H out-of-plane bending vibrations.[18] Painter *et al.* found that after deconvolution two bands at 888 and 864 cm^{-1} resulted that could be ascribed to lone aromatic C-H groups in different local environment. The very weak band at 1717 cm^{-1}, present in the spectrum of the fishbone nanofibres, is attributed to the C=O stretching vibration of carbonyl or carboxylic acid groups.[14, 18, 20, 21]

TGA-MS analysis showed that a small weight loss is accompanied with the evolution of CO with the parallel nanofibres and the release of CO and CO_2 with the fishbone CNFs. Apparently, some oxygen is already present on untreated nanofibres. Considering the finding that only fishbone CNFs lose CO_2 when heated in Ar, the 1717 cm^{-1} band may be associated with the C=O vibration of carboxyl groups.[12, 22, 23] Finally, the additional band at 1454 cm^{-1} in the spectrum of the parallel fibres is assigned to CH_2 and CH_3 bending vibrations.[18, 24] Painter *et al.*[18] and Gómez-Serrano and co-workers[24] observed this vibration at 1450 cm^{-1} and 1460 cm^{-1}, respectively.

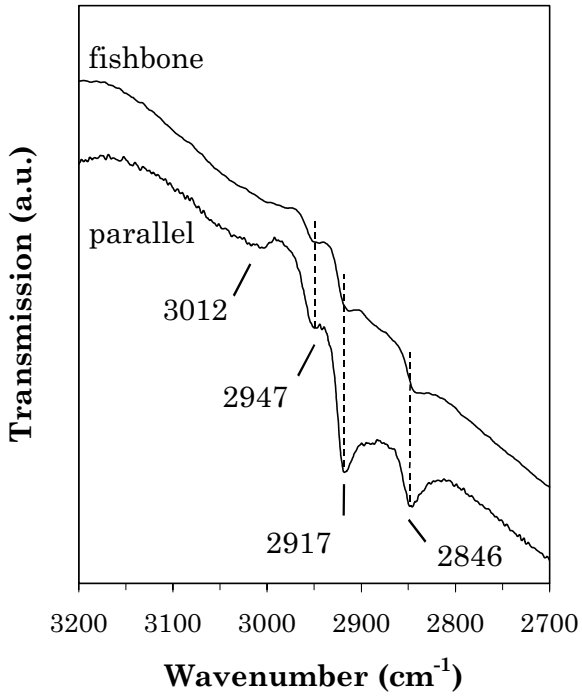

Figure 2.5 IR spectra of untreated parallel and fishbone carbon nanofibres. 3200-2700 cm^{-1} range.

The 3200-2700 cm^{-1} range of the spectra provides more insight into the presence of carbon-hydrogen groups on the fibres (see Figure 2.5). Four minima can be distinguished at 3012, 2947, 2917 and 2846 cm^{-1}, respectively. The peak at 3012 cm^{-1} can be assigned to aromatic C-H stretching vibrations, whereas the other three absorptions are associated with CH_2 and CH_3 stretching vibrations. Painter and co-workers[18] observed these bands at about 2950, 2920 and 2850 cm^{-1}. On the basis of the assignments most often made in this region of the spectrum, it is tempting to attribute the peak at 2947 cm^{-1} to antisymmetric stretching modes of CH_3 groups and the minima at 2917 and 2846 cm^{-1} to the antisymmetric and symmetric vibrations of CH_2 groups. Unfortunately, with carbonaceous materials these bands must be considered a composite of various

overlapping contributions.[18] Infrared studies of hydroaromatic model compounds have shown that the position of the vibrational bands of both methyl and methylene groups is dependent upon the structure of those compounds. Only the absorption at about 2850 cm^{-1} is not very sensitive to the structure and thus can point to the presence of CH_2 groups. In summary, the three modes between 3000 and 2800 cm^{-1} give information about the CH_2/CH_3 content in carbonaceous materials, but a distinction between CH_2 and CH_3 groups cannot easily be made.

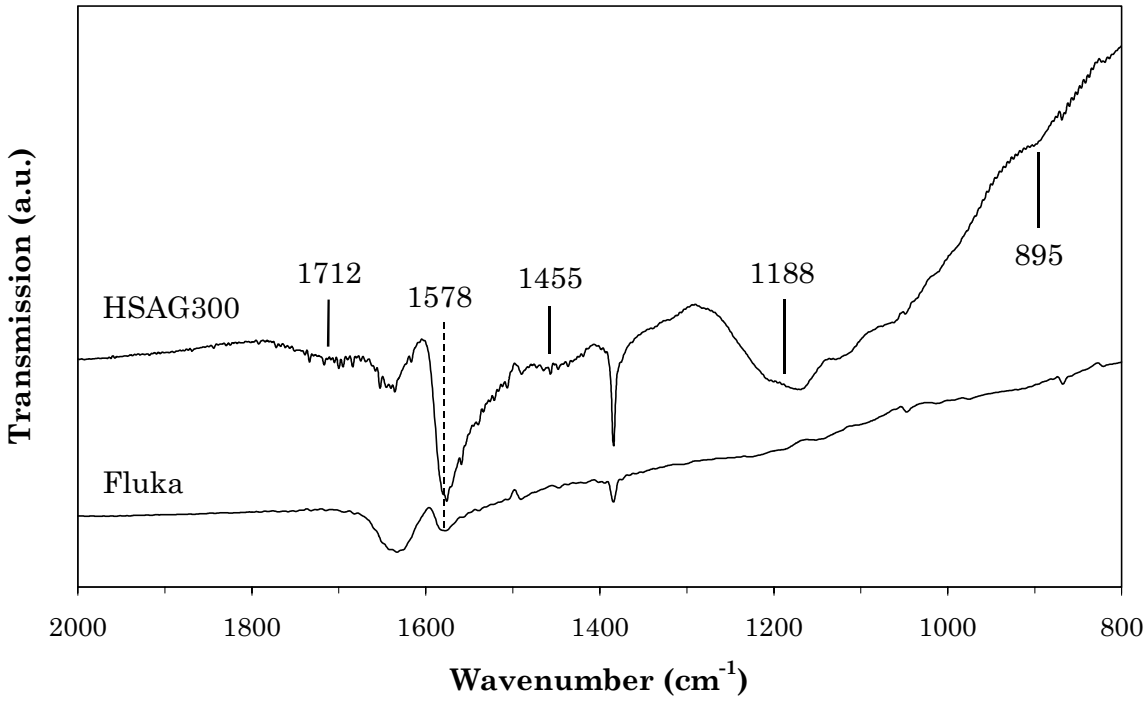

Figure 2.6 IR spectra of graphite with a low surface area (Fluka) and a high surfac area (HSAG300). 2000-800 cm^{-1} range.

Infrared graphite

Spectra were recorded of graphite with a low surface area (Fluka, <10 m^2/g) and a high surface area (TIMCAL, TIMREX HSAG300, 300 m^2/g). Figure 2.6 represents the 2000-800 cm^{-1} range of both graphites. The Fluka graphite only shows a weak band at 1578 cm^{-1}, attributed to aromatic ring vibration. The HSAG300 graphite, in contrast, shows four additional absorptions at 1712, 1455, 1188, and 895 cm^{-1}. Furthermore, the intensity of the 1578 cm^{-1} band is enhanced considerably. Figure 2.7 shows the 3100-2700 cm^{-1} range of the spectra of both graphites. It is clear that the Fluka graphite does not possess any CH_2/CH_3 groups, whereas the carbon-hydrogen stretching vibrations are clearly visible in the spectrum of the HSAG300 graphite. A weak band at 3008 cm^{-1} can also be distinguished.

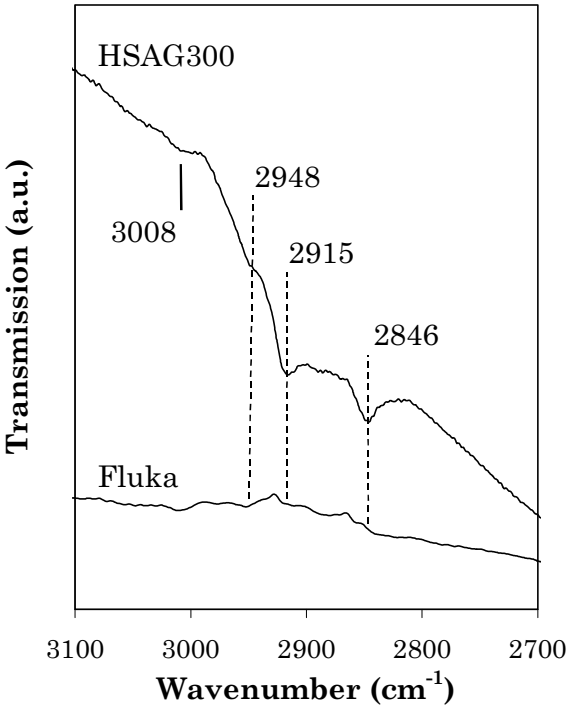

Figure 2.7 IR spectra of graphite with a low surface area (Fluka) and a high surfac area (HSAG300). 3100-2700 cm^{-1} range.

2.4 Discussion

The electron microscopy and XRD data indicate that defects are present in the graphitic structure of the carbon nanofibres. With high resolution TEM the defects can be imaged. The bending of the fibres themselves has to result from defects in the graphitic structure. The d(002) value of 0.344 nm found with XRD is significantly larger than the d(002) spacing of graphite of 0.336 nm.[25] Together with the relatively large width of the d(002) peak this implies less graphitic ordering than in graphite and thus a defect-rich structure.

The infrared data show that aromatic C-H as well as CH_2/CH_3 groups are present on the CNFs. These groups must be localised at defect sites and, for the fishbone fibres, at the edges of the planes. The presence of the 1200 cm^{-1} C-C stretching vibration also points to the existence of defects. Both the 1580 cm^{-1} and the 1200 cm^{-1} bands are present in the spectrum of a heat-treated carbon black.[14] However, single-walled carbon nanotubes, heated to 800°C in vacuum, show only the vibration at 1580 cm^{-1}.[19] The band at 1200 cm^{-1}, therefore, has to be associated with defects in carbonaceous materials.[15]

In order to get further information about which bands can be associated with defects in graphitic materials, spectra were recorded of a low and a high surface area graphite. Because of the high surface area of the HSAG300 graphite, it is assumed that the graphitic domains are small and that defects are present in the

structure, in contrast to the Fluka graphite, which has a low surface area. This assumption is supported by the larger width of the XRD d(002) peak measured for the HSAG300 graphite. The Fluka graphite, which supposedly has perfectly ordered graphitic domains, shows only a weak aromatic ring vibration at 1578 cm^{-1}. In contrast to the Fluka graphite, the HSAG300 graphite shows a clear, broad absorption at 1188 cm^{-1}. These results clearly indicate that the absorption at 1200 cm^{-1} in graphitic materials is related to the presence of defects in the structure. Along with the defects in the structure other bands appear in the infrared spectrum as well. First, the peaks at 1455, 2846, 2915, and 2948 cm^{-1} show that CH_2/CH_3 groups are present. The absorptions at 895 and 3008 cm^{-1} point out that the presence of defects leads to aromatic C-H groups and the 1712 cm^{-1} band indicates the appearance of some oxygen containing surface groups. Finally, the decrease of the size of the graphitic domains results in an increase of the intensity of the 1578 cm^{-1} absorption, because symmetry restrictions are relieved for more aromatic rings.

The infrared results obtained with the two graphites enable us to interpret the spectra of the parallel and the fishbone carbon nanofibres in more detail. We conclude that the graphitic structure of both types of fibres is rich in defects as their spectra show the C-C stretching vibration at 1200 cm^{-1}. These defects give rise to the presence of CH_2/CH_3 groups as well as aromatic C-H groups on both types of fibres. Moreover, on the fishbone CNFs some surface oxides were formed at the defect sites. For the parallel fibres, the presence of aromatic C-H groups is clearly shown by bands at 872 and 3012 cm^{-1}. The fishbone fibres, on the other hand, show only a band at 882 cm^{-1}. The difference in position of the isolated aromatic C-H out-of-plane bending vibration at 882 cm^{-1} for the fishbone CNFs and at 872 cm^{-1} for the parallel fibres points to differences in local environment.[18] For the presence of CH_2/CH_3 groups, the same trend is visible. CH_2/CH_3 groups are clearly present on the parallel CNFs (minima at 1454, 2846, 2917, and 2947 cm^{-1}), whereas for the fishbone fibres only weak absorptions in the 3000-2800 cm^{-1} range can be distinguished.

Since with parallel fibres the CH_2/CH_3 bands are more intense in the 3000-2800 cm^{-1} region and a peak at 1454 cm^{-1} is visible, it seems that the concentration of these groups is higher with the parallel than with the fishbone fibres. However, other factors may also influence the intensity of these bands. Because of the very high absorption of the CNFs, it is likely that the penetration dept of the IR radiation is smaller than the diameter of the fibres. Therefore, most of the radiation is blocked by the nanofibres. Only at the edges of the fibres the light passes through. This explains the very low sample concentrations needed to obtain a signal. Consequently, the diameter of the fibres and thus their external surface area influences the intensity of the IR signal. The external surface area of parallel fibres is higher than that of fishbone CNFs and as a result more intense CH_2/CH_3 bands are detected. This explanation is supported by the finding that parallel fibres with an external surface area of 300 m^2/g

(grown out of supported Fe particles) exhibited even more intense CH_2/CH_3 bands. Another factor that can play a role is the macroscopic density of the carbon nanofibre bodies. Bodies of parallel fibres are much less dense than those of fishbone CNFs. Therefore, more infrared light can pass through a particle of parallel carbon nanofibres.

Thus, the higher intensity of the CH_2/CH_3 bands in parallel carbon nanofibres cannot be unambiguously associated with a higher concentration of those groups. Therefore, we conclude that, overall, there is not much difference between parallel and fishbone carbon nanofibres.

At first sight, the present results obtained with infrared and the findings of Teunissen *et al.* with EELS[6] seem partly contradictory. Teunissen found that with the parallel carbon nanofibres no carbon-hydrogen bonds could be detected. For the fishbone CNFs, aliphatic CH_2 groups were detected and no conclusion could be drawn concerning the presence or absence of aromatic C-H groups. However, the EELS results were obtained by analysing a perfectly ordered region of a parallel CNF. The findings described above have made clear that the presence of CH_2/CH_3 groups is related to defects in the graphitic structure. In view of this, both observations are complementary. The infrared results obtained with fishbone nanofibres have led to the conclusion that these fibres contain CH_2/CH_3 groups. Unfortunately, no distinction between these groups can be made. These findings are in accordance with the conclusions drawn by Teunissen. The presence of aromatic C-H was not observed by EELS, but IR has been able to detect these groups on both types of fibres. Considering the structure of the fishbone CNFs, it is very likely that the carbon edges end in CH_2/CH_3 or aromatic C-H groups.

Because of the defect-rich graphitic structure of both parallel and fishbone carbon nanofibres, there does not seem to be much difference in their surface composition. It is, therefore, also very well possible that the surface reactivity of parallel and fishbone fibres does not differ significantly. The surface reactivity of carbon nanofibres towards oxidising agents will be dealt with in Chapter 3. It should be noted that from a practical point of view fishbone CNFs are more favourable as catalyst support than parallel fibres. Fishbone fibres have a higher cluster density and are mechanically stronger. Furthermore, they can be grown in higher yields.

2.5 Conclusions

Untreated parallel and fishbone carbon nanofibres were studied with transmission infrared spectroscopy. With DRIFT spectroscopy no useful spectra of CNFs could be obtained. From a comparison of the spectra of the nanofibres and two graphites, we conclude that both parallel and fishbone carbon nanofibres have a defect-rich graphitic surface structure. These defects lead to the presence of CH_2/CH_3 groups as well as aromatic C-H groups on both types of fibre. Moreover, on the fishbone CNFs some surface oxides form at the defect sites. Not much difference between parallel and fishbone carbon nanofibres is found, suggesting that the surface reactivity of parallel and fishbone carbon nanofibres is about the same.

Acknowledgements

We wish to acknowledge prof. dr. J.H. van der Maas of the Department of Vibrational Spectroscopy, Utrecht University, for the discussions about the IR data.

References

1 K.P. de Jong and J.W. Geus, *Catal. Rev.-Sci. Eng.* **42-4** (2000), 481
2 E. Boellaard, P.K. de Bokx, A.J.H.M. Kock, and J.W. Geus, *J. Catal.* **96** (1985), 481
3 M.S. Hoogenraad, PhD Thesis (1995), Utrecht University, The Netherlands
4 M.S. Hoogenraad, M.F. Onwezen, A.J. van Dillen, and J.W. Geus, *Stud. Surf. Sci. Catal.* **101** (1995), 1331
5 J.W. Geus, M.S. Hoogenraad, and A.J. van Dillen in Synthesis and Properties of Advanced Catalytic Materials (Eds. E. Iglesia, P.W. Lednor, D.A. Nagaki, and L.T. Thompson), Materials Research Society Pittsburgh, Pittsburgh, 1995, p. 87
6 W. Teunissen, PhD Thesis (2000), Utrecht University, The Netherlands
7 R.T.K. Baker in Carbon Fibers Filaments and Composites (Eds. J.L. Figueiredo, C.A. Bernardo, R.T.K. Baker, and K.J. Hüttinger), NATO ASI series C Vol. 177, Kluwer Academic Publishers, Dordrecht, 1990, p. 405
8 J.L. Figueiredo and C.A. Bernardo in Carbon Fibers Filaments and Composites (Eds. J.L. Figueiredo, C.A. Bernardo, R.T.K. Baker, and K.J. Hüttinger), NATO ASI series C Vol. 177, Kluwer Academic Publishers, Dordrecht, 1990, p. 441
9 A. Sacco in Carbon Fibers Filaments and Composites (Eds. J.L. Figueiredo, C.A. Bernardo, R.T.K. Baker, and K.J. Hüttinger), NATO ASI series C Vol. 177, Kluwer Academic Publishers, Dordrecht, 1990, p. 459
10 N.M. Rodriguez, *J. Mater. Res.* **8-12** (1993), 3233

11 J.R. Anderson, Structure of Metallic Catalysts, Academic Press, London, 1975, p. 81
12 H.P. Boehm, *Adv. Catal.* **16** (1966), 179
13 J.W.Geus, *Stud. Surf. Sci. Catal.* **16** (1983), 1
14 W.M. Prest and R.A. Mosher in Colloids and Surfaces in Reprographic Technology (Eds. M. Hair and M. Croucher), ACS Symposium Series Vol. 200, ACS, Washington, 1982, p. 225
15 M.S.P. Shaffer, X. Fan, and A.H. Windle, *Carbon* **36-11** (1998), 1603
16 K. Nakamoto, Infrared and Raman Spectra of Inorganic and Coordination Compounds 4th edition, John Wiley, New York, 1986, p. 124
17 U. Zielke, K.J. Hüttinger, and W.P. Hoffman, *Carbon* **34-8** (1996), 983
18 P. Painter, M. Starsinic, and M. Coleman in Fourier Transform Infrared Spectroscopy, Applications to Chemical Systems (Eds. J.R. Ferraro and L.J. Basile), Vol. 4, Academic Press, Inc., Orlando, 1985, p. 169
19 D.B. Mawhinney, V. Naumenko, A. Kuznetsova, and J.T. Yates, *J. Am. Chem. Soc.* **122** (2000), 2383
20 J. Chen, M.A. Hamon, H. Hu, Y. Chen, A.M. Rao, P.C. Eklund, and R.C. Haddon, *Science* **282** (1998), 95
21 A. Kuznetsova, D.B. Mawhinney, V. Naumenko, J.T. Yates, J. Liu, and R.E. Smalley, *Chem. Phys. Lett.* **321** (2000), 292
22 H.P. Boehm, *Carbon* **32-5** (1994), 759
23 J.L. Figueiredo, M.F.R. Pereira, M.M.A. Freitas, and J.J.M. Órfão, *Carbon* **37** (1999), 1379
24 V. Gómez-Serrano, F. Piriz-Almeida, C.J. Durán-Valle, and J. Pastor-Villegas, *Carbon* **37** (1999), 1517
25 The Powder Diffraction File, release 1993, International Centre for Diffraction Data

3

Surface Oxidation of Carbon Nanofibres

Abstract

Carbon nanofibres of the fishbone and parallel type were surface-oxidised by several methods. The untreated and oxidised fibres were studied with infrared spectroscopy, thermogravimetric analysis and XPS. Oxidation in a mixture of concentrated nitric and sulfuric acid turned out to be the most effective method for creating oxygen-containing surface groups. This treatment results not only in the formation of carboxyl and carboxylic anhydride groups, but also in the formation of ether-type oxygen groups in between graphitic layers that are puckered at their edges. The infrared results clearly show that the formation of oxygen-containing surface groups occurs at defect sites on the carbon nanofibres and that the oxidation proceeds via carbonyl groups and other oxides to carboxyl and carboxylic anhydride groups. Due to the presence of defects, both types of fibre have about the same surface reactivity. With parallel nanofibres, in contrast to fishbone fibres, the macroscopic structure was severely affected by the HNO_3/H_2SO_4 treatment. Finally, the HNO_3/H_2SO_4-treated fibres show a high wettability by water.

3.1 Introduction

Carbon nanofibres (CNFs) that are obtained by catalytic decomposition of carbon-containing gases on small metal particles are a promising catalyst support material for liquid-phase reactions. The fibres are mechanically strong and can withstand the forces involved in vigorous agitation of the reaction medium. Furthermore, the skeins of fibres possess a mesoporeus macrostructure, which decreases the possibility to encounter diffusion limitation during catalytic reactions in the liquid phase. The structure of the CNFs can be tuned by changing the growth conditions and their hydrophobicity can be controlled by surface oxidation. Moreover, carbon nanofibres are very pure. They contain no other types of carbon, such as carbon onions, fullerenes or amorphous carbon, and no heteroatoms, such as sulphur, are incorporated during synthesis. They are chemically inert and can be used in strongly acidic or basic liquids. When grown in a fluidised bed reactor, carbon nanofibres can be obtained at low cost, making application as a catalyst support material possible.[1] Finally, after deactivation of the catalyst CNFs can be readily combusted to recover the precious metal component of spent catalysts, without leaving ash residues.

To employ carbon nanofibres as a catalyst support it is important to be able to modify their surface, for instance by the introduction of oxygen-containing surface groups. Upon oxidation, the hydrophobic fibres become more hydrophilic. Wetting properties are very important in catalyst preparation and use. Furthermore, a better interaction of the fibres with catalyst precursor complexes can be achieved. It is possible to use oxygen-containing species as anchoring sites for the immobilisation of larger molecules and metal-ligand systems as well. The route via reaction with carboxyl groups is a very feasible one. Therefore, knowledge about the nature and amount of oxygen-containing groups on the surface of CNFs as well as the mechanism of oxidation is essential for the application of CNFs in catalysis.

Classical carbon materials, such as activated carbon and carbon black, are well-known support materials in catalysis. Treatment of these types of carbon with oxidising agents in the gas phase or the liquid phase results in the formation of oxidic groups, which can be either acidic or basic in nature.[2, 3, 4] The oxidation occurs at the edges of the graphitic planes.[2, 5, 6] The presence of acidic groups makes the carbon surface more hydrophilic and decreases the pH of the point of zero charge.[3, 7] The dispersion of an active metal phase on activated carbon catalysts increases with an increasing amount of surface oxygen.[8] The presence of carboxyl groups gives rise to cation exchange properties.[3] Figure 3.1 presents several structures of oxygen-containing groups that can be present on the surface of carbon materials. Carboxyl groups (a) can form carboxylic anhydrides (b) if they are situated at a short distance. Lactonic groups (c) can be present as well. Hydroxyl groups (d) at the edge of graphitic planes would be of phenolic character. The existence of carbonyl groups is very likely. They can

either be isolated (e) or be arranged in a quinone-like way (f). Finally, xanthene- or ether-type oxygen (g) would substitute an edge carbon atom.

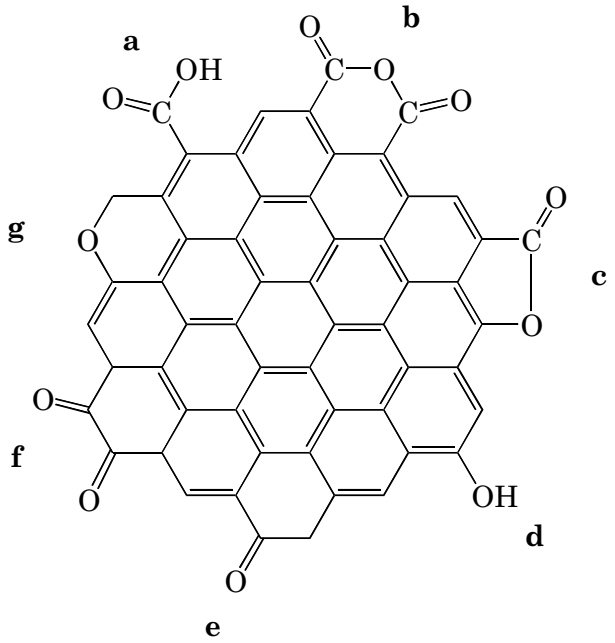

Figure 3.1 Different oxygen-containing surface groups on carbon. a) carboxyl groups b) carboxylic anhydride groups c) lactone groups d) phenol groups e) carbonyl groups f) quinone groups g) xanthene or ether groups.

In contrast to classical carbon materials, the surface oxidation of the relatively new carbon nanotubes and nanofibres has been studied much less up to now. Most of the literature available on the surface oxidation of carbon nanomaterials concerns carbon nanotubes. Raw nanotube material is oxidised for purification purposes: as the nanotubes are much less affected by strong oxidation agents than other forms of carbon, the oxidation results in pure nanotubes.[9-12] Similar procedures are used to obtain opened and shortened tubes.[12-17] Strongly oxidised nanotubes and nanofibres can form stable dispersions in water.[10, 12, 18, 19] From these results it becomes clear that only strong oxidising agents are effective in creating oxygen-containing groups on the surface of carbon nanomaterials. Oxidation of the parallel carbon nanotubes with gas-phase oxygen only results in the formation of hydroxyl and carbonyl groups, whereas with liquid-phase oxidation in concentrated acid mixtures carboxyl groups are formed as well. Liquid-phase oxidation can also be better controlled and proceeds more homogeneously than gas-phase treatments.[20] Although some authors[12, 21] claim that oxidation only occurs at the open end of nanotubes and nanofibres, most reports in literature state that the oxidation proceeds along the full length of

these fibrous materials.[10, 19, 20, 22] The process of oxidation has also been related to defect sites present in the graphene layers.[20, 22]

Much less is known about the oxidation behaviour of carbon nanofibres. Fishbone as well as parallel types of CNFs can be distinguished. With fishbone nanofibres the graphitic planes are oriented at an angle to the fibre axis, whereas with fibres of the parallel type the graphitic layers are oriented parallel to the axis. Some studies on the oxidation of parallel CNFs have been described in literature. [18-21] Hoogenraad *et al.* used carboxyl groups on the surface of parallel fibres for ion exchange synthesis techniques.[23, 24] All their reports concerned parallel CNFs only.

In this investigation we have studied the surface oxidation of parallel and fishbone type carbon nanofibres. The fibres were subjected to several oxidation treatments and, together with other techniques, studied with infrared spectroscopy, thermogravimetric analysis and XPS. It will be shown that the most effective oxidation method is treatment in a mixture of HNO_3 and H_2SO_4. This treatment results, among other groups, in the formation of carboxyl groups on the surface of the fibres. Furthermore, subsurface ether-type groups are formed in between the graphitic layers. The formation of oxygen-containing surface groups occurs at defect sites on the carbon nanofibres. During the oxidation process initially carbonyl, phenol and ether groups are formed, which are subsequently converted into carboxyl, carboxylic anhydride and lactone groups. Not much difference between parallel and fishbone CNFs is observed.

3.2 Experimental

3.2.1 Growth of carbon nanofibres

Carbon nanofibres of the parallel and the fishbone type were produced by catalytic decomposition of CO/H_2 or CH_4 on Ni/Al_2O_3 catalysts, respectively.[23-26]

The Ni/Al_2O_3 catalysts, with 20 or 30 wt% nickel metal loading, were synthesised by the deposition-precipitation technique.[27] Alumina (Alon-C, Degussa) was suspended in an acidified aqueous solution of nickel nitrate (Acros, 99 %) and diluted ammonia was injected within two hours at room temperature under vigorous stirring until the pH had reached a value of 8.5. After overnight stirring, the suspension was filtered, washed, and dried at 120°C. Finally, the catalyst was calcined at 600°C in stagnant air for three hours.

Parallel carbon nanofibres were synthesised in small quantities in a fully automated micro-flow system. Fishbone carbon nanofibres, on the other hand, were grown on a larger scale in a manually operated set-up. Therefore, somewhat different synthesis conditions were employed.

For the growth of parallel carbon nanofibres, 100 mg of the 20 wt% Ni/Al_2O_3 catalyst was reduced at 700°C in 20 % H_2/Ar (flow rate 100 ml/min) in the micro-

flow reactor for two hours. After reduction, the temperature was decreased to 600°C and synthesis gas (20 % CO and 7 % H_2 in Ar, flow rate 100 ml/min) was passed through the reactor during 10 hrs. After reaction, about 0.5 g of parallel CNFs was collected.

For the production of fishbone CNFs, 0.5 g of the 30 wt% Ni/Al_2O_3 catalyst was reduced at 600°C in 14 % H_2/N_2 (flow rate 350 ml/min) in a vertical tubular reactor (diameter 3 cm) for two hours. Subsequently, the temperature was decreased to 570°C and methane (50 % in N_2, flow rate 450 ml/min) was passed through the catalyst bed for 6.5 hours. The yield of fibres amounted to approximately 12 g.

The synthesis of the parallel and fishbone CNFs was confirmed with high resolution TEM.[28]

3.2.2 Oxidation of carbon nanofibres

Fishbone and parallel carbon nanofibres were subjected to several gas-phase and liquid-phase oxidation treatments.

Fishbone CNFs were heated in a flow of 20 % O_2/He at 300°C for 72 hrs, resulting in a 6 % burn-off. Parallel fibres were oxidised in stagnant air at 500°C for 1 hr. In this case the burn-off level was more than 50 %.

Both fishbone and parallel nanofibres were oxidised in refluxing concentrated nitric acid and in a 1:1 mixture of concentrated nitric and sulphuric acid (HNO_3: Lamers & Pleuger, 65 %, pure; H_2SO_4: Merck, 95-97 %, p.a.). The CNFs (3-10 g) were boiled in 40 ml HNO_3 or 80 ml HNO_3/H_2SO_4 for 30 or 60 min. Upon cooling and dilution with demineralised water, the suspensions were filtered over a Teflon membrane filter with a pore diameter of 0.2 μm, washed with water until the washings showed no significant acidity, and dried at 120°C for 16 hrs. Fishbone fibres were also oxidised by boiling for 2 hrs in 30 % H_2O_2 (Merck, 30 %, medical extra pure, stabilised) or in 0.5 M $KMnO_4$ (Merck, cryst. extra pure) in 5 % H_2SO_4. After the permanganate treatment, the fibres were immersed in concentrated hydrochloric acid to remove MnO_2. The oxidised fibres were further thoroughly washed and dried at 120°C for 16 hrs. For the fibres treated with acid or peroxide, material losses were less than 5 %, whereas the permanganate oxidation procedure resulted in a 15 % loss of CNFs.

3.2.3 Characterisation of carbon nanofibres

Both untreated and oxidised material was characterised by nitrogen physisorption, X-ray diffraction (XRD), scanning electron microscopy (SEM), transmission electron microscopy (TEM), infrared spectroscopy (IR), thermogravimetric analysis (TGA), and X-ray photo-electron spectroscopy (XPS).

CNF samples were de-gassed at 120°C in vacuum for at least 16 hours and nitrogen adsorption-desorption isotherms were measured at –196°C on a Micromeretics ASAP 2400 apparatus. Specific surface areas and pore volumes were calculated from the data obtained.

SEM images were obtained on a Philips XL30FEG microscope at an accelerating voltage of 20 kV. TEM samples were prepared by dispersing ground nanofibres in ethanol by ultrasound and drying a drop on a copper grid covered by a holey carbon film. They were imaged in a Philips EM-420 electron microscope operated at an accelerating voltage of 120 kV.

Powder XRD measurements were performed using an ENRAF-NONIUS X-ray diffraction system equipped with a curved position-sensitive INEL detector operating up to a width of 120°2θ. The applied radiation was Co K_α (λ = 1.78897 Å).

Transmission infrared data were recorded on a Perkin Elmer 2000 spectrometer equipped with an air dryer for removal of water vapour and carbon dioxide. One hundred scans were co-added at a resolution of 8 cm^{-1} and a boxcar apodisation. Samples were prepared by thoroughly mixing a small amount of ground nanofibres with pre-dried KBr. Tablets were pressed at 4 tons/cm^2 in vacuum for two minutes. The concentration of the nanofibres ranged from 0.1 to 1 ‰ (m/m). All spectra were baseline corrected.

TGA analyses were carried out on a Netzsch STA-429 thermobalance. The gases evolved during analysis were monitored by a Fisons Thermolab quadropole mass spectrometer, using a capillary situated directly above the sample cup. Samples of 20-100 mg were heated in 60 ml/min Ar or 20 % O_2/Ar at a rate of 300°C/h to 850°C.

The XPS data were obtained with a Vacuum Generators XPS system, using a CLAM-2 hemispherical analyser for electron detection. Non-monochromatic Al(K_α) X-ray radiation was utilised, employing an anode current of 20 mA at 10 keV. The pass energy of the analyser was set at 20 eV.

3.3 Results

N_2-physisorption

The results of the analysis of the N_2-physisorption data for the untreated and the oxidised carbon nanofibres are presented in Table 3.1. Untreated fishbone CNFs have a specific surface area of 103 m^2/g and a pore volume of 0.31 ml/g. The average pore diameter is about 12 nm without any micropores present. Upon oxidation in acid or potassium permanganate, the average pore diameter does not change and no micropores are formed. However, a slight increase in specific surface area and pore volume is observed. Oxidation in peroxide or oxygen did not result in any textural changes.

For the untreated parallel carbon nanofibres, a specific surface area of 158 m^2/g and a pore volume of 1.16 ml/g is found. The relatively open macroscopic structure is reflected in a higher average pore diameter of 29 nm, again without any micropores present. Oxidation in nitric acid results in a slight increase in surface area and pore volume, comparable to the results obtained with the fishbone CNFs. Treatment with HNO_3/H_2SO_4, on the other hand, leads to a considerable decrease in surface area, pore volume, and average pore diameter. However, no micropores are formed. Oxidation in air at 500°C also changes the texture of parallel CNFs severely. The surface area is increased, but the pore volume and the average pore diameter are decreased.

Table 3.1 N_2-physisorption data of untreated and oxidised carbon nanofibres.

	BET surface area (m^2/g)	Pore vol. (ml/g)	Micropore vol. (ml/g)	Average pore diameter (nm)
Fishbone				
Untreated	103	0.31	0.001	12
60 min HNO_3	123	0.30	0.001	10
60 min HNO_3/H_2SO_4	120	0.34	0.001	11
120 min $KMnO_4$-H^+	122	0.37	0.001	12
Parallel				
Untreated	158	1.16	0.004	29
30 min HNO_3	184	1.26	0.002	27
30 min HNO_3/H_2SO_4	116	0.54	0.003	19
60 min 500°C in air	180	0.87	0.012	19

Electron microscopy

Figure 3.2 shows some SEM images of untreated and acid-oxidised fishbone and parallel carbon nanofibres. With fishbone CNFs no significant change was observed after oxidation in HNO_3/H_2SO_4 for 60 minutes (Figure 3.2A and B). However, the SEM images of untreated and 30 min HNO_3/H_2SO_4 oxidised parallel fibres (Figure 3.2C and D) show that the macrostructure of these fibres is severely affected by the oxidative treatment. Upon oxidation, the macrostructure becomes denser.

A TEM study of the fishbone nanofibres did not show much difference between untreated and 60 min HNO_3/H_2SO_4 treated fibres (images not displayed). In both cases, long isolated fibres were found and the structure of individual fibres remained unchanged. Careful examination of bright field and dark field

micrographs gave the impression that the acid-treated fibres became slightly shorter and less ordered. Some indication of surface roughening was found as well. It must be noted that these results are difficult to interpret. Fibre diameters of 15-20 nm with untreated parallel and 20-90 nm with untreated fishbone CNFs were found.

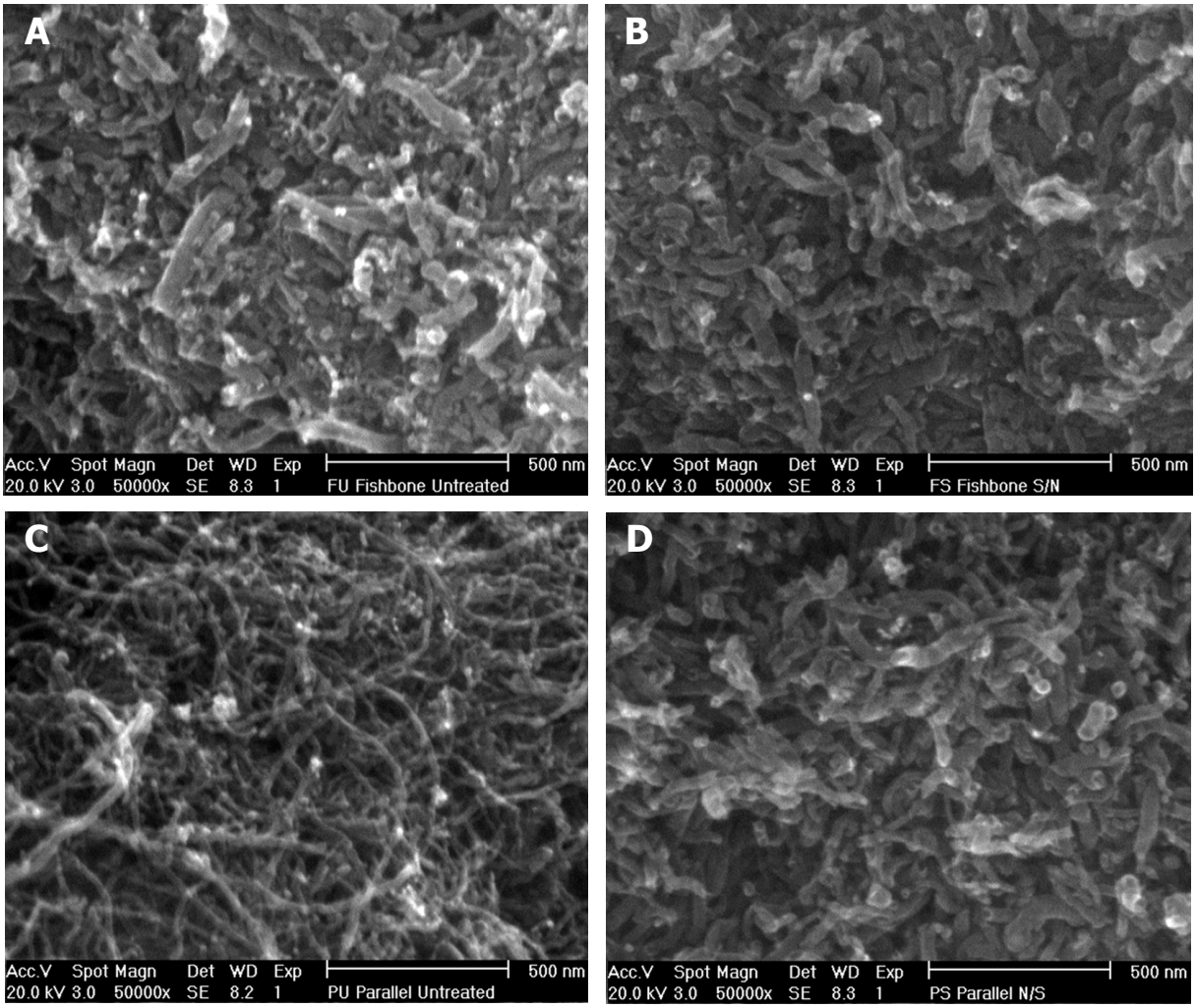

Figure 3.2 SEM micrographs of carbon nanofibres. A) untreated fishbone, B) fishbone 60 min HNO_3/H_2SO_4, C) untreated parallel, and D) parallel 30 min HNO_3/H_2SO_4

X-ray diffraction

The XRD patterns of untreated fishbone CNFs and of fibres that had been treated for 30 min in HNO_3/H_2SO_4 are presented in Figure 3.3. In the pattern of the untreated fibres, several graphite peaks can be distinguished, among which the strongest d(002) reflection at $30^o2\theta$. Furthermore, peaks can be assigned to Ni and Al_2O_3 originating from the growth catalyst used. The oxidised nanofibres

still exhibit all graphite reflections, while the d(002) reflection is not changed in position or width. In addition, no nickel reflections are present anymore and only the alumina reflection at 53°2θ is still visible after oxidation. With the parallel carbon nanofibres similar results were obtained (XRD results not shown).

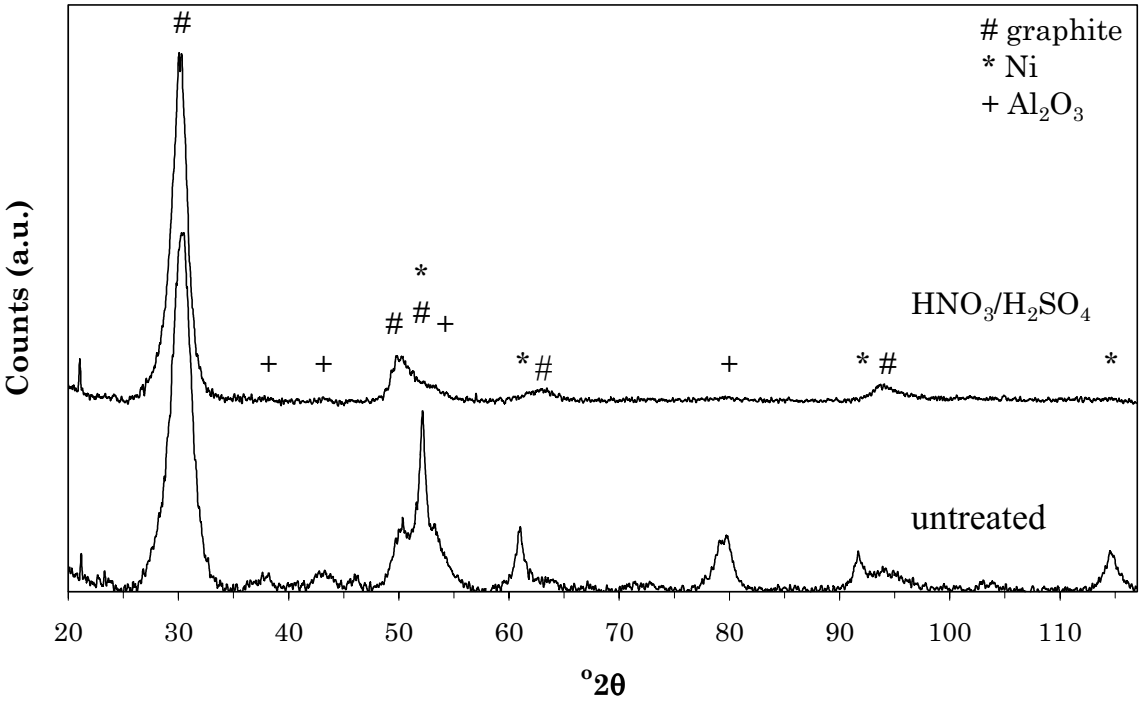

Figure 3.3 XRD diffraction patterns of untreated and 30 min HNO_3/H_2SO_4-treated fishbone carbon nanofibres.

Infrared

The presence of oxygen-containing surface groups on carbon nanofibres was established by infrared spectroscopy. To allow comparison, transmission levels of all spectra were kept approximately the same. It was ascertained that, within the transmission window used, the intensity of the bands did not depend upon the transmission level of the spectra. Figure 3.4 displays the 2000-800 cm^{-1} range of the IR spectra of untreated, 30 min HNO_3/H_2SO_4-, 60 min HNO_3-, and 60 min HNO_3/H_2SO_4-oxidised fishbone carbon nanofibres. All band assignments are summarised in Table 3.2 and all changes observed in the IR spectra after the different oxidative treatments are recapitulated in Table 3.3. The assignment of the bands of the untreated fibres is given and discussed in chapter 2. The absorptions at 1633 and 1384 cm^{-1} are due to water and nitrate, respectively, adsorbed on the KBr and can be discounted.[19, 29-31] The minimum at 1581 cm^{-1} originates from an aromatic ring vibration, while the broad 1200 cm^{-1} absorption

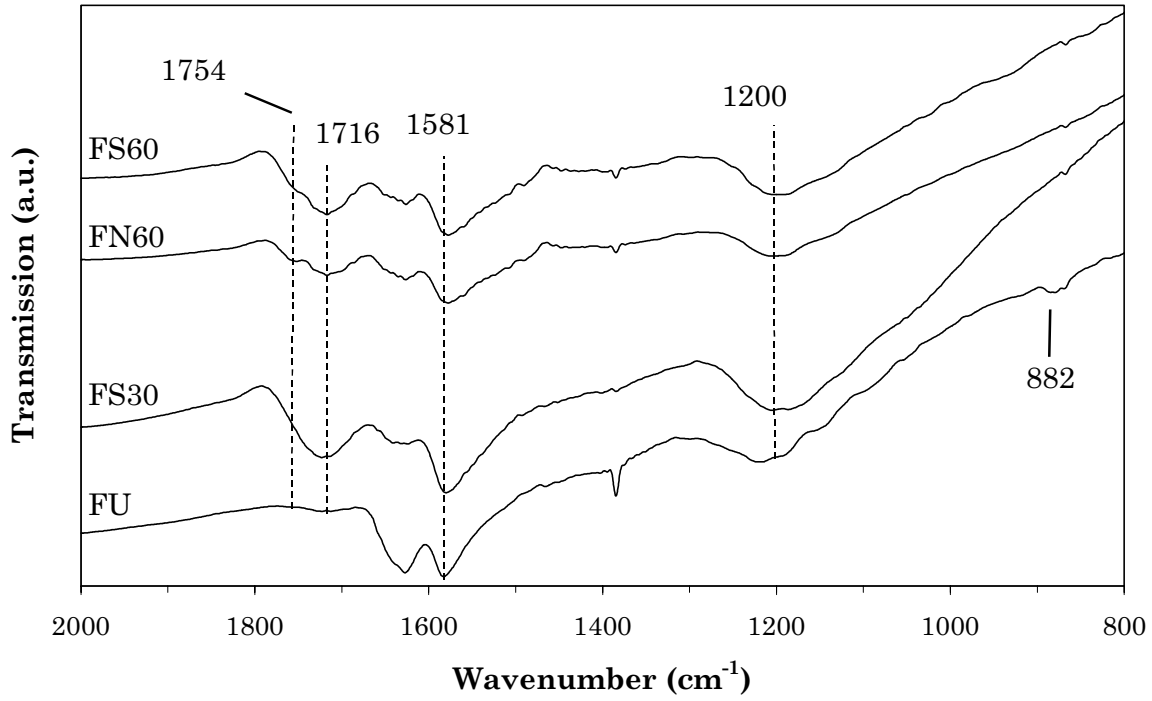

Figure 3.4 IR spectra of untreated (FU), 30 min HNO_3/H_2SO_4- (FS30), 60 min HNO_3- (FN60), and 60 min HNO_3/H_2SO_4- (FS60) oxidised fishbone carbon nanofibres. 2000-800 cm^{-1} range.

Table 3.2 Assignments of infrared absorptions found for untreated and oxidised fishbone and parallel carbon nanofibres.

Wavenumber (cm^{-1})	Assignment	Reference
3012	aromatic C-H stretching	32
2947	CH_2/CH_3 stretching	32
2917-2912	CH_2/CH_3 stretching	32
2846-2841	CH_2/CH_3 stretching	32
1754	C=O stretching anhydride & lactone	3, 19, 29, 35
1725-1714	C=O stretching carbonyl & carboxyl	19, 29, 32, 34
1633	adsorbed water	19, 29
1581-1578	aromatic ring stretching	29, 32, 33
1454	CH_2/CH_3 bending	32, 36
1384	nitrate	30, 31
1217-1188	C-C stretching	29, 32
882-872	isolated aromatic C-H out-of-plane bending	32

Table 3.3 Changes in the IR spectra of fishbone and parallel carbon nanofibres after the different oxidative treatments. Legend: + band appears, - band disappears, i intensity band increases, d intensity band decreases, s band shifts.

Treatment	Observations
Fishbone	
60 min HNO_3	+ 1716, 1754; - 882
30 min HNO_3/H_2SO_4	+ 1716; - 882; i 1200
60 min HNO_3/H_2SO_4	+ 1716, 1754; - 882; d 2947, 2912, 2841
$KMnO_4$-H^+	+ 1716; - 882; i 1200
20 % O_2/He 300°C	no change
H_2O_2	+ 1724
Parallel	
30 min HNO_3	+ 1714; - 872, 1454; i 1200; d 3012, 2947, 2917, 2846
30 min HNO_3/H_2SO_4	+ 1714; - 872, 1454; i 1200; - 3012, 2947, 2917, 2846
air 500°C	+ 1725; s 872; i 1200

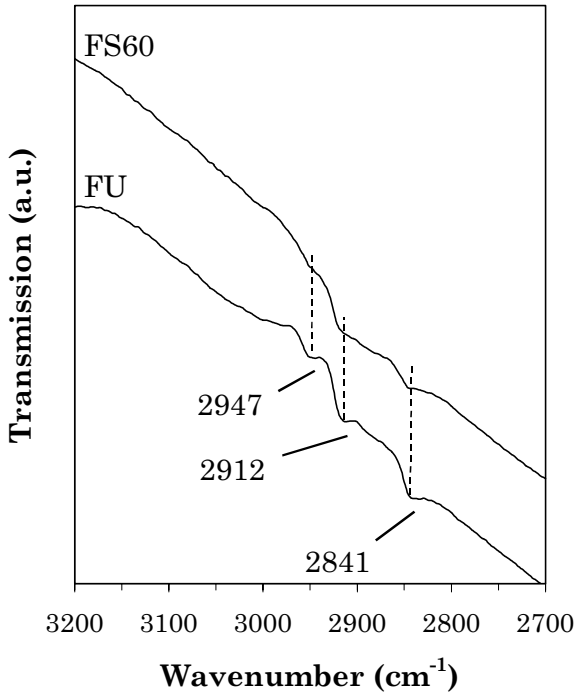

Figure 3.5 IR spectra of untreated (FU) and 60 min HNO_3/H_2SO_4-oxidised (FS60) fishbone carbon nanofibres. 3200-2700 cm^{-1} range.

is attributed to the C-C stretching vibration.[29, 32, 33] The peak at 882 cm^{-1} is ascribed to the isolated aromatic C-H out-of-plane bending mode.[32]

Upon oxidation in acid for 60 minutes, two additional bands appear in the spectrum of the fibres at 1716 and 1754 cm^{-1} (see Figure 3.4). The peak at 1716 cm^{-1} can be assigned to the C=O stretching vibration of carboxyl or carbonyl groups, while that at 1754 cm^{-1} is associated with carboxylic anhydride or lactone groups.[3, 19, 29, 32, 34, 35] The aromatic C-H vibration at 882 cm^{-1} disappears upon oxidation. The intensity of the C=O bands is higher for the HNO_3/H_2SO_4-oxidised fibres than for the HNO_3-treated CNFs. Fibres, treated with HNO_3/H_2SO_4 for only 30 minutes (see Figure 3.4), do not show the band at 1754 cm^{-1}, although it might be obscured by the broad 1716 cm^{-1} absorption. Moreover, the intensity of the 1200 cm^{-1} absorption is significantly enhanced. In this region CO stretching and OH bending vibrations occur as well.[32] Figure 3.5 shows the 3200-2700 cm^{-1} range of the untreated and the 60 min HNO_3/H_2SO_4-oxidised fishbone fibres. The bands at 2947, 2912, and 2841 cm^{-1} arise from CH_2/CH_3 stretching vibrations.[28, 32] Upon oxidation, the intensity of the CH_2/CH_3 minima of the treated sample is decreased considerably.

The spectrum of the fibres treated in oxygen at 300°C is identical to that of untreated fibres. H_2O_2-oxidised fibres, on the other hand, exhibit a weak minimum at 1724 cm^{-1}. Finally, oxidation in $KMnO_4$-H^+ results in a spectrum very similar to that of 30 min HNO_3/H_2SO_4-treated fishbone nanofibres (spectra not shown).

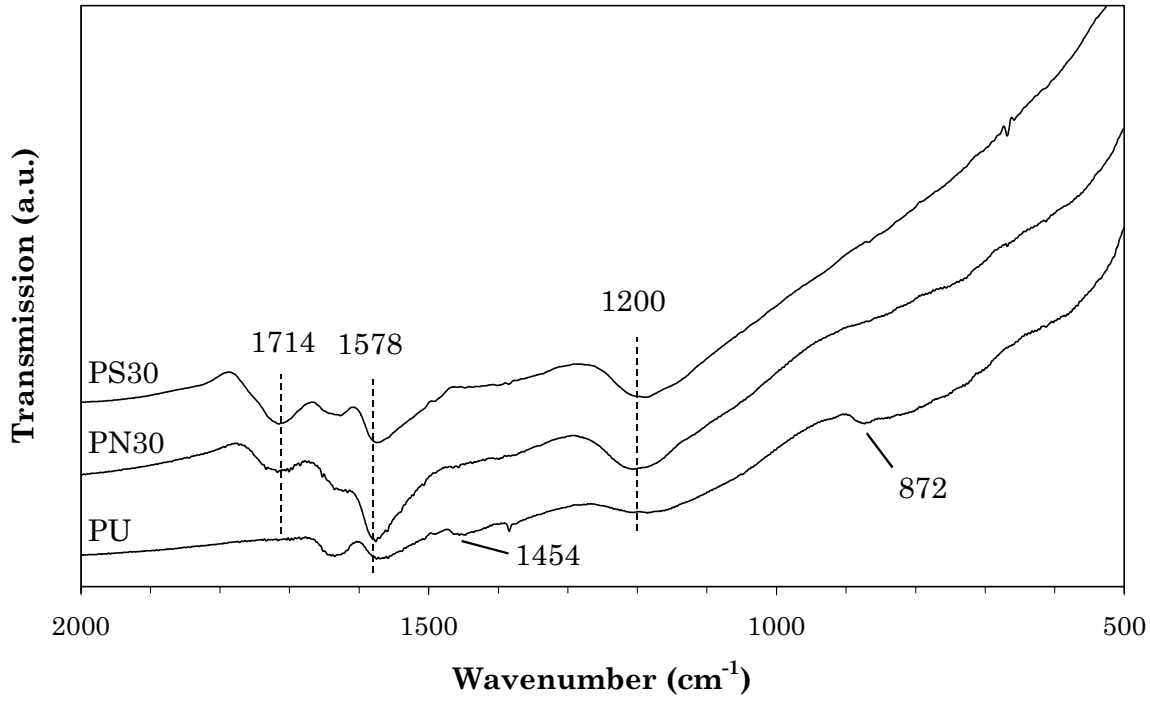

Figure 3.6 IR spectra of untreated (PU), 30 min HNO_3- (PN30), and 30 min HNO_3/H_2SO_4-oxidised (PS30) parallel carbon nanofibres. 2000-500 cm^{-1} range.

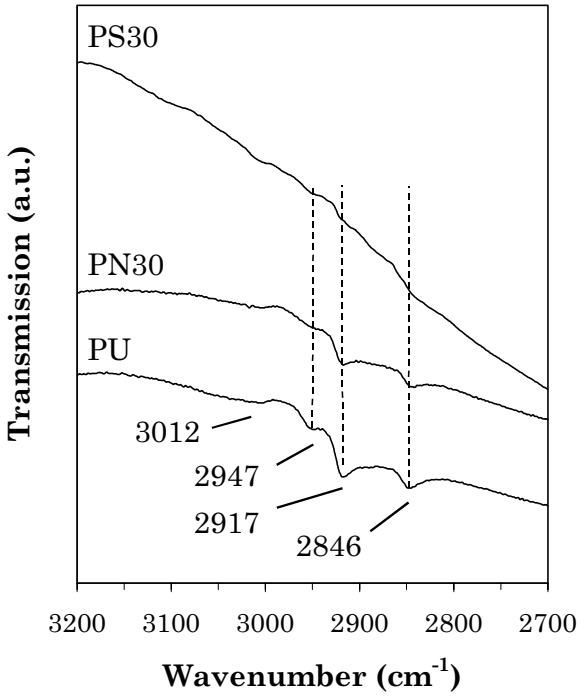

Figure 3.7 IR spectra of untreated (PU), 30 min HNO_3- (PN30), and 30 min HNO_3/H_2SO_4-oxidised (PS30) parallel carbon nanofibres. 3200-2700 range.

Figures 3.6 and 3.7 display the infrared results for the oxidation of parallel fibres in acid. These fibres were oxidised in HNO_3 and HNO_3/H_2SO_4 for only 30 minutes. The band at 1454 cm^{-1} in the spectrum of the untreated fibres is attributed to CH_2/CH_3 bending vibrations.[28, 32, 36] Upon oxidation in acid, the formation of the carbonyl/carboxyl band at 1714 cm^{-1} is accompanied by an increase in intensity of the 1200 cm^{-1} absorption, due to CO and OH groups. The anhydride/lactone band at about 1750 cm^{-1} is lacking, although the absorption might be obscured by the asymmetric 1714 band with the HNO_3/H_2SO_4 treated fibres. Both the CH_2/CH_3 peak at 1454 cm^{-1} and the aromatic C-H vibration at 872 cm^{-1} disappear upon oxidation. The intensity of the CH_2/CH_3 stretching minima and the aromatic C-H stretching vibration at 3012 cm^{-1} in the 3200-2700 cm^{-1} range clearly show a trend (see Figure 3.7). Whereas HNO_3 treatment diminishes the intensity of all bands significantly, with the HNO_3/H_2SO_4 treated fibres no absorptions can be observed anymore.

Air oxidised parallel fibres show a band at 1725 cm^{-1} (spectrum not shown). The 1454 cm^{-1} peak, however, remains present and the 872 cm^{-1} band has shifted to 834 cm^{-1}. The intensity of the 1200 cm^{-1} absorption increases significantly.

Thermogravimetric analysis in inert environment

The results obtained with TGA-MS provide additional information about the oxygen-containing surface groups that have been formed on the carbon nanofibres. Figure 3.8 shows a typical TGA-MS profile (both for fishbone and parallel fibres) for $KMnO_4$-H^+ or acid-oxidised carbon nanofibres (fishbone, 60 min HNO_3/H_2SO_4). A considerable weight loss of more than 8 % is accompanied by the release of H_2O, CO and CO_2. The value of the loss of weight at 850°C is used for further analysis. This value could be reproduced within 2-4 % of the absolute value. Due to the limitations of the experimental set-up, the interpretation of the evolved gas peaks can only be qualitative. Moreover, although the shape of the peaks remained the same in control experiments, the temperature values for the on-set and the maximum of the CO and CO_2 peaks varied. These values, therefore, must also be considered qualitatively.

Figure 3.8 shows that, upon heating in inert, fishbone fibres treated for 60 min with HNO_3/H_2SO_4 release water up to approximately 375°C with a peak at about 150°C and a shoulder at 230°C. The CO_2-profile displays two peaks at about 300°C and 500°C. A shoulder at high temperature (i.e., above 750°C) can be distinguished as well. The CO-liberation pattern exhibits one broad peak with a maximum at around 600°C and a shoulder at higher temperatures. The TGA-MS peak assignments are summarised in Table 3.4. The water peak at around 150°C can be ascribed to physisorbed water.[7] The H_2O shoulder at 230°C may provide

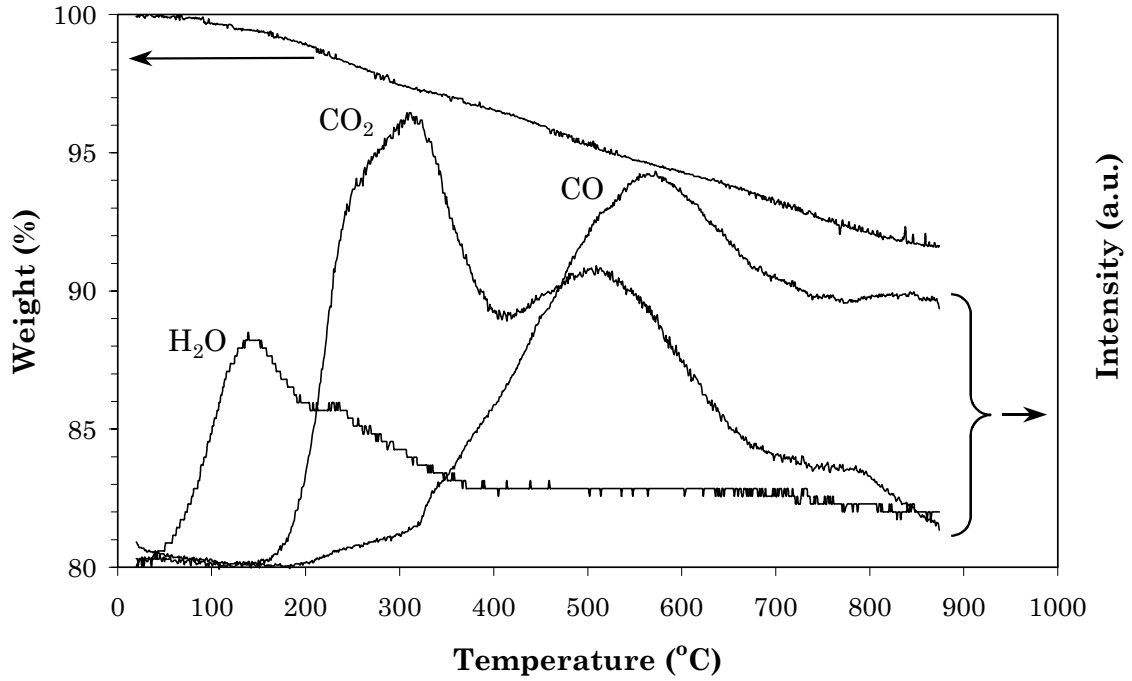

Figure 3.8 Typical TGA-MS pattern in Ar of an acid-oxidised carbon nanofibre (fishbone, 60 min HNO_3/H_2SO_4).

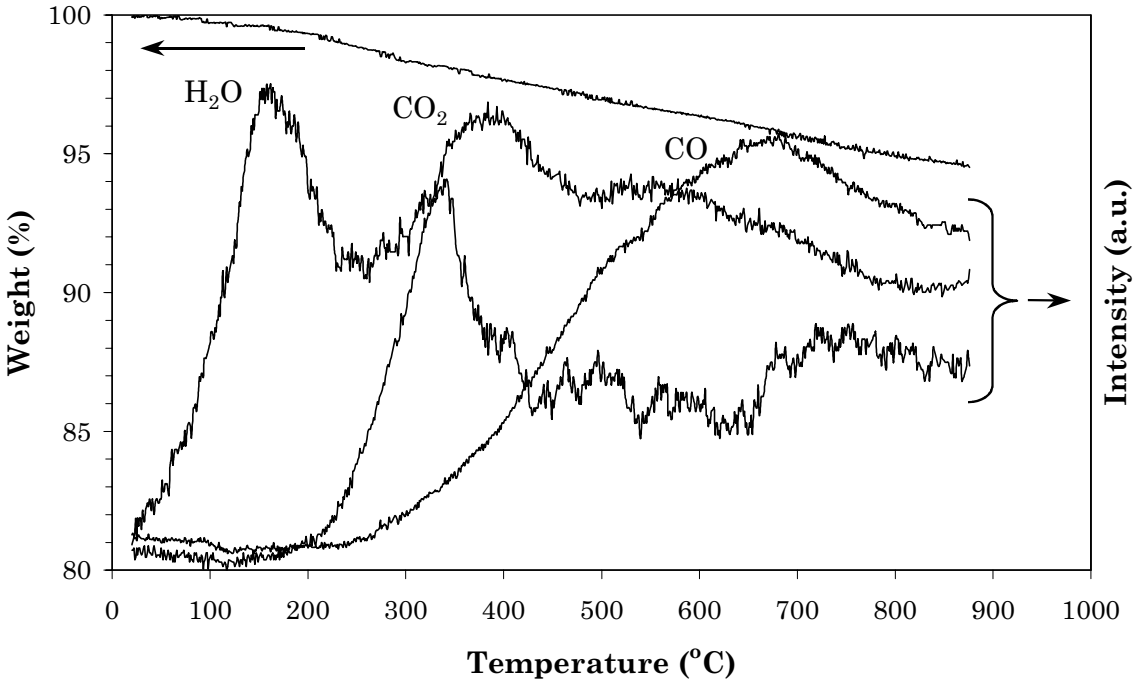

Figure 3.9 TGA-MS pattern in Ar of 30 min HNO_3/H_2SO_4 oxidised fishbone carbon nanofibres.

Table 3.4 Peak assignments of the TGA-MS profiles in Ar.

Peak	Assignment	Reference
H_2O		
150°C	physisorbed water	7
230°C	formation of anhydrides during experiment	7
>300°C	phenols	38
CO_2		
300°C	carboxylic acids	2, 3, 29, 35, 37
500°C	carboxylic anhydrides	3, 7, 35
>750°C	lactones	35
CO		
600°C	phenols, carbonyls, quinones, ethers	7, 35

evidence for the formation of carboxylic anhydrides from adjacent carboxyl groups during the TGA experiment.[7] The first CO_2 peak can undoubtedly be attributed to carboxylic acid functions.[2, 3, 29, 35, 37] Anhydrides, on the other hand, evolve CO_2 and CO at higher temperatures.[3, 7, 35] Thus, the CO_2 evolution at higher temperatures probably originates from anhydrides. The CO_2-shoulder above 750°C may tentatively be assigned to lactonic groups.[35] Considering the CO evolution profile, researchers have been much more cautious to assign specific groups to peaks or shoulders. In general, CO would originate from phenol, carbonyl, quinone, and ether groups.[7, 35]

Fishbone fibres that were treated with HNO_3/H_2SO_4 for only 30 minutes exhibit a somewhat different TGA-MS profile (see Figure 3.9). A second H_2O peak above 300°C appears, which can be ascribed to phenolic groups.[38] Furthermore, the high-temperature CO_2 peak, attributed to carboxylic anhydrides, is merely a shoulder. Finally, the CO evolution pattern has its maximum at a significantly higher temperature (~700°C).

Table 3.5 TGA-MS weight losses in Ar at 850°C after correction for physisorbed water for untreated and oxidised carbon nanofibres.

	Weight loss at 850°C after corr. phys. H_2O (%)
Fishbone	
Untreated	1.4
72 hrs 300°C O_2/He	1.1
120 min H_2O_2	2.0
120 min $KMnO_4$-H^+	4.2
60 min HNO_3	3.9
30 min HNO_3/H_2SO_4	4.3
60 min HNO_3/H_2SO_4	7.0
Parallel	
Untreated	2.5
60 min 500°C in air	6.4
30 min HNO_3	4.5
30 min HNO_3/H_2SO_4	4.9

Untreated carbon nanofibres do not evolve H_2O. Both types of untreated fibre liberate a broad CO band, but only untreated fishbone fibres lose CO_2 above 400°C. The evolved-gas patterns for fibres treated in the gas phase (72 hrs at

300°C in 20 % O_2/He for the fishbone fibres and 1 hr at 500°C in air for the parallel CNFs) are similar to those of the untreated fibres, except that treated parallel nanofibres also show loss of CO_2 above 400°C. Finally, the CO_2 evolution profile of the H_2O_2-treated fishbone carbon nanofibres exhibits a peak at around 300°C, indicative for carboxyl groups. However, no H_2O is evolved.

In Table 3.5 the weight losses at 850°C after correction for the loss of physisorbed water are presented. Figure 3.8 shows that the physisorbed water peak is relatively isolated. Well after the H_2O peak maximum CO_2 starts to evolve. Therefore, the weight loss due to the presence of physisorbed water can be subtracted from the total weight loss at 850°C. It is apparent that, except for the oxygen treatment at 300°C, the weight loss of the oxidised samples is considerably higher than that of the untreated fibres.

Table 3.6 O/C ratios of untreated and 60 min HNO_3/H_2SO_4 oxidised fishbone carbon nanofibres obtained by XPS. Samples were measured either without further pre-treatment or after an *in situ* evacuation at 150°C for one hour.

	O_{1s}/C_{1s} ratio
No pre-treatment	
Untreated	0.22
60 min HNO_3/H_2SO_4	0.36
1 hr vacuum 150°C	
Untreated	0.30
60 min HNO_3/H_2SO_4	0.46

XPS

The surface oxidation of the fishbone CNFs was also studied by measuring the XPS C_{1s} and O_{1s} peaks of untreated fishbone fibres and CNFs oxidised for 60 min in HNO_3/H_2SO_4. The measurements were executed on the same sample before and after an *in situ* evacuation at 150°C for one hour in order to remove physisorbed water. Upon oxidation, no change in the shape of the C_{1s} peak was observed. However, the ratio of the areas of the O_{1s} and C_{1s} peaks changed. The results are shown in Table 3.6. The untreated fibres already contain a considerable amount of oxygen at the surface. After oxidation in HNO_3/H_2SO_4, the O/C ratio increases by about 60 %, independent of the treatment before the XPS measurement.

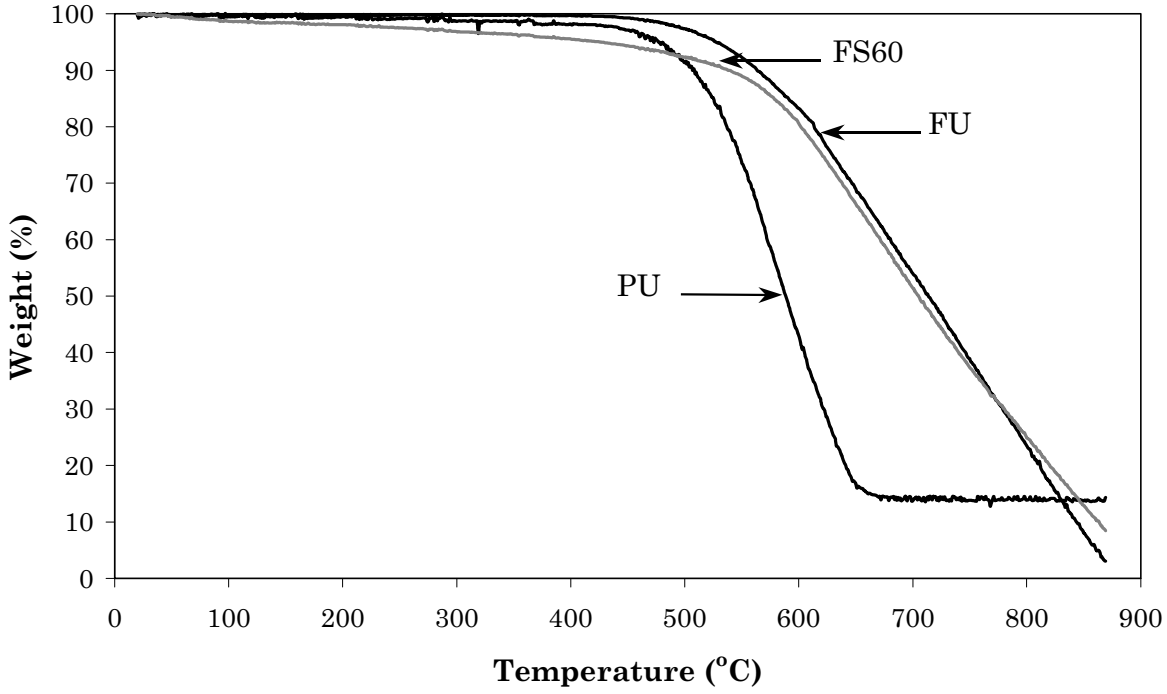

Figure 3.10 TGA profiles in 20 % O_2/Ar of untreated parallel (PU), untreated fishbone (FU), and 60 min HNO_3/H_2SO_4-oxidised fishbone (FS60) carbon nanofibres.

Thermogravimetric analysis in oxidative environment

Thermogravimetric analysis was also performed in 20 % O_2/Ar. These experiments were carried out to gain more knowledge about the crystallinity of the fibres (a lower crystallinity results in a lower on-set temperature of bulk oxidation) and about the effect of surface oxidation on the bulk oxidation of the CNFs. The results for untreated parallel and fishbone carbon nanofibres and fishbone CNFs surface-oxidised for 60 min in HNO_3/H_2SO_4 are shown in Figure 3.10. The on-set of bulk oxidation lies at about 450°C for both the untreated parallel and fishbone CNFs. The loss of weight recorded below this temperature is also observed during TGA in argon alone and is, therefore, not due to bulk oxidation of the fibres. The maximum rate of oxidation occurs at a much lower temperature for the parallel fibres than for the fishbone CNFs. The on-set temperature of bulk oxidation for the surface-oxidised fishbone fibres is about 530°C. The weight loss detected below this temperature originates from the decomposition of surface oxides (see above). Finally, above about 600°C, the bulk oxidation curves for the untreated and surface-oxidised fishbone CNFs are identical.

Hydrophobicity

In order to roughly assess the hydrophobicity of the untreated and acid-oxidised fishbone carbon nanofibres, ground samples of 1 mg were ultrasonically dispersed in 5 ml 1:1 water/hexane mixtures for 30 minutes. The CNFs were first wetted with either water or hexane. The results are shown in Figure 3.11. The upper layer is the hexane layer. Most of the untreated CNFs are situated at the water/hexane interface and some can be detected in the hexane layer (Fig. 3.11A). The 60 min HNO_3/H_2SO_4-oxidised fibres are well-dispersed in the water layer (Fig. 3.11C). No light penetrates this layer anymore. With the 60 min HNO_3-treated fibres, however, the results depend on the liquid the fibres are first wetted with. When these CNFs are first wetted with water, they badly disperse in the water layer, forming larger aggregates, and are found on the bottom of the test tube too (Fig. 3.11B). When the fibres are first wetted with hexane, they show only affinity for the water/hexane interface, comparable to the untreated fibres.

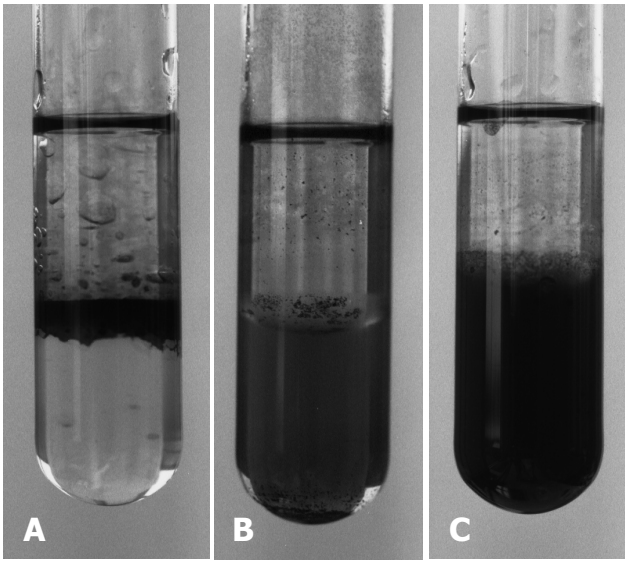

Figure 3.11 Fishbone carbon nanofibres dispersed in H_2O/hexane. A) untreated, B) 60 min HNO_3, and C) 60 min HNO_3/H_2SO_4. Hexane is the upper layer.

3.4 Discussion

Macrostructure

Upon oxidation of fishbone carbon nanofibres in acid or $KMnO_4$-H^+, a slight increase in specific surface area and pore volume is observed. The weight fraction of the original Ni/Al_2O_3 growth catalyst in the untreated fibres is only about 4 %. Therefore, changes in surface area and pore volume cannot be attributed to removal of the growth catalyst upon oxidation. As there are no micropores

present, the measured surface area can be regarded as the external surface of the fibres. Accordingly, the pore volume is the space in between the fibres. Apparently, upon oxidation in HNO_3/H_2SO_4 or $KMnO_4$-H^+, the macrostructure of this type of fibres becomes a little less dense, resulting in a slightly higher pore volume. Surface roughening of the fibres by the oxidation treatments can explain the increase in surface area. Another explanation could be a difference in affinity of N_2 for untreated and oxidised fibres, resulting in a different surface area. The changes in macrostructure are probably small, as they are not observable with SEM.

With the parallel fibres oxidation in HNO_3/H_2SO_4 or air results in considerable changes in the macrostructure. The treatment in the acid mixture probably breaks or completely removes some fibres, which induces a partial collapse of the macroscopic structure. The decrease in surface area, pore volume, and average pore diameter might suggest that the thinner fibres are preferentially removed. After oxidation in air the macroscopic structure collapses as well, which leads to a decrease in the pore volume. A considerable enhancement of surface roughness probably causes the increase in surface area. This is supported by the appearance of some micropores after gas-phase oxidation. The N_2-physisorption results are supported by the SEM data, which show a change in macrostructure for the parallel fibres only. Furthermore, the SEM images of untreated parallel fibres and CNFs treated for 30 min in HNO_3/H_2SO_4 suggest that, upon oxidation in the acid mixture, indeed thinner fibres are removed. The diameter of the fibres after oxidation in HNO_3/H_2SO_4 seems to be larger on average than before oxidation.

From the BET surface areas average fibre diameters can be calculated, assuming that the fibres have the same density as graphite (2.25 kg/m^3).[39] Fenelonov *et al.*[40] found that the density of fishbone fibres is only slightly lower than that of graphite. With the untreated fishbone CNFs an average fibre diameter of 17 nm is thus calculated, and with untreated parallel fibres a value of 11 nm is acquired. The values observed with TEM, however, are much larger. The diameter of the fishbone fibres varies between 20 and 90 nm and that of parallel fibres ranges from 15 to 20 nm. These differences can be explained by assuming that the fibres have a considerable surface roughness. This explanation is supported by a publication of Shaikhutdinov,[41] who performed scanning tunnelling microscopy (STM) experiments on fishbone CNFs, grown from methane on a Ni/Al_2O_3 catalyst. He found substantial differences in height on the surface of the fibres and calculated the ratio of the measured topographical surface area and the geometrical area of a corresponding reference plane. Values of 4.2 and 4.7 were obtained, indicating a major enhancement of the surface area as compared to the surface area of fibres with smooth surfaces. Considering these results, it is likely that the surface of the fibres used in this study is rough as well. Then, we can also conclude that the surface roughness of the fishbone CNFs is appreciably higher than that of the parallel fibres, as the difference between

the diameters resulting from N_2-physisorption and TEM is larger. This is likely, taking into account the difference in orientation of the graphitic planes with both types of fibre. Upon oxidation, the surface roughness can be further enhanced. The considerable surface roughness of parallel fibres is another strong indication of the high concentration of defects on this type of fibre.

In conclusion, the texture of fishbone carbon nanofibres was not significantly affected by any of the oxidation methods. With parallel CNFs, on the other hand, only treatment in nitric acid left the macroscopic structure intact. HNO_3/H_2SO_4 or air at 500°C changed the texture drastically. Furthermore, we conclude that the surface of the fibres is considerably roughened.

Graphitic structure

To establish whether the graphitic structure of the carbon nanofibres is affected by the oxidation treatments, XRD and TEM measurements were carried out. After oxidation, all graphite peaks are still visible in the XRD spectrum of both fishbone and parallel fibres. This observation demonstrates that the graphitic structure of the fibres is unchanged after treatment. Furthermore, the nickel and most of the alumina reflections disappear. This indicates that oxidation in HNO_3/H_2SO_4 removes most of the nickel and alumina present in between the untreated fibres. Separate experiments revealed that boiling in HNO_3 or HNO_3/H_2SO_4 for 60 min resulted in a loss of the alumina support of at least 50 and 80 %, respectively.

Also, the TEM study of fishbone CNFs did not indicate any changes in the structure of the fibres. Therefore, we conclude that although some of the oxidation treatments affect the texture of parallel carbon nanofibres, the graphitic structure of both fishbone and parallel fibres is maintained after gas-phase or liquid-phase oxidation treatments.

Infrared

The infrared results show that gas-phase oxygen and H_2O_2 oxidation treatments are not suitable to create surface oxides on carbon nanofibres (see also Table 3.3). Only after considerable burn-off, C=O containing surface oxides result from gas-phase treatments. The H_2O_2-oxidised fibres only show a weak C=O band. It can thus be concluded that $KMnO_4$-H^+ or acid treatment is necessary to produce a considerable amount of surface oxides without affecting the macroscopic structure of the fibres. Oxidation in HNO_3/H_2SO_4 is found the most effective method. Not much difference is observed between fishbone and parallel CNFs. Unfortunately, no distinction could be made between carbonyl and carboxyl groups. Therefore, we conclude that the presence of carboxyl groups is very likely as there are carboxylic anhydride groups present as well, though their presence has not unambiguously been demonstrated with infrared.

An important conclusion can be drawn from a comparison of the spectra of untreated and oxidised fibres. We showed that the CH_2/CH_3 band at 1454 cm^{-1}

and the aromatic C-H minimum at about 875 cm^{-1} disappear due to liquid-phase oxidation and that the CH_2/CH_3 peaks in the 3000-2800 cm^{-1} range are clearly affected. With the fishbone fibres, a significant decrease in intensity of the CH_2/CH_3 bands in the 3000-2800 cm^{-1} range is observed after HNO_3/H_2SO_4 treatment. The parallel fibres show a decrease in intensity of these bands after oxidation with HNO_3 and a total disappearance of these peaks after the treatment in HNO_3/H_2SO_4. In chapter 2, we have concluded that the bands attributed to CH_2/CH_3 vibrations originate from defects in the graphitic structure of the carbon nanofibres. The above-described results clearly show that the formation of oxygen-containing surface groups occurs at defect sites on the CNFs. With the parallel fibres, all defect carbon-hydrogen bonds are converted into carbon-oxygen bonds. With the fishbone fibres, on the other hand, only part of all defect CH sites are transformed. We have argued that the graphitic planes of fishbone fibres end in CH_2/CH_3 groups.[28] Consequently, due to spacial restrictions not all carbon-hydrogen bonds can be converted into carbon-oxygen bonds. It is also likely that the acid treatment creates new defects. Upon oxidation in air, the carbon-hydrogen bonds do not disappear. In other words, gas-phase oxidation does not initiate on defect sites on carbon nanofibres. Considering that not much difference exists between fishbone and parallel CNFs, we conclude that the surface reactivity of both types of fibre is about the same due to high defect concentrations.

The spectra of fishbone fibres oxidised for 30 min in HNO_3/H_2SO_4 show an increase of the intensity of the 1200 cm^{-1} absorption, whereas fishbone fibres oxidised for 60 min do not. In this region of the spectrum CO stretching and OH bending vibrations overlap with the broad CC stretching mode.[32] Furthermore, upon oxidation for 30 minutes, only carbonyl or carboxyl groups are observed, whereas treatment for 60 minutes results in the formation of carboxylic anhydride or lactone groups as well. Gustafson *et al.*[42] stated that during the initial stages of oxidation phenol and carbonyl groups are formed. Upon continuation of the oxidation, these groups are converted into carboxyl groups. It is also stated in literature that with the most vigorous oxidation agents, such as HNO_3/H_2SO_4, preferentially carboxylic groups are formed.[6, 20] We can, therefore, conclude that oxidation for 60 minutes in HNO_3/H_2SO_4 mainly results in the formation of carboxylic groups on the surface and that, consequently, the intensity of the 1200 cm^{-1} absorption does not increase observably. Oxidation for only 30 minutes, on the other hand, results in a mixture of different surface oxides and, thus, in an increase of the 1200 cm^{-1} absorption. The appearance of the 1754 cm^{-1} band after oxidation for 60 minutes is in accordance with the above explanation. Oxidation for a longer period of time in HNO_3/H_2SO_4 leads, at the cost of carbonyl groups and other oxides, to a higher concentration of carboxyl groups which, subsequently, can react to carboxylic anhydrides.

In summary, with IR it is shown that oxidation in acid or potassium permanganate is necessary to create surface oxides on carbon nanofibres.

Treatment with HNO_3/H_2SO_4 appears to be the most effective method. The results show that the formation of oxygen-containing surface groups occurs at defect sites on the carbon nanofibres and that the oxidation proceeds via carbonyl groups and other oxides to carboxyl and carboxylic anhydride groups. The surface reactivity of both types of fibre is about the same due to their high defect concentrations.

Thermogravimetric analysis in inert environment and XPS

The acid- and $KMnO_4$-H^+-treated fibres undoubtedly have carboxyl groups on their surface. In addition, carboxylic anhydrides are formed as well as other CO-evolving surface oxides. Untreated fibres already possess some oxygen-containing surface groups. With the fishbone fibres, some of these are carboxylic anhydride or lactonic groups, because the CO_2 is liberated at higher temperatures. Not much difference between fishbone and parallel carbon nanofibres is observed. Comparison of the TGA-MS profiles of fishbone CNFs treated in HNO_3/H_2SO_4 for 30 and 60 min confirm the oxidation mechanism found with infrared. Oxidation for 30 minutes results in the presence of phenolic groups and in less carboxylic anhydride groups than treatment for a longer period of time. Furthermore, as the CO evolution profiles are different, CO-evolving oxides are present in a different ratio on both kinds of oxidised fibres.

As the weight loss is related to the amount of oxygen-containing surface groups, its value is a measure for the concentration of surface oxides. From Table 3.5 it is apparent that oxidation in HNO_3/H_2SO_4 is the most effective method in creating oxygen groups. With parallel fibres treatment at 500°C in air also results in a considerable amount of oxidic surface groups, but more than 50 % of the fibres is lost due to burn-off. Moreover, only the liquid-phase treatments succeed in creating carboxyl groups on the surface of the fibres. Although not much difference between parallel and fishbone carbon nanofibres is found, it seems that the parallel fibres are more severely affected by the oxidation treatments than the fishbone fibres. However, the difference in surface area should also be taken into account.

The results obtained with TGA-MS correlate well with the IR data. Both techniques indicate that treatment in HNO_3/H_2SO_4 is the most effective oxidation treatment. Moreover, both techniques point to the presence of carboxyl and carboxylic anhydride groups on the surface of the carbon nanofibres. Because the evolved gas profiles should only be considered qualitatively, a CO_2/CO ratio cannot be calculated. It is, therefore, difficult to quantify the amount of CO-evolving surface oxides present on the nanofibres. The infrared results may indicate that after treatment in HNO_3/H_2SO_4 for 60 minutes mostly carboxyl and carboxylic anhydrides have been formed. However, TGA-MS seems to contradict this finding as CO is liberated up to high temperatures. The CO could originate solely from carbonyl groups, which vibrate at around 1700 cm^{-1} and not in the 1200 cm^{-1} range, but the presence of ether-type oxygen is likely as well.

Although no quantification of the evolved gases is possible, the weight losses give information about the amount of oxygen-containing groups on the carbon nanofibres. If one assumes that CO and CO_2 are evolved in a 1:1 ratio, the surface coverage of oxygen-containing groups would be about 10 groups per nm^2 for the fishbone fibres treated for 60 min in HNO_3/H_2SO_4 (7 % weight loss, 120 m^2/g). This value is clearly too elevated to include the surface only. Further examination of the mass spectrometry data showed no loss of NO_x or SO_x, originating from HNO_3 or H_2SO_4, during TGA. Furthermore, up to a mass of 100, additional peaks were only found at mass 12, 16, and 32. The signal-to-noise ratio of these peaks indicate that their intensity is low to very low. The XPS measurements, which did not show any N or S on the surface of the fibres, confirm the TGA results. Hoogenraad[23] also found a weight loss of about 10 wt% for parallel fibres grown out of supported Fe particles and treated for 60 min in nitric acid. Therefore, it seems that the weight losses recorded are relevant and that these solely come from oxygen-containing groups.

The TGA-MS results are supported by the XPS results, which show high O/C ratios on the CNFs. The finding that the C_{1s} peak does not change shape upon oxidation can be explained by taking into account the penetration dept of XPS of about 2 nm for carbon. Most of the carbon that is detected is situated below the surface of the fibres and, consequently, the fraction of carbon that is bonded to oxygen is low and a change in peak shape cannot be observed. The O/C ratios can be converted to a number of oxygen atoms per square meter by standard techniques, using a fit program.[43] With the untreated CNFs before pre-treatment a value of $1.2*10^{19}$ atoms/m^2 (12/nm^2) is obtained and with the oxidised fibres after pre-treatment the number amounts to $2.5*10^{19}$ atoms/m^2 (25/nm^2). It should be kept in mind that the untreated fibres contain about 4 wt% of Al_2O_3. This amount of alumina could already be responsible for $0.7*10^{19}$ oxygen atoms/m^2 (7 nm^2), still leaving an appreciable number of 5 oxygen atoms per nm^2. Upon oxidation in HNO_3/H_2SO_4, about 80 % of the Al_2O_3 is removed. We can, therefore, estimate that the amount of oxygen exclusively present on the fibres increases by a factor of 4 to 5 upon oxidation for 60 minutes in HNO_3/H_2SO_4. The obtained ratio of the oxygen atoms present before and after oxidation in HNO_3/H_2SO_4 agrees well with the results obtained with TGA-MS.

Although the relative change in oxygen content of the untreated and the oxidised CNFs is reliable, the absolute values that were obtained are very high. $1.2*10^{19}$ atoms/m^2 would already constitute a monolayer of oxygen. However, the number of oxygen atoms per unit surface area was calculated from the XPS data by assuming a perfectly smooth surface of the carbon nanofibres. It was already argued above that the CNFs have a considerable surface roughness and that a surface enhancement factor of 4 is not unlikely for fishbone fibres. The concentration of oxygen on the surface of the fibres would, therefore, only be one quarter of the value obtained with XPS. Even then, it can be doubted if all of the oxygen can be accommodated solely at the surface of the carbon nanofibres.

The increase in the O/C ratio after the evacuation treatment at 150°C for both the untreated and the oxidised fibres is striking. The opposite effect was expected, because the treatment should remove physisorbed water. This effect may be explained by assuming that oxygen-containing groups are present in between the graphite sheets of the fibres and that the oxygen moves towards the surface of the fibres upon treatment in high vacuum. This explanation would support the other results obtained with XPS and TGA.

Values for the concentration of surface oxides on activated carbons and graphite wear dust, mentioned by experts in base titration, are about one group per nm^2. [2, 3, 44] However, it is also stated in literature that chemical titration fails to account for more than 50 % of the oxygen content found by elemental analysis.[2, 3, 35] Hennig[5] has shown that oxygen is only bound at the edge planes of graphite. He also found that the oxygen content exceeded the number of peripheral carbon atoms significantly. According to Hennig it is likely that part of the oxygen is bound in between the carbon layers forming ether links between adjacent layers. He stated that the graphite lattice would only be slightly contracted by the oxygen atoms. This idea was later confirmed by Boehm, who added that the carbon layers should be puckered at their edges.[2, 3] Others mention the possibility of the formation of graphitic oxide at the first external layers of carbon fibres or graphite by $KMnO_4$-H_2SO_4 or anodic oxidation in sulphuric acid or sulphate solutions.[37, 45, 46] Indeed, many authors find very high oxygen concentrations on carbons. Thermal desorption and nitrogen physisorption data by Figueiredo[35] show that not all the oxygen detected by TPD can be accommodated on the surface of activated carbons. Several XPS studies have revealed that for strongly oxidised multi-walled carbon nanotubes and parallel carbon nanofibres up to 15 % of the carbon atoms were bonded to oxygen.[10, 20, 47] As the probing depth of XPS is about 2 nm for carbon, five to six carbon layers are analysed by XPS. If the oxide groups would be solely present at the surface of the nanomaterials, almost all surface carbons should be bonded to oxygen. This seems highly unlikely, taking also into account that Mawhinney[22] found that only about 4 % of the carbon atoms of single-walled carbon nanotubes had been oxidised after treatment in HNO_3/H_2SO_4.

In summary, weight losses found by TGA-MS are due to the release of CO and CO_2 from oxygen-containing groups on the carbon nanofibres. As the concentration of these groups is too high to be accommodated solely at the surface of the CNFs, it is likely that ether-type oxygen groups have been formed in between the graphite layers that are puckered at their edges. This finding is supported by the XPS data. With IR we found that the oxidation of carbon nanofibres occurs at defect sites on the surface of the fibres. The very high values for the concentration of oxygen-containing groups on CNFs found with XPS and TGA, pointing to a total coverage of the surface with surface oxides, seem to contradict this mechanism. This difference may be explained by assuming that

the whole surface of the CNFs is defect rich. With fishbone fibres this is possible, as the exposed graphitic edges probably do not end in a perfect aromatic ring. With parallel fibres, on one hand, this assumption is more unlikely, considering the orientation of the graphitic planes and TEM studies.[28] On the other hand, the observed surface roughness points to an imperfect structure of at least the outer graphitic plane. Another explanation could be that surface oxidation initiates at defect sites and then continues towards more perfectly structured regions.

Thermogravimetric analysis in oxidative environment

Because of the identical on-set temperature of bulk oxidation, we conclude that the parallel and fishbone CNFs have about the same crystallinity. Once started, the parallel fibres oxidise much easier and faster than the fishbone CNFs, resulting in a maximum rate of oxidation at lower temperature. As the TGA measurement is a dynamic process, these differences could be due to differences in diffusion of oxygen to the fibres. The parallel fibres are less dense than the fishbone CNFs (see N_2-physisorption results) and therefore less material is used for TGA. However, because the oxidation process proceeds at high temperature, we feel that it is more likely that the intrinsic burning properties of the parallel fibres are different. Once started at a parallel graphene sheet, oxidation should be able to proceed very rapidly along the whole sheet, in contrast to the fishbone oriented graphene sheets.

From a comparison between the untreated and the surface-oxidised fishbone carbon nanofibres several conclusions can be drawn. Firstly, as the maximum rate of bulk oxidation is identical, the rate of oxidation is not affected by nickel present in the untreated fibres. Secondly, as the on-set temperatures are different, the bulk oxidation of the untreated fibres is probably preceded by a surface oxidation step. The HNO_3/H_2SO_4 treated fibres are already surface-oxidised and they, therefore, display a higher on-set temperature. Finally, by taking into account that the bulk oxidation proceeds identically for treated and untreated fibres, we can conclude that the number of defect sites on the fishbone CNFs has not changed significantly after surface oxidation in HNO_3/H_2SO_4. In other words, defects already present on the fibres were surface-oxidised by the acid mixture. This finding supports the results obtained with IR.

Hydrophobicity

It is well-known that the hydrophobic surface of carbons becomes hydrophilic when covered with oxygen-containing groups.[3] Generally, acidic surface oxides, such as carboxyl groups, are thought to be responsible for the change in affinity for liquids.[4] The untreated CNFs do not show much affinity for hexane. Probably this solvent is too apolar for the fishbone fibres. This can be due to the low concentration of acidic (i.e., CO_2 evolving) surface oxides already present on the fibres, as was evident from the TGA-MS results. Hoogenraad[23] also performed test tube experiments with water/nitrobenzene mixtures and parallel fibres. The

untreated fibres were completely situated in the organic phase, whereas after treatment in HNO_3 the CNFs showed some affinity for water. Although we saw with TGA-MS that untreated parallel fibres do not have acidic surface oxides, the results obtained by Hoogenraad indicate that the liquids need some polarity for wetting untreated carbon nanofibres.

The results obtained with the HNO_3-treated carbon nanofibres are very interesting. Clearly, the affinity of these treated fibres for water or hexane is influenced by the liquid they are first contacted with. The results might be explained by assuming that there are small hydrophobic and hydrophilic domains on the surface of such treated fibres. Accordingly, the fibres have an affinity both for polar and apolar liquids. When the fibres are first wetted with a polar liquid, the apolar liquid will be repelled and vice versa.

Only when a strong oxidation treatment in HNO_3/H_2SO_4 is executed, a sufficiently high affinity for water is achieved. In this case, the fibres disperse very well in water, independent of the wetting sequence. These results are in accordance with the findings of Esumi *et al.*[18], who oxidised parallel nanofibres in HNO_3/H_2SO_4 and performed sedimentation experiments in water, ethanol, and hexane.

These results are important for the use of carbon nanofibres as a catalyst support in liquid-phase reactions. By various methods of surface oxidation, the hydrophobicity of the fibres can be fine-tuned. Consequently, it now becomes possible to design a catalyst support with optimal wetting properties for the desired reaction medium.

3.5 Conclusions

Fishbone and parallel carbon nanofibres have been oxidatively treated in the gas phase and in the liquid phase. We found that with fishbone CNFs the macroscopic structure was not severely affected by any of the treatments used. Only treatment in HNO_3, on the other hand, left the macroscopic structure of the parallel fibres intact. However, the graphitic structure of both types of fibre was maintained after oxidation. Because of the discrepancy between the average diameter of the fibres calculated from N_2-physisorption data and that observed with TEM, it is likely that the CNFs have a considerable surface roughness. This is supported by a comparison of TGA-MS and XPS data.

IR and TGA-MS measurements revealed that the most effective oxidation method is treatment in a mixture of HNO_3 and H_2SO_4. This treatment results, amongst other groups, in the formation of carboxyl and carboxylic anhydride groups on the surface of the fibres. Treatment for a longer period of time gives more surface oxides. The high weight losses found with TGA-MS can be solely ascribed to CO/CO_2 evolution from oxygen-containing surface groups. This is supported by XPS data. As the concentration of these groups is too high to be

accommodated exclusively at the surface of the CNFs, it is concluded that upon oxidation also ether-type oxygen groups are formed in between the graphite layers that are puckered at their edges. Not much difference between parallel and fishbone CNFs was observed.

The IR results clearly show that the formation of oxygen-containing surface groups occurs at defect sites on the carbon nanofibres. This finding is supported by TGA experiments in oxidative environment. For the parallel fibres, all defect CH bonds react to CO bonds. For the fishbone CNFs, on the other hand, only part of all CH sites is transformed due to spacial restrictions on the edge surface. Considering that not much difference exists between fishbone and parallel CNFs, we conclude that the surface reactivity of both types of fibre is about the same due to high defect densities. From the IR and TGA-MS data it also becomes evident that the surface oxidation of CNFs proceeds via carbonyl groups and other oxides to carboxylic and carboxylic anhydride groups.

From TGA experiments in oxidative environment it can be concluded that parallel and fishbone fibres have about the same crystallinity. Parallel fibres, however, combust faster due to the orientation of the graphene sheets. It is also shown that the bulk oxidation of fishbone fibres is preceded by a surface oxidation step.

Dispersion experiments with differently treated fishbone carbon nanofibres made clear that only HNO_3/H_2SO_4-treated fibres have a good affinity for water. Although untreated fibres are hydrophobic, a liquid needs some polarity for wetting untreated fibres. HNO_3-oxidised fibres have hydrophilic and hydrophobic domains on their surface. Their wetting behaviour is, therefore, dependent on the solvent the fibres are first contacted with.

The results described above are important for the modification of carbon nanofibres and for the synthesis of carbon nanofibre-supported catalysts.

Acknowledgements

We wish to acknowledge prof. dr. J.H. van der Maas of the Department of Vibrational Spectroscopy, Utrecht University, for the discussions about the IR data. We also thank A. Broersma for the generation of the TGA data.

References

1 K.P. de Jong and J.W. Geus, *Catal. Rev.-Sci. Eng.* **42-4** (2000), 481
2 H.P. Boehm, *Adv. Catal.* **16** (1966), 179
3 H.P. Boehm, *Carbon* **32-5** (1994), 759
4 S.S. Barton, M.J.B. Evans, E. Halliop, and J.A.F. MacDonald, *Carbon* **35-9** (1997), 1361
5 G.R. Hennig, Proc. 5th Conf. Carbon Vol. I, Pergamon Press, Oxford, England, 1962, p. 143
6 J.R. Anderson, Structure of Metallic Catalysts, Academic Press, London, 1975, p. 81
7 C. Moreno-Castilla, M.A. Ferro-García, J.P. Joly, I. Bautista-Toledo, F. Carrasco-Marín, and J. Rivera-Utrilla, *Langmuir* **11** (1995), 4386
8 C. Prado-Burguete, A. Linares-Solano, F. Rodríguez-Reinoso, and C. Salinas-Martínez de Lecea, *J. Catal.* **115** (1989), 98
9 T.W. Ebbesen, P.M. Ajayan, H. Hiura, and K. Tanigaki, *Nature* **367** (1994), 519
10 H. Hiura, T.W. Ebbesen, and K. Tanigaki, *Adv. Mater.* **7-3** (1995), 275
11 R.M. Lago, S.C. Tsang, K.L.Lu, Y.K. Chen, and M.L.H. Green, *J. Chem. Soc., Chem. Commun.* (1995), 1355
12 J. Liu, A.G. Rinzler, H. Dai, J.H. Hafner, R.K. Bradley, P.J. Boul, A. Lu, T. Iverson, K. Shelimov, C.B. Huffman, F. Rodriguez-Macias, Y.-S. Shon, T.R. Lee, D.T. Colbert, and R.E. Smalley, *Science* **280** (1998), 1253
13 S.C. Tsang, Y.K. Chen, P.J.F. Harris, and M.L.H. Green, *Nature* **372** (1994), 159
14 K.C. Hwang, *J. Chem. Soc., Chem. Commun.* (1995), 173
15 J. Cook, J. Sloan, and M.L.H. Green, *Chemistry & Industry* (1996), 600
16 M.A. Hamon, J. Chen, H. Hu, Y. Chen, M.E. Itkis, A.M. Rao, P.C. Eklund, and R.C. Haddon, *Adv. Mater.* **11-10** (1999), 834
17 A. Kuznetsova, D.B. Mawhinney, V. Naumenko, J.T. Yates, J. Liu, and R.E. Smalley, *Chem. Phys. Lett.* **321** (2000), 292
18 K. Esumi, M. Ishigami, A. Nakajima, K. Sawada, and H. Honda, *Carbon* **34** (1996), 279
19 M.S.P. Shaffer, X. Fan, and A.H. Windle, *Carbon* **36-11** (1998), 1603
20 H. Ago, T. Kugler, F. Cacialli, W.R. Salaneck, M.S.P. Shaffer, A.H. Windle, and R.H. Friend, *J. Phys. Chem. B* **103** (1999), 8116
21 Z. Jia, Z. Wang, J. Liang, B. Wei, and D. Wu, *Carbon* **37** (1999), 903
22 D.B. Mawhinney, V. Naumenko, A. Kuznetsova, J.T. Yates, J. Liu, and R.E. Smalley, *Chem. Phys. Lett.* **324** (2000), 213
23 M.S. Hoogenraad, PhD Thesis (1995), Utrecht University, The Netherlands
24 M.S. Hoogenraad, M.F. Onwezen, A.J. van Dillen, and J.W. Geus, *Stud. Surf. Sci. Catal.* **101** (1995), 1331
25 J.W. Geus, M.S. Hoogenraad, and A.J. van Dillen in Synthesis and Properties of Advanced Catalytic Materials (Eds. E. Iglesia, P.W. Lednor, D.A. Nagaki, and L.T. Thompson), Materials Research Society Pittsburgh, Pittsburgh, 1995, p. 87
26 W. Teunissen, PhD Thesis (2000), Utrecht University, The Netherlands
27 J.W.Geus, *Stud. Surf. Sci. Catal.* **16** (1983), 1
28 See Chapter 2 of this thesis

29 W.M. Prest and R.A. Mosher in Colloids and Surfaces in Reprographic Technology (Eds. M. Hair and M. Croucher), ACS Symposium Series Vol. 200, ACS, Washington, 1982, p. 225
30 K. Nakamoto, Infrared and Raman Spectra of Inorganic and Coordination Compounds 4th edition, John Wiley, New York, 1986, p. 124
31 U. Zielke, K.J. Hüttinger, and W.P. Hoffman, *Carbon* **34-8** (1996), 983
32 P. Painter, M. Starsinic, and M. Coleman in Fourier Transform Infrared Spectroscopy, Applications to Chemical Systems (Eds. J.R. Ferraro, L.J. Basile), Vol. 4, Academic Press, Inc., Orlando, 1985, p. 169
33 D.B. Mawhinney, V. Naumenko, A. Kuznetsova, and J.T. Yates, *J. Am. Chem. Soc.* **122** (2000), 2383
34 J. Chen, M.A. Hamon, H. Hu, Y. Chen, A.M. Rao, P.C. Eklund, and R.C. Haddon, *Science* **282** (1998), 95
35 J.L. Figueiredo, M.F.R. Pereira, M.M.A. Freitas, and J.J.M. Órfão, *Carbon* **37** (1999), 1379
36 V. Gómez-Serrano, F. Piriz-Almeida, C.J. Durán-Valle, and J. Pastor-Villegas, *Carbon* **37** (1999), 1517
37 P. Ehrburger in Carbon Fibers Filaments and Composites (Eds. J.L. Figueiredo, C.A. Bernardo, R.T.K. Baker, and K.J. Hüttinger), NATO ASI series C Vol. 177, Kluwer Academic Publishers, Dordrecht, 1990, p. 147
38 K. Miura and T. Morimoto, *Langmuir* **10** (1994), 807
39 CRC Handbook of Chemistry and Physics (Eds. R.C. Weast, M.J. Astle, and W.H. Beyer), 69th Ed., CRC Press Inc., Boca Raton, 1988, p. B-82
40 V.B. Fenelonov, L.B. Avdeeva, V.I. Zheivot, L.G. Okkel', O.V. Goncharova, and L.G. Pimneva, *Kinet. Catal. (Eng. Trans.)* **34-3** (1993), 483
41 Sh. K. Shaikhutdinov, *Kinet. Catal. (Eng. Trans.)* **36-4** (1995), 549
42 B.-W. Chun, C. R. Davis, Q. He, and R.R. Gustafson, *Carbon* **30-2** (1992), 177
43 O.L.J. Gijzeman, unpublished results
44 T. Kuretzki, PhD Thesis (1993), Ludwig-Maximilian University München, Germany
45 A.D. Jannakoudakis, P.D. Jannakoudakis, and E. Theodoriou, *J. Appl. Electrochem.* **20** (1990), 619
46 J.W. Peckett, P. Trens, R.D. Gougeon, A. Pöppl, R.K. Harris, and M.J. Hudson, *Carbon* **38** (2000), 345
47 C. Niu, E.K. Sichel, R. Hoch, D. Moy, and H. Tennent, *Appl. Phys. Lett.* **70-11** (1997), 1480

4

Rhodium Complexes with (N-phenyl) Anthranilic Acid Ligands as Catalysts for Hydrogenation

Abstract

The complexes of rhodium with N-phenyl anthranilic acid and anthranilic acid were synthesised and their structure was investigated with IR spectroscopy. It appears that rhodium interacts with N-phenyl anthranilic acid via the carboxyl and the amine groups. With anthranilic acid the bond with the amine could not be unambiguously established. X-ray diffraction and elemental analysis data suggest that the complexes are not pure and that the presence of Rh(0) is likely. Catalytic hydrogenation results and mercury poisoning experiments confirm the presence of Rh(0).

4.1 Introduction

Chekrii and co-workers first reported on the rhodium complex with N-phenyl anthranilic acid in the late 1960s.[1-4] The structure of N-phenyl anthranilic acid (PAA) is shown in Figure 4.1. The DMF-soluble Rh(I) complex with PAA was claimed to be a remarkably active hydrogenation catalyst. Benzene and polyaromatic compounds were hydrogenated rapidly at room temperature and one atmosphere hydrogen pressure.[3] The complex was synthesised by heating equimolar amounts of rhodium chloride and N-phenyl anthranilic acid in ethanol followed by treatment of the reaction mixture with sodium borohydride.[4] Various analytical data suggested that the RhPAA complex was a dimer.[1] The monosubstituted ring of the N-phenyl anthranilate ion forms a half-sandwich structure through π-bonds with one of the rhodium atoms, while the ionised carboxyl group co-ordinates to the second rhodium atom.

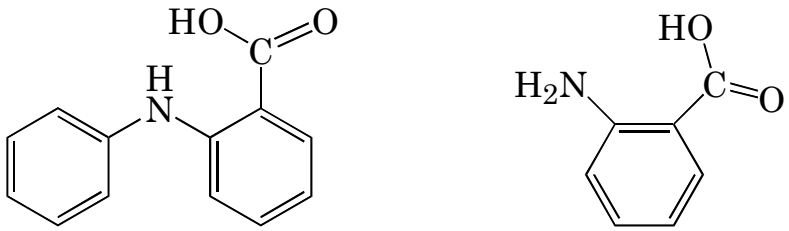

PAA AA

Figure 4.1 Structure of N-phenyl anthranilic acid (PAA) and anthranilic acid (AA).

The RhPAA catalyst has not received much attention, although it was the first to be used in the hydrogenation of aromatic compounds. It has been doubted severely whether the catalyst is really homogeneous.[5-7] The proposed structure has also been disputed. The suggested interaction of rhodium with the phenyl ring was based on very small changes in the frequencies of the infrared bands of the C-H vibrations. In the absence of other data such slight band shifts are a questionable proof of metal-ring bonds.[7, 8] Moreover, the infrared spectrum published differed from the tabulated band shifts.[2] Finally, the elemental analysis data were not in agreement with the proposed structure.[7]

In view of the above uncertainties concerning the structure and the homogeneity of the RhPAA complex, Borowski and co-workers studied the system again.[7] The synthesis procedure of Chekrii *et al.* was modified in order to prevent reduction of unreacted rhodium chloride to metallic rhodium by sodium borohydride. Borowski *et al.* also pointed out that the ethanol used in the synthesis is already capable of reducing the rhodium to Rh(0). Based on an infrared study of the complex, it was established that the Rh was co-ordinated to

the ionised carboxyl group in a bridging mode (bridging between two Rh atoms, thus suggesting a dimer structure). No interaction of Rh with the phenyl or the amine group was found. However, a definite structure of the RhPAA complex could not be given. It was postulated that the complex consisted of large molecules linked by carboxylate and/or chloride ions. In other publications[9-11] the use of the rhodium complex with anthranilic acid, presumably obtained according to the same synthesis procedure, was reported. The structure of anthranilic acid (AA) is given in Figure 4.1. Borowski and co-workers claimed hydrogenation activities of RhPAA to be an order of magnitude higher than those found by Chekrii *et al.*. Contrary to the first-mentioned report, these publications stated that in both complexes the rhodium binds to the ligand by co-ordination to both the carboxylate and the amine group. Unfortunately, no experimental evidence was given.

The current interest in the RhPAA and RhAA complexes was raised by publications by Holy, [6, 12, 13] who immobilised these catalysts onto polystyrene. Upon immobilisation of RhPAA, the catalyst did not display any activity. When anthranilic acid instead of N-phenyl anthranilic acid was used, a highly active immobilised Rh(I) catalyst was obtained. The immobilised complex also showed hydrogenation activity with Ni as the active metal.[14] The anthranilic acid complex is an example of an immobilised complex that does not have a well-defined homogeneous analogue. However, polystyrene is not a very suitable support material for application of the catalyst in an industrial environment. In our laboratory, we intend to immobilise the RhAA complex onto carbon nanofibres (CNFs), which are mechanically strong and have a mesoporous macrostructure. In order to be able to execute the immobilisation, more knowledge is needed about the homogeneous RhPAA and RhAA systems. More insight is desired about the factors that influence the synthesis procedure and more information should be obtained about the interaction of Rh with the different functional groups of PAA and AA. Furthermore, the homogeneity of the complexes has to be thoroughly checked.

In this study, we have performed the synthesis of RhPAA and RhAA based on the procedure used by Borowski.[7] The interaction of the ligands with Rh was studied with IR spectroscopy. Emphasis was put on investigating whether the complexes are genuinely homogeneous. One of the techniques used was mercury poisoning, a well-described and accepted technique in literature.[15-19] Mercury selectively poisons the catalytic activity of metal particles and not that of homogeneous complexes. Therefore, addition of mercury can establish whether the catalytic activity originates from a metal complex or from small metal particles. It will be shown that Rh interacts with PAA via the carboxyl and the amine group, whereas with AA the bond with the amine could not be established definitively. The systems turned out to be impure and the presence of Rh(0) is very likely.

4.2 Experimental

4.2.1 Synthesis of rhodium (N-phenyl) anthranilic acid

The synthesis procedure of rhodium (N-phenyl) anthranilic acid [Rh(P)AA] was derived from the preparation method used by Borowski.[7] Every synthesis step was carried out under a nitrogen atmosphere, using standard Schlenk techniques. Solvents (demineralised water and *pro analyse* ethanol from Merck) were de-gassed by vacuum suction prior to use. Anthranilic acid (98+ %), N-phenyl anthranilic acid (98 %), and $RhCl_3 \cdot 2H_2O$ (99.9 %) were purchased from Acros. $NaBH_4$ (99 %) was obtained from Alfa.

Equimolar amounts of $RhCl_3 \cdot 2H_2O$ (1.00 g, 4 mmole) and N-phenyl anthranilic acid (0.85 g, 4 mmole) in 50 ml water-ethanol (2:1) were refluxed for 1 hour. Upon cooling, the dark green-black precipitate was separated from the light pink-red solution by centrifugation and decantation, washed with water-ethanol (2:1), and dried under vacuum (yield 1.1 g). The RhPAA complex was reduced with sodium borohydride by re-suspension in 50 ml water-ethanol (2:1) at 0°C and slow addition of $NaBH_4$ (0.4 g, 0.01 mole) in 4 ml water (0°C) under vigorous stirring, whereupon the colour of the suspension darkened. The reduced complex was separated by centrifugation and decantation, washed with water-ethanol (2:1), and dried under vacuum (yield 0.7 g).

Equimolar amounts of $RhCl_3 \cdot 2H_2O$ (1.00 g, 4 mmole) and anthranilic acid (0.52 g, 4 mmole) in 50 ml water-ethanol (2:1) were refluxed for 1 and 20 hours. Upon cooling, the precipitate was separated by centrifugation and decantation, washed with water-ethanol (2:1), and dried under vacuum. Refluxing for 1 and 20 hours resulted in yields of 0.4 and 0.6 g, respectively. Upon refluxing for 1 hour, the colour of the precipitate was green-brown, whereas after reaction for 20 hours the colour had changed to black. In both cases the colour of the solution was yellow-orange. The RhAA complex was reduced with sodium borohydride by re-suspension in 50 ml water-ethanol (2:1) at 0°C and slow addition of $NaBH_4$ (0.4 g, 0.01 mole) in 4 ml water (0°C) under vigorous stirring. The reduced complex was separated by centrifugation and decantation, washed with water-ethanol (2:1), and dried under vacuum (yield 0.5 g for the 20-hrs synthesis). The colour of the RhAA complex that was refluxed for only 1 hour changed to black upon reduction with $NaBH_4$.

For reasons of comparison, metallic Rh on carbon nanofibres (Rh/CNFs, 1 wt%) was prepared by heating under reflux 3.0 g of fishbone carbon nanofibres in a solution of 73 mg $RhCl_3 \cdot 2H_2O$ in ethanol for two hours. The catalyst was filtered from the colourless solution, washed with ethanol and air-dried.

4.2.2 Characterisation of rhodium (N-phenyl)anthranilic acid

Elemental analyses were performed by Dornis und Kolbe, Mikroanalytisches Laboratorium (Mülheim, Germany).

Powder XRD measurements were carried out using an ENRAF-NONIUS X-ray diffraction system equipped with a curved position-sensitive INEL detector operating up to a width of 120 $^{o}2\theta$. The applied radiation was Co K_α (λ = 1.78897 Å). Powdered samples and dispersions in de-gassed silicon grease (under N_2) were prepared.

Transmission infrared data were recorded on a Perkin Elmer 2000 spectrometer equipped with an air dryer for removal of water vapour and carbon dioxide. One hundred scans were co-added at a resolution of 4 cm^{-1} and a boxcar apodisation. Samples were prepared by dispersion of the complexes in de-gassed paraffin oil (spectroscopy grade) under N_2 (measured between NaCl windows) as well as by dispersion in pre-dried KBr. Tablets were pressed at 4 tons/cm^2 in vacuum for two minutes. Sample concentrations were about 1 % (m/m) in KBr.

4.2.3 Catalytic test experiments

General

The catalytic activity of the Rh complexes and the Rh/CNFs catalyst for the hydrogenation of cyclohexene was measured in a semi-batch slurry reactor, operated at a constant pressure of 1200 mbar H_2. The thermostated, double-walled reaction vessel was equipped with vertical baffles and a gas-tight stirrer with a hollow shaft and blades for gas recirculation. The stirrer was operated at 2000 rpm. Solvent (N, N-dimethylformamide [DMF], Merck p.a.) and reactant (cyclohexene, Acros 99 %) were de-gassed by vacuum suction prior to use. During reaction, the hydrogen consumption was automatically monitored by a mass flow meter. It was assured that, under the conditions used, the rate of dissolution of H_2 in DMF was higher than the maximum measurable rate of H_2-uptake.

In a typical experiment, the reaction vessel was evacuated and filled with N_2, whereafter a solution of the complex in DMF (14-18 mg in 100 ml DMF, 500 mg for Rh/CNFs) was transferred into the vessel under a stream of nitrogen. Next, the reactor was thermostated at 25°C, evacuated, filled with H_2, and pressurised. The reaction was started by injection of 0.5-5 ml cyclohexene with a syringe and was allowed to proceed until total hydrogenation of the cyclohexene.

Mercury poisoning experiments

A first catalytic run was executed with 1 ml cyclohexene to check the activity of the catalyst under investigation. After total hydrogenation of the added reactant, another dose of 5 ml of cyclohexene was injected. The hydrogenation of the second dose of cyclohexene was stopped after 3 minutes by turning off the

stirrer, removal of the H_2 by evacuation, and addition of N_2. Next, the temperature was raised to 50°C and mercury (mole ratio of Hg-to-Rh 300:1) was injected with a syringe. After stirring for 3 hours at this temperature, the reaction mixture was cooled to 25°C, H_2 was admitted and the catalytic run was continued.

4.3 Results

4.3.1 Characterisation

General

The very dark brown to black complexes turned out to be only sparingly soluble in organic solvents. The RhAA complex is soluble in DMF up to about 0.1 g/l, while the RhPAA complex is soluble in DMF (> 1 g/l), 3-pentanon (~0.5 g/l), pyridine (~0.6 g/l, and tetrahydrofuran (~0.4 g/l). Due to the low solubility of the complexes, we were not able to obtain NMR spectra on a Varian Inova 300 MHz spectrometer in DMF/benzene-d6. Furthermore, attempts to crystallise the complexes from DMF solutions (in an ethanol vapour environment) failed. The attempts only led to the formation of metallic rhodium.

Elemental analysis

Table 4.1 represents the results of the elemental analysis of RhPAA and RhAA. The relative content of carbon, hydrogen, nitrogen, and chlorine was determined. The rhodium and oxygen content could not be assessed.

Table 4.1 Results of the elemental analysis of rhodium N-phenyl anthranilic acid (RhPAA) and rhodium anthranilic acid (RhAA).

	C (%)	H (%)	N (%)	Cl (%)
RhPAA	40.69	3.70	2.97	0.65
RhAA	26.08	3.05	3.23	4.63

X-ray diffraction

The X-ray diffraction patterns of RhPAA and RhAA measured in air show typical rhodium metal reflections at d-values of 2.196, 1.902, 1.345, and 1.147 Å (diffraction patterns not shown). The width at half height of these peaks was used to calculate the average rhodium particle diameter using the Scherrer equation.[20] Average particle sizes of 5-6 nm were found. Besides the Rh peaks, the X-ray pattern of RhAA did not show any other reflections. The diffractogram of RhPAA, however, exhibited some sharp peaks at low 2θ values (< 20°2θ).

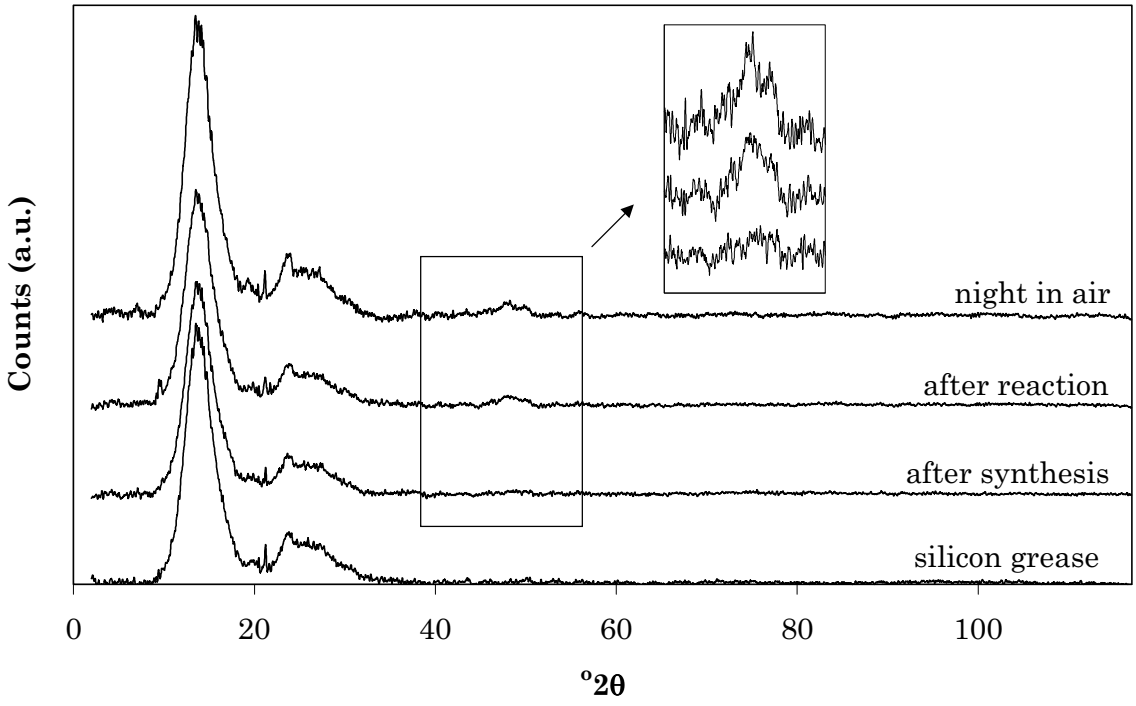

Figure 4.2 XRD patterns of RhPAA in silicon grease after several treatments.

In order to establish whether metallic rhodium is already present in the complexes after synthesis or whether the metal is formed after contact with air, the complexes were also measured in silicon grease. Figure 4.2 displays the results for RhPAA. As shown, the diffractogram of silicon grease alone already shows some peaks between 9 and 32°2θ. Due to the dispersion in silicon grease, the intensity of all rhodium peaks decreased considerably and only the most intense Rh d(111) reflection at 48.1°2θ could be monitored. After synthesis, the RhPAA complex does not show any metallic rhodium. However, after reaction or after contact with air for one night some metallic rhodium can be detected. The measurement after reaction was repeated and in this case no Rh(0) was detected. The RhAA complex also showed no rhodium after synthesis, whereas after one night in air the metal was evident in the X-ray pattern.

The average particle size of the 1 wt% Rh/CNFs catalyst was also determined with XRD. The average diameter found was 11 nm.

Infrared

First, spectra of the complexes were measured in paraffin oil before and after exposure to air for several days. No difference in the spectra was found and, therefore, all other spectra were obtained with KBr disks.

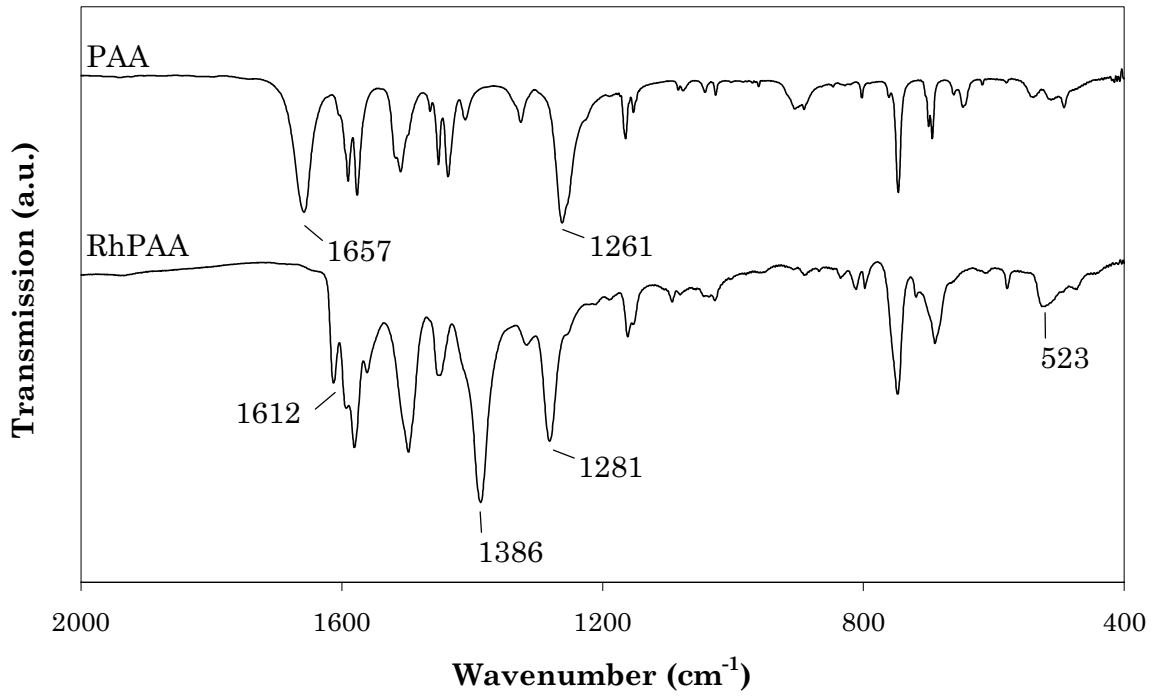

Figure 4.3 Infrared spectra of N-phenyl anthranilic acid (PAA) and rhodium N-phenyl anthranilic acid (RhPAA).

Figure 4.3 shows the infrared spectra of N-phenyl anthranilic acid (PAA) and rhodium N-phenyl anthranilic acid (RhPAA). The assignments of relevant bands are summarised in Table 4.2. Besides aromatic ring and other vibrations, two important vibrations at 1657 cm^{-1} and 1261 cm^{-1} occur in the spectrum of PAA. The band at 1657 cm^{-1} is attributed to the C=O stretching vibration of the carboxyl group[2, 21] and that at 1261 cm^{-1} can be ascribed to the C-N stretching vibration.[21] Upon complexation with rhodium, the C=O stretching vibration disappears and two peaks at 1612 and 1386 cm^{-1} emerge. The two peaks are assigned to the antisymmetric and the symmetric stretching vibration of the ionised carboxylate group, respectively.[2, 21] Furthermore, the C-N stretching vibration at 1261 cm^{-1} shifts 20 cm^{-1} to 1281 cm^{-1}. The new broad band at 523 cm^{-1} originates from the Rh-N stretching vibration.[22] Finally, the N-H stretching vibration at 3334 cm^{-1} is broadened and slightly shifted to 3343 cm^{-1} (band not

shown in Figure 4.3). When the complex had been 'aged' for several months under N_2, a weak band at 1643 cm^{-1} was present. This absorption probably originates from the C=O stretching vibration of the carboxyl group. The results described above were reproduced with repeated syntheses of the complex.

Table 4.2 Assignments of relevant bands in the spectra of PAA, RhPAA, AA, and RhAA.

Wavenumber (cm^{-1})	Assignment	Reference
1664-1657	C=O stretching	2, 21
1612-1610	antisymmetric COO^- stretching	2, 21
1531	NH_2 bending	21
1392-1386	symmetric COO^- stretching	2, 21
1281-1261	C-N stretching	21
523	Rh-N stretching	22

Figure 4.4 represents the spectra of anthranilic acid (AA) and the rhodium anthranilic acid complex (RhAA). As the spectrum of anthranilic acid is very rich in the region displayed, the assignment of relevant bands is more difficult than with N-phenyl anthranilic acid. However, the C=O stretching vibration at 1664 cm^{-1} can easily be distinguished. Similar to N-phenyl anthranilic acid the carboxyl group ionises upon complexation, resulting in the antisymmetric and symmetric COO^- stretching vibrations at 1610 and 1392 cm^{-1}, respectively. Additionally, a band appears at 1531 cm^{-1}, which can be ascribed to a NH_2 bending vibration. This peak could be the shifted absorption that is visible as a shoulder at 1554 cm^{-1} in the spectrum of anthranilic acid. In contrast to the spectrum of RhPAA, that of RhAA displays only few bands and hardly resembles the spectrum of anthranilic acid. Therefore, no statements can be made about the presence or absence of Rh-N and C-N vibrations. Lastly, the two sharp N-H stretching vibrations at 3324 and 3237 cm^{-1} are replaced by weak, broad bands at 3434 and 3232 cm^{-1}, which could well be due to adsorbed water or lattice water[23] (bands not shown in Figure 4.4). Spectra of the RhAA complexes that were obtained by refluxing for either 1 or 20 hours were identical, as were the spectra of the complex before and after reduction with $NaBH_4$ (1 hour reflux).

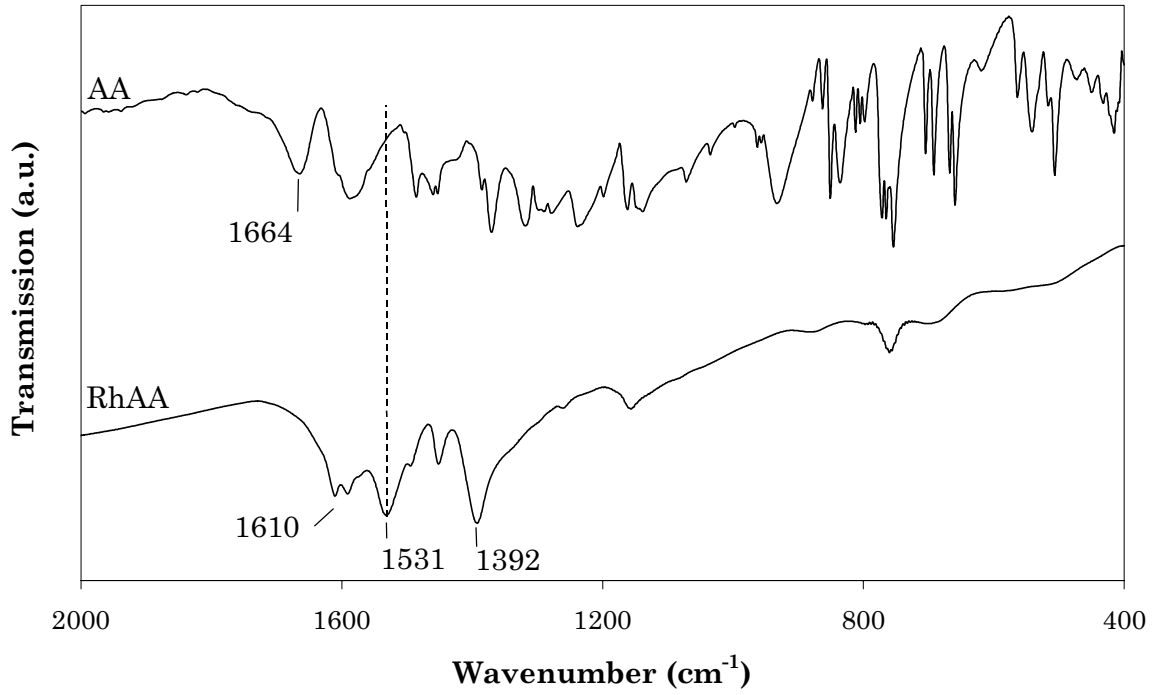

Figure 4.4 Infrared spectra of anthranilic acid (AA) and rhodium anthranilic acid (RhAA).

4.3.2 Catalytic activity

General

In Figure 4.5 the H_2-flow patterns and the H_2-uptake curves of RhPAA and RhAA for the hydrogenation of 1 ml cyclohexene are shown. The H_2-flow pattern was integrated to get the H_2-uptake curve, which was used to calculate initial activities (i.e., the activity at t = 0 min). Initial activities of 7 and 6 mole H_2/g_{cat}*h were found for RhPAA and RhAA, respectively. The values for the initial activities were difficult to reproduce. With RhPAA deviations of up to 20 % were found. Upon storage under nitrogen, the activity of the complex showed a strong deactivation in time of up to 75 %. With RhAA this deactivation was also observed. Not much difference in activity before and after reduction was found with the RhAA complex. With the 1 wt% Rh/CNFs catalyst the initial activity amounted only to 0.03 mole H_2/g_{cat}*h.

The order with respect to cyclohexene for the RhPAA, RhAA, and Rh/CNFs catalysts was determined using the power rate law.[24] To this end, the logarithm of the initial activity was plotted against the logarithm of the initial cyclohexene concentration. Figure 4.6 displays the results. For RhAA these measurements were carried out with the deactivated complex (i.e., the complex that had been stored under N_2 for several weeks). The orders with respect to cyclohexene found are 0.8 for RhPAA, 0.6 for RhAA, and 0.7 for Rh/CNFs.

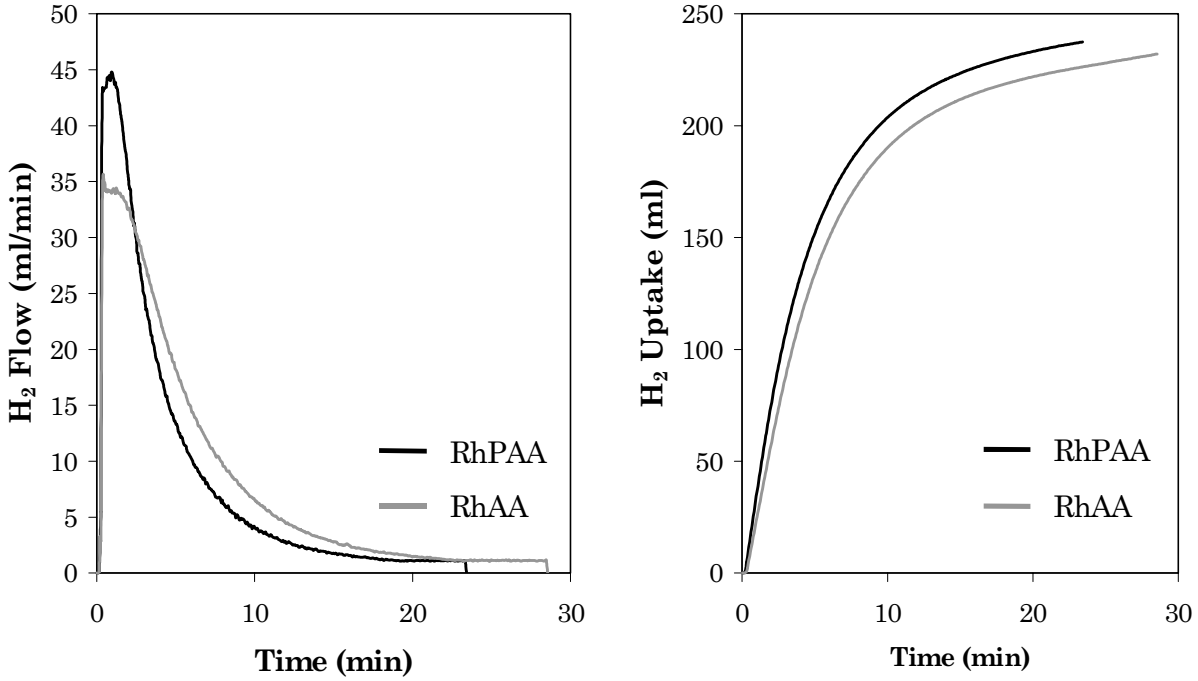

Figure 4.5 H_2-flow patterns and H_2-uptake curves of RhPAA (18.3 mg) and RhAA (14.4 mg) for the hydrogenation of 1 ml cyclohexene.

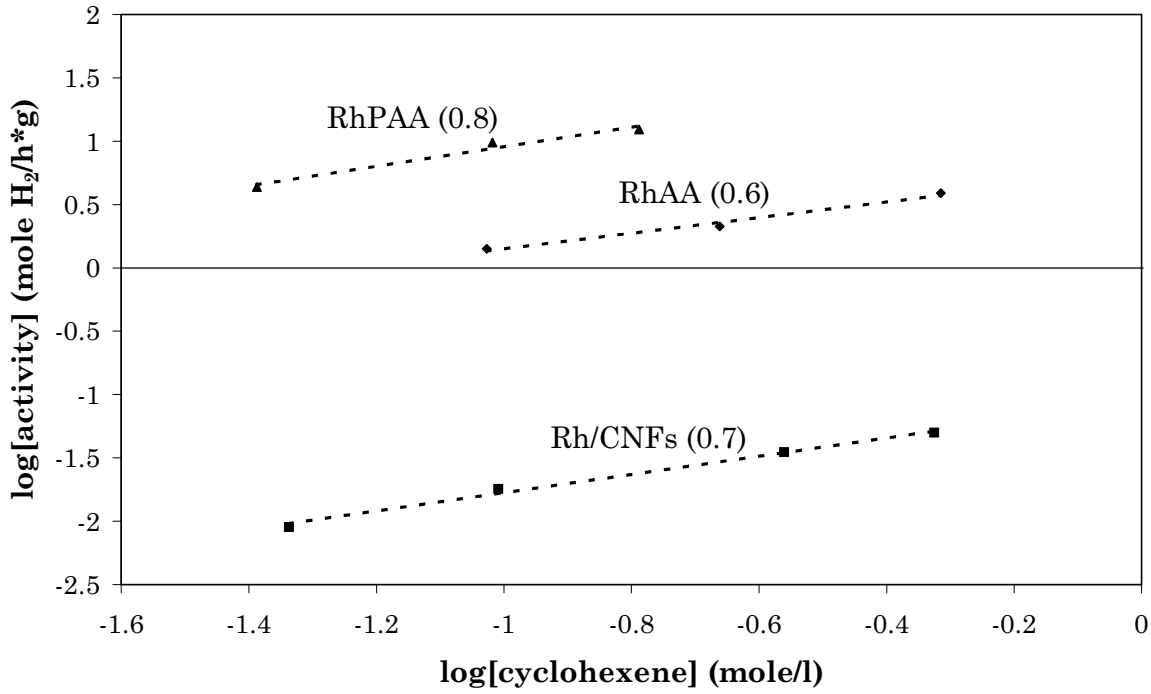

Figure 4.6 Determination of the order in cyclohexene for RhPAA, RhAA, and Rh/CNFs.

Mercury poisoning

All catalytic runs concerning the mercury poisoning experiments were carried out at 25°C. Table 4.3 summarises the results. The concept of poisoning the catalytic activity of Rh(0) with Hg was first tested with the 1 wt% Rh/CNFs catalyst. The activity of this catalyst was totally blocked after stirring with Hg in ethanol at 25°C. However, when the experiment with the Rh/CNFs catalyst was executed in DMF, the activity was not affected. The reaction mixture had to be stirred at 50°C with mercury for several hours before all activity was blocked (see Table 4.3).

Table 4.3 Initial activities of 1 wt% Rh/CNFs, RhPAA and RhAA before and after stirring at 50°C in DMF (blank) and mercury poisoning at 50°C in DMF (Hg).

Catalyst	Initial activity (mole H_2/g_{cat}*h)	
	Before treatment	After treatment
1 wt% Rh/CNFs		
Hg	0.03	0
RhPAA		
Blank	9	0.2
Hg	8	0 (2^{nd}:3)
RhAA		
Blank	4	14
Hg	4	0

The data of Table 4.3 indicate that the activities of the complexes are much more elevated than that of the Rh/CNFs catalyst. This is due to the fact that only 1 wt% Rh was deposited on the CNFs. Accordingly, the initial activity of the catalyst is much lower per gram catalyst than that of the complexes. In order to investigate the effect of the thermal treatment without the presence of mercury on the activity of the rhodium complexes, the same experiments were performed without mercury (denoted as "blank"). After stirring in DMF at 50°C for 3 hrs the initial activity of the RhPAA complex had decreased strongly from 9 to 0.2 mole H_2/g_{cat}*h. When Hg was added the initial activity of 8 mole H_2/g_{cat}*h was totally lost. Adding another dose of 5 ml cyclohexene, however, resulted in an activity of 3 mole H_2/h*g (shown in between brackets in Table 4.3). With RhAA the blank experiment resulted in an increase in the initial activity from 4 to 14 mole

H_2/g_{cat}*h. This activity was subsequently totally blocked by poisoning with Hg. The experiments with RhAA were performed with the complex stored under N_2 for several weeks.

4.4 Discussion

Elemental analysis

The results of the elemental analysis point out that the systems under investigation are not simple ones. The data cannot be fitted with the assumption that (P)AA is co-ordinated to Rh in a 1:1 ratio and that water or ethanol is also present in the co-ordination sphere. The amounts of chlorine found are too small for reasonable fits with one chlorine atom and, therefore, indicate that the material is polluted. For RhAA the amount of chlorine could point to the presence of a bridging chloride ion. Reasonable fits of the data may be obtained by assuming that about half of the rhodium is present as Rh(0) and that (P)AA and ethanol are co-ordinated to the other half. The rhodium content would then be about 40 % for RhPAA and about 50 % for RhAA. The elemental analysis data differ from the values reported by Borowski[7] for RhPAA (C: 40.15 %, H: 4.1 %, N: 4.9 %, Cl: 3.0 %, and Rh 24.4 %).

X-ray diffraction

The X-ray diffraction data clearly show that after contact with air small rhodium particles are present in Rh(P)AA. The results obtained with the complex in silicon grease seem to suggest that indeed air induces the formation of metal particles and that in the complexes that are well kept under N_2 no Rh(0) is present. The formation of Rh(0) might be explained by the assumption that in contact with air by the catalytic action of Rh the (P)AA is oxidised and that the oxidised ligand subsequently reduces the Rh.[25-29] The oxidation of the amine group to a nitro group is most likely. The IR absorptions of the nitro group could be obscured by other vibrations occurring at that frequency.[21] However, these findings must be interpreted with care. Metal particles smaller than about 2 nm are not detected by XRD. Moreover, due to the low concentration of the complex in grease it is well possible that not all of the rhodium metal present is detected. Because the same trends were observed with RhPAA and RhAA, it is probable that the amount of Rh(0) increases after exposure to air. Nevertheless, with IR no difference was found in the spectra after exposure to air. For instance, no C=O vibration at 1643 cm^{-1} was observed. Hence, the increase in Rh(0) content should not be very significant. Taking into account the synthesis procedure it is likely that the complexes have already been polluted with rhodium metal before exposure to air, because ethanol is capable of reducing rhodium chloride at elevated temperatures. This is exemplified by the synthesis of Rh/CNFs by

refluxing $RhCl_3 \cdot 2H_2O$ in ethanol. Furthermore, the strong reductant $NaBH_4$ can also easily reduce Rh(III) to Rh(0).

Infrared spectroscopy

Both RhPAA and RhAA complexes have an ionised carboxylate group, which indicates that the rhodium interacts with the carboxyl group of the ligand. According to Nakamoto,[23] the distance between the antisymmetric and the symmetric vibration of the COO^- group (denoted as Δ) gives information about the mode of interaction with a metal atom. Unidentate complexes show Δ values that are much larger than the ionic form, whereas with chelating complexes Δ is significantly smaller. Finally, the Δ values of bridging complexes (bridging between two rhodium atoms) are close to the ionic values. Borowski[7] showed that the Δ value of RhPAA is identical to that of NaPAA (i.e., the ionic form). This would mean that the mode of co-ordination of the carboxylate group to rhodium is bridging. Consequently, the complex should be a dimer, as two Rh atoms are needed for a bridging co-ordination. However, the above-described approach was based on formate and acetate ions. For more complex ligands, such as PAA and AA, the situation might be different. If one considers the absolute Δ values for Rh acetates, the mode of co-ordination could well be unidentate in the RhPAA and RhAA complexes.

The interaction of Rh with the amine group of PAA is ascertained by the presence of the Rh-N band. Moreover, the C-N stretching vibration shows a shift, which indicates that the environment around this bond has changed. The N-H band, however, remains present. Thus, the amine functionality is probably not ionised. As the amount of chlorine is negligible in RhPAA, we can, therefore, conclude that rhodium is in the monovalent oxidation state. Only the charge of the ionised carboxyl group is compensated for by the Rh(I) metal centre. With RhAA it is more difficult to draw conclusions about the possible interaction of Rh with the amine group. Because of the rich spectrum of AA, no Rh-N band can be discerned. The appearance of the NH_2 bending band at 1531 cm^{-1}, however, shows that the environment around this group has changed. The two N-H stretching minima seem to disappear, indicating a change as well. Unfortunately, on the basis of only these changes an interaction of Rh with N cannot be ascertained unambiguously. For RhAA it is, therefore, also possible that the oxidation state of rhodium is monovalent.

Upon aging under N_2, the C=O vibration of the carboxyl group appears in the spectrum of RhPAA. Probably, the rhodium is no longer co-ordinated to the carboxylate group. The position of the C=O band is not situated at the same position as with pure PAA, because the Rh is still present in the environment of the carboxyl group. As no changes are observed in the IR spectra when the RhPAA is exposed to air for a few days, the process must be a slow one and is likely to be initiated by traces of air.

Catalytic Activity

The bad reproducibility of the initial activities of the complexes could point out that small rhodium metal particles are formed during the catalytic hydrogenation reaction and that these are at least partially responsible for the observed activities. Therefore, the order with respect to cyclohexene was determined for the Rh(P)AA complexes and Rh/CNFs. Due to the variation in initial activities it was difficult to obtain reliable data for the order measurements. Hence, the obtained orders contain a considerable error and it should be concluded that RhPAA, RhAA, and Rh/CNFs have about the same order in cyclohexene. This does not necessarily mean that all the activity of RhPAA and RhAA originates from Rh(0), but the opposite is not proven either.

In a separate experiment, solutions of RhPAA and RhAA in DMF were flushed with H_2 and the complexes were isolated by evaporation of the DMF. The IR spectra show C=O stretching bands at 1643 and 1660 cm^{-1}, respectively. Apparently, some of the complex had disintegrated upon this treatment and rhodium metal had been formed. The formed Rh(0) could then be responsible for the activity. However, the C=O band at 1643 cm^{-1} was also found with deactivated RhPAA. In that case, the formation of metal particles would lead to a lower activity. The experimental results indicate that the interpretation of the data obtained remains difficult.

If one compares the initial activities of Rh/CNFs and deactivated RhAA, taking into account the rhodium content of the catalysts (1 % versus 50 %, respectively) and the surface area of the metal particles (diameter ~10 nm and ~5 nm), the activities compare very well. This means that the activity of this catalyst could well originate from Rh(0) only. In contrast, the activities of the freshly prepared complexes cannot solely be ascribed to zerovalent rhodium as their activity is too high.

Mercury poisoning

Unfortunately, poisoning with mercury only works in DMF after stirring at 50°C. This is probably due to the strong co-ordinating properties of DMF. The blank thermal treatment already results in a very strong decrease in activity of RhPAA, which is accompanied by the formation of a C=O band at 1643 cm^{-1}. Because of the strong deactivation of the RhPAA complex upon stirring at 50°C, the mercury poisoning experiment is difficult to interpret. The activity observed during the second run after Hg poisoning might indicate that at least some of the catalytic activity originates from the homogeneous complex. With RhAA, on the other hand, the blank experiment shows an increase in activity, which can be totally ascribed to Rh(0) as the activity is subsequently blocked by Hg. Clearly, the stability of the complexes is such that stirring at 50°C already causes major changes in their chemical state. Therefore, the results must be interpreted with much care.

Table 4.4 Summary of results after compilation of all data

	Synthesis	Reduction $NaBH_4$	Catalytic reaction	Storage under N_2
RhPAA	- PAA complexed to Rh(I) via COO^- and N - Formation x Rh(0)	Same or more Rh(0)	Complex and Rh(0) is active	Oligomerisation complex or formation big Rh particles
RhAA	- AA complexed to Rh(I) via COO^- and maybe N - Formation y Rh(0) - $y > x$	Same or more Rh(0)	Rh(0) is active and probably complex as well	Oligomerisation complex or formation big Rh particles

General discussion

The results presented above have made clear that the two systems under investigation are not simple. However, by careful analysis of the data obtained some general remarks can be made about the composition of the complexes. Table 4.4 summarises the essential conclusions. It is likely that both the RhPAA and the RhAA complex already contain Rh(0) after synthesis. This is due to the reducing properties of ethanol. Not all rhodium is, therefore, complexed to (P)AA. However, all (P)AA is complexed to Rh, because the carboxyl vibration is completely replaced by those of the carboxylate ion. With PAA the interaction with the metal proceeds via the carboxyl and the amine functionality, whereas with AA only the interaction with the COO^- group has been unambiguously established. Based on the elemental analysis data it is likely that RhAA contains more Rh(0) than RhPAA. Probably, PAA is a stronger complexing agent than AA. Although the presence of monomeric ligand-metal species is very likely, it is also possible that dimers or oligomers are present. The carboxylate as well as the chloride group could act as a bridge. It is also likely that a mixture of different structures exists. Reduction with $NaBH_4$ does not bring about much changes. Maybe some more Rh(0) is formed. As discussed above, it is plausible that rhodium is already in the monovalent oxidation state in Rh(P)AA before reduction with sodium borohydride. Furthermore, no changes in the IR spectrum or in the catalytic activity were observed upon reduction with $NaBH_4$. The catalytic activity observed with RhPAA is partially caused by the complex and partially by Rh(0). With RhAA Rh(0) is surely active and probably the complex as well. During reaction zerovalent rhodium is also formed, which accounts for the bad reproducibility of the activities. Storage under N_2 results in a drastic decrease in activity. This could be due to the formation of big Rh particles, initiated by traces of air, that are not very active. However, stirring at 50°C results in the formation of Rh particles with RhAA, which increase the activity considerably. Therefore, it is probably more likely that the structure of the complex itself changes. Oligomerisation of the complex, accompanied by a loss in activity, could be a plausible explanation.

4.5 Conclusions

The infrared results have shown that complexes of rhodium with PAA and AA have been formed. With both ligands interaction of Rh with the carboxyl group is observed. With PAA the Rh is also bonded to the amine group, while this interaction is not certain in RhAA. In view of the synthesis procedure and the characterisation results, it is also likely that Rh(0) is already present in the as-synthesised complexes. The catalytic activity probably originates from both the metal complexes and small rhodium metal particles. With RhPAA surely part of the activity arises from the complex itself. With RhAA it is likely that the

complex itself is active as well, although the results are more difficult to interpret.

The results described above have made clear that the RhPAA and RhAA systems are not pure and that no clear structure of the complexes can be given. The non-selective synthesis procedure is responsible for these observations. Therefore, it can be concluded that the immobilisation of these complexes should proceed by first attaching the ligand and then the metal, because simultaneous immobilisation of ligand and metal would lead to a non-uniform system. Furthermore, the catalytic behaviour of the immobilised catalyst should not be compared with its 'homogeneous' counterpart, because the measured catalytic activity originates from zerovalent rhodium as well as from the metal-ligand complex.

Acknowledgements

This chapter was based on the experimental work executed by Martijn van der Lee within the framework of his graduate research project.

References

1 O.N. Efimov, M.L. Khidekel', V.A. Avilov, P.S. Chekrii, O.N. Eremenko, and A.G. Ovcharenko, *J. Gen. Chem. USSR (Eng. Trans.)* **38** (1968), 2581

2 V.A. Avilov, Yu. G. Borod'ko, V.B. Panov, M.L. Khidekel', and P.S. Chekrii, *Kinet. Catal. (Eng. Trans)* **9** (1968), 582

3 O.N. Efimov, O.N. Eremenko, A.G. Ovcharenko, M.L. Khidekel', and P.S. Chekrii, *Bull. Acad. Sci. USSR, Div. Chem. Sci. (Eng. Trans)* (1969), 778

4 V.A. Avilov, M.L. Khidekel, O.N. Eremenko, O.N. Efimov, A.G. Ovcharenko, and P.S. Chekry, *US patent* 3,755,194 (1973)

5 E.L. Muetterties and F.J. Hirsekorn, *J. Am. Chem. Soc.* **96-12** (1974), 4063

6 N.L. Holy, *Fundam. Res. Homogeneous Catal.* **3** (1979), 691

7 A.F. Borowski, *Transition Met. Chem.* **8** (1983), 266

8 R.P.A. Sneeden, Organochromium Compounds, Academic Press, New York, 1975, p. 114

9 I. Rajca and A. Borowski, *Symp. Rhodium Homogeneous Catal., [Proc.]* (1978), 58

10 I. Rajca, A. Borowski, and A. Marzec, *Erdöl und Kohle* **35-1** (1982), 36

11 I.W. Rajca, V.V. Abalayeva, and A.F. Borowski, *Fuel* **61** (1982), 1292

12 N.L. Holy, *Tetrahedron Lett.* **42** (1977), 3703

13 N.L. Holy, *Chemtech* (1980), 366

14 E.N. Frankel, J.P. Friedrich, T.R. Bessler, W.F. Kwolek, and N.L. Holy, *J. Am. Oil Chem. Soc.* (1980), 349

15 R.H. Crabtree, The organometallic chemistry of the transition metals, 2nd Ed., John Wiley & Sons, Inc., New York, 1994, p. 219
16 D.R. Anton and R.H. Crabtree, *Organometallics* **2** (1983), 855
17 G.M. Whitesides, M. Hackett, R.L. Brainard, J.-P.P.M. Lavalleye, A.F. Sowinski, A.N. Izumi, S.S. Moore, D.W. Brown, and E.M. Staudt, *Organometallics* **4** (1985), 1819
18 Y. Lin and R.G. Finke, *Inorg. Chem*. **33** (1994), 4891
19 K.S. Weddle, J.D. Aiken III, and R.G. Finke, *J. Am.Chem. Soc.* **120** (1998), 5653
20 P. Scherrer, *Gött. Nachr*. **2** (1918), 98
21 B.S. Furniss, A.J. Hannaford, P.W.G. Smith, and A.R. Tatchell, Vogel's textbook of practical organic chemistry, 5th Ed., Longman, London, 1989, p. 254
22 V.M. Frolov, L.P. Shuikina, K.K. Turisbekova, and G.N. Bondarenko, *Kinet. Catal. (Eng. Trans.)* **35-6** (1994), 800
23 K. Nakamoto, Infrared and Raman Spectra of Inorganic and Coordination Compouds, part B: Applications in Coordination, Organometallic, and Bioinorganic Chemistry, 5th Ed., John Wiley & Sons, Inc., New York, 1997
24 G.C. Bond, Heterogeneous Catalysis: Principles and Applications, 2nd Ed., Clarendon Press, Oxford, 1987, p. 49
25 M.J. Bennett and P.B. Donaldson, *Inorg. Chem*. **16-7** (1977), 1581
26 M.C. Baird, D.N. Lawson, J.T. Mague, J.A. Osborn, and G. Wilkinson, *Chem. Commun*. (1966), 129
27 M.T.Atlay, L. Carlton, and G.Read, *J. Mol. Catal.* **19** (1983), 57
28 C. Larpent, R. Dabard, and H. Patin, *New J. Chem*. **12** (1988), 907
29 B. Richter, A.L. Spek, G. van Koten, and B.-J. Deelman, *J. Am. Chem. Soc.* **122-16** (2000), 3945

5

Modification of Carbon Nanofibres for Immobilisation of Metal Complexes. A Case Study with Rhodium-Anthranilic Acid

Abstract

The immobilisation of the rhodium-anthranilic acid complex onto fishbone carbon nanofibres was executed via the following steps: (i) surface oxidation of the fibres, (ii) conversion of the carboxyl groups into acid chloride groups, (iii) attachment of anthranilic acid and (iv) complexation of rhodium by the attached anthranilic acid. The immobilisation process was followed and the resulting surface species were characterised by IR, XPS, XAFS spectroscopy, and molecular modelling. Anthranilic acid bonds to the CNFs by an amide linkage with the carboxyl groups that are present after surface oxidation of the fibres. The immobilised anthranilic acid co-ordinates to rhodium via the nitrogen atom and the carboxyl group. The as-synthesised Rh(III) complex itself is not active in the liquid-phase hydrogenation of cyclohexene. After reduction with sodium borohydride in order to obtain a Rh(I) complex, small (d = 1.5-2 nm) rhodium metal particles result, which are highly active. The results indicate that different activation procedures for the immobilised Rh/anthranilic acid system should be applied, such as reduction with a milder reduction agent or direct complexation of the rhodium in the Rh(I) state.

5.1 Introduction

The immobilisation of homogeneous catalysts onto solid supports has been studied extensively since the 1970s.[1-4] The objective is to combine the advantages of homogeneous catalysts, such as a high selectivity and metal efficiency, with an easy recovery of the catalyst. A number of immobilisation methods can be distinguished, such as encapsulation or entrapment, supported liquid phase, and immobilisation by covalent bonding.

In general, immobilisation by covalent bonding ('immobilisation') of homogeneous hydrogenation catalysts is executed by first attaching one ligand to the support. This ligand is usually the most important ligand, for example, a bulky bidentate ligand that causes the immobilised catalyst to be enantioselective. Next, the metal complex is co-ordinated to the immobilised ligand by a ligand exchange reaction. Other immobilisation procedures are used as well, such as reaction of a metal salt with the immobilised ligand, which may be followed by a further co-ordination of other ligands to the metal atom, and direct reaction of the metal centre with a surface atom of the support. Most immobilisation techniques try to maintain the structure of the immobilised catalyst as close as possible to that of its homogeneous precursor. The first 15 years of research into immobilisation have learned that simply immobilising a successful homogeneously active metal complex catalyst to a functionalised support mostly yields an inferior version of the homogeneous catalyst.[2] However, it has also been shown that by careful design supported metal complex catalysts can be prepared that have advantages not exhibited in homogeneous catalysis. Although some of the immobilised metal complex catalysts have properties that are as good or even better than their homogeneous counterparts, in 1998 none had an industrial application.[4] This is correlated to the frequent observation of significant metal leaching, although other important factors, such as the mechanical and macroscopic properties of the support are decisive too. The problem of leaching is often directly related to the mechanism of the catalytic reaction. For instance, immobilised phosphine-containing metal complexes will leach under hydrogenation conditions, because during catalysis one phosphine ligand must desorb to allow the required co-ordination of the olefin. This problem can sometimes be circumvented by using multidentate ligands.

An alternative approach could be to purposely change the electronic and steric features of the complex by immobilisation. This approach has been exemplified by Holy, who studied the immobilisation of rhodium N-phenyl anthranilic acid (RhPAA) and rhodium anthranilic acid (RhAA) onto polystyrene.[5-7] Figure 5.1 shows the structure of N-phenyl anthranilic acid and anthranilic acid. The DMF-soluble Rh(I) complex of PAA was known as a remarkably active hydrogenation catalyst.[8-11] However, upon immobilisation onto polystyrene the catalyst did not display any activity. In contrast, when anthranilic acid was immobilised, a highly active Rh(I) catalyst was obtained after reduction of the metal complex with

$NaBH_4$. Monovalent rhodium is able to undergo the oxidative addition-reductive elimination cycle that is needed for catalysing hydrogenation reactions. The rhodium-anthranilic acid complex was not known as a homogeneous catalyst. In addition, the immobilised complex of anthranilic acid with nickel showed hydrogenation activity.[12] This example demonstrates that the catalytic properties of immobilised complexes often differ from that of the non-supported counterparts. It could, therefore, be the best approach to design immobilised catalysts that do not have homogeneous analogues. A weak ligand in solution, e.g., an amine ligand, which may easily dissociate from the metal resulting in reduction of the metal under hydrogenation conditions, could be a suitable ligand for an immobilised system.

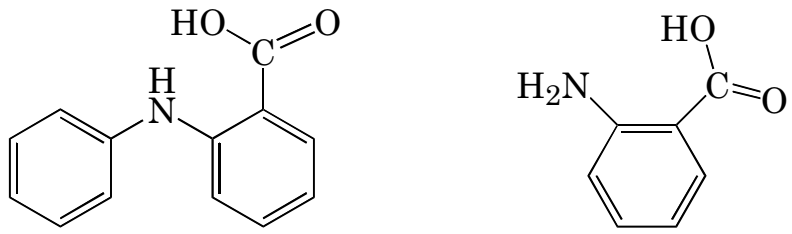

PAA AA

Figure 5.1 Structure of N-phenyl anthranilic acid (PAA) and anthranilic acid (AA).

Although the Rh/anthranilic acid complex has been successfully immobilised on polystyrene, the relatively low thermal and mechanical stability, the swelling properties and the microporous structure of the polystyrene support complicate the use of the catalyst in an industrial environment. Carbon nanofibres (CNFs), on the other hand, are mechanically very strong and have a macroporous structure. The hydrophobicity of the fibres can be modified by surface oxidation.[13] Furthermore, the CNFs obtained after synthesis are very pure and can be grown at low cost.[14] These advantages cause the CNFs to be a suitable support for catalytic reactions in the liquid phase. Consequently, we decided to immobilise RhAA onto fishbone type carbon nanofibres.

As yet the immobilisation (i.e., by covalent bonding) of metal complexes onto carbon nanofibres or carbon nanotubes has, to our best knowledge, not been explored. Some reports describe the impregnation or adsorption of homogeneous catalysts on these new carbon materials.[15-17] Moreover, only few articles have been published about the immobilisation of metal complexes on carbon in general. Kagan *et al.*[18] synthesised a chiral rhodium catalyst on partially graphitised carbon, while McCabe and Orchin[19] attached cobalt and tin complexes to bituminous coal. The inertness of CNFs and, to a lesser extent, of carbon in general makes immobilisation with these materials much more difficult

than with polymers or oxidic supports, such as silica or alumina. However, already in the 1970s Miller and co-workers[20] modified graphite electrodes for the attachment of amines on their surface. The electrodes were kept at high temperature in air, the resulting carboxyl groups were converted into acid chloride groups by the action of thionyl chloride, and these groups were subsequently reacted with an amine. The approach of Miller has been used by several other researchers for the attachment of molecules or even metal-ligand systems to carbon electrodes, although the experimental conditions for oxidation and attachment of amine varied considerably.[21-24] Smalley and co-workers[25] and, more importantly, Haddon and co-workers.[26, 27] employed the method of conversion of carboxyl groups on carbons to acid chloride groups and subsequent attachment of amines to shortened single-walled carbon nanotubes (SWNTs). Haddon *et al.* used this procedure to solubilise the SWNTs by bonding of long-chain organic molecules to its surface. Raw SWNTs were oxidised and shortened by prolonged sonication in a mixture of nitric and sulfuric acid. The carboxyl groups, which were presumably positioned at the edges of the tubes of a length of 300 nm, were converted to acid chloride groups by refluxing in thionyl chloride [containing some N,N-dimethylformamide (DMF)] for 24 hrs. The DMF acts as a catalyst in the formation of acid chloride groups by $SOCl_2$.[28] Haddon *et al.* emphasised that reaction of the $SOCl_2$-treated SWNTs with octadecylamine (ODA) in toluene was unsuccessful. The key to the preparation was the reaction of the tubes with pure molten ODA for an extended period of time. It is obvious that severe reaction conditions are required for derivatisation of carbon nanomaterials.

In this investigation we have studied the immobilisation of the rhodium-anthranilic acid complex onto fishbone carbon nanofibres. The reports by Haddon and co-workers and by Holy served as a basis to develop an immobilisation scheme. It will be shown that the Rh(III)/anthranilic acid system immobilised on carbon nanofibres can indeed be synthesised. The complex is bonded to the fibres by an amide linkage of the CNF carboxyl groups and the amine functionality of anthranilic acid. The immobilised Rh(III) complex is not active in the hydrogenation of cyclohexene. Upon reduction with $NaBH_4$, a very active catalyst consisting of extremely small rhodium metal particles results. Milder activation procedures may lead to an active immobilised Rh(I) complex.

5.2 Experimental

5.2.1 Growth of fishbone carbon nanofibres

Carbon nanofibres of the fishbone type were produced by catalytic decomposition of CH_4 on a Ni/Al_2O_3 catalyst.[29-32]

The Ni/Al_2O_3 catalyst with 30 wt% Ni metal loading was synthesised by the deposition-precipitation technique.[33] Alumina (Alon-C, Degussa) was suspended in an acidified aqueous solution of nickel nitrate (Acros, 99 %) and diluted ammonia was injected within two hours at room temperature under vigorous stirring until the pH had reached a value of 8.5. After overnight stirring, the suspension was filtered, washed, and dried at 120°C. Finally, the catalyst was calcined at 600°C in stagnant air for three hours.

For the production of fishbone CNFs, 0.5 g of the 30 wt% Ni/Al_2O_3 catalyst was reduced at 600°C in 14 % H_2/N_2 (flow rate 350 ml/min) in a vertical tubular reactor (diameter 3 cm) for two hours. After having decreased the temperature to 570°C, methane (50 % in N_2, flow rate 450 ml/min) was passed through the catalyst bed for 6.5 hours. The yield of fibres amounted to approximately 12 g.

5.2.2 Immobilisation of Rh/anthranilic acid onto fishbone carbon nanofibres

Figure 5.2 represents schematically the experimental procedures used for the immobilisation of Rh/anthranilic acid onto fishbone CNFs. The carbon nanofibres were first oxidised in a mineral acid mixture in order to create carboxyl groups on the surface and to remove the original Ni/Al_2O_3 growth catalyst (1). These carboxyl groups were converted into acid chloride groups by the action of thionyl chloride and DMF (2). Anthranilic acid was bonded to the fibres by reaction with these acid chlorides (3). Subsequently, the immobilised anthranilic acid was complexed to rhodium by refluxing the fibres in an aqueous solution of rhodium(III) chloride (4). Finally, the Rh/anthranilic acid complex was reduced with sodium borohydride (procedure not shown in Figure 5.2). Steps 2 and 3 (generation of acid chloride groups and attachment of anthranilic acid) were carried out under a nitrogen atmosphere, using standard Schlenk techniques.

The fishbone carbon nanofibres were oxidised in a mixture of concentrated nitric and sulphuric acid. Five grams of CNFs were boiled under reflux in 80 ml HNO_3/H_2SO_4 1:1 for 30 min (HNO_3: Lamers & Pleugers, 65 %, pure; H_2SO_4: Merck, 95-97 %, p.a.). Upon cooling and dilution with demineralised water, the suspension was filtered over a Teflon membrane filter with a pore diameter of 0.2 μm, washed with demineralised water until the washings showed no significant acidity, and dried at 120°C for 16 hrs.

Three grams of oxidised fibres were treated with 50 ml $SOCl_2$/DMF 50:1 (DMF: N, N-dimethylformamide) by boiling under reflux for 24 hrs in a N_2 atmosphere ($SOCl_2$: Acros, 99.5+ %; DMF: Merck, p.a.). After cooling, the reaction mixture was decanted from the fibres, which were, subsequently, dried in vacuum at 40°C for five hours. Another batch of fibres was dried in vacuum for 17 hours at room temperature to make sure that all DMF was removed from the $SOCl_2$-treated fibres.

Twenty grams of anthranilic acid (Acros, 98+ %) were dried in vacuum at 40°C for two hours and transferred under N_2 to the $SOCl_2$-treated fibres. This mixture was kept at a temperature above the melting point of anthranilic acid (144-148°C) for 96 hrs. Upon cooling, the resulting purple liquid suspension was filtered over a Teflon membrane filter with a pore diameter of 0.2 μm, thoroughly washed with ethanol, and dried in vacuum at room temperature for 17 hours. In an additional experiment the $SOCl_2$-treated fibres were reacted with a solution of anthranilic acid in DMF. The fibres were boiled under reflux for 96 hrs in a 1 M solution of dried anthranilic acid in molsieve-dried DMF (20 ml). These fibres were washed with DMF and further treated identically.

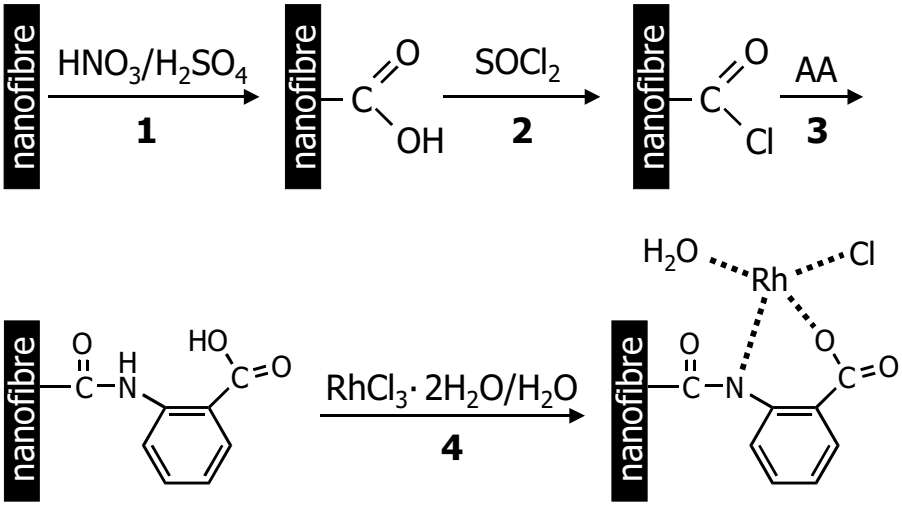

Figure 5.2 Schematic depiction of the experimental procedures used for the immobilisation of Rh/anthranilic acid on fishbone carbon nanofibres.

Two grams of anthranilic acid-reacted fibres were dispersed in 30 ml demineralised water, 48 mg $RhCl_3 \cdot 2H_2O$ (0.2 mmole) was added, and the suspension was boiled under reflux for 72 hours. Upon cooling, the Rh-loaded fibres (max. 1 wt%) were separated from the colourless water fraction by filtration, washed with demineralised water, and dried in vacuum at room temperature for 17 hours.

Reduction of the immobilised Rh/AA complex was carried out by dispersing one gram of Rh/AA/CNFs in 10 ml ethanol (Merck, p.a.) and by adding 55 mg

$NaBH_4$ (Alfa, 99 %) in 10 ml ethanol. The evolution of gas indicated an immediate reaction. After stirring for 30 minutes at room temperature, the reduced catalyst was filtered from the colourless solution, washed with ethanol, and dried in vacuum at room temperature for 17 hours.

Table 5.1 contains the codes of the intermediate products and the final immobilised catalysts.

Table 5.1 Codes for the intermediate products and the final immobilised catalysts.

Code	Description
Intermediate products	
CNF-U	Untreated fibres
CNF-OX	Oxidised fibres
CNF-$SOCl_2$	$SOCl_2$-treated fibres
CNF-AA	Anthranilic acid reacted fibres
Final catalysts	
RhAA/CNF(17)	Dried for 17 hrs after $SOCl_2$ treatment
RhAA/CNF(17, BH)	Dried for 17 hrs, reduction with $NaBH_4$
RhAA/CNF(5)	Dried for 5 hrs after $SOCl_2$ treatment
RhAA/CNF(17, DMF)	Dried for 17 hrs, reaction AA in DMF

5.2.3 Characterisation

Characterisation of the samples was carried out by infrared spectroscopy (IR), X-ray photoelectron spectroscopy (XPS), X-ray absorption fine structure (XAFS) spectroscopy, and molecular modelling.

Infrared spectroscopy

Transmission infrared spectra were recorded on a Perkin Elmer 2000 spectrometer equipped with an air dryer for removal of water vapour and carbon dioxide. One hundred scans were co-added at a resolution of 8 cm^{-1} and a boxcar apodisation. Samples were prepared by thoroughly mixing a small amount of ground nanofibres with pre-dried KBr. Tablets were pressed at 4 tons/cm^2 in vacuum for two minutes. The concentrations of the nanofibres ranged from 0.1 to 1 ‰ (m/m). All transmission spectra were baseline corrected.

X-ray photoelectron spectroscopy

The XPS data were obtained with a Vacuum Generators XPS system, using a CLAM-2 hemispherical analyser for electron detection. Non-monochromatic

Al(K_α) X-ray radiation was utilised by employing an anode current of 20 mA at 10 keV. The pass energy of the analyser was set at 20 eV.

Due to the overlap of the Rh_{3d} signal with the broad C_{1s} peak, the C_{1s} signal of CNF-AA was subtracted from the C_{1s}/Rh_{3d} peak of the rhodium-loaded catalysts, resulting in the isolation of the Rh signal. It was ascertained that the error in the intensity of the subtracted spectrum at the position of the maximum of the C_{1s} peak was not more than the intensity of the Rh signal and that the baseline was exhibiting zero intensity after subtraction.

XAFS spectroscopy

XAFS data collection. XAFS spectra at the Rh K edge (23220 eV) were obtained at the HASYLAB (Hamburg, Germany) synchrotron beamline X1.1, which was equipped with a Si(311) double crystal monochromator. The monochromator was detuned to 50 % of the maximum intensity to minimise the presence of higher harmonics. All measurements were performed in the transmission mode using ionisation chambers filled with an Ar/N_2 mixture to have an absorbance of 20 and 80 % in the first and the second ionisation chamber, respectively.

The CNF-samples (300 mg) were pressed into self-supporting wafers and mounted into an *in situ* EXAFS cell equipped with Be windows.[34] Due to the low concentration of Rh (1 wt%), the calculated edge step was about 0.2. The Rh_2O_3 and $RhCl_3$ reference compounds (Aldrich, 99.8 % and 98 %, respectively) were diluted with boron nitride (Alfa, 99.8 %) and pressed into self-supporting wafers (calculated edge step 1). The rhodium reference foil (Aldrich, 99.9 %, 25 μm thickness) was mounted on the sample holder with Kapton tape. The EXAFS cell was flushed with purified He for 15 minutes and cooled down to liquid nitrogen temperature prior to measurement.

XAFS data-processing. Extraction of the EXAFS data from the measured absorption spectra was performed with the XDAP code developed by Vaarkamp *et al.*[35] Two or three scans were averaged and the pre-edge was subtracted using a modified Victoreen curve.[36] The background was subtracted employing cubic spline routines with a continuously adjustable smooth parameter.[37, 38] Normalisation was performed by dividing the data by the height of the absorption edge at 50 eV.

EXAFS phase-shifts and backscattering amplitudes. Data for phase shifts and backscattering amplitudes were obtained from the reference compounds: Rh foil for Rh-Rh, $RhCl_3$ for Rh-Cl, and Rh_2O_3 for Rh-O, Rh-C and Rh-N contributions.[38] Table 5.2 gives the crystallographic data and the forward and inverse Fourier transform ranges used to create the EXAFS references. Both the reference spectra and the samples were measured at liquid nitrogen temperature. This means that no temperature effect has to be included in the difference in Debye-

Waller factor ($\Delta\sigma^2$) between sample and reference as obtained in the EXAFS data-analysis.

Table 5.2 Crystallographic data and the forward and inverse Fourier Transform ranges used to make the EXAFS references.

						Forward FT	Inverse FT
Atom pair	Ref compd	Ref	N^{ref}	R^{ref} (Å)	k^n	ΔK (Å^{-1})	ΔR (Å)
Rh-Rh	Rh foil	39	12	2.69	3	2.7-22.7	1.4-3.1
Rh-O	Rh_2O_3[a]	40	6	2.05	1	3.7-16.3	0.0-2.3
Rh-Cl	$RhCl_3$	41	6	2.30	1	3.1-18.0	0.0-2.9

[a] it was established with XRD that the Rh_2O_3 was in the hexagonal form.

R-space fitting, difference file technique and weight factor k^n. The EXAFS data-analysis program XDAP allows one to perform multiple-shell fitting in R-space by minimising the residuals between both the magnitude and the imaginary part of the Fourier transforms of the data and the fit. R-space fitting has important advantages compared to the usually applied fitting in k-space, and is extensively discussed in a recent paper by Koningsberger *et al.*[38]

The difference file technique was applied together with phase-corrected Fourier transforms to resolve the different contributions in the EXAFS data.[38] The difference file technique allows one to optimise each individual contribution with respect to the other contributions present in the EXAFS spectrum. If the experimental spectrum is composed of different contributions, then:

$$\text{Exp.Data} = \sum_{i=1}^{N} (\text{Fit})_i \,, \tag{5.1}$$

whereby $(\text{Fit})_i$ represents the fitted contribution of co-ordination shell *i*. For each individual contribution the following equation should then be valid:

$$(\text{Fit})_j = \text{Exp.Data} - \sum_{i=1 \text{ and } i \neq j}^{N} (\text{Fit})_i \tag{5.2}$$

The right-hand side of this equation is further denoted as the difference file of shell *j*. A good fit is only obtained if the total fit and each individual contributing co-ordination shell describe correctly the experimental EXAFS and the difference file, respectively. In this way, not only the total EXAFS fit, but also the individual fits of all separate contributions can be determined reliably.

Both high Z (e.g. Metal-Metal) and low Z (e.g. Metal-Oxygen) contributions may be present in the EXAFS data collected on metal complexes immobilised on supports of a high surface area. The low Z contributions may arise from the ligands and/or from the support. A k^3 weighting emphasises the high Z contributions to the spectrum, since high Z elements have more scattering power at high values of k than low Z elements. However, the use of a k^3 weighted EXAFS spectrum or Fourier transform makes the analysis much less sensitive to the presence of low Z contributions in the EXAFS data. In this study, the EXAFS fits have been checked by applying k^1, k^2 and k^3 weightings in order to be certain that the results are the same for all weightings.

Number of independent data points, variance and statistical significance. The number of independent data points (N_{indp}) was determined as outlined in the "Reports on Standard and Criteria in XAFS Spectroscopy":[42]

$$N_{indp} = \frac{2\Delta k \Delta R}{\pi} + 2 \tag{5.3}$$

The variances of the magnitude and imaginary part of the Fourier transforms of fit and data were calculated according:

$$\text{Variance} = \frac{\int \left[k^n \left(FT^n_{model}(R) - FT^n_{exp}(R) \right) \right]^2 dR}{\int \left[k^n FT^n_{exp}(R) \right]^2 dR} \times 100 \tag{5.4}$$

In this study the statistical significance of a contribution has been checked by a comparison of the amplitude of $(Fit)_j$ with the noise level present in the difference file (the noise in the difference file is essentially the same as the noise in the experimental data).

Molecular modelling

Molecular modelling was executed with the force-field based program Cerius[2]. The universal force-field routine was used. A (part of a) carbon nanofibre was simulated by taking several unit cells of graphite.

5.2.4 Catalytic test experiments

The catalytic activity of the immobilised Rh complexes in the hydrogenation of cyclohexene was tested in a semi-batch slurry reactor, operated at a constant pressure of 1200 mbar H_2. The thermostated, double-walled reaction vessel was equipped with vertical baffles and a gas-tight stirrer with a hollow shaft and blades for gas recirculation. The stirrer was operated at 2000 rpm. During reaction, the hydrogen consumption was automatically monitored by a mass flow meter. It was assured that, under the conditions used, the rate of dissolution of H_2 in the solvent was higher than the maximum measurable rate of H_2-uptake.

In a typical experiment, the reaction vessel was filled with 100 mg of catalyst and 100 ml of ethanol (Merck p.a.). Next, the reactor was thermostated at 25°C, evacuated, filled with H_2, and pressurised. The reaction was started by injection of 1 ml cyclohexene (Acros 99 %) with a syringe and was allowed to proceed until total hydrogenation of the cyclohexene.

5.3 Results

Infrared spectroscopy

Figure 5.3 shows the infrared spectra of CNF-U, CNF-OX, CNF-AA and of a physical mixture of carbon nanofibres and anthranilic acid. To allow comparison, transmission levels of all spectra were kept approximately the same. It was established that, within the transmission window used, the intensity of the bands did not depend upon the transmission level of the spectra. Table 5.3 summarises the band assignments. The assignment of the bands of untreated fibres and of oxidised fibres have been given and discussed in Chapter 2 and Chapter 3, respectively. Concerning the untreated fibres, the absorptions at about 1630 and at 1384 cm^{-1} are due to adsorbed water and nitrate on the KBr, respectively, and can be discounted.[43-46] The minimum at 1582 cm^{-1} originates from an aromatic ring vibration, while the broad 1200 cm^{-1} absorption is attributed to the C-C stretching vibration. [44, 47, 48] Upon oxidation, an additional band appears in the spectrum of the fibres at 1724 cm^{-1}. This peak originates from the C=O stretching vibration of carboxyl and/or carbonyl groups.[43, 44, 47, 49] Furthermore, the intensity of the 1200 cm^{-1} absorption intensifies due to CO stretching and OH bending vibrations, occurring in that region.[47] The intensity of the 1582 cm^{-1} band also increases, because, upon oxidation, symmetry restrictions are relieved for more aromatic rings.[50]

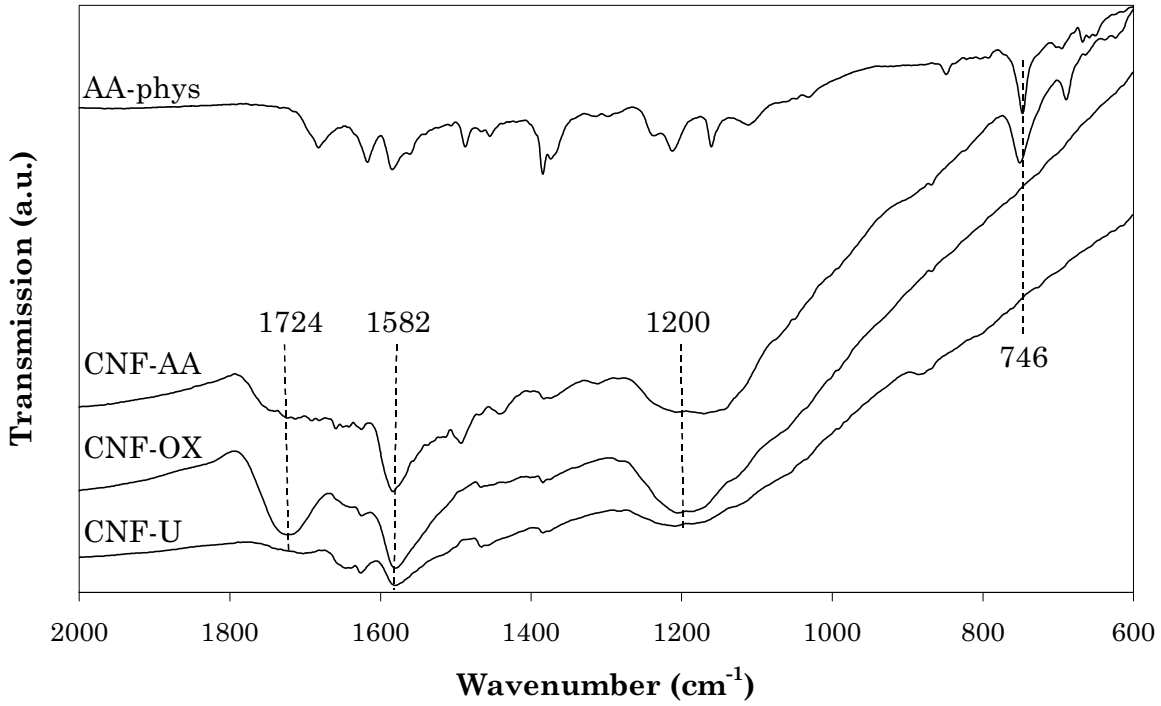

Figure 5.3 IR spectra of untreated (CNF-U), oxidised (CNF-OX), anthranilic acid reacted (CNF-AA) carbon nanofibres, and of a physical mixture of anthranilic acid and CNFs (AA phys).

Table 5.3 Assignments of infrared absorptions found for CNF-U, CNF-OX, CNF-AA and a physical mixture of CNFs and anthranilic acid.

Wavenumber (cm^{-1})	Assignment	Reference
1724	C=O stretching carbonyl & carboxyl	43, 44, 47, 49
1633	adsorbed water	43, 44
1582	aromatic ring stretching	44, 47, 48
1384	nitrate	45, 46
1200	C-C stretching	44, 47
746	aromatic C-H bending anthranilic acid	51

A comparison of the IR spectrum of a physical mixture of anthranilic acid and CNFs (AA-phys) with that of pure AA (not shown) indicates that due to the strong IR absorbance of CNFs many bands visible in the spectrum of pure AA diminish, shift or even disappear upon mixing with carbon nanofibres. Therefore, the aromatic C-H bending mode at 746 cm^{-1} (indicative for four adjacent H atoms[51]) occurring in the spectrum of CNF-AA appears to be the best indication

for the presence of anthranilic acid on the surface of the CNFs. Besides, other absorptions are visible in the spectrum of CNF-AA that can be attributed to anthranilic acid. Furthermore, in the spectrum of CNF-AA the carboxyl C=O stretching vibration at 1724 cm^{-1} of CNF-OX has almost disappeared, indicating that an amide bond between the carboxyl groups on the CNFs and the amine groups of anthranilic acid has been formed.

The spectrum of CNF-$SOCl_2$ (not shown) was identical to that of CNF-OX. The spectrum of the fibres that were treated with anthranilic acid in DMF showed only a weak band at 753 cm^{-1}. Furthermore, the C=O stretching vibration at 1724 cm^{-1} was only slightly diminished.

X-ray photoelectron spectroscopy

The process of immobilisation was followed with XPS as well. Figure 5.4 shows the Cl_{2p} (Fig. 5.4A) and the N_{1s} (Fig. 5.4B) region of CNF-OX, CNF-$SOCl_2$, CNF-AA, and RhAA/CNF(5). Oxidised fibres do not contain chlorine, but after treatment with $SOCl_2$ this element is clearly present. Upon reaction with anthranilic acid, the chlorine is removed, whereas after complexation of Rh (with $RhCl_3 \cdot 2H_2O$) it reappears on the surface of the CNFs. The presence of nitrogen on oxidised fibres is not detected with XPS. The small peak appearing in the spectrum of CNF-$SOCl_2$ can be attributed to small traces of DMF that is used during this synthesis step. The spectrum of CNF-$SOCl_2$ in Figure 5.4B has been obtained from CNF-$SOCl_2$ fibres that were dried only for five hours under vacuum. The CNF-AA fibres clearly contain nitrogen, which remains present

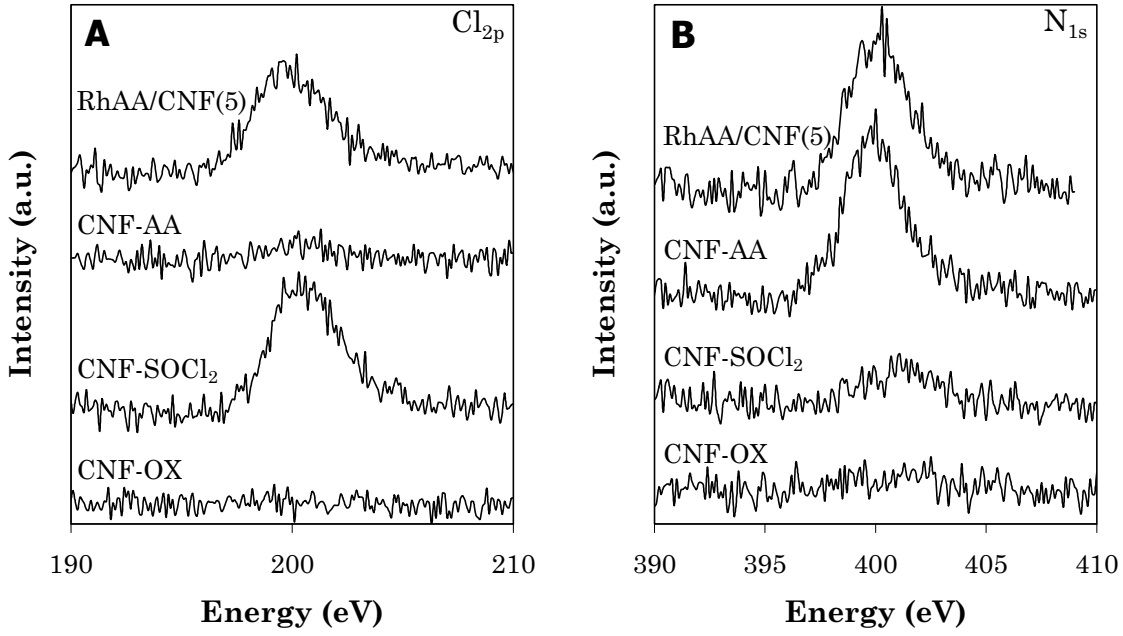

Figure 5.4 XPS spectra of A) the Cl_{2p} region and B) the N_{1s} region of CNF-OX, CNF-$SOCl_2$, CNF-AA, and RhAA/CNF(5).

after complexation of Rh. Reduction with $NaBH_4$ or catalytic reaction does not affect the intensity of the N_{1s} peak (spectra not shown).

The presence and the oxidation state of Rh was studied by monitoring the Rh_{3d} peak. Figure 5.5 displays the results. The $Rh_{3d5/2}$ and $Rh_{3d3/2}$ transitions are both clearly visible. Only the $Rh_{3d5/2}$ peaks were used for further analysis. The spectrum of RhAA/CNF(17) shows one broad $Rh_{3d5/2}$ peak centred at 308.9 eV. Literature values for the $Rh_{3d5/2}$ peak in Rh_2O_3 and $RhCl_3$ are 308.2-308.8 eV and 310.1 eV, respectively.[52] We can, therefore, conclude that the Rh is in the trivalent oxidation state in this complex. Upon reduction of the RhAA/CNF(17) complex with $NaBH_4$ (denoted as RhAA/CNF(17, BH)), a second peak at about 307.4 eV has become the most intense one and the peak at 308.9 eV is visible as a shoulder. As the $Rh_{3d5/2}$ peak for rhodium metal lies at 307.2 eV,[52] this new maximum indicates the presence of Rh(0). Clearly, a large part of the Rh is in the zerovalent state after reduction with $NaBH_4$. A Rh(I) complex would have given a peak at about 308 ev.[52]

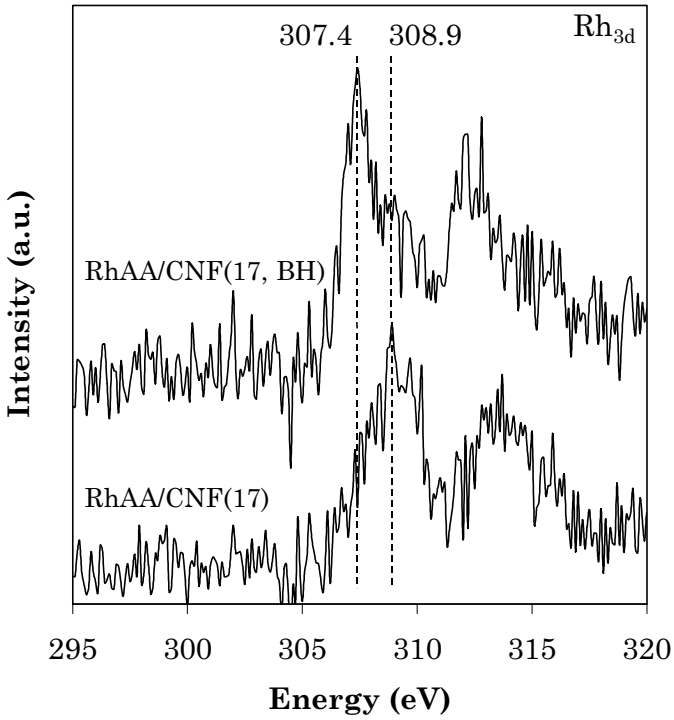

Figure 5.5 XPS spectra of the Rh_{3d} region of RhAA/CNF(17) and RhAA/CNF(17, BH).

XAFS spectroscopy

XANES. The X-ray absorption near edge spectra of RhAA/CNF(17) and RhAA/CNF(17, BH) are shown in Figure 5.6 together with the data for Rh-foil and Rh_2O_3. By comparison of the spectra of the RhAA/CNF(17) and RhAA/CNF(17, BH) samples with the reference compounds, information can be

obtained about the oxidation state of the rhodium. The absorption edge of RhAA/CNF(17) is almost identical to that of Rh_2O_3. Thus, we can conclude that the Rh in RhAA/CNF(17) is in the trivalent oxidation state. No Rh-Rh is present.

The position of the lower half of the absorption edge of RhAA/CNF(17, BH) is at a lower energy than that of RhAA/CNF(17) and closer to that of Rh-foil. The increase in absorption intensity in this region of the absorption edge is typical of zerovalent rhodium. This suggests that part of the rhodium is in the zerovalent oxidation state.

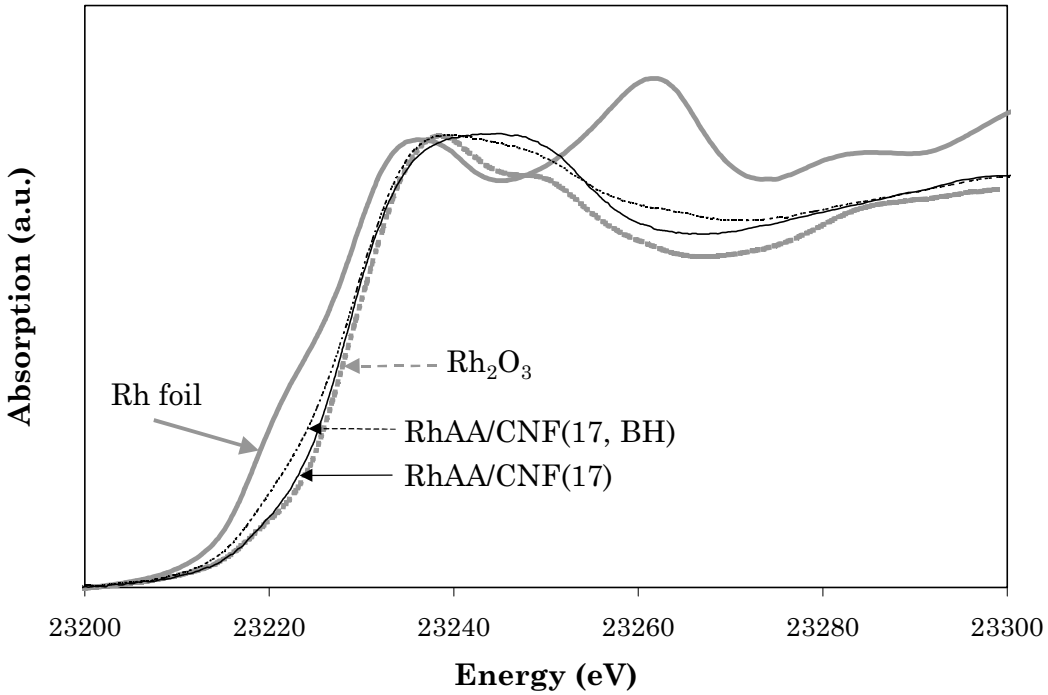

Figure 5.6 XANES spectra of RhAA/CNF(17) (solid black) and RhAA/CNF(17, BH) (dotted black) together with Rh foil (solid grey) and Rh_2O_3 (dotted grey).

EXAFS analysis. Figure 5.7 shows the experimental EXAFS data of RhAA/CNF(17) (Figure 5.7A) and RhAA/CNF(17, BH) (Figure 5.7C). The data quality is excellent. The signal-to-noise ratio at k = 4.4 $Å^{-1}$ amounts to approximately 150 for RhAA/CNF(17) and 75 for RhAA/CNF(17, BH). It can clearly be seen that the EXAFS intensity of sample RHAA/CNF(17, BH) at larger values of k (k > 10 $Å^{-1}$) is higher than for RhAA/CNF(17), indicating the presence of a high Z scatterer.[38] The k^2-Fourier transform of the EXAFS data of RhAA/CNF(17) and RhAA/CNF(17, BH) are displayed in Figure 5.7B and D, respectively. Whereas the peak at 1.6 Å in both samples originates from low Z scatterers, such as oxygen, the peak at 2.4 Å in the uncorrected Fourier transform of the EXAFS data of RhAA/CNF(17, BH) is due to a Rh-Rh

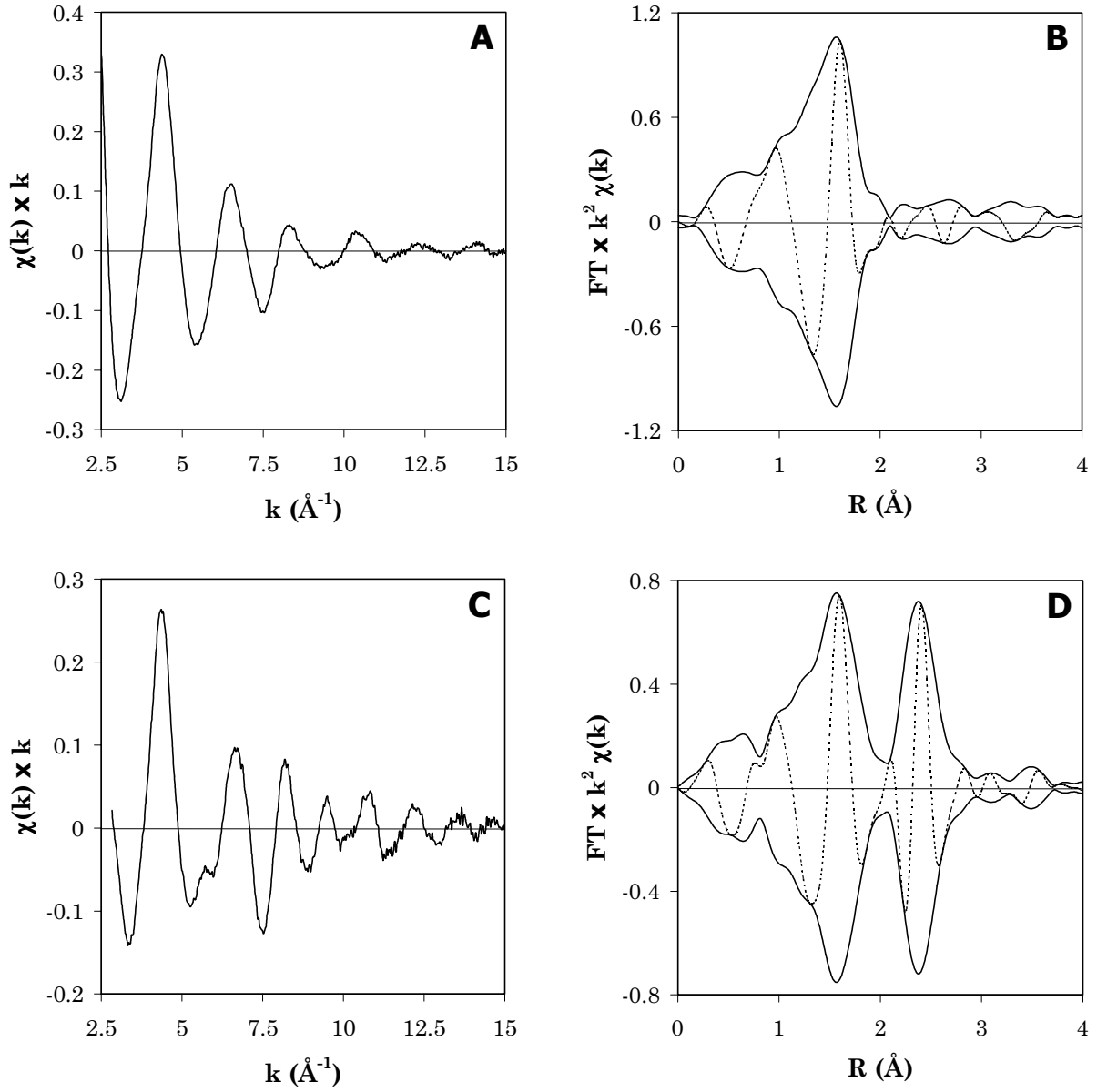

Figure 5.7 A) Experimental EXAFS spectrum of RhAA/CNF(17) (k^1 weighted)
B) Corresponding uncorrected Fourier transform (k^2 weighted, Δk = 2.7-15.9 $Å^{-1}$)
C) Experimental EXAFS spectrum of RhAA/CNF(17, BH) (k^1 weighted)
D) Corresponding uncorrected Fourier transform (k^2 weighted, Δk = 2.9-15.9 $Å^{-1}$).

contribution. Also, the intensity of the first shell region at 1.6 Å is lower, indicating a change in co-ordination after reduction.

Figure 5.8A shows the Fourier transform of the experimental EXAFS data of RhAA/CNF(17) together with the FT of the total fit. The fit quality is excellent for the used fit range (ΔR = 1-2.8 Å). In RhAA/CNF(17) Rh-O/N, Rh-Cl and Rh-C contributions could be determined. The phase-corrected Fourier transforms of the fits of each individual contribution together with their corresponding difference

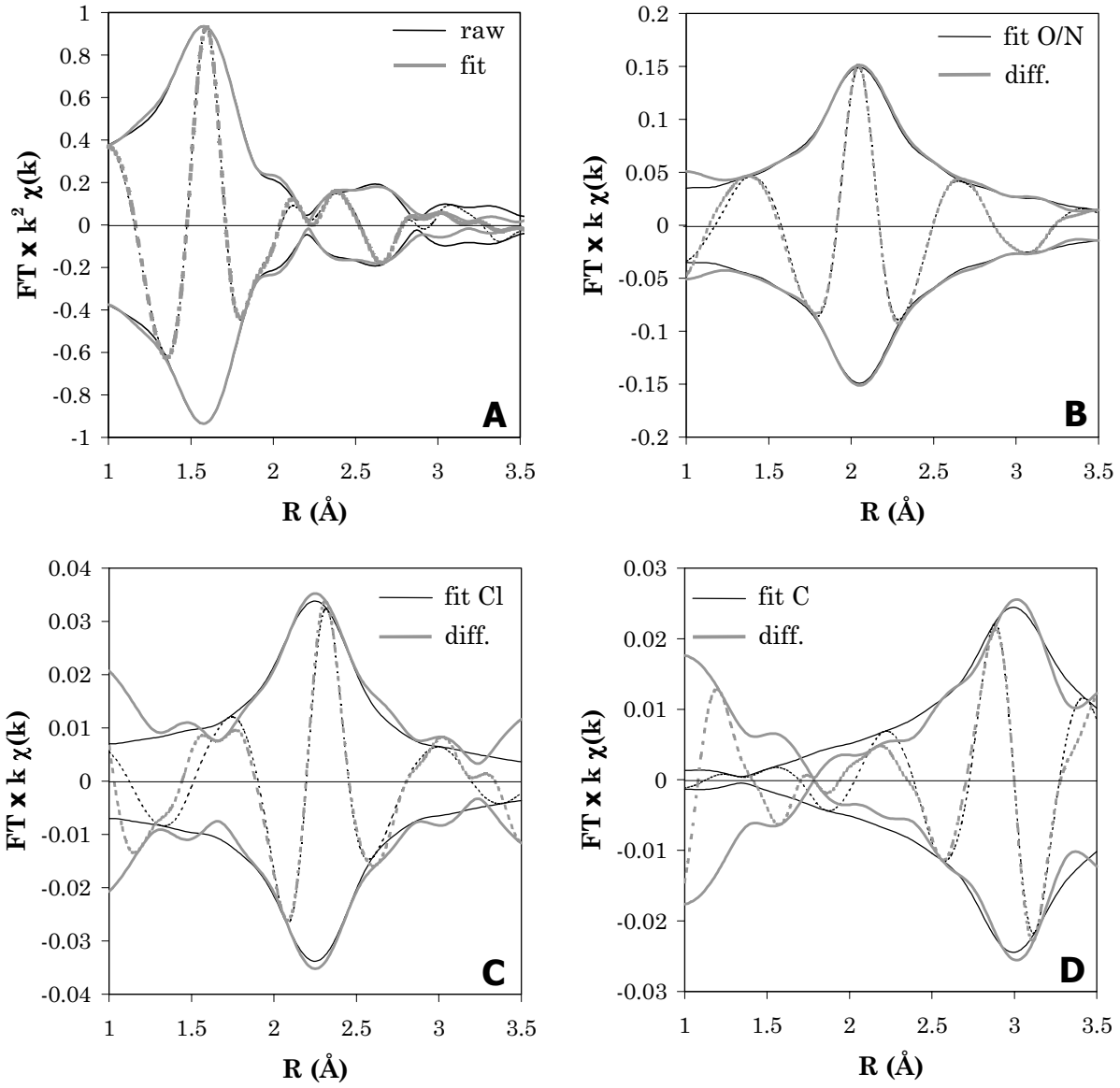

Figure 5.8 Fit results of RhAA/CNF(17) (Δk = 3.9-14 Å^{-1}, ΔR = 1-2.8 Å) A) Fourier transform of experimental EXAFS data and total fit (k^2 weighted, uncorrected) B) Rhodium-oxygen fit and corresponding difference file (k^1 weighted, Rh-O phase-corrected) C) Rhodium-chlorine fit and corresponding difference file (k^1 weighted, Rh-Cl phase-corrected) D) Rhodium-carbon fit and corresponding difference file (k^1 weighted, Rh-C phase-corrected).

files are shown in Fig. 5.8B, C, and D for the Rh-O/N, Rh-Cl, and Rh-C contributions, respectively. The fit quality of each individual contribution is very good, indicating that reliable fit results for the weaker EXAFS contributions have been obtained as well. Table 5.4 presents the fit parameters of the EXAFS spectra resulting from the multiple shell fits in R-space and the variances of the

imaginary and absolute part of the fits for all catalysts. All variances obtained are well below 1 %, indicating that excellent fit results for all catalysts have been acquired.[38] Furthermore, the calculated number of independent data points (see Equation 5.3) is 14, showing that a fit with three shells is possible (N_{indp} = 12). Because the contributions of carbon, oxygen or nitrogen in RhAA/CNF(17) cannot be easily distinguished, all these interactions were fitted with the Rh_2O_3 reference. The rhodium atom in the immobilised complex has five oxygen or nitrogen neighbours at a distance of 2.05 Å. The presence of carbon at such a distance is unlikely. One chlorine atom is also present in the co-ordination sphere of Rh at a distance of 2.28 Å. At a larger distance of 2.94 Å three neighbours are fitted, which are most likely carbon atoms. No Rh-Rh interactions could be fitted.

Table 5.4 Fit parameters of EXAFS spectra and variances of fits (Δk = 3.9-14 Å^{-1}, ΔR = 1-2.8 Å, k^2 weighted).

Catalyst	Atom	N	R (Å)	$\Delta\sigma^2$ (Å^2)	ΔE_0 (eV)	k^2-variance (%)	
		± 5 %	± 1 %	± 5 %	± 10 %	Im	Abs
RhAA/CNF(17)	O/N	5.0	2.05	0.001	-3.1	0.12	0.05
	Cl	1.0	2.28	0.004	4.4		
	C	2.9	2.94	0.003	-10.6		
RhAA/CNF(17, BH)	Rh	4.5	2.68	0.006	9.9	0.25	0.12
	O	3.4	2.05	0.001	-4.4		
	C	1.6	2.25	0.008	-8.6		
RhAA/CNF(5)	Rh	2.0	2.69	0.006	7.0	0.06	0.03
	O	4.1	2.07	0.006	-9.2		
	Cl	2.6	2.28	0.004	10.7		
RhAA/CNF(17, DMF)	Rh	8.2	2.69	0.000	5.6	0.10	0.04
	O	1.3	2.05	0.004	-8.5		

The fit results of RhAA/CNF(17, BH) are shown in Figure 5.9. Again, very good results are obtained for the total fit and the three separate Rh-Rh, Rh-O and Rh-C contributions. At a distance of 2.68 Å 4.5 Rh neighbours are situated (see Table 5.4). The co-ordination number of oxygen neighbours amounts to 3.4 at 2.05 Å. Finally, 1.6 carbon atoms are visible at a distance of 2.25 Å.

Figure 5.10 shows the experimental EXAFS data of RhAA/CNF(5) (Figure 5.10A) and RhAA/CNF(17, DMF) (Figure 5.10C). The signal-to-noise ratio at k = 4.4 Å^{-1} amounts to approximately 50 for RhAA/CNF(5) and 150 for RhAA/CNF(17, DMF). The spectrum of RhAA/CNF(5) is similar to that of

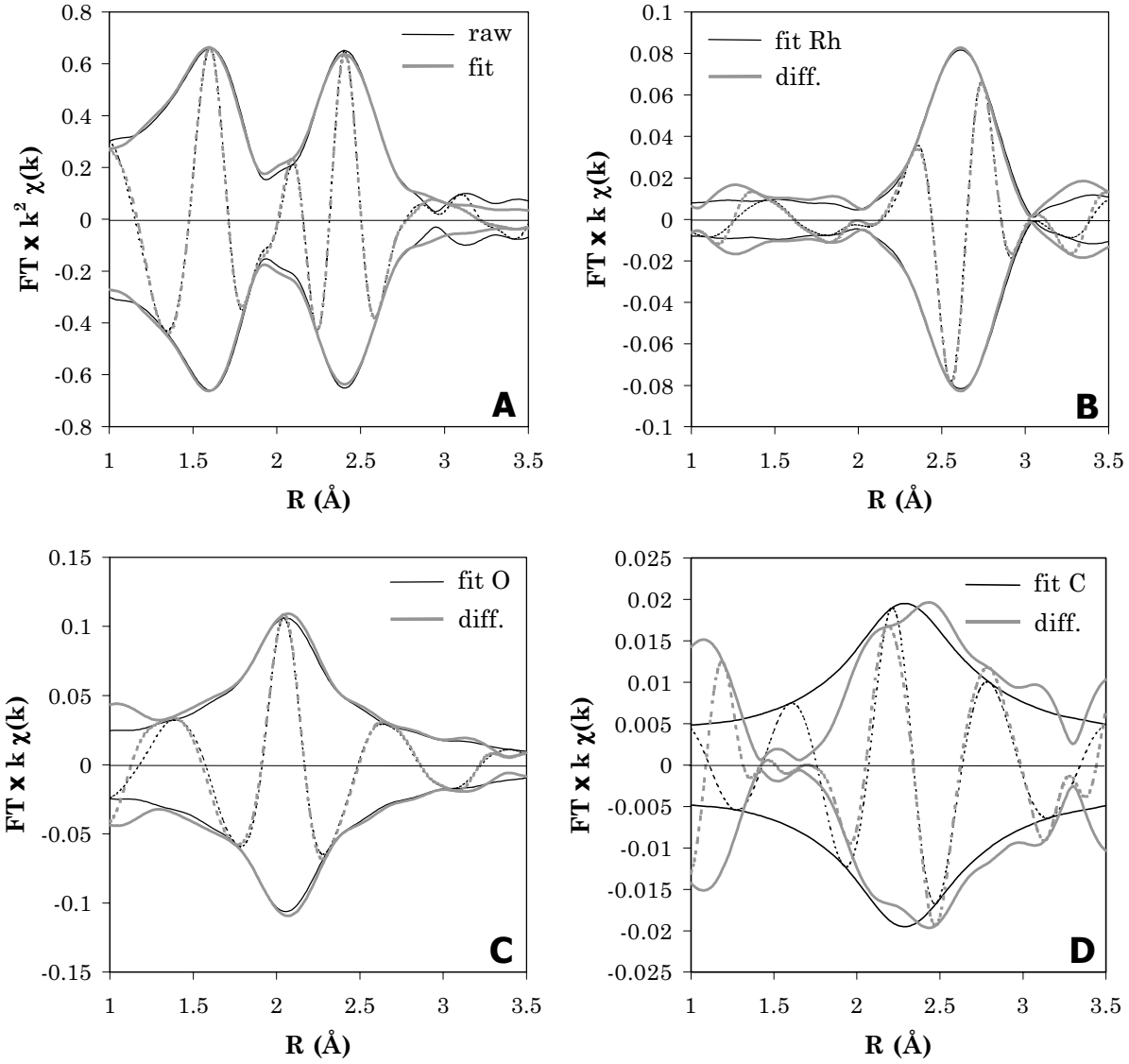

Figure 5.9 Fit results of RhAA/CNF(17, BH) (Δk = 3.9-14 Å^{-1}, ΔR = 1-2.8 Å) A) Fourier transform of experimental EXAFS data and total fit (k^2 weighted, uncorrected) B) Rhodium-rhodium fit and corresponding difference file (k^1 weighted, Rh-Rh phase-corrected) C) Rhodium-oxygen fit and corresponding difference file (k^1 weighted, Rh-O phase-corrected) D) Rhodium-carbon fit and corresponding difference file (k^1 weighted, Rh-C phase-corrected).

RhAA/CNF(17). However, at large k values (k > 10 Å^{-1}) a somewhat higher intensity is found, indicating the presence of Rh-Rh in this catalyst. This is supported by the peak at 2.4 Å in the uncorrected FT of the EXAFS data (Figure 5.10B). The EXAFS spectrum of RhAA/CNF(17, DMF) displays a much higher intensity up to large k values (k > 10 Å^{-1}), evidencing the presence of relatively

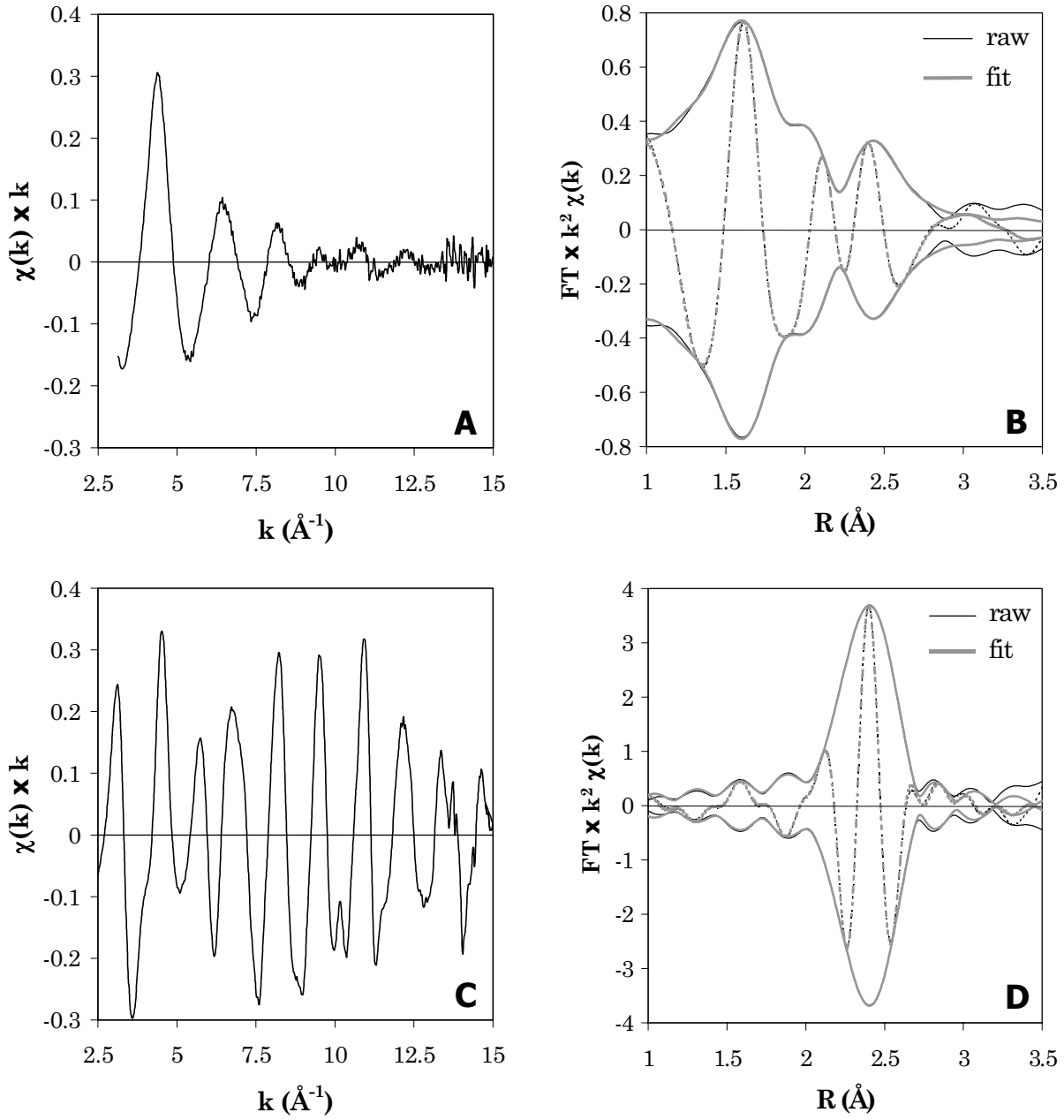

Figure 5.10 A) Experimental k^1 weighted EXAFS spectrum of RhAA/CNF(5) B) Corresponding uncorrected Fourier transform and total fit (Δk = 3.9-14 $Å^{-1}$, ΔR = 1-2.8 Å, k^2 weighted) C) Experimental k^1 weighted EXAFS spectrum of RhAA/CNF(17, DMF) D) Corresponding uncorrected Fourier transform and total fit (Δk = 3.9-16.3 $Å^{-1}$, ΔR = 1-2.8 Å, k^2 weighted).

large Rh particles. Indeed, the FT of the EXAFS data mainly displays a large peak at 2.4 Å. The fit parameters displayed in Table 5.4 show that, besides oxygen and chlorine contributions (N_O = 4.1, R_O = 2.07, N_{Cl} = 2.6, R_{Cl} = 2.28), RhAA/CNF(5) indeed contains some Rh-Rh (N = 2.0, R = 2.69). A reasonable fit

can also be obtained with less chlorine. RhAA/CNF(17, DMF) contains almost exclusively Rh-Rh (N = 8.2, R = 2.69). Some Rh-O is present as well (N = 1.3, R = 2.05).

It should be noted that with all catalysts edge steps were obtained that were equal to the theoretical edge step for 1 wt% Rh on carbon. In other words, all catalysts indeed contain 1 wt% of Rh. The total discoloration of the water phase (containing the equivalent of 1 wt% Rh) after complexation of rhodium supports these observations.

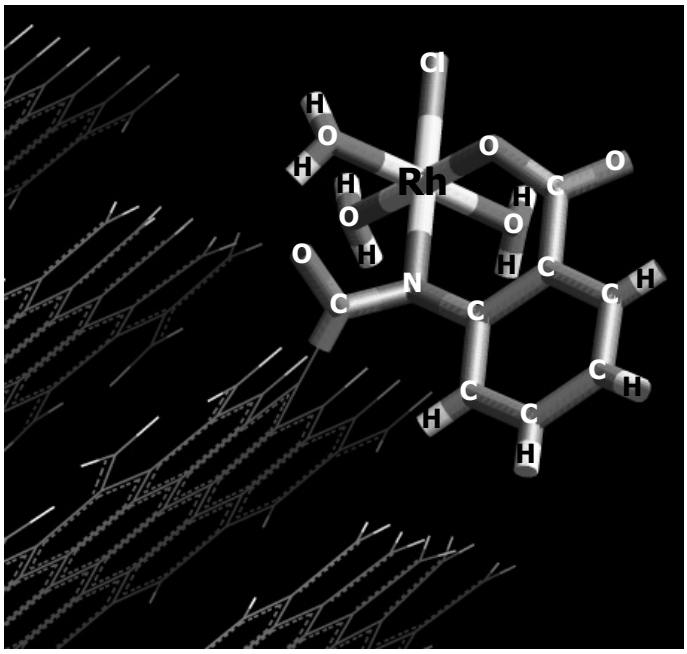

Figure 5.11 Outcome of the molecular modelling study of RhAA/CNF(17).

Molecular modelling

The outcome of the EXAFS fit results of RhAA/CNF(17), i.e., the number and nature of neighbours of Rh, were used as input for the molecular modelling study. It was assumed that the rhodium is in the trivalent oxidation state and that, for reasons of charge compensation, both the carboxyl and the amide group of anthranilic acid are ionised. The result is shown in Figure 5.11. On the left-hand side of the figure the carbon nanofibre structure is visible. Anthranilic acid is bonded to the fibre via an amide bond with a carboxyl group on the surface of the CNF. Rh is co-ordinated to anthranilic acid via one oxygen of the carboxyl group (of AA) and via the nitrogen atom. Besides one chloride anion, the co-ordination sphere of the rhodium atom is completed by three water molecules (the last synthesis step was performed in water). Thus, the Rh atom is octahedrally surrounded. Table 5.5 gives the distances of several atoms to the central Rh atom. For comparison, the EXAFS results have been included as well. The oxygen

atoms of the three water molecules are situated at a distance of 1.9 Å. The oxygen atom of the carboxyl group of anthranilic acid is found at 2.0 Å, as is the AA nitrogen atom. Chloride resides at a distance of 2.3 Å. Three carbon atoms are found at distances of 2.8 Å (C of carboxyl group AA), 3.0 Å (carbon of benzyl ring) and 3.0 Å (C of carboxyl group CNF). These distances agree very well with the EXAFS results.

Table 5.5 Distances between Rh and several atoms in the molecular model of RhAA/CNF(17). For comparison, the EXAFS results have been included.

	Modelling		EXAFS	
Atom	Nr of atoms	Distance (Å)	N	R (Å)
O_{H2O}	3	1.9 (3x)		
$O_{carb.}$	1	2.0	5.0	2.05
N	1	2.0		
Cl	1	2.3	1.0	2.28
C	3	2.8, 3.0, 3.0	2.9	2.94

Catalytic measurements

The catalytic measurements resulted in a plot of the H_2-flow against time (see Figure 5.12 for RhAA/CNF(17, BH)). This curve was integrated to get an H_2-uptake pattern, which, in turn, was used to calculate the normalised initial activity (i.e., the activity at t = 0). The results are summarised in Table 5.6. Both RhAA/CNF(17) and RhAA/CNF(5) do not display any hydrogenation activity. The catalyst reduced with $NaBH_4$, on the other hand, is highly active. The activity of RhAA/CNF(17, BH) amounts to 1.1 mole H_2/g_{cat}*h. RhAA/CNF(17, DMF) shows an intermediate activity of 0.3 mole H_2/g_{cat}*h.

5.4 Discussion

Infrared spectroscopy

The appearance of the aromatic C-H bending vibration of anthranilic acid at 746 cm^{-1} and the strong decrease in intensity of the C=O stretching band at 1724 cm^{-1} in the infrared spectrum of CNF-AA strongly indicate that anthranilic acid has been bonded to the carboxyl groups of the oxidised carbon nanofibres via an amide linkage. Reaction of anthranilic acid via the carboxyl group is highly unlikely, because an acyclic acid anhydride, which is very unstable, would be the result.[53] Unfortunately, no amide C=O stretching vibration could be observed.

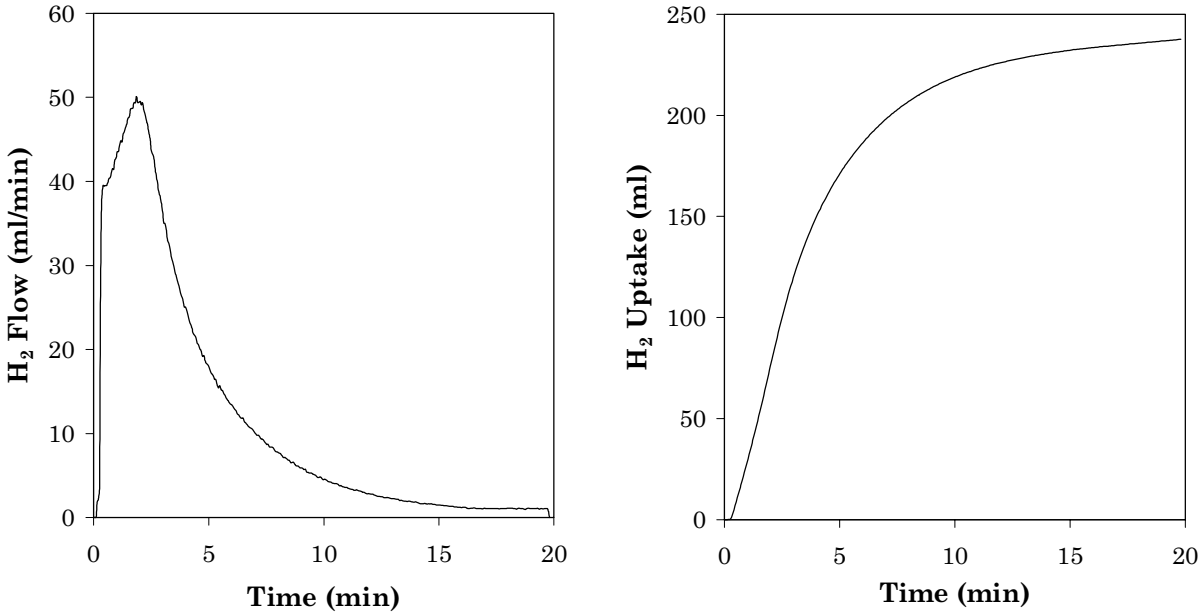

Figure 5.12 H_2-flow and H_2-uptake curves of RhAA/CNF(17, BH).

Table 5.6 Initial activities for the different catalysts.

Catalyst	Initial activity (mole H_2/g_{cat}*h)
RhAA/CNF(17)	0.0
RhAA/CNF(5)	0.0
RhAA/CNF(17, BH)	1.1
RhAA/CNF(17, DMF)	0.3

This band would be expected to be situated at about 1650 cm^{-1}.[24, 26, 27, 51] In this region the adsorbed water peak and bands originating from anthranilic acid occur as well and, therefore, no clear statement concerning the presence or absence of this vibration can be made.

The IR spectrum of CNF-$SOCl_2$ is identical to that of oxidised fibres. No evidence for acid chloride groups could be found. However, it is possible that the acid chloride groups are not stable and that they are converted back to carboxylic acid groups during IR sample preparation under the influence of water vapour in the air. Another explanation could be that anthranilic acid reacts directly with the carboxyl groups of the CNFs under the conditions used (usage of pure molten AA). To investigate this, oxidised carbon nanofibres were reacted with pure

molten anthranilic acid without prior treatment with $SOCl_2$. The infrared spectrum of these CNFs is very similar to that of CNF-AA. In other words, the anthranilic acid 746 cm^{-1} band is clearly visible and the 1724 cm^{-1} C=O stretching vibration of the carboxyl group has almost disappeared. This result makes clear that anthranilic acid can react directly with the CNF carboxyl groups. This reaction was also investigated by Pittman *et al.*, [54] who reacted PAN carbon fibres oxidised with HNO_3 with tetraethylenepentamine at 190°C. In conclusion, water-sensitive acid chloride groups may be formed on the surface of the CNFs, but their formation is not necessary to achieve the bonding of AA to carbon nanofibers.

X-ray photoelectron spectroscopy

The N_{1s} XPS spectra show the appearance of nitrogen on the surface of the CNFs after reaction with anthranilic acid. This nitrogen is not removed by any of the further treatments that are done with the CNF-AA fibres (complexation of Rh, catalytic reaction and/or reduction with $NaBH_4$), indicating that it must be tightly bound to the carbon nanofibre surface. XPS also shows that, after treatment with $SOCl_2$, the fibres should be dried in vacuum for a long period of time in order to remove all DMF from the surface of the fibres. The effect of traces of DMF on the surface of the CNFs is dealt with later in this section.

The XPS Cl_{2p} results also provide valuable information about the followed immobilisation sequence. Chlorine appears on the surface of the fibres after reaction with $SOCl_2$ and disappears again after bonding of anthranilic acid. This suggests that acid chloride groups have been formed that are subsequently used for the bonding of AA. If the acid chloride groups are unstable in air, the XPS Cl signal then probably originates from HCl that is formed during the decomposition reaction. After complexation of Rh chlorine is present again, implying that this element is present near the rhodium.

XAFS spectroscopy

The outcome of the analysis of the EXAFS data of RhAA/CNF(17) demonstrates that the central rhodium atom has six nearest neighbours (typical for Rh[III]) and that one of these neighbours is a chlorine atom. Furthermore, the EXAFS fit reveals an interaction with three carbon atoms at a longer distance. The EXAFS results imply that, for reasons of charge compensation of the Rh(III), the carboxyl group as well as the nitrogen atom of the former amine group of anthranilic acid is ionised. The three carbon atoms may originate from the benzyl ring of anthranilic acid or from the carbon nanofibre support.

The EXAFS data also shed more light on the structure of the $NaBH_4$-reduced catalyst RhAA/CNF(17, BH). Because no reduction prior to the EXAFS measurement was carried out, the result of the analysis of the EXAFS data points to small rhodium particles that are partly oxidised. The particles probably have a core of rhodium metal surrounded by rhodium oxide. As an interaction of

the Rh atoms with the carbon support is also observed, it is most likely that the rhodium particle is semi-spherical. Because the rhodium particles are partially oxidised, it is not possible to directly estimate the particle size from the co-ordination number. However, the particles should be small, because an interaction with the support is still observed and the catalyst displays a high hydrogenation activity. We roughly estimate the particle size to be in between 1.5 and 2 nm.

The complex RhAA/CNF(5) contains some Rh-Rh. As this complex probably contains a mixture of different structures, a reliable interpretation of the EXAFS data cannot be given. The RhAA/CNF(17, DMF) catalyst consists of Rh particles that have an oxidised outer surface. These particles are fairly large: no interaction with the CNF support can be distinguished.

General discussion

All characterisation techniques agree very well with each other. With IR an amide bond between the carboxyl groups on the surface of the carbon nanofibres and anthranilic acid was observed, while the XPS N_{1s} region showed the presence of tightly bound nitrogen on the CNF surface after attachment of AA. Furthermore, XPS showed that the rhodium in the as-synthesised RhAA/CNF(17) complex is in the trivalent oxidation state and that after reduction with $NaBH_4$ zerovalent Rh is formed. The XANES results are fully in agreement with these observations.

Although the EXAFS data give very valuable information about the nature and amount of neighbours of Rh and their mutual distance, a structure is not easily visualised. Therefore, the molecular modelling program was used. The constructed model of RhAA/CNF(17) agrees very well with the EXAFS results. The six nearest neighbours have distances that accord with EXAFS. More importantly, the three nearest carbon atoms in the model have an average distance that matches the EXAFS distance. As one of these carbon atoms belongs to the former carboxyl group of the carbon nanofibre, this is another strong indication for the covalent bonding of the complex to the fibres. The model also shows that although the complex is closely bonded to the CNF surface and steric hindrance is expected, the Rh in the Rh-anthranilic acid complex is able to obtain a regular octahedral surrounding.

The catalytic data have shown that when the Rh in the Rh-anthranilic acid complex is in the trivalent oxidation state, no catalytic activity is observed. Only after formation of rhodium metal particles the catalyst is active in the hydrogenation of cyclohexene. It is known that Rh(I) is able to perform the oxidative addition-reductive elimination cycle that is needed for catalysis of hydrogenation reactions by metal complexes. Therefore, it was tried to reduce the Rh(III) in RhAA/CNF(17) to the univalent oxidation state by the action of $NaBH_4$. This reductor has been used before for this purpose for the polystyrene-immobilised Rh(III)-AA complex.[5] The XPS and XANES data have shown that a

large part of the rhodium in RhAA/CNF(17, BH) has become Rh(0) after reduction. Clearly, the reduction of the Rh(III) to Rh(I) cannot be achieved with $NaBH_4$. Its reducing properties are probably too strong. Therefore, the activation of the immobilised Rh-anthranilic acid complex should be executed differently. One option could be the use of a milder reductant than $NaBH_4$. Another alternative might be to introduce the rhodium already as Rh(I) and not as Rh(III). A risky reducing step would then be circumvented.

As was already shown above with XPS, treatment of the oxidised fibres with $SOCl_2$/DMF results in the presence of DMF on the fibres if the drying procedure in vacuum is carried out only for a few hours. The final complex RhAA/CNF(5) contains some Rh-Rh. Likewise, when it is attempted to use a solution of anthranilic acid in DMF for the attachment of this ligand to the fibres, this procedure leads to the formation of large Rh particles (RhAA/CNF(17, DMF). As Rh(0) is formed in both cases, we postulate that zerovalent rhodium is formed by the reducing properties of DMF. When DMF is present on the surface of the carbon nanofibres, some or all of the rhodium chloride is reduced to Rh(0). Only when DMF is totally removed, which presumably was achieved with the RhAA/CNF(17) complex after evacuation for 17 hrs, the rhodium can fully co-ordinate to anthranilic acid.

5.5 Conclusions

The immobilisation of Rh/anthranilic acid onto fishbone carbon nanofibres was executed via (i) surface oxidation of the fibres, (ii) conversion of the carboxyl groups into acid chloride groups, (iii) attachment of anthranilic acid and (iv) complexation to rhodium(III). We have shown that anthranilic acid bonds to the CNFs by an amide linkage with carboxyl groups that are present after surface oxidation of the fibres. The immobilised anthranilic acid complexes to rhodium via the nitrogen atom and the carboxyl group. The co-ordination sphere of the trivalent Rh atom is further occupied by three water molecules and a chloride ion. To our best knowledge, this is the first example of a metal-ligand complex immobilised by covalent bonding on carbon nanofibres or carbon nanotubes.

The as-synthesised complex is not active in the hydrogenation of cyclohexene. Therefore, we reduced the rhodium with sodium borohydride in order to get monovalent rhodium. Rh(I) can undergo the oxidative addition-reductive elimination cycle that is needed for catalysis. However, the reduction procedure with $NaBH_4$ results in the formation of small rhodium particles with an estimated diameter of 1.5-2 nm on the CNFs. The hydrogenation activity of these particles is very high. We conclude that another activation procedure for the immobilised Rh/anthranilic acid system, such as reduction with a milder reduction agent or complexation of the rhodium in the Rh(I) state, must be designed. Solvents with reducing properties should be used carefully during the

immobilisation sequence. We have shown that traces of DMF on the surface of the carbon nanofibres already results in the formation of some zerovalent rhodium. Usage of anthranilic acid in DMF gives rhodium metal particles as well. The formation of acid chloride groups by the action $SOCl_2$ is not necessary to bring about the bonding of anthranilic acid to the CNFs. Under the conditions used, anthranilic acid can react directly with the carboxylic groups of the fibres.

Acknowledgements

We wish to acknowledge A. Mens for the generation of the XPS spectra and dr. O. Gijzeman for the discussions concerning the XPS data. We would like to thank the HASYLAB (Hamburg, Germany) for the opportunity to perform EXAFS measurements at beamline station X1.1. We are grateful for the collection of the EXAFS data by the EXAFS measurement team.

References

1 C.U. Pittman, Jr. in Comprehensive Organometallic Chemistry (Eds. G. Wilkinson, F.G.A. Stone, and E.W. Abel), vol 8, Pergamon Press, Oxford, 1982, p. 553
2 F.R. Hartley, Supported Metal Complexes, D. Reidel publishing company, Dordrecht, 1985
3 Yu. I. Yermakov and L.N. Arzamaskova, *Stud. Surf. Sci. Catal.* **27** (1986), 459
4 A. Choplin and F. Quignard, *Coord. Chem. Rev.* **178-180** (1998), 1679
5 N.L. Holy, *Tetrahedron Lett.* **42** (1977), 3703
6 N.L. Holy, *Fundam. Res. Homogeneous Catal.* **3** (1979), 691
7 N.L. Holy, *Chemtech* (1980), 366
8 O.N. Efimov, M.L. Khidekel', V.A. Avilov, P.S. Chekrii, O.N. Eremenko, and A.G. Ovcharenko, *J. Gen. Chem. USSR (Eng. Trans.)* **38** (1968), 2581
9 V.A. Avilov, Yu. G. Borod'ko, V.B. Panov, M.L. Khidekel', and P.S. Chekrii, *Kinet. Catal. (Eng. Trans.)* **9** (1968), 582
10 O.N. Efimov, O.N. Eremenko, A.G. Ovcharenko, M.L. Khidekel', and P.S. Chekrii, *Bull. Acad. Sci. USSR, Div. Chem. Sci. (Eng. Trans.)* (1969), 778
11 V.A. Avilov, M.L. Khidekel, O.N. Eremenko, O.N. Efimov, A.G. Ovcharenko, and P.S. Chekry, *US patent* 3,755,194 (1973)
12 E.N. Frankel, J.P. Friedrich, T.R. Bessler, W.F. Kwolek, and N.L. Holy, *J. Am. Oil Chem. Soc.* 1980, 349
13 See Chapter 3 of this thesis
14 K.P. de Jong and J.W. Geus, *Catal. Rev.-Sci. Eng.* **42-4** (2000), 481
15 A.A. Keterling, A.S. Lisitsyn, V.A. Likholobov, A.A. Gall', and A.S Trachum, *Kinet. Catal. (Eng. Trans.)* **31-6** (1990), 1273

16 Yu. Yu. Volodin, A.T. Teleshev, V.V. Morozova, A.V. Tolkachev, Yu. S. Mardashev, and E.E. Nifantyev, *Russ. Chem. Bull.* **48-5** (1999), 899
17 Y. Zhang, H.-B. Zhang, G.-D. Lin, P. Chen, Y.-Z. Yuan, and K.R. Tsai, *Appl. Catal., A* **187** (1999), 213
18 H.B. Kagan, T. Yamagishi, J.C. Motte, and R. Setton, *Isr. J. Chem* **17** (1978), 274
19 M.V. McCabe and M. Orchin, *Fuel* **55** (1976), 266
20 B.F. Watkins, J.R. Behling, E. Kariv, and L.L. Miller, *J. Am. Chem. Soc.* **97-12** (1975), 3549
21 M. Fujihira, A. Tamura, and T. Osa, *Chem. Lett.* (1977), 361
22 L. Horner and W. Brich, *Liebigs Ann. Chem.* (1977), 1354
23 J.C. Lennox and R.W. Murray, *J. Am. Chem. Soc.* **100-12** (1978), 3710
24 T. Atoguchi, A. Aramata, A. Kazusaka, and M. Enyo, *J. Electroanal. Chem.* **318** (1991), 309
25 J. Liu, A.G. Rinzler, H. Dai, J.H. Hafner, R.K. Bradley, P.J. Boul, A. Lu, T. Iverson, K. Shelimov, C.B. Huffman, F. Rodriguez-Macias, Y.-S. Shon, T.R. Lee, D.T. Colbert, and R.E. Smalley, *Science* **280** (1998), 1253
26 J. Chen, M.A. Hamon, H. Hu, Y. Chen, A.M. Rao, P.C. Eklund, and R.C. Haddon, *Science* **282** (1998), 95
27 M.A. Hamon, J. Chen, H. Hu, Y. Chen, M.E. Itkis, A.M. Rao, P.C. Eklund, and R.C. Haddon, *Adv. Mater.* **11-10** (1999), 834
28 J.S. Pizey in Synthetic Reagents (Ed. J.S. Pizey), vol. 1, Ellis Horwood, Chichester, 1974, p. 321
29 M.S. Hoogenraad, PhD Thesis (1995), Utrecht University, The Netherlands
30 M.S. Hoogenraad, M.F. Onwezen, A.J. van Dillen, and J.W. Geus, *Stud. Surf. Sci. Catal.* **101** (1995), 1331
31 J.W. Geus, M.S. Hoogenraad, and A.J. van Dillen in Synthesis and Properties of Advanced Catalytic Materials (Eds. E. Iglesia, P.W. Lednor, D.A. Nagaki, and L.T. Thompson), Materials Research Society Pittsburgh, Pittsburgh, 1995, p. 87
32 W. Teunissen, PhD Thesis (2000), Utrecht University, The Netherlands
33 J.W.Geus, *Stud. Surf. Sci. Catal.* **16** (1983), 1
34 M. Vaarkamp, B.L. Mojet, F.S. Modica, J.T. Miller, and D.C. Koningsberger, *J. Phys. Chem.* **99-43** (1995), 16067
35 http://www.xsi.nl
36 M. Vaarkamp, I. Dring, R.J. Oldman, E.A. Stern, and D.C. Koningberger, *Phys. Rev. B* **50** (1994), 7872
37 J.W. Cook Jr and D.E. Sayers, *J. Appl. Phys.* **52** (1981), 5024
38 D.C. Koningsberger, B.L. Mojet, G.E. van Dorssen, and D.E. Ramaker, *Top. Catal.* **10** (2000), 143
39 R.W.G. Wyckhoff, Crystal Structures, vol. 1, 2nd Ed., John Wiley & Sons, Inc., New York, 1963, p. 10
40 J.M.D. Coey, *Acta Cryst.* **B26** (1970), 1876
41 H. Bärnighausen and B.K. Handa, *J. Less-Common Metals* **6** (1964), 226
42 D.C. Koningsberger *Jpn. J. Appl. Phys.* **32** (1993), 877.

43 M.S.P. Shaffer, X. Fan, and A.H. Windle, *Carbon* **36-11** (1998), 1603
44 W.M. Prest and R.A. Mosher in Colloids and Surfaces in Reprographic Technology (Eds. M. Hair and M. Croucher), ACS Symposium Series Vol. 200, ACS, Washington, 1982, p. 225
45 K. Nakamoto, Infrared and Raman Spectra of Inorganic and Coordination Compounds 4th edition, John Wiley, New York, 1986, p. 124
46 U. Zielke, K.J. Hüttinger, and W.P. Hoffman, *Carbon* **34-8** (1996), 983
47 P. Painter, M. Starsinic, and M. Coleman in Fourier Transform Infrared Spectroscopy, Applications to Chemical Systems (Eds. J.R. Ferraro, L.J. Basile), Vol. 4, Academic Press, Inc., Orlando, 1985, p. 169
48 D.B. Mawhinney, V. Naumenko, A. Kuznetsova, and J.T. Yates, *J. Am. Chem. Soc.* **122** (2000), 2383
49 H.P. Boehm, *Carbon* **32-5** (1994), 759
50 See Chapter 2 of this thesis
51 B.S. Furniss, A.J. Hannaford, P.W.G. Smith, and A.R. Tatchell, Vogel's textbook of practical organic chemistry, 5th Ed., Longman, London, 1989, p. 254
52 J.F. Moulder, W.F. Stickle, P.E. Sobol, and K.D. Bomben, Handbook of X-ray Photoelectron Spectroscopy, Perkin-Elmer corporation, United States, 1992, p. 117
53 M.A. Fox and J.K. Whitesell, Organic Chemistry, 2nd Ed., Jones and Bartlett Publishers, Boston, 1997, p. 629
54 C.U. Pittman, Jr., G.-R. He, B. Wu, and S.D. Gardner, *Carbon* **35-3** (1997), 317

6

Preparation and Activity of Small Rhodium Metal Particles on Fishbone Carbon Nanofibres

Abstract

A number of different impregnation and ion exchange methods have been employed to synthesise very small rhodium metal particles on HNO_3/H_2SO_4-oxidised fishbone carbon nanofibres. The surface oxidation of the nanofibres with HNO_3/H_2SO_4 is a prerequisite for a good interaction between aqueous catalyst precursor solutions and the fibres. Depending upon the preparation technique applied and using 1 wt% rhodium metal loadings, average particle sizes ranging from 1.1 to 2.1 nm were detected with XAFS spectroscopy. The rhodium metal particles are so small that metal-support interactions on carbon nanofibres can be investigated with XAFS spectroscopy. All catalysts are highly active in the liquid-phase hydrogenation of cyclohexene. No significant effect of particle size on the catalytic activity is observed, suggesting that other factors, such as clustering of the support particles in the liquid phase, are much more important.

6.1 Introduction

Currently, there is much interest in the physical and chemical properties of carbon nanotubes and carbon nanofibres (CNFs). Whereas carbon nanotubes are usually synthesised by arc discharge techniques, CNFs are obtained by catalytic decomposition of carbon-containing gases on small supported metal particles. The arc discharge technique can produce carbon nanotubes only in small quantities. Furthermore, thus produced tubes are polluted with other forms of carbon, such as carbon onions, fullerenes or amorphous carbon. Carbon nanofibres, on the other hand, do not contain other forms of carbon. Additionally, no heteroatoms, such as sulphur, are incorporated during synthesis. The metal and support of the catalyst originally used to grow the CNFs, however, has to be removed after synthesis. Investigation of use of carbon nanotubes and carbon nanofibres as catalyst support has only started recently. Carbon nanotubes are mostly employed to study the effects of this novel carbon material on the properties of the final supported catalyst. The arc discharge procedure, however, is too expensive to envisage thus produced carbon nanotubes as a support on a commercial scale. Carbon nanofibres, on the other hand, are a promising catalyst support material. The perspective is that, when grown in a fluidised bed reactor, carbon nanofibres can be obtained at low cost, making commercial application possible.[1] The properties of CNFs make them especially suitable for liquid-phase reactions. The fibres are mechanically strong and can withstand the forces involved in vigorous agitation of the reaction medium. Furthermore, the skeins of fibres possess a mesoporeus macrostructure, which decreases the possibility to encounter diffusion limitations during catalytic reactions in the liquid phase with respect to microporous materials, such as activated carbon. The structure of the CNFs can be tuned by changing the growth conditions and their hydrophobicity can be controlled by surface oxidation. The fibres are chemically inert and can be used in strongly acidic or basic liquids. Finally, after deactivation of the catalyst, CNFs can be readily combusted to recover the precious metal component of spent catalysts without leaving ash residues.

The use of carbon nanofibres and nanotubes as catalyst support has been reviewed recently.[1] A strong incentive for their use is the replacement of activated carbon (AC) for liquid-phase reactions. The properties of ACs are difficult to control. Unsatisfactory reproducibility, as well as the microporosity of activated carbon, has often impeded catalyst development. The sometimes inadequate mechanical properties of AC may lead to filtration problems in liquid-phase applications.

Hoogenraad *et al.*[2-6] extensively studied the use of Pd/CNFs for the hydrogenation of nitrobenzene to aniline. The authors prepared fibres with the graphite layers parallel to the fibre axis (parallel fibres) and fibres with the graphite layers at an angle to the fibre axis (fishbone fibres). The smallest Pd particles were obtained when fibres that were oxidised with HNO_3 were ion-

exchanged with a positively charged Pd-ammonia complex under the exclusion or air. With parallel fibres a maximal loading of 3 wt% was obtained, while with fishbone fibres only 1.5 wt% Pd could be exchanged.[3] On parallel fibres Pd particles of about 1.5 nm were obtained.[6] The Pd/CNFs catalyst turned out to be more active than a Pd/AC catalyst of a higher metal loading.[2] Though the authors did not offer an explanation for the higher activity of the fibre-supported catalyst, an effect of the size or the clustering of the carbon support bodies is very likely.

Baker and co-workers studied the activity of several metals on CNFs.[7-11] Fe or FeCu precursors were impregnated on HCl-treated CNFs, ultimately resulting in particles of an average size of 12 nm at 5 wt% loading.[7] In spite of the relatively large size of the metal crystallites, the activity of these catalysts was considerably higher in the hydrogenation of ethylene than Fe(Cu) on activated carbon or alumina. The authors pointed out the possible relationship between this activity enhancement and a unique metal-support interaction between the metal particles and the basal planes of the fibres. In later publications, Ni was impregnated on CNFs, resulting in 6-8 nm sized particles.[8-10] Again, as compared to nickel metal on classical supports, an activity improvement was obtained in the hydrogenation of 1-butene and 1,3-butadiene.[8] Furthermore, differently structured fishbone carbon nanofibres displayed different activities and selectivities.[9] Preferential blocking of either the armchair or the zigzag graphitic edge faces with phosphorus or boron, respectively, indicated that the effects could be ascribed to the catalytic action of Ni residing on the zigzag faces.[10] Similar effects were found when the hydrogenation of crotonaldehyde on Ni/CNFs was studied.[11] The nanofibre-supported catalysts were more active than Ni/Al_2O_3. Moreover, when alumina or 'ribbon' CNFs were used as the support selective hydrogenation of the double bond took place, whereas with 'platelet' CNFs the aldehyde functional group was converted. The results were related to the adsorption of crotonaldehyde on nickel particles on the zigzag faces, which supposedly have a special atomic arrangement.

Other researchers found surprising selectivities in selective hydrogenation reactions as well. Ledoux and co-workers[12] impregnated Pd on acid-treated CNFs and obtained 3-5 nm sized particles at 5 wt% loading. A very high activity and a 98 % selectivity towards the aldehyde was found with the hydrogenation of cinnamaldehyde at atmospheric pressure and 80°C. Planeix *et al.*,[13] on the other hand, observed a selectivity towards cinnamyl alcohol of 92 % with 3-7 nm sized Ru particles on non-purified nanotubes (0.2 wt% loading).

Finally, it is worth to mention the work of Ang *et al.*[14] and of Prinsloo and co-workers.[15] Ang deposited 2 nm sized Pd particles on HNO_3/H_2SO_4-oxidised carbon nanotubes by using an electroless plating technique. He reported that the tubes were densely coated with particles, indicating a high metal loading. Prinsloo used deposition-precipitation from a homogeneous solution to obtain HNO_3-oxidised carbon nanofibres densely coated with cobalt particles of 7 nm diameter.

This research describes the deposition of small rhodium metal particles on fishbone carbon nanofibres by several impregnation and ion exchange techniques. The objective is to assess which fibre pre-treatment procedures are needed to achieve an optimal interaction of the nanofibres with the catalyst precursor. Very small (1-2 nm sized) metal particles can be deposited on surface-oxidised CNFs. Furthermore, the influence of calcination and reduction procedures on the final metal particle size is studied. The size of the particles provides the opportunity to study metal-support interactions with XAFS spectroscopy, which requires very small particles and a narrow particle size distribution. These studies could shed more light on the unusual activities and selectivities described above. The Rh/CNF catalysts were tested in the liquid-phase hydrogenation of cyclohexene. Very high activities were found. Moreover, the results might indicate that other factors, such as clustering of the support particles in the liquid phase, are more important in determining the activity of the catalyst than the metal particle size.

6.2 Experimental

6.2.1 Growth of fishbone carbon nanofibres

Carbon nanofibres of the fishbone type were produced by catalytic decomposition of CH_4 on a Ni/Al_2O_3 catalyst.[2-4, 16]

The Ni/Al_2O_3 catalyst with 30 wt% Ni metal loading was synthesised by the deposition-precipitation technique.[17] Alumina (Alon-C, Degussa) was suspended in an acidified aqueous solution of nickel nitrate (Acros, 99 %) and diluted ammonia was injected within two hours at room temperature under vigorous stirring until the pH had reached a value of 8.5. After overnight stirring, the suspension was filtered, washed, and dried at 120°C. Finally, the catalyst was calcined at 600°C in stagnant air for three hours.

For the production of fishbone CNFs, 0.5 g of the 30 wt% Ni/Al_2O_3 catalyst was reduced at 600°C in 14 % H_2/N_2 (flow rate 350 ml/min) in a vertical tubular reactor (diameter 3 cm) for two hours. After having decreased the temperature to 570°C, methane (50 % in N_2, flow rate 450 ml/min) was passed through the catalyst bed for 6.5 hours. The yield of fibres amounted to approximately 12 g.

6.2.2 Catalyst synthesis

Impregnation

Untreated (as-synthesised) fishbone carbon nanofibres, as well as CNFs that were surface-oxidised with concentrated nitric acid, or a mixture of concentrated nitric acid and sulphuric acid were used for impregnation of an aqueous solution of $RhCl_3 \cdot 2H_2O$.

Ten grams of CNFs were boiled in 40 ml HNO_3 or 80 ml HNO_3/H_2SO_4 1:1 for 60 minutes (HNO_3: Lamers & Pleuger, 65 %, pure; H_2SO_4: Merck, 95-97 %, p.a.). Upon cooling and dilution with demineralised water, the suspensions were filtered over a Teflon membrane filter with a pore diameter of 0.2 μm, washed with water until the washings showed no significant acidity, and dried at 120°C for 16 hrs.

The total pore volume of the differently treated fibres was determined by adding demineralised water to de-gassed CNFs with a syringe until the fibres had a sticky appearance. The values obtained were about 0.4 ml/g. Next, de-gassed CNFs were impregnated in static vacuum with an aqueous solution of $RhCl_3 \cdot 2H_2O$ with a concentration of about 0.3 mol/l in order to get a rhodium metal loading of 1 wt%. De-gassing of the fibres was performed by evacuation at room temperature for several hours. The Rh-impregnated fibres were dried at room temperature for 36 hrs and, subsequently, dried at 120°C for 17 hrs.

The Rh-impregnated fibres were subjected to several calcination-reduction procedures. The catalysts were either calcined and then reduced or directly reduced. Calcination took place at 150°C or 250°C (stagnant air, 5°C/min, 1 hr), while the subsequent reduction temperature was 140°C or 250°C (10 % H_2/Ar, 5.6°C/min, 20 min). The reduction temperature for the direct reduction was either 160°C or 250°C. The reductions at lower temperatures were monitored with a Hot Wire Detector (HWD). The several calcination-reduction treatments along with the catalyst codes are shown in Table 6.1 for the HNO_3/H_2SO_4-oxidised fibres. The untreated and the HNO_3-oxidised fibres were not coded.

Table 6.1 Catalyst codes for the HNO_3/H_2SO_4-oxidised carbon nanofibres. All catalysts contain 1 wt% of Rh.

Code	Description
Rh/CNF(imp, c150, r140)	Impregnated, calcined at 150°C, reduced at 140°C
Rh/CNF(imp, c250, r140)	Impregnated, calcined at 250°C, reduced at 140°C
Rh/CNF(imp, r160)	Impregnated, reduced at 160°C
Rh/CNF(imp, c150, r 250)	Impregnated, calcined at 150°C, reduced at 250°C
Rh/CNF(imp, c250, r250)	Impregnated, calcined at 250°C, reduced at 250°C
Rh/CNF(imp, r250)	Impregnated, reduced at 250°C
Rh/CNF(IET)	Ion exchanged at elevated T, not reduced
Rh/CNF(IET, r200)	Ion exchanged at elevated T, reduced at 200°C
Rh/CNF(IET, r$NaBH_4$)	Ion exchanged at elevated T, reduced with $NaBH_4$
Rh/CNF(IEN, r200)	Ion exchanged with NH_3, reduced at 200°C
Rh/CNF(IENT, r200)	Ion exchanged with NH_3 at elevated T, reduced at 200°C

Ion exchange

Only fibres that were surface-oxidised with HNO_3/H_2SO_4 (see above) were used for ion exchange. As ion exchange with $RhCl_3 \cdot 2H_2O$ in water was not successful at room temperature, 1 g of fibres was refluxed in 30 ml of a $3.3*10^{-3}$ mol/l solution of $RhCl_3 \cdot 2H_2O$ in demineralised water for 48 hrs (maximum loading 1 wt%). Next, the ion-exchanged fibres were filtered and dried at 120°C for 17 hrs. Subsequently, the catalysts were either reduced with H_2 (10 % H_2/Ar, 5.6°C/min, 200°C, 20 min) or with $NaBH_4$. Reduction with $NaBH_4$ was carried out by dispersing one gram of ion-exchanged catalyst in 10 ml ethanol (Merck, p.a.) and by adding 55 mg $NaBH_4$ (Alfa, 99 %) in 10 ml ethanol. The evolution of gas indicated an immediate reduction. After stirring for 30 minutes at room temperature, the reduced catalyst was filtered from the colourless solution, washed with ethanol, and dried under vacuum at room temperature for 17 hours.

The ion exchange procedure was also carried out in a 4 % ammonia solution at room temperature and at refluxing conditions for 48 hrs. Again, the solution contained enough rhodium to obtain a 1 wt% catalyst. These catalysts were reduced at 200°C in H_2 (10 % H_2/Ar, 5.6°C/min, 20 min).

Table 6.1 summarises the several ion exchange procedures together with the accompanying catalyst codes.

6.2.3 Characterisation

Characterisation of the catalysts was carried out by scanning electron microscopy (SEM), transmission electron microscopy (TEM) and X-ray absorption fine structure (XAFS) spectroscopy.

Electron microscopy

SEM images were obtained on a Philips XL30FEG microscope operating at an accelerating voltage of 20 kV. TEM samples were prepared by dispersing ground catalyst in ethanol, using ultrasound, and drying a drop on a copper grid covered by a holey carbon film. They were imaged in a Philips CM-200 FEG electron microscope operating at 200 kV and in a Philips EM-420 electron microscope operated at an accelerating voltage of 120 kV. The CM-200 microscope was equipped with a field emission gun and an EDX facility for elemental analysis.

XAFS spectroscopy

XAFS data collection. XAFS spectra at the Rh K edge (23220 eV) were obtained at the HASYLAB (Hamburg, Germany) synchrotron beamline X1.1, which was equipped with a Si(311) double crystal monochromator. The monochromator was detuned to 50 % of the maximum intensity to minimise the presence of higher harmonics. All measurements were performed in the transmission mode using ionisation chambers filled with an Ar/N_2 mixture to

have an absorbance of 20 and 80 % in the first and the second ionisation chamber, respectively.

The powdered CNF-samples (300 mg) were pressed into self-supporting wafers and mounted into an *in situ* EXAFS cell equipped with Be windows.[18] Due to the low concentration of Rh (1 wt%), the calculated edge step was about 0.2. The Rh_2O_3 reference compound (Aldrich, 99.8 %) was diluted with boron nitride (Alfa, 99.8 %) and pressed into a self-supporting wafer (calculated edge step 1). The rhodium reference foil (Aldrich, 99.9 %, 25 μm thickness) was mounted on the sample holder with Kapton tape. All samples [except Rh/CNF(IET) and Rh/CNF(IET, rNaBH$_4$)] were *in situ* reduced (10 % H_2/He, 5°C/min, 1 hr) and cooled down to liquid nitrogen temperature prior to measurement. All gases were purified before use.

XAFS data-processing. Extraction of the EXAFS data from the measured absorption spectra was performed with the XDAP code developed by Vaarkamp *et al.*[19] Two scans were averaged and the pre-edge was subtracted using a modified Victoreen curve.[20] The background was subtracted employing cubic spline routines with a continuously adjustable smooth parameter[21, 22] Normalisation was performed by dividing the data by the height of the absorption edge at 50 eV.

EXAFS phase-shifts and backscattering amplitudes. Data for phase shifts and backscattering amplitudes were obtained from the reference compounds: Rh foil for Rh-Rh and Rh_2O_3 for Rh-O and Rh-C contributions.[22] Table 6.2 gives the crystallographic data and the forward and inverse Fourier transform ranges used to create the EXAFS references. Both the reference spectra and the samples were measured at liquid nitrogen temperature. This means that no temperature effect has to be included in the difference in Debye-Waller factor ($\Delta\sigma^2$) between sample and reference as obtained in the EXAFS data-analysis.

Table 6.2 Crystallographic data and the forward and inverse Fourier Transform ranges used to produce the EXAFS references.

						Forward FT	Inverse FT
Atom pair	Ref compd	Ref	N^{ref}	R^{ref} (Å)	k^n	ΔK (Å^{-1})	ΔR (Å)
Rh-Rh	Rh foil	23	12	2.69	3	2.7-22.7	1.4-3.1
Rh-O	Rh_2O_3[a]	24	6	2.05	1	3.7-16.3	0.0-2.3

[a] it was established with XRD that the Rh_2O_3 was in the hexagonal form.

R-space fitting, difference file technique and weight factor k^n. The EXAFS data-analysis program XDAP allows multiple-shell fitting in R-space by minimising the residuals between both the magnitude and imaginary part of the Fourier transforms of the data and the fit. R-space fitting has important advantages compared to the usually applied fitting in k-space, and is extensively discussed in a recent paper by Koningsberger *et al.*[22]

The difference file technique was applied together with phase-corrected Fourier transforms to resolve the different contributions in the EXAFS data.[22] The difference file technique allows one to optimise each individual contribution with respect to the other contributions present in the EXAFS spectrum. If the experimental spectrum is composed of different contributions, then:

$$\text{Exp.Data} = \sum_{i=1}^{N} (\text{Fit})_i \,, \tag{6.1}$$

whereby $(\text{Fit})_i$ represents the fitted contribution of co-ordination shell i. For each individual contribution the following equation should then be valid:

$$(\text{Fit})_j = \text{Exp.Data} - \sum_{i=1 \text{ and } i \neq j}^{N} (\text{Fit})_i \,. \tag{6.2}$$

The right-hand side of this equation is further denoted as the difference file of shell j. A good fit is only obtained if the total fit and each individual contributing co-ordination shell describe correctly the experimental EXAFS and the difference file, respectively. In this way, not only the total EXAFS fit, but also the individual fits of all separate contributions can be determined reliably.

Both high Z (e.g. metal-metal) and low Z (e.g. metal-oxygen) contributions may be present in the EXAFS data collected on small metal particles dispersed on high surface area supports. The low Z contributions may arise from the support. A k^3 weighting emphasises the high Z contributions to the spectrum, since high Z elements have more scattering power at high values of k than low Z elements. However, the use of a k^3 weighted EXAFS spectrum or Fourier transform makes the analysis much less sensitive to the presence of low Z contributions in the EXAFS data. In this study, the EXAFS fits have been checked by applying k^1, k^2 and k^3 weightings in order to be certain that the results are the same for all weightings.

Number of independent data points, variance and statistical significance. The number of independent data points (N_{indp}) was determined as outlined in the "Reports on Standard and Criteria in XAFS Spectroscopy":[25]

$$N_{indp} = \frac{2\Delta k \Delta R}{\pi} + 2 . \qquad (6.3)$$

The variances of the magnitude and imaginary part of the Fourier transforms of fit and data were calculated according to the following equation:

$$\text{Variance} = \frac{\int \left[k^n \left(FT^n_{model}(R) - FT^n_{exp}(R) \right) \right]^2 dR}{\int \left[k^n FT^n_{exp}(R) \right]^2 dR} \times 100 . \qquad (6.4)$$

In this study the statistical significance of a contribution has been checked by a comparison of the amplitude of $(Fit)_j$ with the noise level present in the difference file (the noise in the difference file is essentially the same as the noise in the experimental data).

Estimation of particle size. The average particle size of the various catalysts was estimated from the Rh-Rh co-ordination numbers obtained with EXAFS by using a computer program.[26] The program 'cuts' spherical or semi-spherical particles with different diameter from a Rh fcc crystal and calculates the average co-ordination number and the number of atoms in the particle.

6.2.4 Catalytic test experiments

The catalytic activity of the Rh/CNFs catalysts in the hydrogenation of cyclohexene was tested in a semi-batch slurry reactor, operated at a constant pressure of 1200 mbar H_2. The thermostated, double-walled reaction vessel was equipped with vertical baffles and a gas-tight stirrer with a hollow shaft and blades for gas recirculation. The stirrer was operated at 2000 rpm. During reaction, the hydrogen consumption was automatically monitored by a mass flow meter. It was assured that, under the conditions used, the rate of dissolution of H_2 in the solvent was higher than the maximum measurable rate of H_2-uptake.

In a typical experiment, the reaction vessel was filled with 50 mg of powdered catalyst and 100 ml of ethanol (Merck p.a.). Next, the reactor was thermostated at 25°C, evacuated, filled with H_2, and pressurised. After stirring for 1 hour

under H_2 in order to reduce the catalyst, the reaction was started by injection of 1 ml cyclohexene (Acros 99 %) with a syringe and was allowed to proceed until total hydrogenation of cyclohexene.

The presence or absence of internal diffusion limitations was checked by calculation of the internal effectiveness factor η, using the following expression:[27]

$$\eta = \frac{\tanh\varphi}{\phi} \tag{6.5}$$

with:

$$\varphi = \frac{1}{a'_v}\sqrt{\frac{k_{v,p}}{D_{eA}}}\,. \tag{6.6}$$

ϕ is referred to as the Thiele modulus, $k_{v,p}$ is the reaction rate constant per unit catalyst volume and D_{eA} is the effective diffusion constant for reactant A. a'_v is the ratio between the external surface area and the volume of the catalyst particle. Values of η close to 1 indicate that internal diffusion limitations are absent.

For spherical particles a'_v is given by:

$$a'_v = \frac{6}{d_p}, \tag{6.7}$$

where d_p is the particle diameter. D_{eA} is given by:

$$D_{eA} = \frac{\varepsilon_p D_A}{\tau_p}, \tag{6.8}$$

where D_A is the diffusion coefficient of reactant A, ε_p is the void fraction of the particle, and τ_p is the tortuosity of the particle. The reaction rate constant $k_{v,p}$ can be obtained from:

$$C_A = C_{A0}e^{-k_1 t}\,, \tag{6.9}$$

assuming a first order reaction. C_A is the concentration of reactant at time t, C_{A0} is the initial concentration, and k_1 is the reaction rate constant per unit reactor volume. k_1 can easily be converted to $k_{v,p}$ by multiplying it with the ratio of reactor volume and catalyst volume.

6.3 Results

Scanning electron microscopy

Figure 6.1 displays two SEM images of powdered fishbone carbon nanofibres treated with HNO_3/H_2SO_4. Figure 6.1A shows that the bodies of entangled fibres in this sample exhibit a broad particle size distribution. However, no nanofibre particles larger than about 50 μm are observed. Most CNF particles have a dimension between 5 and 20 μm. At larger magnification (Figure 6.1B) the individual fibres become visible. The fibres are entangled and form an open, macroporous structure.[28]

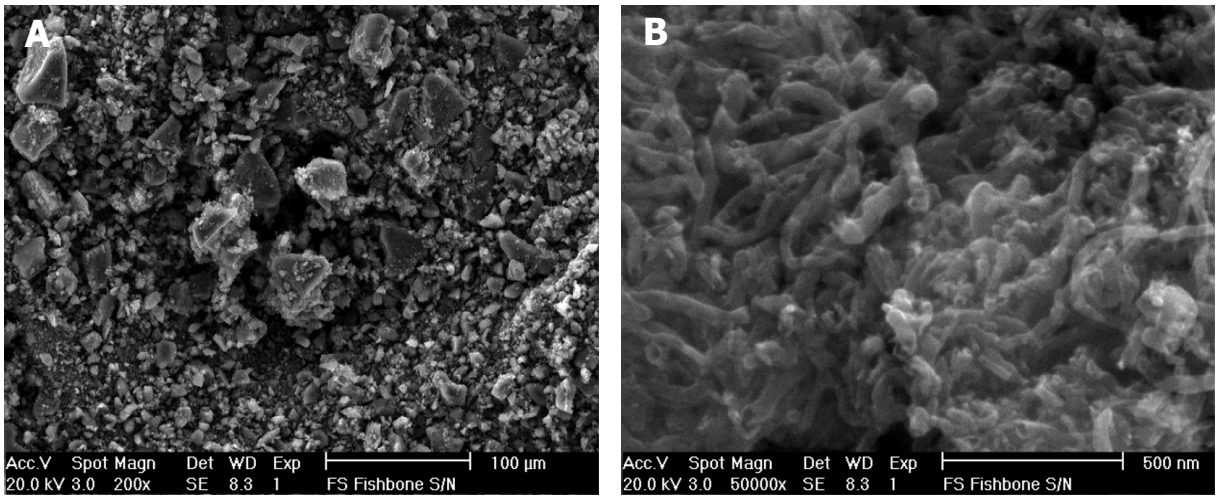

Figure 6.1 SEM images of HNO_3/H_2SO_4-oxidised fishbone carbon nanofibres at different magnifications. A) shows the skeins of fibres and B) images the individual CNFs.

Transmission electron microscopy

The size and distribution of the rhodium particles on untreated, HNO_3-oxidised and HNO_3/H_2SO_4-oxidised fibres was examined with TEM (see Figure 6.2). Within the untreated CNFs rhodium particles are found only very locally. No rhodium particles are observed on the carbon nanofibres (see Figure 6.2A). However, many rhodium particles have been deposited on the holey carbon film (see Figure 6.2B). Most of the deposited rhodium particles are smaller than 10 nm, but larger particles up to 80 nm have been found as well. Detected rhodium

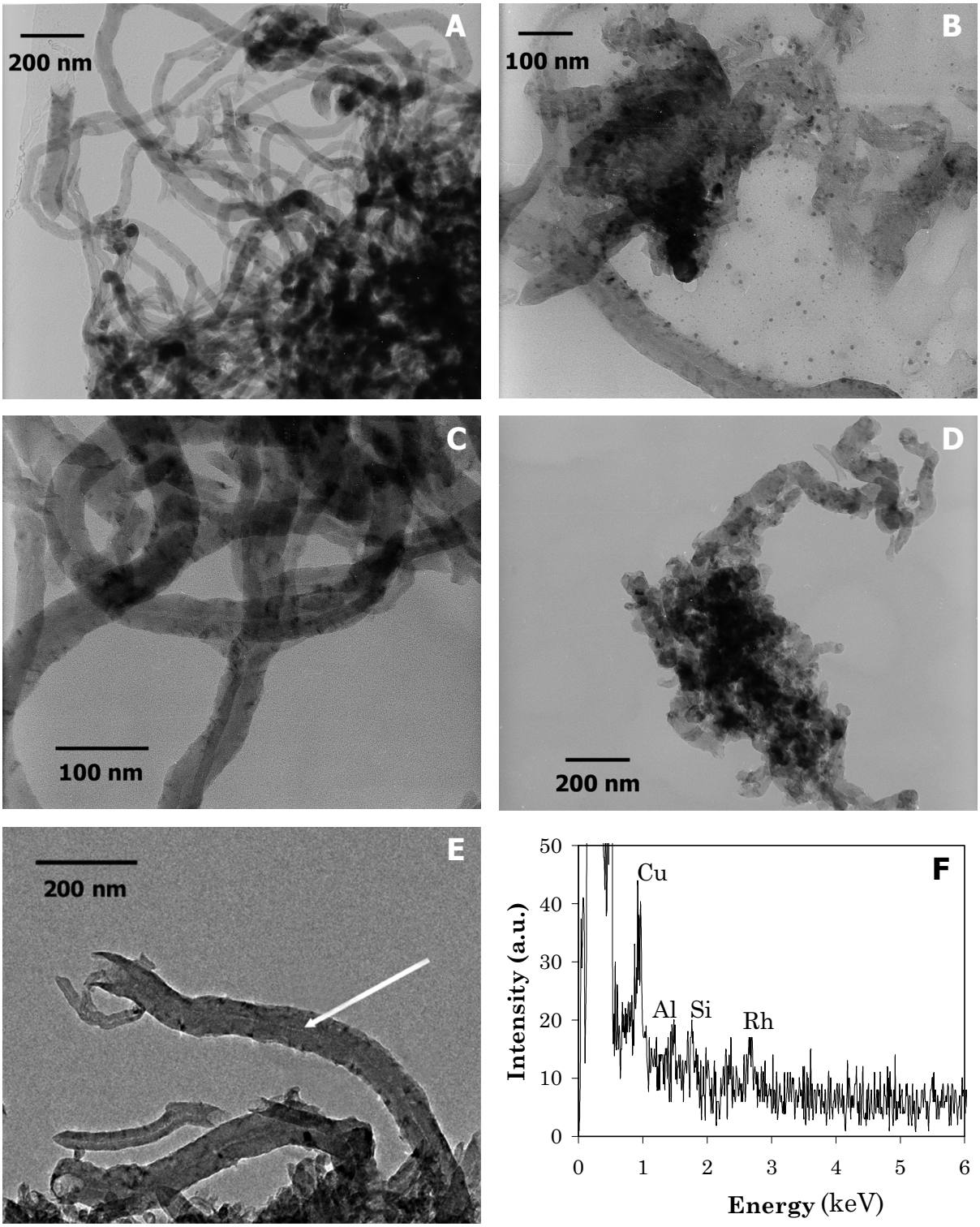

Figure 6.2 A, B) TEM images of rhodium impregnated untreated CNFs (calc. 150°C, red. 140°C) C, D) TEM images of rhodium impregnated HNO_3 oxidised CNFs (calc. 150°C, red. 140°C) E) TEM image of Rh/CNF(imp, c150, r140) F) EDX spot analysis of area indicated with a white arrow in E).

is always associated with the presence of Al_2O_3 that is still present in these fibres (originating from the Ni/Al_2O_3 growth catalyst).

With the HNO_3-oxidised carbon nanofibres most fibres are also bare (see Figure 6.2C). Only occasionally large Rh particles are detected on the CNFs. EDX analysis revealed that Rh was only present within clusters of fibres. An example is shown in Figure 6.2D. These rhodium particles are probably large as well.

In spite of an extended study, no rhodium particles could be imaged at all on the fibres that had been treated with HNO_3/H_2SO_4. The diffraction contrast of the fibres themselves hinders the imaging of very small rhodium particles. However, when an EDX analysis was performed on a single fibre (see Figure 6.2E and F) some rhodium could be detected. The Cu observed originates from the copper grid, the Al comes from some Al_2O_3 that remained in the sample after the oxidation treatment, and Si is probably introduced during the oxidation treatment from the glass round-bottomed flask.

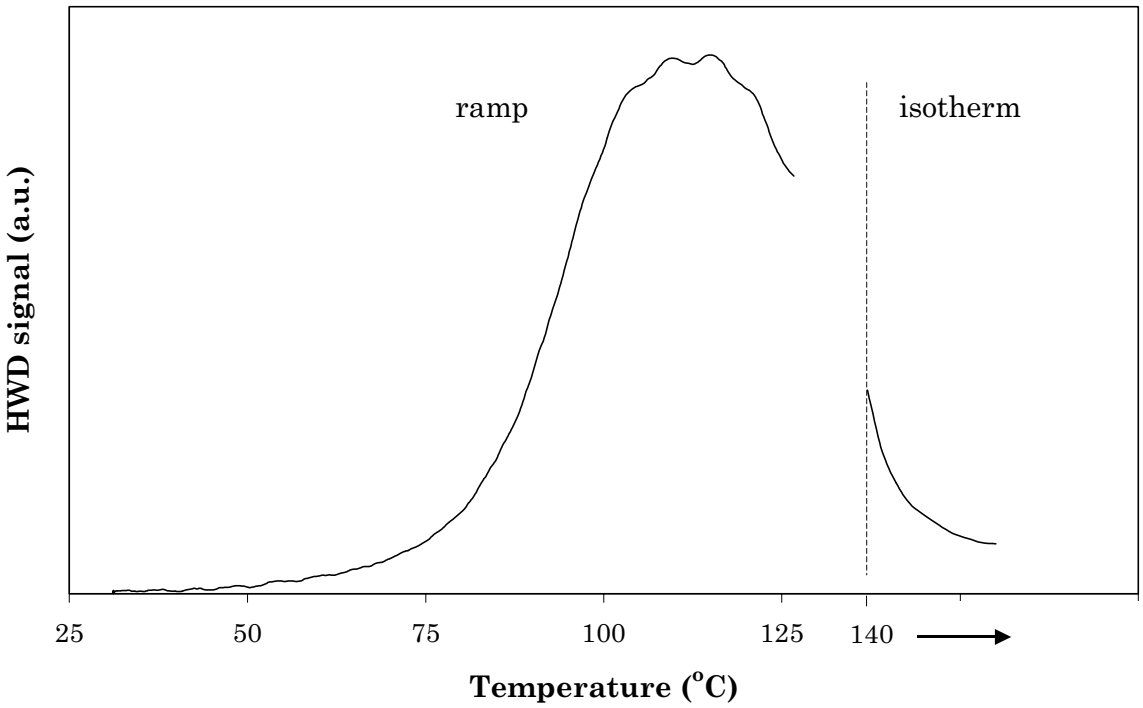

Figure 6.3 Hydrogen consumption profile during reduction of Rh/CNF(imp, c250, r140).

Reduction of the catalysts

The impregnated catalysts were first reduced at the lowest reduction temperature possible (140°C for the reduction of Rh_2O_3 and 160°C for the reduction of $RhCl_3 \cdot 2H_2O$). These temperature levels and the temperatures for the calcination of $RhCl_3 \cdot 2H_2O$ were determined using *in situ* temperature-programmed XRD on pure Rh_2O_3 and $RhCl_3 \cdot 2H_2O$.

Figure 6.3 shows the reduction profile of Rh/CNF(imp, c250, r140). The left part of the figure exhibits the reduction profile during the temperature ramp up to 140°C. Because the plotted temperature is the temperature within the reactor, and the temperature controller uses the temperature of the furnace, the temperature of the catalyst bed is lower than 140°C after the ramp. After a period of stabilisation of the temperature (during which the H_2 consumption is not monitored), the catalyst bed reaches a temperature of 140°C and the reduction is continued isothermally during 20 minutes (right-hand part of the figure). The figure shows that the reduction of Rh/CNF(imp, c250, r140) has just completed at the termination of the program. The same results were obtained for Rh/CNF(imp, c150, r150) and Rh/CNF(imp, r160). The reductions at higher temperatures were not monitored.

XAFS spectroscopy

XAFS analysis. Figure 6.4 shows the experimental EXAFS data of Rh/CNF(imp, c150, r140) [Figure 6.4A] and Rh/CNF(imp, c150, r250) [Figure 6.4C]. The data quality is excellent. The signal-to-noise ratio at k = 4 $Å^{-1}$ amounts to approximately 120 for Rh/CNF(imp, c150, r140) and 90 for Rh/CNF(imp, c150, r250). It can clearly be seen that the EXAFS intensity of Rh/CNF(imp, c150, r250) at larger values of k (k > 10 $Å^{-1}$) is higher than for Rh/CNF(imp, c150, r140), indicating the presence of larger rhodium particles. The corresponding k^1 Fourier transforms of both catalysts (Figure 6.4B and D) confirm this observation. The peak at 2.5 Å, originating from the Rh-Rh contribution, has a higher intensity with Rh/CNF(imp, c150, r250) than with Rh/CNF(imp, c150, r140).

The Fourier transform (FT) of the experimental EXAFS data of Rh/CNF(imp, c150, r140) together with the FT of the total fit is shown in Figure 6.5A. The fit quality is excellent for the used fit range (ΔR = 1-2.8 Å). In Rh/CNF(imp, c150, r140) Rh-Rh and Rh-C contributions could be established. The phase-corrected Fourier transforms of the fits of the two individual contributions together with their corresponding difference files are shown in Fig. 6.5B and C for the Rh-Rh and Rh-C contributions, respectively. The fit quality of each individual contribution is very good. The statistical significance of the fits has been demonstrated in Figure 6.5D. The calculated k^0 weighted Rh-Rh and Rh-C EXAFS spectra that are shown in the figure can be compared with the dotted lines approximately indicating the maximum (peak to peak) noise levels. It is shown that the Rh-C contribution has a higher intensity than the noise level up to high k values, demonstrating that reliable fit results for the weaker Rh-C contribution have been obtained as well.

Table 6.3 presents the fit parameters of the EXAFS spectra resulting from the multiple shell fits in R-space and the variances of the imaginary and absolute part of the fits for all catalysts. All variances obtained are well below 1 %, indicating that excellent fit results for all catalysts have been acquired.[22]

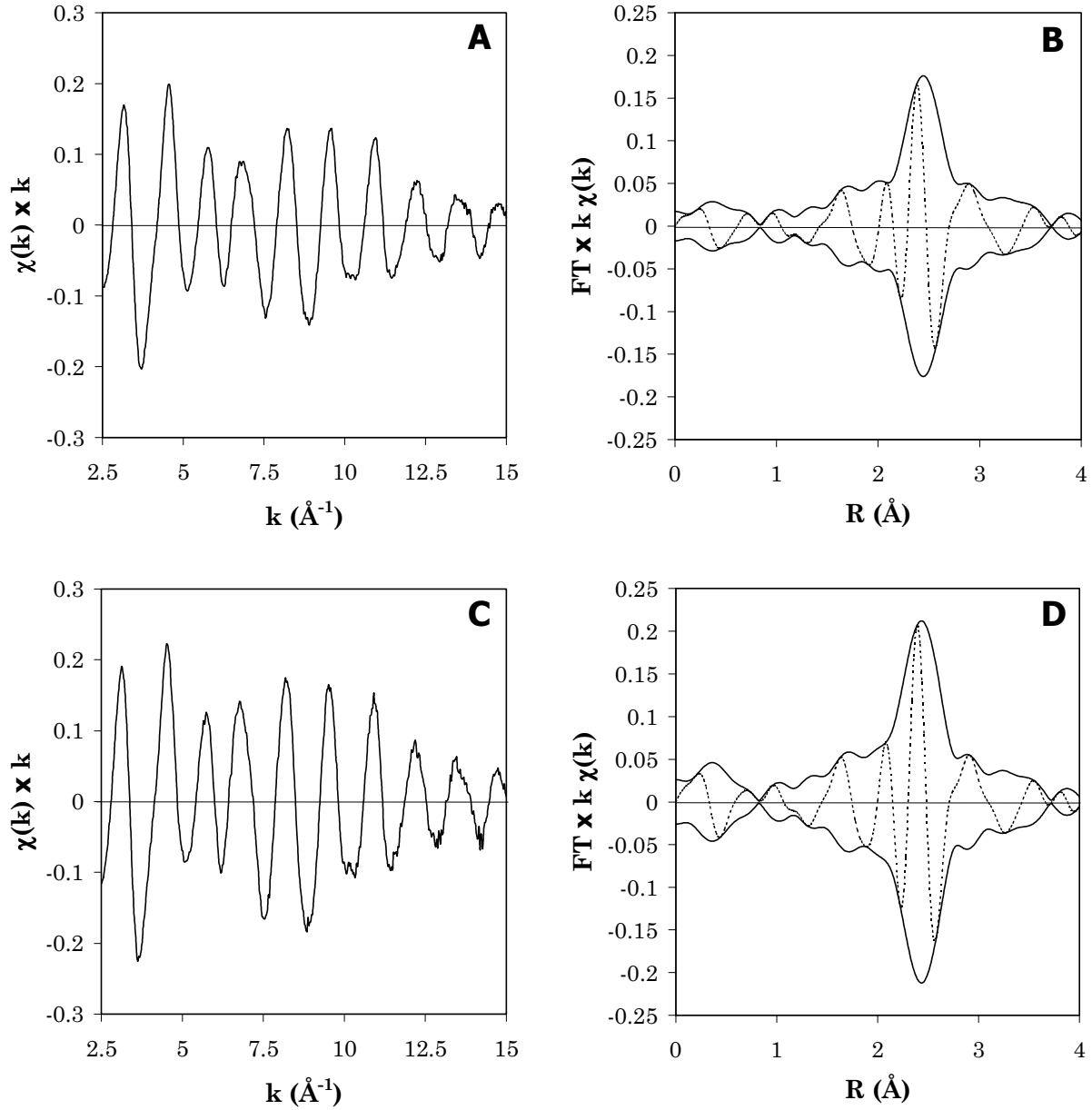

Figure 6.4 A) Experimental k^1 weighted EXAFS spectrum of Rh/CNF(imp, c150, r140)
B) Corresponding uncorrected Fourier transform (k^1 weighted, Δk = 3.9-14 $Å^{-1}$)
C) Experimental k^1 weighted EXAFS spectrum of Rh/CNF(imp, c150, r250)
D) Corresponding uncorrected Fourier transform (k^1 weighted, Δk = 3.9-14 $Å^{-1}$).

Furthermore, the calculated number of independent data points (N_{indp}, see Equation 6.3) is 14, showing that a fit with three shells is possible (N_{indp} = 12). With Rh/CNF(imp, c150, r140) the Rh-Rh co-ordination number amounts to 5.8. In addition, 2.2 carbon atoms are distinguished at a distance of 2.7 Å. Upon reduction at 250°C the Rh-Rh co-ordination number increases to 7.7 [Rh/CNF(imp, c150, r250)]. An increase can also be observed between the catalyst

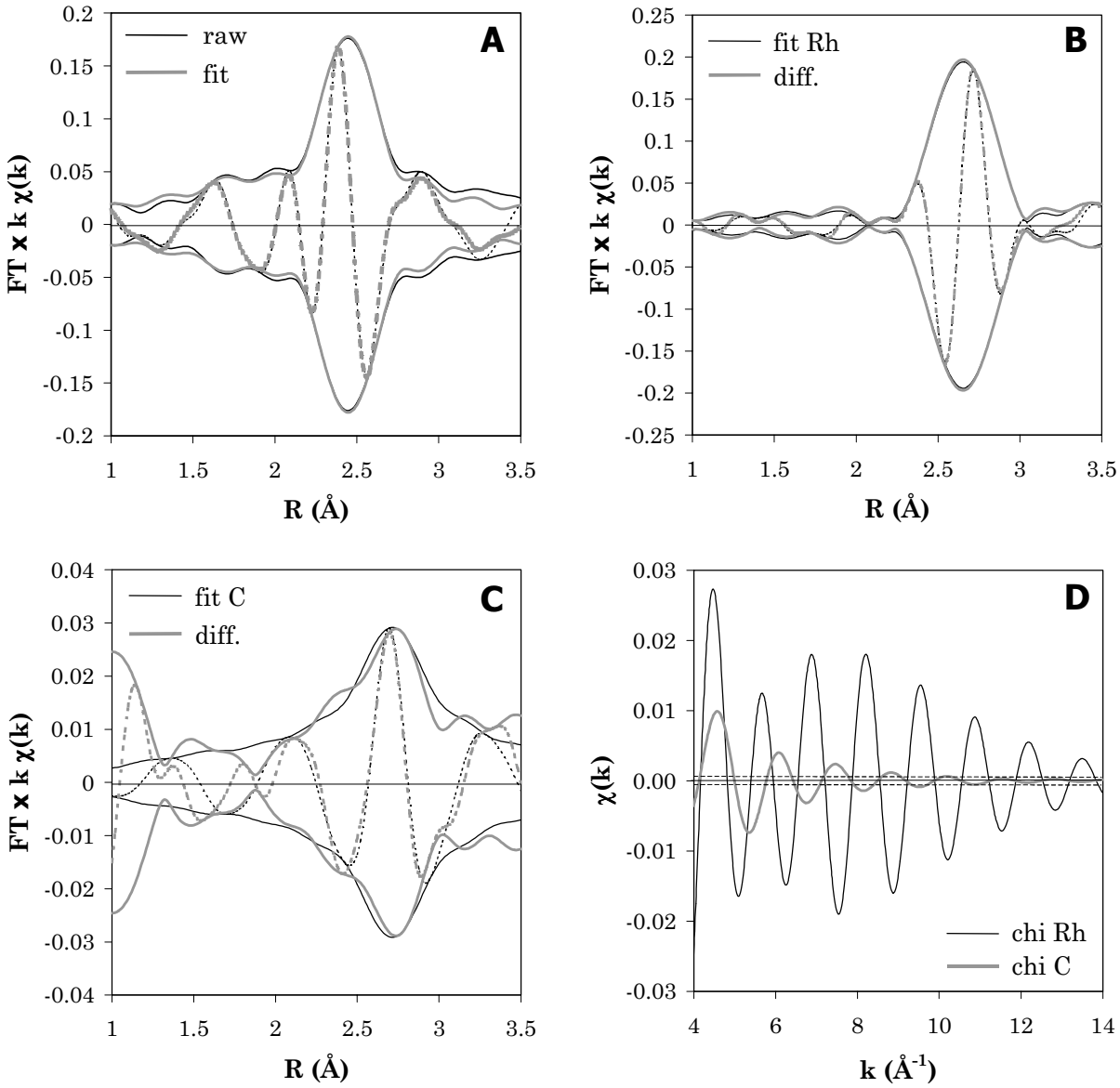

Figure 6.5 Fit results of Rh/CNF(imp, c150, r140) [k^1 weighted, Δk = 3.9-14 $Å^{-1}$, ΔR = 1-2.8 Å]
A) Fourier transform of experimental EXAFS data and total fit (uncorrected)
B) Rhodium-rhodium fit and corresponding difference file (Rh-Rh phase-corrected)
C) Rhodium-carbon fit and corresponding difference file (Rh-C phase-corrected)
D) Calculated k^0 weighted EXAFS spectrum of the Rh-Rh and Rh-C fit. The two dotted lines indicate the noise level of the spectra.

that was calcined and reduced at 250°C and those that were directly reduced. However, calcination at either 150°C or 250°C does not influence the co-ordination number of the rhodium atoms. Direct reduction results in a larger co-ordination number at low reduction temperatures than calcination-reduction. At

Table 6.3 Fit parameters of EXAFS spectra and variances of fits (Δk = 3.9-14 Å^{-1}, ΔR = 1-2.8 Å, k^1 weighted).

Catalyst	Atom	N	R (Å)	$\Delta\sigma^2$ (Å^2)	ΔE_0 (eV)	Variance (%)	
		±5 %	±1 %	±5 %	±10 %	Im	Abs
Rh/CNF(imp, c150, r140)	Rh	5.8	2.68	0.002	5.5	0.37	0.21
	C	2.2	2.70	0.000	-3.6		
Rh/CNF(imp, c250, r140)	Rh	5.9	2.68	0.002	7.0	0.62	0.32
	C	2.0	2.70	0.000	-3.2		
Rh/CNF(imp, r160)	Rh	6.7	2.68	0.002	7.2	0.23	0.13
	C	1.8	2.70	0.000	-3.4		
Rh/CNF(imp, c150, r250)	Rh	7.7	2.68	0.002	7.2	0.18	0.10
	C	2.3	2.70	0.000	-7.3		
Rh/CNF(imp, c250, r250)	Rh	7.5	2.67	0.003	7.2	0.35	0.21
	C	2.5	2.70	0.000	-6.9		
Rh/CNF(imp, r250)	Rh	7.8	2.68	0.002	7.5	0.26	0.15
	C	2.5	2.70	0.000	-7.1		
Rh/CNF(IET)*	O	4.0	2.05	0.001	-6.4	0.19	0.05
	Cl	2.0	2.27	0.004	8.0		
	C	2.7	2.86	0.001	-4.9		
Rh/CNF(IET, r200)	Rh	5.9	2.68	0.004	9.4	0.19	0.11
	C	2.2	2.70	0.000	-1.8		
Rh/CNF(IET, r$NaBH_4$)*	Rh	3.8	2.68	0.010	7.8	0.49	0.20
	O	4.7	2.05	0.001	-2.1		
	C	1.5	2.29	0.008	-5.6		
Rh/CNF(IEN, r200)	Rh	8.9	2.69	0.001	0.3	0.19	0.15
Rh/CNF(IENT, r200)	Rh	8.7	2.69	0.001	-0.8	0.23	0.17

* k^2-fitted

a reduction temperature of 250°C this effect almost disappears. With all impregnated catalysts a Rh-C contribution can be distinguished.

Figure 6.6A, C, and E display the experimental EXAFS data of Rh/CNF(IET), Rh/CNF(IET, r200), and Rh/CNF(IET, r$NaBH_4$), respectively. The signal-to-noise ratio at k = 4 Å^{-1} of these spectra ranges from 50 to 70. The EXAFS intensity of Rh/CNF(IET) [Figure 6.6A] is low at large k values (k > 10 Å^{-1}), indicating that high Z scatterers are absent in this spectrum. Upon reduction with H_2 (Figure 6.6C) the spectrum totally changes. The high EXAFS intensity at large k values (k > 10 Å^{-1}) shows that a significant Rh-Rh contribution is present. The spectrum

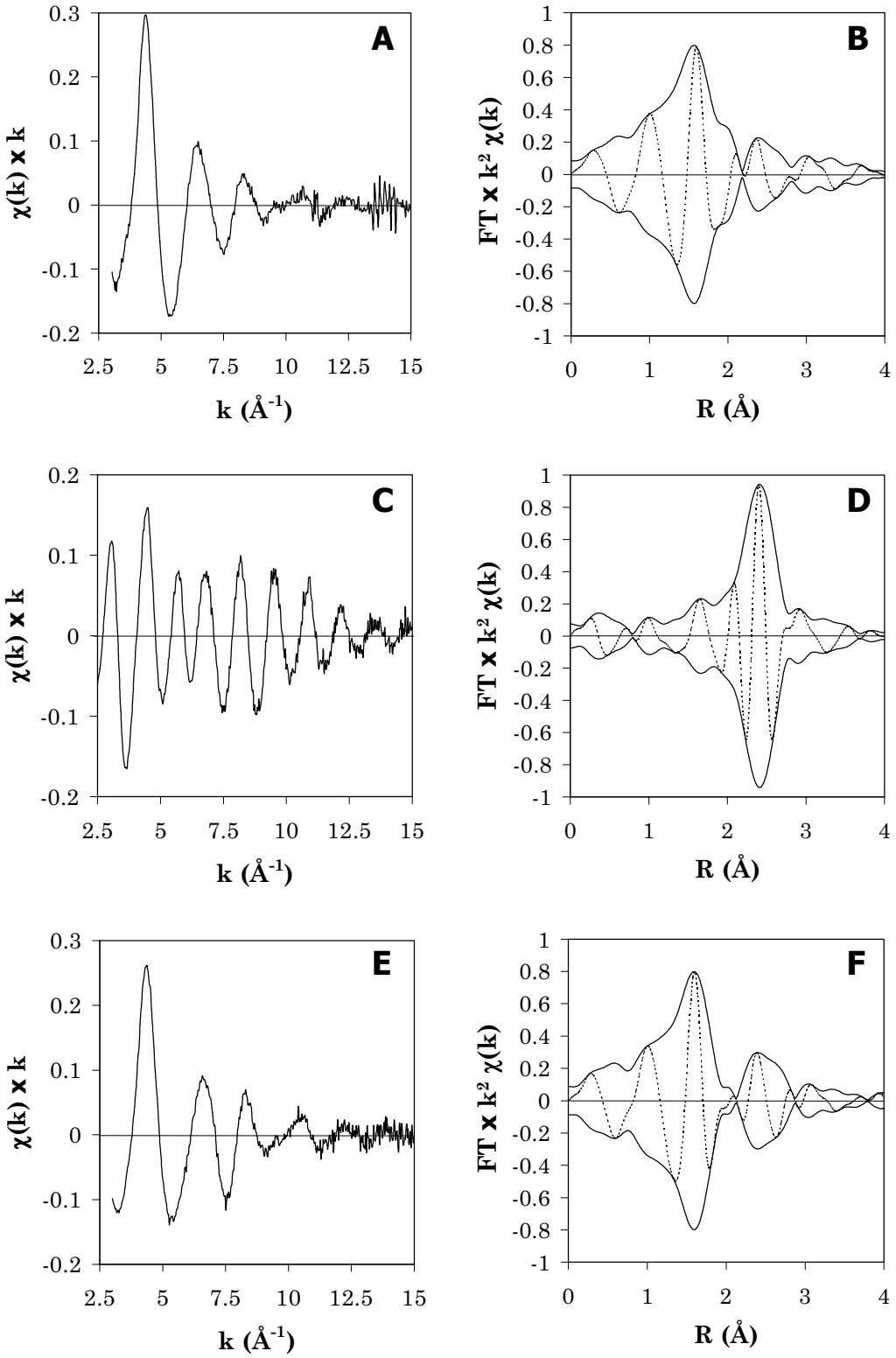

Figure 6.6 Experimental k^1 weighted EXAFS spectra of Rh/CNF(IET) [A], Rh/CNF(IET, r200) [C] and Rh/CNF(IET, $rNaBH_4$) [E] and the corresponding uncorrected Fourier transforms [B, D, and F, respectively] (k^2 weighted, Δk = 3.9-14 $Å^{-1}$).

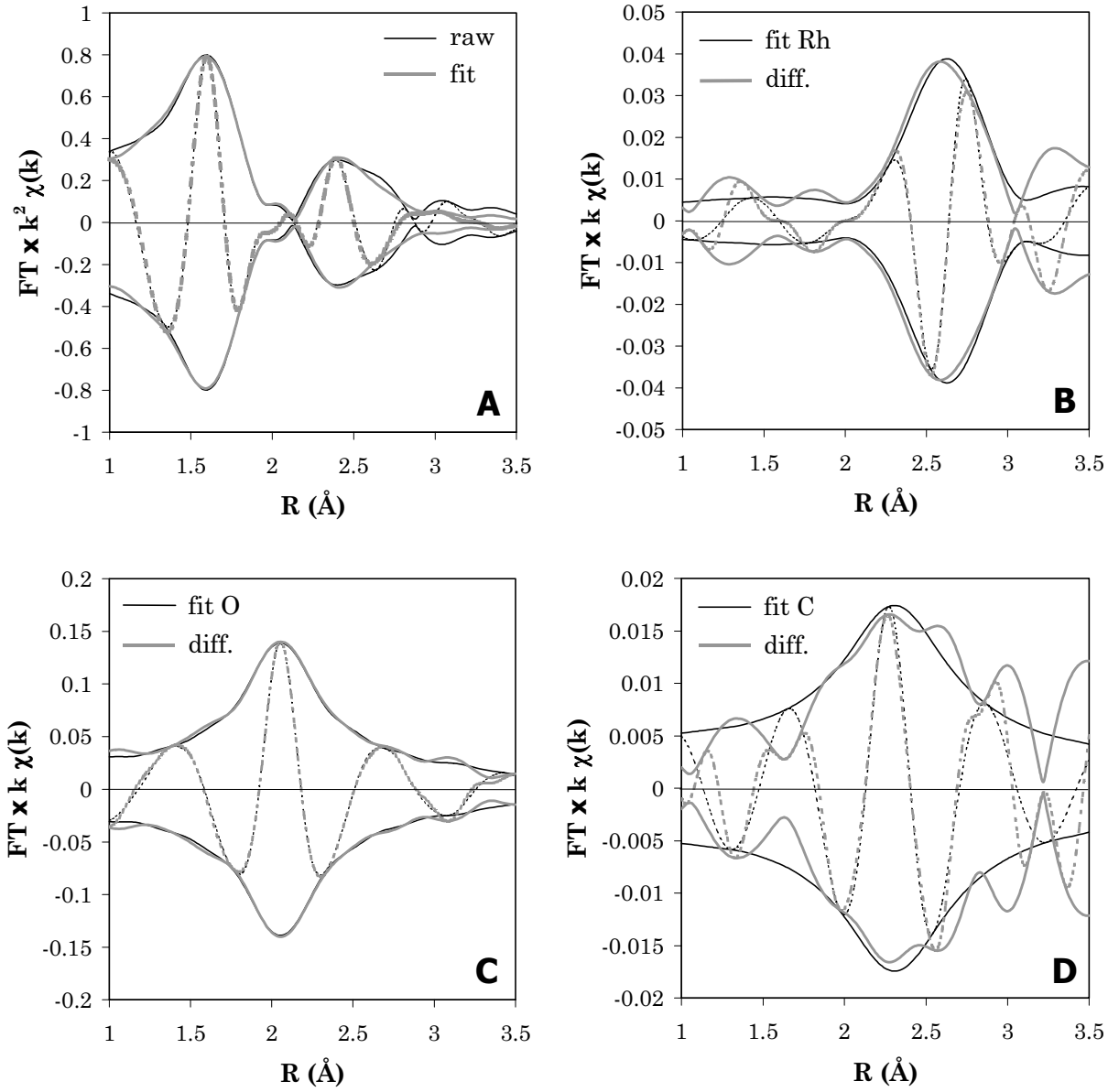

Figure 6.7 Fit results of Rh/CNF(IET, rNaBH$_4$) [Δk = 3.9-14 Å^{-1}, ΔR = 1-2.8 Å] A) Fourier transform of experimental EXAFS data and total fit (k^2 weighted, uncorrected) B) Rhodium-rhodium fit and corresponding difference file (k^1 weighted, Rh-Rh phase-corrected) C) Rhodium-oxygen fit and corresponding difference file (k^1 weighted, Rh-O phase-corrected) D) Rhodium-carbon fit and corresponding difference file (k^1 weighted, Rh-C phase-corrected).

of the catalyst that was reduced with NaBH$_4$ (Figure 6.6E) displays characteristics intermediate to that of the other catalysts. The k^2-Fourier transforms of the experimental EXAFS data are shown in Figure 6.6B, D, and F. Before reduction (Figure 6.6B) mainly contributions at 1.6 Å arising from low Z scatterers are present. Upon reduction with H_2 (Figure 6.6D) an intense peak at 2.4 Å points to the formation of rhodium particles. After reduction with NaBH$_4$

(Figure 6.6F) only a small Rh-Rh contribution at the same distance can be distinguished.

Figure 6.7 shows the fit results of Rh/CNF(IET, rNaBH$_4$). Again, good results are obtained for the total fit and three separate Rh-Rh, Rh-O and Rh-C contributions. At a distance of 2.68 Å an average number of 3.8 Rh neighbours is present (see Table 6.3). The co-ordination number of oxygen neighbours amounts to 4.7 at 2.05 Å. Finally, 1.5 carbon atoms are visible at a distance of 2.29 Å. Before reduction [Rh/CNF(IET)] no Rh-Rh can be fitted in the FT of the experimental EXAFS data. Four oxygen atoms are visible at 2.05 Å, two chlorine atoms reside at 2.27 Å, and 2.7 carbon atoms are distinguishable at 2.86 Å. After reduction with H_2 [Rh/CNF(IET, r200)] the co-ordination number of Rh amounts to 5.9 and 2.2 carbon atoms are present at 2.70 Å.

Figure 6.8 shows the Rh-C fits and the corresponding difference files of Rh/CNF(imp, c150, r140) and Rh/CNF(IET, rNaBH$_4$). After reduction with H_2 a rhodium-carbon contribution is present at 2.70 Å, while after the use of NaBH$_4$ as reductant a Rh-C interaction is present at a much shorter distance of 2.29 Å.

The ion-exchanged catalysts that were prepared in the presence of NH_3 and reduced at 200°C show the largest Rh-Rh co-ordination number (see Table 6.3). Synthesis at room temperature or reflux temperature does not affect the co-ordination number significantly. Values of 8.9 and 8.7 were obtained, respectively. No Rh-C contributions could be fitted.

It should be noted that with all catalysts edge steps in the X-ray absorption spectra were obtained that were equal to the theoretical edge step for 1 wt% Rh on carbon. In other words, all catalysts indeed contain 1 wt% of Rh.

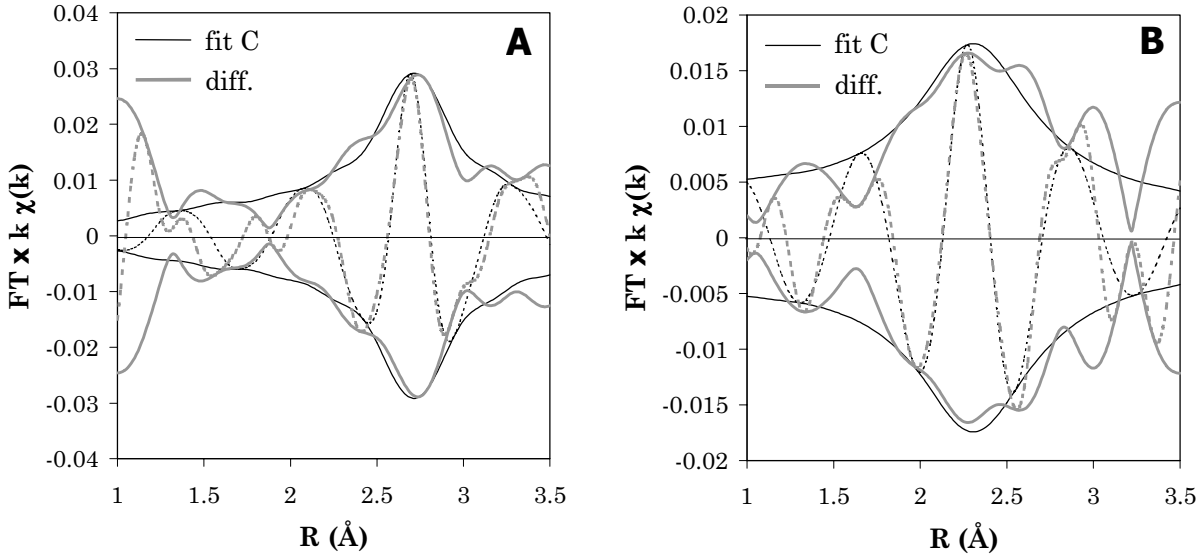

Figure 6.8 Rhodium-carbon fits and corresponding difference files (k^1 weighted, Rh-C phase-corrected) of A) Rh/CNF(imp, c150, r140 and B) Rh/CNF(IET, rNaBH$_4$).

Estimation of particle size. Figure 6.9A shows the relationship between the particle size and the co-ordination number for spherical and semi-spherical particles. Because in some cases no additional rhodium atoms are included in the modelled particle upon increase of its size with 0.1 nm, some points have the same co-ordination number. The datapoints were fitted with logarithmic functions. Figure 6.9B displays the relationship between the particle size and the number of atoms in the particle. The results obtained correspond well with data obtained by Kip *et al.*[29] The figures clearly show that the outcome depends considerably upon the assumed particle shape. However, the geometry of the Rh/CNFs particles is not known. The smallest particles could well be semi-spherical shaped, whereas the larger particles could adapt a more spherical-like shape. Therefore, the average of the particle size obtained for spherical and semi-spherical particles was taken. Table 6.4 displays the results for all catalysts. The size of the rhodium particles in the catalysts ranges from 1.1 to 2.1 nm.

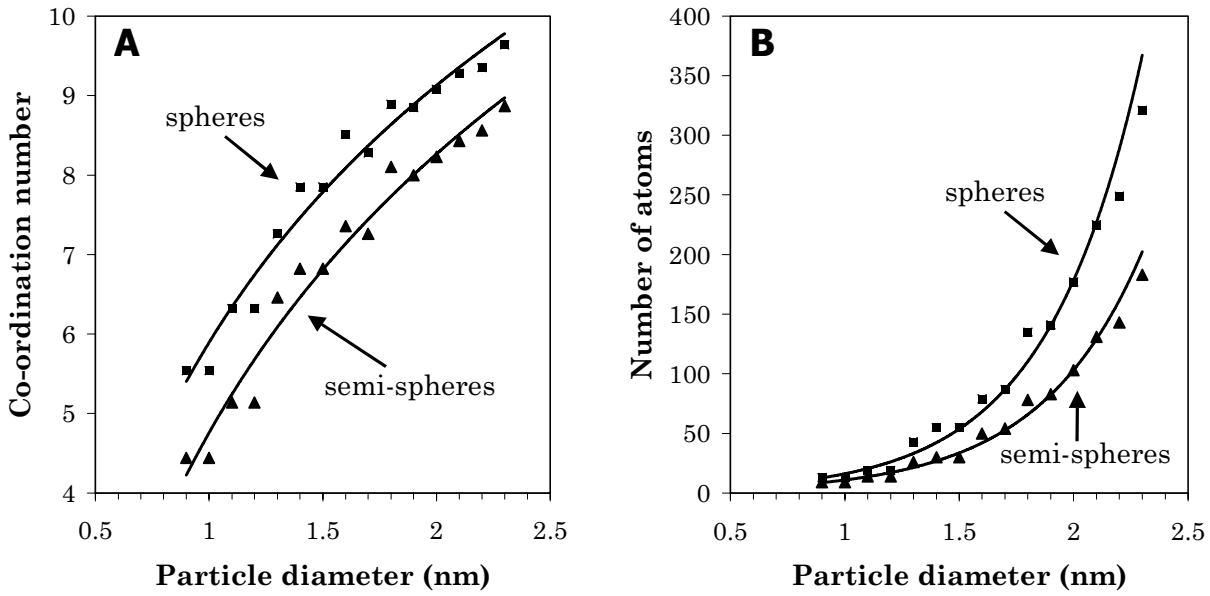

Figure 6.9 A) First shell co-ordination number against particle diameter for spherical and semi-spherical particles. B) Number of atoms against particle diameter for spherical and semi-spherical particles.

Catalytic test experiments

The catalytic measurements resulted in a plot of the H_2-flow against time [see Figure 6.10 for Rh/CNF(imp, c150, r140)]. This curve was integrated to get an H_2-uptake pattern, which, in turn, was used to calculate the initial activity (i.e., the activity in mole H_2/g_{cat}*h at t = 0). The results are summarised in Table 6.5 together with the estimated particle sizes. Figure 6.11 shows a plot of the initial

activities against the particle size. The numbers in the figure correspond to the numbers in Table 6.5. All activities could be reproduced well within 10 %.

Table 6.4 Estimated average particle size for all catalysts.

Catalyst	$N_{Rh\text{-}Rh}$	D (nm)
Rh/CNF(imp, c150, r140)	5.8	1.1
Rh/CNF(imp, c250, r140)	5.9	1.1
Rh/CNF(imp, r160)	6.7	1.4
Rh/CNF(imp, c150, r250)	7.7	1.7
Rh/CNF(imp, c250, r250)	7.5	1.6
Rh/CNF(imp, r250)	7.8	1.7
Rh/CNF(IET, r200)	5.9	1.1
Rh/CNF(IEN, r200)	8.9	2.1
Rh/CNF(IENT, r200)	8.7	2.0

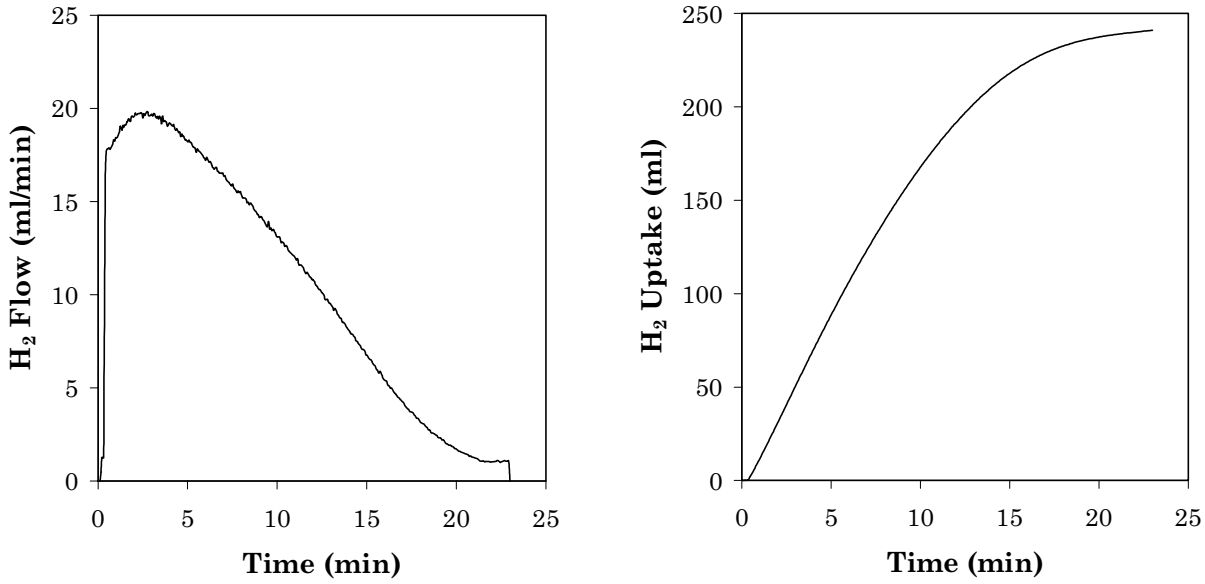

Figure 6.10 H_2-flow and H_2-uptake curves of Rh/CNF(imp, c150, r140).

It is important to determine whether the measured activity is influenced by diffusion of the reactants and products to and from the active sites. In general, three mass transfer phenomena can be distinguished for the reactants in hydrogenation reactions:[27] i) transfer of hydrogen from the gas phase to the

Table 6.5 Initial activities and particle diameters for all catalysts.

Catalyst#	Initial activity (mole H_2/g_{cat}*h)	D (nm)
1. Rh/CNF(imp, c150, r140)	0.78	1.1
2. Rh/CNF(imp, c250, r140)	0.71*	1.1
3. Rh/CNF(imp, r160)	0.74	1.4
4. Rh/CNF(imp, c150, r250)	1.13	1.7
5. Rh/CNF(imp, c250, r250)	0.86	1.6
6. Rh/CNF(imp, r250)	0.83	1.7
7. Rh/CNF(IET, r200)	1.12	1.1
- Rh/CNF(IET, r$NaBH_4$)	1.04	-
8. Rh/CNF(IEN, r200)	0.86	2.1
9. Rh/CNF(IENT, r200)	0.83	2.0

Used catalyst quantity: 50 mg

• With 100 mg the same value was obtained

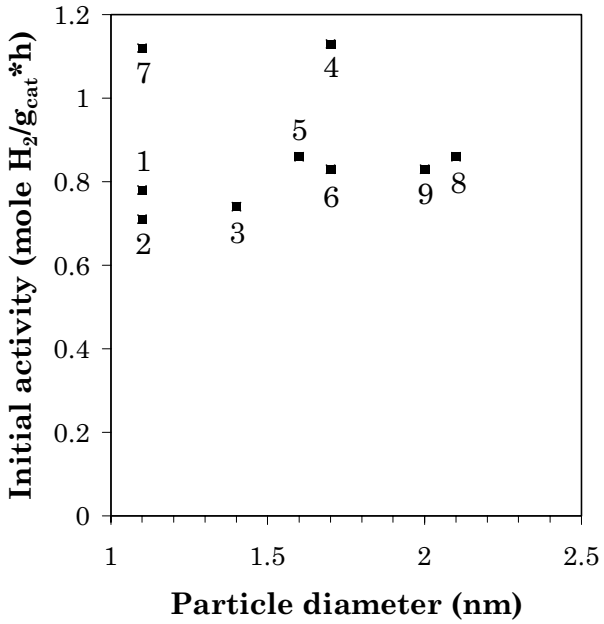

Figure 6.11 Initial activity against particle diameter for all catalysts.

liquid phase ii) transport of the reactants to the external surface of the catalyst particle (external mass transfer) iii) transport of the reactants from the external

surface of the particle through the pores to the active sites on the interior surface (internal mass transfer). As was already pointed out in the experimental section, under the conditions used, the rate of dissolution of H_2 in the solvent is higher than the maximum measurable rate of H_2-uptake. Furthermore, the rate is independent of stirrer frequency. Stirring at a higher speed decreases the stagnant layer around a catalyst particle. In the case of external diffusion limitation, an effect of stirrer frequency on the activity should be expected. Therefore, it is highly unlikely that the reaction rate is affected by transfer of H_2 to the liquid phase or by diffusion of reactants to the external surface of the catalyst particle. What remains is the question whether there is internal diffusion limitation or not. An easy check is to decrease the catalyst particle size. If the reaction rate is not affected by this procedure, the reaction is not limited by internal diffusion. However, the catalysts used in this study are already powdered and it is difficult to control the particle size on such a small scale. Therefore, as a rough check, two catalysts [Rh/CNF(imp, c250, r140) and Rh/CNF(imp, c250, r250)] were powdered with a mortar very thoroughly in order to decrease the particle size even further. Both catalysts showed about a threefold increase in activity. Although these results must be interpreted with care, because other factors, such as the clustering of support bodies, can also play a role when a catalyst is subjected to such mechanical forces, the outcome of this experiment points to the presence of internal diffusion limitation. To shed more light on this diffusion phenomenon the internal effectiveness factor η was calculated. Estimations of the values of the parameters needed to calculate η are shown in Table 6.6.

It was ascertained that the reaction studied was indeed first order with respect to cyclohexene (plotting $\ln(C_0/C)$ against t resulted in a straight line). Cyclohexene concentrations were calculated from the initial concentration and the H_2 uptake pattern. Calculated k_1 values at all concentrations of cyclohexene during reaction with Rh/CNF(imp, c250, r250) were averaged. For particles of 20 μm, which is a reasonable value for these catalysts (see Figure 6.1A), a Thiele modulus φ of 0.44 and an effectiveness factor η of 0.94 is obtained. This calculation shows that it is unlikely that the reaction is limited by internal diffusion of cyclohexene. However, considering that the concentration of H_2 in the bulk solution is much lower than that of cyclohexene ($3.5*10^{-3}$ mol/l[30] to 0.1 mol/l, respectively), the rate of the reaction is probably limited by the availability of H_2. Consequently, the initial activities obtained for the Rh/CNF catalysts should only be considered qualitatively. If we assume that the limitation with respect to H_2 is about the same for all catalysts, different intrinsic activities will still lead to different observed reaction rates, although the differences would be smaller than without any diffusion limitations. It should be noted that after having powdered both catalysts severely the catalyst Rh/CNF(imp, c250, r250) was still more active than the catalyst Rh/CNF(imp, c250, r140). This supports the assumption that the observed activities are related to intrinsic activities.

Table 6.6 Values of the parameters needed to calculate the internal effectiveness factor η for cyclohexene (see Equations 6.5-6.9).

Parameter	Value
d_p	$2*10^{-5}$ m
D_A [1)]	10^{-9} m^2s^{-1}
total pore volume [2)]	0.4 mlg^{-1}
ρ_{fibres} [3)]	$2.25*10^{-3}$ kgm^{-3}
ε_p	0.47
τ	2
D_{eA}	$2.4*10^{-10}$ m^2s^{-1}
k_1 [4)]	$1.7*10^{-3}$ s^{-1}
$k_{v,p}$	4.1 s^{-1}
φ	0.44
η	0.94

1) typical for liquid phase
2) see experimental section
3) $\rho_{graphite} \cong \rho_{fibres}$[31]
4) averaged over all cyclohexene concentrations during reaction

Table 6.5 and Figure 6.11 show that not much effect of the rhodium metal particle size on the catalytic activity is observed. With the exception of Rh/CNF(imp, c150, r250) and Rh/CNF(IET, r200) all catalysts exhibit about the same activity.

6.4 Discussion

Pre-treatment of carbon nanofibres

The TEM results have shown that only on carbon nanofibres that are surface-oxidised with HNO_3/H_2SO_4 small rhodium metal particles are deposited after impregnation with an aqueous solution of $RhCl_3 \cdot 2H_2O$. These findings can be explained by taking into account the wetting properties of the differently treated fibres. It has been shown before[28] that untreated fibres do not show any affinity for water. Fibres treated with HNO_3 have some affinity for water, whereas only HNO_3/H_2SO_4-oxidised fibres are well wetted by this solvent. Consequently, dissolved $RhCl_3 \cdot 2H_2O$ can only reach the surface of the HNO_3/H_2SO_4-oxidised CNFs. With the untreated fibres the rhodium particles are mainly deposited on or near the Al_2O_3 particles that are still present and are deposited as some large

metal lumps. The affinity of the rhodium particles for Al_2O_3 is also not very large, because ultrasonic treatment during the TEM sample preparation dispatches the particles from the Al_2O_3 support (see Figure 6.2B). With the HNO_3-oxidised fibres about 50 % of the original amount of Al_2O_3 is removed during the oxidation treatment,[28] decreasing the chance that the Rh is deposited on or near this oxidic carrier. Furthermore, the fibres have developed some affinity for water. This results in large rhodium particles in between the fibres. Prinsloo obtained similar results with the impregnation of an iron precursor onto HNO_3-oxidised CNFs.[32] The Al_2O_3 within the skeins of fibre that were treated with HNO_3/H_2SO_4 is removed for about 80 %.[28] Furthermore, the remaining Al_2O_3 is most probably α-Al_2O_3 of a low surface area, present in the high surface area γ-Al_2O_3 used for the synthesis of the growth catalyst. Therefore, not much influence of the remaining alumina on the formation of Rh particles on the carbon nanofibres is to be expected. The HNO_3/H_2SO_4-oxidised fibres are nicely wetted with water and small rhodium particles are formed after reduction. In view of the above-described results, the research was continued with only the HNO_3/H_2SO_4-oxidised impregnated catalysts.

The TEM results demonstrate that the wetting properties of the carbon nanofibres are crucial for success of the impregnation. Furthermore, quite a large influence of the remaining Al_2O_3 has been observed. Only during the severe oxidation treatment alumina largely dissolves in the strong acid. These results call for the growth of carbon nanofibres from a growth catalyst with an easily removable support, such as silica. Growth from a Ni/C support would be another option, since the carbon would not pollute the fibres. It would then become possible to obtain pure untreated fibres, which could be impregnated with an organic solution. This could be another interesting method of synthesis of metal particles on CNFs.

Preparation of small rhodium particles on surface-oxidised carbon nanofibres

The EXAFS results have shown that with all catalysts very small rhodium particles have been formed on the fishbone carbon nanofibres. With Rh/CNF(IET, r$NaBH_4$) no particle size could be estimated based on the Rh-Rh co-ordination number, because the particles are partly oxidised. The reduction procedure with $NaBH_4$ was executed *ex situ* and the catalyst was exposed to air afterwards. Most probably, the particles consist of a rhodium metal core surrounded by an oxidic phase. We roughly estimate that the particle size ranges between 1.5 nm and 2 nm. A larger diameter is not likely, because a Rh-C contribution is still observed.

With the impregnated catalysts the particle size ranges from 1.1 to 1.7 nm. The results obtained with the low-temperature reductions, i.e. 140-160°C, have shown that calcination at 150°C or 250°C makes no difference for the particle size obtained. However, direct reduction results in larger particles. This difference can be explained by a higher mobility of rhodium chloride under reducing than under oxidising conditions. Furthermore, the reduction temperature of the direct

reduction is 20°C higher than that of the reduction after calcination. The EXAFS results show that the particles are completely reduced after reduction at 140-160°C. No Rh-O contributions could be fitted in the spectrum. This result agrees well with the profiles obtained during temperature-programmed reduction. Furthermore, no chlorine is present in the co-ordination sphere of the rhodium, although it is still possible that chlorine is present near the rhodium particle. When the catalysts are reduced at 250°C, no differences in particle size are observed anymore. It is, therefore, likely that at this temperature the mobility of the rhodium metal atoms and not the rhodium chloride is decisive for the final size of the particles.

With the ion-exchanged catalysts stirring at room temperature with an aqueous solution of $RhCl_3 \cdot 2H_2O$ was not successful. This result can be explained with the relatively high acidity of this solution. The used solution of $3.7*10^{-3}$ mol/l has a pH of 2.9. Hoogenraad *et al.*[4] found that the iso-electric point of HNO_3-oxidised fibres is about 2.3. At pH values above this point the fibres are negatively charged. The pH of the solution used for ion exchange is, therefore, probably very close to the iso-electric point of the fibres and there will be barely any driving force for ion exchange. Furthermore, the structure and, therefore, the charge of $RhCl_3 \cdot 2H_2O$ in water is uncertain. Complexes, such as $[Rh(H_2O)_6]^{3+}$, $[Rh(OH)_3Cl_3]^{3-}$, and $[RhCl_6]^{3-}$, may be present in solution.[33]

When an aqueous solution of $RhCl_3 \cdot 2H_2O$ is refluxed with the oxidised fibres, on the other hand, a rhodium complex is formed on the CNFs [see EXAFS data of Rh/CNF(IET)]. The synthesis procedure resembles that of procedures used with rhodium complex chemistry.[34, 35] It is, therefore, likely that rhodium has formed a complex with the carboxyl groups on the surface of the fibres. The negatively charged COO^- group and the two chloride ions compensate the charge of the Rh(III) ion. Three water molecules probably complete the co-ordination sphere of the central rhodium ion. Subsequent reduction with H_2 at 200°C gives extremely small rhodium particles of 1.1 nm in size. By optimisation of the reduction procedure it is probably possible to synthesise even smaller particles by this approach. Reduction with $NaBH_4$ gives larger particles of 1.5-2 nm in size. Probably this is due to the relatively rough method of reduction (all $NaBH_4$ was added at once to the fibres that were (badly) stirred in a round-bottomed flask).

Another successful ion exchange procedure involved addition of NH_3 to the aqueous solution of $RhCl_3 \cdot 2H_2O$. Two factors play a role with this procedure: i) the pH of the solution is raised, increasing the driving force of ion exchange between the negatively charged CNF surface and a positively charged complex, ii) most probably the positively charged $[Rh(NH_3)_5Cl]^{2+}$ complex is formed.[36, 37] No effect of an increase of temperature during ion exchange on the final size of the rhodium particles was found using this synthesis procedure. However, the metal particles formed using this ion exchange method are much larger than with other catalyst preparation techniques. This is probably due to the high mobility of

metal ammine complexes under reducing atmospheres.[38, 39] Careful drying and calcination procedures could decrease the particle size obtained considerably.

The particle sizes obtained with the synthesis of the 1 wt% rhodium-on-fishbone carbon nanofibre catalysts are very small as compared to results reported in literature. Deposition of rhodium on carbon nanofibres or nanotubes has not been reported yet, but for other metals several reports exist. Hoogenraad *et al.*[6] synthesised Pd on HNO_3-oxidised parallel CNFs by ion exchange of $[Pd(NH_3)_4](NO_3)_2$ and subsequent reduction at 200°C. They obtained an EXAFS co-ordination number of 7.9 and estimated the size of the particles to be 1.5 nm. Ang and Wang[14] obtained Pd particles of 2 nm size on HNO_3/H_2SO_4-oxidised carbon nanotubes by electroless plating. Ledoux and co-workers[12] impregnated palladium nitrate on CNFs and observed 3-5 nm particles, while Planeix *et al.*[13] prepared 3-7 nm sized Ru particles on carbon nanotubes. Finally, Baker and co-workers[9] impregnated a solution of nickel nitrate in ethanol on CNFs and detected particles of an average diameter of 6-8 nm. The results of this work demonstrate that it is possible to synthesise very small metal particles on oxidised CNFs. With particles of about 1 nm the precious metal component of the catalyst will be optimally used. In other words, all or almost all metal atoms are surface atoms. Furthermore, with particles of this size, metal-support interactions can be studied. Several researchers found increased activities and/or selectivities when carbon nanofibres or nanotubes where used as the support.[7-13] More information about the interaction between the metal and the CNF support could shed some light on these phenomena.

Metal-support interaction in Rh/CNFs

The size of the particles obtained is so small that the metal-support contact can be observed. With the exception of Rh/CNF(IEN, r200) and Rh/CNF(IENT, r200) all catalysts show a Rh-C contribution. The size of the particles in Rh/CNF(IEN, r200) and Rh/CNF(IENT, r200) is too large to observe this contribution. An interesting observation can be made by comparison of a catalyst that is reduced with H_2 [Rh/CNF(imp, c150, r140)] and the $NaBH_4$-reduced catalyst [Rh/CNF(IET, r$NaBH_4$)]. Upon reduction with H_2 the Rh-C distance is observed at 2.70 Å, whereas after reduction with $NaBH_4$ this distance is evident at 2.29 Å. This difference may be explained by assuming the presence of hydrogen at the interface of the rhodium metal particle and the carbon nanofibre support with the H_2-reduced catalyst. A schematic depiction of rhodium particles on carbon nanofibres in Rh/CNF(imp, c150, r140) and Rh/CNF(IET, r$NaBH_4$) is shown in Figure 6.12. As a rhodium-carbon contribution is observed it is likely that the particle has a large interface area with the support. A semi-spherical shape could then be assumed. With Rh/CNF(imp, c150, r140) the rhodium particle is fully metallic. In between the particle and the carbon nanofibre support interface hydrogen is situated, creating a large Rh-C distance. With

Rh/CNF(IET, rNaBH$_4$) the rhodium particle is partly oxidised. A rhodium core is surrounded by an oxidic phase. In this case, no interface hydrogen is present and the Rh-C distance is short.

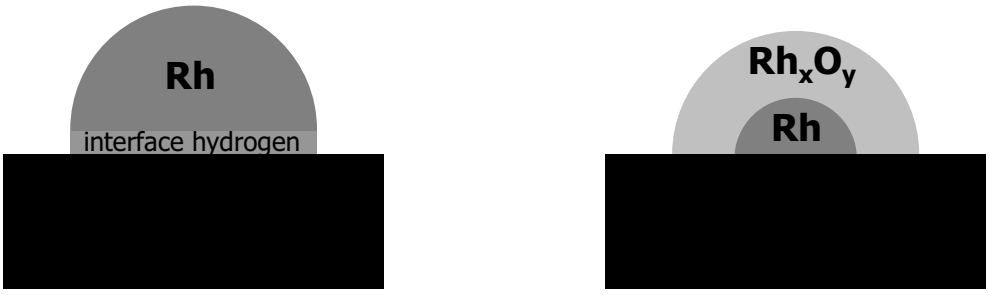

Figure 6.12 Schematic depiction of rhodium particles on carbon nanofibres in Rh/CNF(imp, c150, r140) [left] and Rh/CNF(IET, rNaBH$_4$) [right].

The phenomenon of interface hydrogen has repeatedly been observed with several metals, such as Rh, Ir and Pt, on oxidic carriers (γ-Al_2O_3, TiO_2, zeolite-Y) by Koningsberger and co-workers.[40-45] Reduction of the catalysts at low temperature, i.e., below 300°C, results in a long metal-oxygen distance at about 2.6-2.7 Å. Upon subsequent evacuation at 200°C the M-O distance contracts to about 2.1-2.2 Å. Ensuing reduction restores the long M-O interaction. These results clearly show that the occurrence of the long M-O interaction is associated with hydrogen and that the presence of interface hydrogen is a likely explanation for the above-described observations. With the Rh/CNF catalysts the difference in Rh-C distance can explained by the different reducing agents used. Whereas reduction with H_2 results in a long Rh-C distance, in accordance with earlier observations, reduction with $NaBH_4$ gives a short Rh-C distance, because the catalyst does not come into contact with molecular hydrogen. Thus, reduction with $NaBH_4$ can be compared to evacuation of the catalyst at elevated temperature.

Catalytic test experiments

The presence of internal diffusion limitation with respect to H_2 during the hydrogenation of cyclohexene with the Rh/CNF catalysts is remarkable. With liquid-phase reactions external diffusion limitations would rather be expected to take place, because the stagnant layer around the catalyst particle is large as compared to the size of the particle. Furthermore, the carbon nanofibres have a mesoporous macrostructure, the loading of active metal component is low (1 wt%), and the concentration of cyclohexene is only 1 % v/v. However, the reaction is executed at a H_2 pressure of only 1200 mbar, and the catalysts turn out to be extremely active in this test reaction. A simple solution would be to increase the hydrogen pressure in order to increase the concentration of this gas in the

solvent. Unfortunately, this remedy was not possible with our experimental set-up.

As was already pointed out above, the activities of the catalysts still qualitatively reflect the intrinsic activities. Figure 6.11 shows that, with the exception of Rh/CNF(imp, c150, r250) and Rh/CNF(IET, r200), no effect of the rhodium metal particle size on the catalytic activity is observed. As the rhodium metal surface area decreases with increasing particle size, this means that the turnover frequency (TOF) would increase significantly with the rhodium particle size. The lack of effect of the particle size on the catalytic activity is quite surprising as cyclohexene hydrogenation is generally reported to be a structure-insensitive reaction. With a structure-insensitive reaction a decrease of activity should be found with increasing particle size. Boudart *et al.*, for instance, found that the liquid-phase hydrogenation of cyclohexene was independent of particle size for Rh/Al_2O_3[46], Pd/SiO_2 and Pd/Al_2O_3[47], and Ni/SiO_2[48] catalysts. However, Jackson and co-workers[49] did find a dependence of metal crystallite size on the activity in cyclohexene hydrogenation for Pd on alumina, carbon, silica and zirconia. An optimum size of about 3 nm was found. This behaviour they related to the strength and mode of adsorption of cyclohexene, although the adsorption characteristics of H_2 could play a role as well. The same conclusion was drawn by Busser *et al.*,[50] who, surprisingly, found a decrease in TOF with increasing particle size for polymer-stabilised rhodium colloids. Augustine *et al.*[51] reported that with Pt catalysts several alkene hydrogenation sites exist that are related to the mode of adsorption of hydrogen. Müller *et al.*[52] showed that the adsorption and desorption as well as the Faradaic hydrogenation of cyclohexene are structure-sensitive. The rate of hydrogenation was higher on Pt(110) or roughened surfaces.

The results reported in this work, however, indicate that the effect of metal particle size on the activity in the liquid-phase hydrogenation of cyclohexene is low. In our opinion, other effects, such as the clustering of the support bodies in the liquid phase, the effect of water present in the system, and the influence of oxygen-containing groups of the surface, are much more important. It should be stressed that all activities obtained in this study could be reproduced well within 10 %. The high activities of Rh/CNF(imp, c150, r250) and Rh/CNF(IET, r200) are striking and reflect that much more factors play a role in liquid-phase reactions than only the size of the metal particles. As yet we do not have enough knowledge about the system under investigation, such as the clustering of the macroporous carbon bodies and the density of hydrophilic groups on the surface of the CNFs after reduction at the different temperatures, to present a conclusive explanation.

6.5 Conclusions

This study describes the synthesis of very small rhodium metal particles on HNO_3/H_2SO_4-oxidised fishbone carbon nanofibres by several methods. The surface oxidation with HNO_3/H_2SO_4 is a prerequisite for a good interaction between aqueous catalyst precursor solutions and the CNFs. Particle sizes ranging from 1.1 to 2.1 nm are obtained with 1 wt% Rh metal loadings. The smallest rhodium particles result with impregnation, subsequent calcination at 150°C, and reduction at 140°C or with ion exchange at elevated temperature with an aqueous solution of $RhCl_3 \cdot 2H_2O$ and reduction at 200°C. The size of the particles makes investigation of the metal-support interaction on carbon nanofibres possible. All catalysts are very active in the hydrogenation of cyclohexene. Not much effect of the metal particle size on the catalytic acitivity is observed, suggesting that other parameters, such as the clustering of support bodies in the liquid phase, are more important.

Acknowledgements

This chapter was based on the experimental work executed by Daphne Keller within the framework of her graduate research project. We would like to thank the HASYLAB (Hamburg, Germany) for the opportunity to perform EXAFS measurements at beamline station X1.1. We are grateful for the collection of the EXAFS data by the EXAFS measurement team.

References

1 K.P. de Jong and J.W. Geus, *Catal. Rev.-Sci. Eng.* **42-4** (2000), 481

2 M.S. Hoogenraad, PhD Thesis (1995), Utrecht University, The Netherlands

3 M.S. Hoogenraad, M.F. Onwezen, A.J. van Dillen, and J.W. Geus, *Stud. Surf. Sci. Catal.* **101** (1995), 1331

4 J.W. Geus, M.S. Hoogenraad, and A.J. van Dillen in Synthesis and Properties of Advanced Catalytic Materials (Eds. E. Iglesia, P.W. Lednor, D.A. Nagaki, and L.T. Thompson), Materials Research Society Pittsburgh, Pittsburgh, 1995, p. 87

5 M.S. Hoogenraad, R.A.G.M.M. van Leeuwarden, G.J.B. van Breda Vriesman, A.Broersma, A.J. van Dillen, and J.W. Geus in Preparation of Catalysts VI (Eds. G. Poncelet *et al.*), Elsevier, Amsterdam, 1995, p. 263

6 B.L. Mojet, M.S. Hoogenraad, A.J. van Dillen, J.W. Geus, and D.C. Koningsberger, *J. Chem. Soc., Faraday Trans.* **93-24** (1997), 4371

7 N.M. Rodriguez, M.-S. Kim, and R.T.K. Baker, *J. Phys. Chem.* **98** (1994), 13108

8 A. Chambers, T. Nemes, N.M. Rodriguez, and R.T.K. Baker, *J. Phys. Chem. B* **102** (1998), 2251
9 C. Park and R.T.K. Baker, *J. Phys. Chem. B* **102** (1998), 5168
10 C. Park and R.T.K. Baker, *J. Phys. Chem. B* **103** (1999), 2453
11 F. Salman, C. Park, and R.T.K. Baker, *Catalysis Today* **53** (1999), 385
12 C. Pham-Huu, N. Keller, L.J. Charbonniere, R. Ziessel, and M.J. Ledoux, *Chem. Commun.* (2000), 1871
13 J.M. Planeix, N. Coustel, B. Coq, V. Brotons, P.S. Kumbhar, R. Dutartre, P. Geneste, P. Bernier, and P.M. Ajayan, *J. Am. Chem. Soc.* **116** (1994), 7935
14 L.-M. Ang, T.S. Andy Hor, G.-Q. Xu, C.-H. Tung, S. Zhao, and J.L.S. Wang, *Chem. Mater.* **11** (1999), 2115
15 M. Keyser and F.F. Prinsloo, *J. Mol. Catal.*, submitted
16 W. Teunissen, PhD Thesis (2000), Utrecht University, The Netherlands
17 J.W.Geus, *Stud. Surf. Sci. Catal.* **16** (1983), 1
18 M. Vaarkamp, B.L. Mojet, F.S. Modica, J.T. Miller, and D.C. Koningsberger, *J. Phys. Chem.* **99-43** (1995), 16067
19 http://www.xsi.nl
20 M. Vaarkamp, I. Dring, R.J. Oldman, E.A. Stern, and D.C. Koningberger, *Phys. Rev. B* **50** (1994), 7872
21 J.W. Cook Jr and D.E. Sayers, *J. Appl. Phys.* **52** (1981), 5024
22 D.C. Koningsberger, B.L. Mojet, G.E. van Dorssen, and D.E. Ramaker, *Top. Catal.* **10** (2000), 143
23 R.W.G. Wyckhoff, Crystal Structures, vol. 1, 2nd Ed., John Wiley & Sons, Inc., New York, 1963, p. 10
24 J.M.D. Coey, *Acta Cryst.* **B26** (1970), 1876
25 D.C. Koningsberger. *Jpn. J. Appl. Phys.* **32** (1993), 877.
26 E.H. Voogt, THEBE, BOLLIE and NUBIE computer program, Surface Science Division, Debye Institute, Utrecht University, 1996
27 F. Kapteijn, G.B. Marin, and J.A. Moulijn in Catalysis-An integrated approach to homogeneous, heterogeneous, and industrial catalysis (Eds. J.A. Moulijn, P.W.N.M. van Leeuwen, and R.A. van Santen), Elsevier, Amsterdam, 1993, p. 251
28 See chapter 3 of this thesis
29 B.J. Kip, F.B.M. Duivenvoorden, D.C. Koningsberger, and R. Prins, *J. Catal.* **105** (1987), 26
30 C.L. Young, Solubility Data Series, Vol. 5/6 Hydrogen and Deuterium, Pergamon Press, Oxford, 1981, p. 187
31 V.B. Fenelonov, L.B. Avdeeva, V.I. Zheivot, L.G. Okkel', O.V. Goncharova, and L.G. Pimneva, *Kinet. Catal. (Eng. Trans.)* **34-3** (1993), 483
32 F.F. Prinsloo, M.Sc Thesis (2000), University of Cape Town, South Africa
33 R.J. Meyer and E. Pietsch, Gmelins Handbuch der Anorganischen Chemie, 8th Ed., Ruthenium/Rhodium, Verlag Chemie G.M.B.H., Berlin, 1938, p. 58

34 A.E. Bukanova, I.V. Prokof'eva, and L.K. Shubochkin, *Russian J. Inorg. Chem.* **25-6** (1980), 875
35 H. Frye, C. Luschak, and D. Chinn, *Z. Naturforsch.* **22b** (1967), 268
36 R.J. Meyer and E. Pietsch, Gmelins Handbuch der Anorganischen Chemie, 8th Ed., Ruthenium/Rhodium, Verlag Chemie G.M.B.H., Berlin, 1938, p. 134
37 R. Bramley, B.N. Figgis, and R.S. Nyholm, *J. Chem. Soc. A* (1967), 861
38 R.A. Dalla Batta and M. Boudart, *Proc. 5th Int. Conf. Catal.*(1973), 1329
39 W. Zou and R.D. Gonzales, *J. Catal.* **133** (1992), 202
40 J.B.A.D. van Zon, D.C. Koningsberger, H.F.J. van 't Blik, and D.E. Sayers, *J. Chem. Phys.* **82** (1985), 5742
41 D.C. Koningsberger, J.H.A. Martens, R. Prins, D.R. Short, and D.E. Sayers, *J. Phys. Chem.* **90** (1986), 3047
42 M. Vaarkamp, F.S. Modica, J.T. Miller, and D.C. Koningsberger, *J. Catal.* **163** (1996), 294
43 D.C. Koningsberger, F.B.M. van Zon, M. Vaarkamp, and A. Muñoz-Paez in X-ray Absorption Fine Structure for Catalysts and Surfaces (Ed. Y. Iwasawa), Series on Synchrotron Radiation Techniques and Applications, Vol. 2, World Scientific Publishing, Singapore, 1996, p. 257
44 G.E. van Dorssen, PhD Thesis (1999), Utrecht University, The Netherlands
45 D.C. Koningsberger, J. de Graaf, B.L. Mojet, D.E. Ramaker, and J.T. Miller, *Appl. Catal. A* **191** (2000), 205
46 M. Boudart and D.J. Sajkowski, *Faraday Discuss.* **92** (1991), 57
47 E.E. Gonzo and M. Boudart, *J. Catal.* **52-3** (1978), 462
48 M. Boudart and W.-C. Cheng, *J. Catal.* **106** (1987), 134
49 S.D. Jackson, G.J. Kelly, S.R. Watson, and R. Gulickx, *Appl. Catal. A: general* **187** (1999), 161
50 G.W. Busser, J. G. van Ommen, and J.A. Lercher, *Adv. Catal. Nanostruct. Mater.* (1996), 213
51 R.L. Augustine, M.M. Thompson, and M.A. Doran, *J. Chem. Soc., Chem. Commun.* (1987), 1173
52 U. Müller, U. Schmiemann, A. Dülberg, and H. Baltruschat, *Surf. Sci. 335* (1995), 333

7
Summary

The work described in this thesis has provided valuable information about the modification and use of carbon nanofibre supports in catalysis. The potential of CNFs as a catalyst support material is high. The properties of CNFs, such as their mechanical strength and mesoporous structure, make them especially suitable as a catalyst support for liquid-phase applications. A strong incentive for their use is the replacement of activated carbon, whose properties are often difficult to control. The results contribute to a better fundamental understanding of the surface structure and the surface reactivity of CNFs. This study describes the importance of the presence of defects on the surface reactivity of nanofibres. Furthermore, the value of surface modification for the preparation of nanofibre-supported catalysts has been exemplified in several chapters. Modification by surface oxidation as well as the use of the oxygen-containing groups for further modification and immobilisation have been described. It has been shown that it is possible to covalently attach metal complexes to CNFs. Furthermore, several tools for the synthesis of very small, highly active rhodium metal particles on carbon nanofibres have been developed, which opens the way to investigation of metal-support interactions on CNFs.

The inertness and hydrophobicity of CNFs is a drawback for the use of these fibres as catalyst support material. Due to these properties, the application and anchoring of the active phase is difficult to achieve. Therefore, it is important to be able to modify their surface, for instance, by the introduction of hydrophilic oxygen-containing surface groups. A better wetting of the fibres with aqueous solutions of catalyst precursor complexes can thus be achieved. The oxidic surface groups can act as anchoring sites for catalyst precursor complexes and the final metal particles as well. Furthermore, by oxidation the hydrophobicity of the final CNF-supported catalyst can be altered. This is not only important for the wetting properties of the catalyst during reaction, the oxygen-containing surface groups can also bring about different activities and/or selectivities. Finally, it is viable to use the surface oxides as anchoring sites for the immobilisation of metal-ligand systems. Concluding, surface modification of CNFs opens a whole range of new

possibilities. As a first step towards an understanding of the surface reactivity and modification of carbon nanofibres, it is important to gain more knowledge about the surface structure of the fibres.

Chapter 2 describes an infrared study on the surface structure of untreated parallel and fishbone carbon nanofibres. With the parallel fibres the surface consists of basal graphitic planes, while with fishbone fibres the edges of the graphitic layers are exposed. Consequently, it is likely to assume that with parallel CNFs no carbon-hydrogen species are present on the surface. With fishbone fibres, on the other hand, the graphitic edges could very well be terminated by hydrogen. However, we demonstrated from a comparison of the infrared spectra of the CNFs with those of defect-poor and defect-rich graphite that both parallel and fishbone fibres have a defect-rich surface structure. These defects bring about the presence of CH_2/CH_3 groups as well as aromatic C-H groups on both types of fibre. Not much difference in chemical structure between parallel and fishbone carbon nanofibres is found, which suggests, in contrast to what would be expected on the basis of the graphitic structure of the fibres alone, that the surface reactivity of parallel and fishbone carbon nanofibres is about the same. These results give more insight in the surface properties of CNFs that determine their surface reactivity.

Our study on the surface oxidation of parallel and fishbone carbon nanofibres is dealt with in **Chapter 3**. The fibres were subjected to several gas-phase and liquid-phase oxidation treatments and, together with other techniques, studied with infrared spectroscopy, thermogravimetric analysis and XPS. With the fishbone CNFs the macroscopic structure was not severely affected by any of the treatments used. With the parallel fibres, on the other hand, only treatment in HNO_3 left the macroscopic structure intact. However, the graphitic structure of both types of fibres was maintained after oxidation. Oxidation in a mixture of concentrated nitric and sulfuric acid turned out the most effective method for creating oxygen-containing surface groups. This treatment results, amongst other groups, in the formation of carboxyl and carboxylic anhydride groups on the surface of the fibres. Treatment for a longer period of time gives more surface oxides. As the concentration of these groups is too high to be accommodated exclusively at the surface of the CNFs, it is concluded that upon oxidation also ether-type oxygen groups are formed in between the graphitic layers that are puckered at their edges. The results clearly show that the formation of oxygen-containing surface groups occurs at defect sites on the carbon nanofibres and that the surface oxidation of CNFs proceeds via carbonyl groups and other oxides to carboxyl and carboxyl anhydride groups. With the parallel fibres all CH species residing at defect sites react to oxygen-containing groups. With the fishbone CNFs, on the other hand, only part of all CH sites is involved in the reaction due to spacial restrictions on the edge surface. Not much difference in oxidation behaviour was found between fishbone and parallel CNFs. We conclude, therefore, that the surface reactivity of both types of fibre is about the same due

to high defect densities. Dispersion experiments with differently treated fishbone carbon nanofibres made clear that only HNO_3/H_2SO_4-oxidised fibres have a good affinity for water. Much more knowledge has been obtained about the nature and amount of oxygen-containing surface groups after several oxidation treatments and about the mechanism of oxidation. The important role of defects in the surface oxidation of CNFs should be stressed.

Chapter 4 deals with rhodium complexes with (N-phenyl)anthranilic acid. Their synthesis, characterisation and activity in the liquid-phase hydrogenation of cyclohexene was investigated. Despite earlier studies, uncertainties concerning the structure and the homogeneity of the rhodium N-phenylanthranilic acid complex (RhPAA) existed. The current interest was raised by earlier reports about the immobilisation of RhPAA and rhodium anthranilic acid (RhAA) onto polystyrene. According to the literature the RhPAA did not display any activity upon immobilisation onto polystyrene. In contrast, when anthranilic acid was used a highly active Rh(I) catalyst was obtained. The synthesis of RhPAA and RhAA described in this thesis was derived from published procedures. Infrared results show that complexes of rhodium with PAA and AA are formed. With both compexes interaction of Rh with the carboxyl group is observed. With RhPAA the Rh ion is also bonded to the amine group, while this interaction is not certain in RhAA. Emphasis was put on investigating whether the complexes are really homogeneous or react to small metal particles. One of the techniques used to establish the presence of rhodium metal particles was mercury poisoning. In view of the synthesis procedure and the characterisation results, it is likely that Rh(0) is already present in the as-synthesised complexes. The catalytic activity probably originates both from the metal complexes and from small rhodium metal particles. These results make clear that the RhPAA and RhAA systems are not pure and that no clear and unambiguous structure of the complexes can be given. The non-selective synthesis procedure is responsible for these observations.

The immobilisation of rhodium-anthranilic acid onto carbon nanofibres is described in **Chapter 5**. This complex was chosen because it is an example of an immobilised complex that does not have a well-defined homogeneous analogue. The catalytic properties of immobilised complexes often differ from that of the non-supported counterparts. It could, therefore, be the best approach to design bound catalysts that do not have homogeneous analogues. A weak ligand in solution, e.g., an amine ligand, which may easily dissociate from the metal resulting in reduction of the metal to a lower valence state under hydrogenation conditions, could be a suitable ligand for an immobilised system. The immobilisation of Rh/anthranilic acid onto fishbone carbon nanofibres was executed via (i) surface oxidation of the fibres, (ii) conversion of the carboxyl groups into acid chloride groups, (iii) attachment of anthranilic acid, and (iv) complexation of rhodium(III). The immobilisation process was monitored and the final complex was characterised by IR, XPS, XAFS spectroscopy, and by

molecular modelling. It is shown that anthranilic acid bonds to the CNFs by an amide linkage with carboxyl groups that are present after surface oxidation of the fibres. The formation of acid chloride groups by reaction with $SOCl_2$ appeared not necessary to bring about bonding of anthranilic acid to the CNFs. Under the conditions employed, anthranilic acid can react directly with the carboxyl groups of the fibres. The immobilised anthranilic acid complexes to a rhodium(III) ion via the nitrogen atom and the carboxyl group. The co-ordination sphere of the trivalent Rh atom is further occupied by three water molecules and a chloride ion. The as-synthesised complex is not active in the liquid-phase hydrogenation of cyclohexene. Reduction with $NaBH_4$ results in the formation of small rhodium particles on the CNFs of a diameter of 1.5-2 nm. In contrast, the hydrogenation activity of these rhodium particles is very high. This chapter describes the first example of a covalently bonded metal-ligand complex on carbon nanofibres. Future research could focus on the activation of the immobilised rhodium-anthranilic acid complex, for instance, by reduction with a milder reduction agent or complexation of rhodium in the Rh(I) state to produce a Rh(I) complex and to avoid reaction to metallic rhodium particles, or on the use of the described modification techniques for the immobilisation of other metal complexes.

The preparation and catalytic performance of small rhodium metal particles on fishbone carbon nanofibres are presented in **Chapter 6**. The Rh particles were deposited on the fibres by several impregnation and ion exchange techniques with $RhCl_3 \cdot 2H_2O$ as precursor salt. It was investigated which fibre pre-treatment methods are required to achieve an optimal interaction of the nanofibres with the aqueous catalyst precursor solution. Furthermore, the influence of calcination and reduction procedures on the final metal particle size was studied. The catalysts were characterised with transmission electron microscopy and with XAFS spectroscopy. The surface oxidation with a mixture of nitric and sulfuric acid turned out to be a prerequisite for a good wetting of the CNFs with aqueous precursor solutions and thus for the formation of small metal particles on the fibres. Particle sizes ranging from 1.1 to 2.1 nm are obtained with 1 wt% Rh metal loadings. The smallest particles result from impregnation, subsequent calcination at 150°C, and reduction with H_2 at 140°C or with ion exchange at elevated temperatures with an aqueous solution of $RhCl_3 \cdot 2H_2O$ and reduction at 200°C with H_2. All catalysts are very active in the liquid-phase hydrogenation of cyclohexene. Not much effect of the metal particle size on the catalytic acitivity is observed, suggesting that other parameters, such as the clustering of support bodies in the liquid phase, are more important. The size of the particles makes investigation with XAFS spectroscopy of metal-support interactions on carbon nanofibres possible. Studying the interaction between metal and CNF support is interesting because several researchers found enhanced activities and/or selectivities with CNF-supported metal catalysts. These findings were related to the unique properties of the supports used.

Samenvatting

Het onderzoek dat in dit proefschrift is beschreven heeft waardevolle informatie opgeleverd over de modificatie en het gebruik van kooldraden als dragermateriaal in de katalyse. Het gebruik van kooldraden als katalysator dragermateriaal is veelbelovend. De eigenschappen van de draden, zoals de mechanische sterkte en macroporeuze structuur, maakt ze bij uitstek geschikt voor toepassing in vloeistoffase reacties. Een sterke drijfveer voor het gebruik van dit materiaal is het vervangen van actieve kool. Actieve kool heeft dikwijls moeilijk te controleren eigenschappen. De resultaten van dit onderzoek dragen bij tot betere en meer fundamentele kennis over de oppervlaktestructuur en de oppervlaktereactiviteit van kooldraden. De aanwezigheid van oppervlaktedefecten en hun effect op de oppervlaktereactiviteit van kooldraden blijkt van groot belang te zijn. Bovendien is in verschillende hoofdstukken de waarde van oppervlaktemodificatie voor de synthese van kooldraad gedragen katalysatoren duidelijk gemaakt. Zowel modificatie door oppervlakteoxidatie als het gebruik van zuurstofhoudende groepen voor verdere modificatie en immobilisatie wordt in het proefschrift beschreven. Voorts blijkt dat het mogelijk is om covalent metaalcomplexen op kooldraden te binden. Bovendien zijn verschillende methoden ontwikkeld voor de synthese van zeer kleine, zeer actieve rhodium metaaldeeltjes op kooldraden, waardoor het bestuderen van metaal-drager interacties op kooldraden mogelijk wordt.

De inertie en de hydrofobiciteit van kooldraden vormen een minpunt in het gebruik als katalysator dragermateriaal. Door deze eigenschappen is het aanbrengen en het verankeren van de actieve fase moeilijk te bewerkstelligen. Om die reden is het belangrijk om het oppervlak te kunnen modificeren, bijvoorbeeld door het aanbrengen van hydrofiele, zuurstofhoudende oppervlaktegroepen. Zo kan een betere bevochtiging van de draden met waterige oplossingen van katalysatorprecursor complexen verkregen worden. De zuurstofhoudende oppervlaktegroepen kunnen dienen als ankerplaatsen voor de katalysatorprecursor complexen en voor de uiteindelijke metaaldeeltjes. Bovendien kan de hydrofobiciteit van de kooldraad gedragen katalysator door oppervlakteoxidatie gemodificeerd worden. Dit is niet alleen belangrijk voor de bevochtigingseigenschappen van de katalysator tijdens reacties. De zuurstofhoudende oppervlaktegroepen kunnen ook een andere activiteit en/of selectiviteit induceren. Tenslotte is het mogelijk om de zuurstofhoudende oppervlaktegroepen te gebruiken als ankerplaatsen voor de immobilisatie van

metaal-ligand systemen. Door oppervlaktemodificatie van kooldraden worden dus vele nieuwe mogelijkheden toegankelijk. Als een eerste stap naar meer inzicht in de reactiviteit van het oppervlak en het mechanisme van oppervlaktemodificatie is het belangrijk om meer kennis te verzamelen over de oppervlaktestructuur van kooldraden.

Hoofdstuk 2 beschrijft een infraroodstudie naar de oppervlaktestructuur van onbehandelde parallelle en visgraat kooldraden. Het oppervlak van parallelle draden bestaat uit basale grafitische vlakken en dat van visgraat draden uit de randen van de grafitische vlakken. Om die reden kan men enerzijds aannemen dat het oppervlak van parallelle draden geen C-H groepen bevat. Bij visgraat kooldraden is het anderzijds zeer waarschijnlijk dat de grafietranden getermineerd worden door waterstof atomen. Wij hebben echter op grond van een vergelijking van de infrarood spectra van de kooldraden met defectarm en defectrijk grafietmateriaal aangetoond dat het oppervlak van zowel parallelle als visgraat kooldraden defectrijk is, hetgeen betekent dat op beide typen draden CH_2/CH_3 groepen en aromatische C-H groepen voorkomen. Er werd weinig verschil in chemische structuur tussen parallelle en visgraat kooldraden waargenomen, waardoor verondersteld mag worden dat ook de oppervlaktereactiviteit van beide soorten draden ongeveer hetzelfde is. Dit is tegengesteld aan wat verwacht zou worden op grond van alleen de grafitische structuur van de draden. Deze resultaten geven meer inzicht in de specifieke oppervlakteeigenschappen van kooldraden die de oppervlaktereactviteit bepalen.

Oppervlakteoxidatie van parallelle en visgraat kooldraden is weergegeven in **hoofdstuk 3**. De draden werden behandeld met verschillende gasfase en vloeistoffase oxidatiemiddelen en werden onder andere bestudeerd met infrarood spectroscopie, thermogravimetrische analyse en XPS. De macrostructuur van visgraat draden werd niet noemenswaard beïnvloed door de verschillende oxidatiemiddelen. Bij parallelle draden bleef de macrostructuur alleen intact tijdens behandeling met salpeterzuur. De grafitische structuur van beide typen draden werd echter niet aangetast door de oxidaties. Oxidatie door een mengsel van geconcentreerd salpeterzuur en zwavelzuur bleek de meest effectieve methode te zijn om zuurstofgroepen op het oppervlak te creëren. Deze behandeling introduceert, naast andere groepen, carboxyl- en carboxyl anhydridegroepen op het oppervlak van de draden. Een langere oxidatietijd geeft meer oppervlakteoxides. Aangezien de concentratie van deze groepen te hoog is om ze uitsluitend te huisvesten op het oppervlak van de draden, is geconcludeerd dat tijdens de oxidatie ook ether-achtige groepen gevormd zijn tussen geplooide grafietlagen. De resultaten laten duidelijk zien dat de vorming van zuurstofhoudende oppervlaktegroepen plaatsvindt op defectlocaties op de kooldraden en dat de oppervlakteoxidatie verloopt via carbonyl en andere groepen naar carboxyl en carboxyl anhydride groepen. Bij parallelle draden reageren alle “CH” verbindingen die aanwezig zijn op de defecten tot zuurstofhoudende groepen. Bij visgraat kooldraden daarentegen is slechts een deel van de “CH” groepen betrokken bij de reactie vanwege ruimtelijke restricties aan de randen van de grafitische vlakken. Omdat er weinig verschil gevonden werd tussen visgraat en parallelle draden, concluderen wij dat de oppervlaktereactiviteit van beide soorten draden ongeveer gelijk is door de hoge defectconcentraties. Dispersie experimenten met verschillend behandelde kooldraden hebben duidelijk gemaakt dat

alleen draden die behandeld zijn met HNO_3/H_2SO_4 een goede affiniteit met water hebben. Hierdoor is veel meer kennis verkregen over het soort en de hoeveelheid zuurstofhoudende oppervlaktegroepen na verschillende oxidatieve behandelingen en over het mechanisme van oxidatie. Met name de belangrijke rol van defecten tijdens de oppervlakteoxidatie van kooldraden kan worden genoemd.

Hoofdstuk 4 beschrijft rhodium complexen met (N-fenyl)antranilzuur. De synthese, de karakterisering en de activiteit in de vloeistoffase hydrogenering van cyclohexeen werd bestudeerd. Ondanks eerder onderzoek door anderen bestond er nog onduidelijkheid over de structuur en de homogeniteit van het rhodium N-fenylantranilzuur complex (RhPAA). Onze interesse voor dit probleem werd gewekt door eerdere publicaties over de immobilisatie van RhPAA en rhodium antranilzuur (RhAA) op polystyreen. Volgens de literatuur vertoonde het RhPAA complex geen enkele activiteit na immobilisatie op polystyreen. Bij het gebruik van antranilzuur daarentegen werd een zeer actieve Rh(I) katalysator verkregen. De synthese van RhPAA en RhAA die in dit proefschrift is beschreven is gebaseerd op gepubliceerde procedures. Infrarood resultaten laten zien dat complexen van rhodium met PAA en AA gevormd worden. Met beide complexen is een interactie van Rh met de carboxylgroep waar te nemen. In RhPAA is het Rh ook gebonden aan de aminegroep. Het bestaan van deze laatste interactie is bij RhAA niet zeker. De nadruk werd gelegd op onderzoek naar de homogeniteit van de complexen. Eén van de technieken die gebruikt werd om de aanwezigheid van kleine rhodium metaaldeeltjes te constateren was kwikvergiftiging. Gezien de syntheseprocedure en de karakteriseringresultaten is het waarschijnlijk dat Rh(0) al in het product aanwezig is na synthese. De katalytische activiteit is waarschijnlijk afkomstig van de complexen en van kleine rhodium metaaldeeltjes. De resultaten maken duidelijk dat de RhPAA en RhAA systemen niet zuiver zijn en dat geen goed gedefinieerde structuur van de complexen gegeven kan worden. De niet-selectieve syntheseprocedure is verantwoordelijk voor deze waarnemingen.

De immobilisatie van rhodium-antranilzuur op kooldraden wordt beschreven in **hoofdstuk 5**. De keuze is op dit complex gevallen omdat het een voorbeeld is van een geïmmobiliseerd complex dat geen goed gedefinieerde homogene analoog heeft. De katalytische eigenschappen van geïmmobiliseerde complexen verschillen vaak met die van de ongedragen tegenhangers. De beste benadering van immobilisatie zou kunnen zijn gebonden katalysatoren te ontwerpen die geen homogene analogen hebben. Een zwak ligand in oplossing, bijvoorbeeld een amine groep, kan gemakkelijk dissociëren van het metaal, waardoor het metaal ion gereduceerd wordt onder hydrogeneringscondities. Voor een geïmmobiliseerd systeem zou het echter wel een geschikt ligand kunnen zijn. De immobilisatie van Rh/antranilzuur op visgraat kooldraden werd uitgevoerd via
(i) oppervlakteoxidatie van de draden, (ii) conversie van de carboxylgroepen in zuurchlorides, (iii) het binden van antranilzuur aan de zuurchlorides en (iv) complexering van rhodium(III). Het immobilisatieproces werd gevolgd en het uiteindelijke complex werd gekarakteriseerd met behulp van IR, XPS, XAFS spectroscopie en moleculair modeleren. De resultaten wijzen erop dat antranilzuur aan de kooldraden bindt door middel van een amidebinding met carboxylgroepen die na oppervlakteoxidatie aanwezig zijn op de draden. De vorming van zuurchlorides

met $SOCl_2$ bleek geen noodzakelijke stap te zijn voor het binden van antranilzuur aan de kooldraden. Onder de gekozen reactieomstandigheden kan antranilzuur direct met de carboxylgroepen van de draden reageren. Het geïmmobiliseerde antranilzuur complexeert aan een rhodium(III) ion met het stikstofatoom en de carboxylgroep. Het trivalente Rh atoom is verder omringd door drie water moleculen en een chloride ion. Het complex na synthese is niet actief in de vloeistoffase hydrogenering van cyclohexeen. Door reductie met $NaBH_4$ worden kleine rhodium deeltjes met een geschatte diameter van 1.5-2 nm op de kooldraden gevormd. De hydrogeneringsactiviteit van deze deeltjes is zeer hoog. Dit hoofdstuk beschrijft het eerste voorbeeld van een covalent gebonden metaal-ligand complex op kooldraden. Toekomstig onderzoek zou zich kunnen richten op de activering van het geïmmobiliseerde rhodium-anthranilzuur complex, bijvoorbeeld door reductie met een milder reductiemiddel of directe complexering van het rhodium als Rh(I) om een Rh(I) complex te verkrijgen en om een reactie naar rhodium metaaldeeltjes te vermijden. Een andere mogelijkheid is verder onderzoek naar het gebruik van de beschreven modificatietechnieken bij het immobiliseren van andere metaalcomplexen.

De resultaten van het onderzoek naar de synthese en de activiteit van kleine rhodium metaaldeeltjes op visgraat kooldraden worden gepresenteerd in **hoofdstuk 6**. De deeltjes werden op de draden gebracht met behulp van verschillende impregnatie- en ionenwisselingstechnieken, waarbij gebruik werd gemaakt van $RhCl_3 \cdot 2H_2O$ als het precursorzout. Er werd onderzocht welke voorbehandelingsprocedures van de draden nodig waren voor een optimale interactie van de draden met de waterige oplossingen van de katalysatorprecursor. Ook werd de invloed van calcinatie- en reductieprocedures op de uiteindelijke deeltjesgrootte bestudeerd. De katalysatoren werden gekarakteriseerd met transmissie elektronenmicroscopie en met XAFS spectroscopie. De oppervlakteoxidatie met een mengsel van salpeterzuur en zwavelzuur is noodzakelijk voor een goede bevochtiging van de kooldraden met waterige katalysatorprecursor oplossingen en dus voor de vorming van kleine metaaldeeltjes op de kooldraden. Deeltjesgroottes variërend van 1.1 tot 2.1 nm werden verkregen bij beladingen van 1 % m/m rhodium. De kleinste deeltjes werden verkregen door impregnatie, calcinatie bij 150°C en reductie bij 140°C of door ionenwisseling bij verhoogde temperatuur met een waterige oplossing van $RhCl_3 \cdot 2H_2O$ gevolgd voor reductie bij 200°C. Alle katalysatoren bleken zeer actief te zijn in de vloeistoffase hydrogenering van cyclohexeen. Er werd weinig effect gevonden van de grootte van de metaaldeeltjes op de katalytische activiteit. Deze resultaten wijzen erop dat andere effecten, zoals de clustering van de dragerdeeltjes in de vloeistoffase, veel belangrijker zijn. De grootte van de deeltjes maakt het mogelijk om metaal-drager interacties op kooldraden te onderzoeken met XAFS spectroscopie. Bestudering van dit fenomeen is interessant omdat verschillende onderzoekers verhoogde activiteiten en/of selectiviteiten vonden met kooldraad gedragen metaalkatalysatoren. Deze resultaten werden gerelateerd aan de unieke eigenschappen van de gebruikte dragers.

Samenvatting voor leken

Deze samenvatting voor leken is bedoeld voor mensen die graag willen weten wat ik de afgelopen vijf jaar heb uitgevoerd aan de universiteit, maar niet erg bekend zijn met scheikunde. Ik hoop dat er mensen zijn die na het lezen van deze samenvatting genoeg moed hebben verzameld om ook eens naar de "echte" tekst te kijken. Daarom zal ik verwijzen naar figuren uit de verschillende hoofdstukken, al zijn ze misschien erg abstract voor de leek. Ik ben me er van bewust dat de informatiedichtheid voor velen erg hoog zal zijn in dit stuk. Daarom raad ik mensen aan om deze samenvatting in delen te lezen. Ook ben ik er niet aan ontkomen om bepaalde chemische termen te gebruiken. Anders zou de samenvatting véél langer en daarmee onduidelijker zijn geworden. Sommige dingen moet de lezer maar voor gegeven aannemen. Tot slot wil ik iets kwijt over de opzet van het stuk. Het vakgebied waarin ik werk is chemisch, maar we gebruiken een heel scala aan fysische meettechnieken om iets over de katalysator te weten te komen. Ieder resultaat van een meettechniek is een puzzelstukje. Alle resultaten samen vormen de uiteindelijke puzzel en (hopelijk) de oplossing van het probleem. Door deze manier van werken is de materie naar mijn mening moeilijker te doorgronden voor een leek. Bovendien ontkom je er niet aan om uit te leggen wat voor technieken je gebruikt hebt als je iets gedetailleerder op het onderzoek in wilt gaan. Om bovenstaande redenen leg ik een aantal technieken uit in deze samenvatting en heb ik geprobeerd aan te geven wat bij mij de puzzelstukjes waren die tot resultaat geleid hebben.

Katalyse

Het onderzoeksgebied waarin ik werk heet de katalyse. Een katalysator is een stof die een chemische reactie versnelt zonder daarbij zelf verbruikt te worden. In bijna alle productieprocessen in de industrie worden katalysatoren gebruikt. De werking van een katalysator kun je vergelijken met die van een tunnel door een berg. Zonder tunnel kost het véél meer tijd om aan de andere kant van de berg te komen dan met tunnel. Hoe beter de tunnel is (hoe actiever de katalysator), des te eerder je door de berg heen bent (des te sneller de reactie). Verder kun je door

de tunnel maar één kant op, terwijl je, als je over de berg heen trekt, verschillende kanten op kan. Een katalysator kan dus ook de reactie sturen zodat voornamelijk het gewenste product gevormd wordt. Dit begrip heet selectiviteit.

Er bestaan verschillende soorten katalysatoren. Ik heb me met twee soorten bezig gehouden: metaalcomplexen en kleine metaaldeeltjes op een drager. Een metaalcomplex bestaat uit een centraal metaalatoom omgeven door organische groepen (een organische verbinding is een verbinding met koolstofatomen erin. Alcohol is een voorbeeld). Deze groepen heten liganden. Het metaalatoom is het katalytisch actieve centrum. De liganden eromheen zorgen ervoor dat het metaalatoom zijn werk kan doen en sturen ook de reactie. Door te spelen met de groepen die om het metaalatoom heen zitten kan de activiteit en de selectiviteit van de katalysator veranderd worden. Dit soort metaalcomplexen wordt meestal in een oplossing gebruikt. De reactie heet dan een vloeistoffase reactie.

De andere soort katalysator bestaat uit kleine metaaldeeltjes. Hierbij vindt de reactie op het oppervlak van de katalysator plaats. Het is belangrijk om een zo groot mogelijk metaaloppervlak te creëren door de deeltjes zo klein mogelijk te maken. Hoe kleiner het deeltje, des te groter het oppervlak per gram materiaal is. Bovendien wordt het vaak dure metaal dan optimaal gebruikt, want bij hele kleine deeltjes bevinden alle atomen zich aan het oppervlak en doet ieder metaalatoom dus mee in de reactie. Het probleem is echter dat hele kleine deeltjes onder invloed van de reactieomstandigheden weer één groot deeltje kunnen worden. Het voordeel van een groot oppervlak is dan weer weg. Dit verschijnsel heet sinteren. Daarbij komt dat het heel moeilijk is om met zulke kleine deeltjes om te gaan. Als je zulk soort deeltjes in een vloeistoffase reactie gebruikt, krijg je ze heel moeilijk weer uit de vloeistof, omdat ze zo klein zijn.

Als oplossing voor deze problemen worden katalysator dragers gebruikt. Een katalysator drager is te vergelijken met een spons. Van binnen zitten allemaal kanalen, die ook een oppervlak hebben. Daardoor heeft het materiaal een groot intern oppervlak. Dat oppervlak kan oplopen tot wel duizend vierkante meter per gram. De kleine metaaldeeltjes kunnen gestabiliseerd worden op de grotere dragerdeeltjes. Hierdoor zijn de deeltjes beter bestand tegen sinteren en kan je de katalysator makkelijker verwijderen uit een vloeistof.

Het soort reactie waar ik me mee bezig heb gehouden heet hydrogenering. Tijdens een hydrogenering wordt bijvoorbeeld een dubbele binding tussen twee koolstofatomen omgezet in een enkele binding door er waterstof aan te plakken (bij een dubbele binding zijn vier elektronen betrokken en bij een enkele binding maar twee elektronen. De twee overige elektronen vormen na hydrogenering bindingen met waterstofatomen). Hydrogeneringreacties worden veel gebruikt in de industrie. Een voorbeeld van een hydrogeneringsreactie is de vetharding van oliën om er boter van te maken. Omdat het onderzoek in dit proefschrift al redelijk fundamenteel is en om het onderzoek niet nodeloos ingewikkeld te maken heb ik ervoor gekozen om de kooldraadkatalysatoren alleen te gebruiken in een simpele testreactie, die industrieel gezien minder relevant is. Als

testreactie is de hydrogenering van cyclohexeen gebruikt. Dit molecuul bestaat uit een ring van zes koolstofatomen met één dubbele koolstof-koolstof binding. In principe kan alleen deze binding gehydrogeneerd worden en is er maar één product mogelijk. Deze testreactie geeft alleen informatie over de activiteit van een katalysator. Omdat de reactie zo simpel is, is hij geschikt om snel katalysatoren te testen.

Kooldraden zijn een nieuw materiaal en erg geschikt als katalysator dragermateriaal (zie verder). Tijdens mijn onderzoek heb ik me bezig gehouden met het bestuderen van het gebruik van kooldraden als katalysator dragermateriaal. Dit hield in dat ik meer te weten moest komen over de kooldraden zelf. Hoe ziet bijvoorbeeld het oppervlak van kooldraden er precies uit en wat voor invloed heeft dat op de reactiviteit van de kooldraden? Ook wilde ik te weten komen hoe de kooldraden op een gemakkelijke manier gemodificeerd konden worden. Vervolgens heb ik de kooldraden gebruikt als drager voor twee verschillende soorten katalysatoren: metaalcomplexen en metaaldeeltjes.

Kooldraden

Kooldraden zijn hele kleine draadjes van koolstof. De diameter hiervan ligt tussen de vijftien en de honderd miljoenste millimeter. Ze kunnen enkele duizendste millimeter lang worden. De structuur van de kooldraden komt overeen met die van grafiet. Grafiet zit bijvoorbeeld in de kern van potloden. Grafiet bestaat uit lagen van gecondenseerde aromaatringen. Een aromaatring bestaat uit een zesring van koolstofatomen. De vlakken van één ring vormen ook een vlak van een andere ring (zie Figuur 3.1). Vandaar de naam gecondenseerd. Een grafietvlak is het beste te vergelijken met een vel papier. Grafiet bestaat dan uit een stapel papiervellen. Met deze “vellen papier” kunnen we kooldraden maken. Het vel papier kunnen we vouwen tot een koker of een cilinder. Als we verschillende cilinders maken en die in elkaar schuiven, hebben we een voorbeeld van een parallelle kooldraad. Wanneer we een dwarsdoorsnede maken (Figuur 1.2) is te zien dat de grafietvlakken parallel aan de as van de draad lopen. Het oppervlak van een parallelle draad bestaat uit het vlak van het vel papier, de zogeheten basale grafietvlakken. Bij een visgraat kooldraad vormen de grafietvlakken geen cilinders, maar kegels. Deze kegels zijn in elkaar geschoven en vormen zo een draad. Denk maar aan een stapel in elkaar geschoven patatzakken. Een dwarsdoorsnede (Figuur 1.2) maakt duidelijk dat de grafietvlakken een hoek met de as van de draad maken. De structuur lijkt op die van een visgraat. Het oppervlak van een visgraat kooldraad bestaat, in tegenstelling tot dat van een parallelle draad, uit de randen van de grafietvlakken.

Figuur 1.1 laat heel schematisch de synthese van kooldraden zien. Over kleine metaaldeeltjes op een drager wordt een koolstofhoudend gas geleid. Dit gas valt uit elkaar op het metaaldeeltje en de koolstof lost op in het deeltje. Aan de andere kant van het deeltje “groeit” dan de kooldraad en het metaaldeeltje wordt van de

drager afgedrukt. Door een juiste keuze van het metaal en de synthesecondities kunnen parallelle of visgraat kooldraden gemaakt worden. Als kooldraadgroei per ongeluk gebeurt tijdens een reactie kan de hele katalysator verwoest worden. Sterker nog, doordat de draden zo sterk zijn, kunnen zelfs hele reactoren ernstig beschadigd worden.

Kooldraden zijn een heel geschikt katalysator dragermateriaal. Doordat de draden zo klein zijn hebben ze een groot (buiten)oppervlak. De draden zelf zijn niet poreus. Ze kunnen zo gemaakt worden dat ze helemaal door elkaar heen zitten en een grotere structuur vormen (een macrostructuur). Deze clusters van draden worden ook wel vogelnestjes genoemd. De macroscopische deeltjes van kooldraden zijn mechanisch erg sterk en zijn daardoor erg geschikt voor vloeistoffase reacties. Bij vloeistoffase reacties wordt het reactiemengsel sterk geroerd en bestaat het gevaar dat de katalysator verpulverd wordt door de krachten die ontstaan tijdens het roeren. Hierdoor is de katalysator moeilijk van de producten te scheiden. De mechanische sterkte van kooldraden gaat de verpulvering van de deeltjes tegen. Naast deze en andere voordelen is de goed gedefinieerde structuur van kooldraden ook een pluspunt. Hierdoor kan beter bestudeerd worden wat de invloed is van de drager op de katalytische activiteit van het metaaldeeltje. De drager stabiliseert niet alleen de metaaldeeltjes, maar beïnvloedt ook de eigenschappen van deze deeltjes. Door de drager te veranderen kan de selectiviteit of de activiteit van de katalysator veranderd worden. Met metaaldeeltjes op kooldraden zijn zulke effecten ook waargenomen, maar een goede verklaring is er nog niet voor gevonden.

Kooldraden zijn een relatief nieuw materiaal. Het onderzoek naar kooldraden heeft zich tot nu toe vooral toegespitst op het begrijpen en het controleren van de synthese van de draden. Veel minder studies hebben zich bezig gehouden met het gebruik van de draden als katalysator dragermateriaal. Er is nog veel meer kennis nodig over kooldraden en de interactie tussen kooldraden en bijvoorbeeld metaaldeeltjes voor een goed gebruik van de draden als drager. De resultaten beschreven in dit proefschrift geven hierin meer inzicht.

De oppervlaktestructuur van kooldraden

Om kooldraden goed te kunnen gebruiken als katalysator dragermateriaal is het belangrijk om te weten hoe het oppervlak van de draden er precies uitziet. Kennis over de structuur van het oppervlak van kooldraden geeft informatie over de reactiviteit van het oppervlak en daarmee over de mogelijkheden tot oppervlaktemodificatie. Het is bijvoorbeeld belangrijk om zuurstofhoudende groepen op de draden aan te kunnen brengen, omdat dit een noodzakelijke stap is bij de synthese van katalysatoren op kooldraden. De studie naar de oppervlaktestructuur van kooldraden staat beschreven in hoofdstuk twee. Twee technieken die in dit hoofdstuk gebruikt zijn zal ik kort uitleggen.

Elektronenmicroscopie werkt in principe hetzelfde als een lichtmicroscoop. Doordat bij elektronenmicroscopie gebruik gemaakt wordt van een

elektronenbundel in plaats van licht kunnen veel hogere vergrotingen bereikt worden. Details van één miljoenste millimeter (één nanometer of nm) kunnen zo afgebeeld worden. Met behulp van elektronenmicroscopie zijn in Figuur 2.2 kooldraden afgebeeld en in Figuur 2.1 zelfs de aparte grafietvlakken van de individuele draden.

Infrarood (IR) spectroscopie maakt gebruik van het verschijnsel dat de atomen in een verbinding vibreren. Verschillende groepen in een verbinding vibreren met verschillende frequenties. Een waterstofatoom aan een koolstofatoom vibreert bijvoorbeeld met een hogere frequentie dan een zuurstofatoom aan een koolstofatoom. Als er infrarood licht op een groep valt met dezelfde frequentie als die van de vibratie, dan zal de groep het licht gedeeltelijk absorberen. Door infrarood licht met verschillende frequenties op een stof te laten vallen zal er licht bij bepaalde frequenties geabsorbeerd worden. Die frequenties geven informatie over het soort groepen in de bestudeerde verbinding. De IR plaatjes in dit proefschrift laten de intensiteit van het doorgelaten infrarood licht ten opzichte van de frequentie van dat licht zien. Als er licht door een vibrerende groep geabsorbeerd wordt, zal er dus minder licht door de stof heenkomen en vinden we op die frequentie een minimum (ook wel band genoemd).

De foto's die gemaakt zijn met de elektronenmicroscoop (Figuur 2.1 en 2.2) laten zien dat de kooldraden geen perfecte structuur hebben. Veel grafietvlakken zijn krom en sommige vlakken verdwijnen. Op andere foto's is te zien dat vlakken afgebroken zijn (het vel papier is doorgescheurd). Ook zijn de draden zelf niet recht. Dat kan alleen als er defecten zijn in de grafietstructuur. De aanwezigheid van deze defecten kan heel belangrijk zijn voor de reactiviteit van het oppervlak. Met behulp van infrarood spectroscopie is het gelukt om de aanwezigheid van bepaalde infrarood banden te koppelen aan de aanwezigheid van defecten (zie ook Figuur 2.4 en Tabel 2.2). Het gaat hier om vibraties van koolstof-waterstof (C-H) bindingen en enkelvoudige koolstof-koolstof (C-C) bindingen. Perfecte grafietvlakken hebben alleen dubbele koolstof-koolstof (C=C) bindingen en alleen aan de randen van de vlakken (de rand van het vel papier) kunnen koolstof-waterstof verbindingen gevormd worden. Bij parallelle draden zou je dus geen vibraties van C-H of C-C bindingen moeten zien, omdat het oppervlak bestaat uit de basale grafietvlakken (het vlak van het vel papier). Bij visgraat draden verwacht je alleen wat vibraties van C-H bindingen, omdat het oppervlak bestaat uit de randen van de grafietvlakken. Uit mijn onderzoek blijkt dat op zowel parallelle als visgraat draden zich C-C en verschillende soorten C-H verbindingen bevinden. Ook heb ik aangetoond dat deze verbindingen zich bevinden op de defecten in de grafietstructuur. Door de aanwezigheid van deze defecten vond ik weinig verschil in oppervlaktestructuur tussen parallelle en visgraat draden. Dit resultaat was verrassend, omdat er tot nu toe vanuit gegaan was dat er een groot verschil was in oppervlaktestructuur tussen beide soorten draden.

Oxidatie van kooldraden

In hoofdstuk drie zijn parallelle en visgraat kooldraden geoxideerd met verschillende methoden. Het doel was om zoveel mogelijk zuurstofhoudende groepen op het oppervlak van de draden te creëren. Verschillende zuurstofgroepen die gevormd kunnen worden na oxidatie van kool zijn te vinden in Figuur 3.1.

De oxidatie van de kooldraden mag er niet toe leiden dat de grafietstructuur of de macrostructuur van de draden aangetast wordt. Tijdens mijn onderzoek bleek dat de meest effectieve oxidatiemethode, oxidatie in een mengsel van kokend geconcentreerd salpeterzuur en zwavelzuur (HNO_3/H_2SO_4), geen invloed had op de structuur van visgraat draden. Bij parallelle draden werd echter de macrostructuur wel aangetast. De infrarood metingen laten zien dat de oxidatie van de draden juist plaatsvindt op de defecten in de grafietstructuur. Na oxidatie zijn namelijk de koolstof-waterstof banden (die aanwezig zijn op de defecten) verdwenen en de koolstof-zuurstof banden verschenen (zie bv Figuur 3.4 en Tabel 3.2). Dit betekent dat op de defecten de koolstof-waterstof verbindingen omgezet zijn in koolstof-zuurstof verbindingen. De parallelle draden worden ongeveer net zo makkelijk geoxideerd als visgraat draden. Dit resultaat is verrassend, omdat altijd gedacht werd dat parallelle draden minder reactief zijn dan visgraat draden. De randen van grafietvlakken zijn namelijk veel reactiever dan de vlakken zelf. De grote hoeveelheid defecten in de structuur heffen dit effect blijkbaar op. De resultaten wijzen erop dat er zoveel zuurstofgroepen gevormd worden tijdens de oxidatiemethode dat deze niet allemaal op het oppervlak van de kooldraden passen. Er gaan ook zuurstofgroepen vlak onder het oppervlak tussen de grafietvlakken zitten. Een voorbeeld van het belang van oxidatie is te vinden in Figuur 3.11. Deze figuur laat zien dat alleen door te oxideren in HNO_3/H_2SO_4 de draden een goede affiniteit met water hebben (de draden worden goed bevochtigd met water). Veel katalysator synthesetechnieken maken gebruik van waterige oplossingen en dus is de bevochtiging van de draden met water erg belangrijk.

Rhodium-antranilzuur en kooldraden

Met de kennis verkregen in hoofdstuk twee en drie is het mogelijk om kooldraden te gebruiken als dragermateriaal voor katalysatoren. Twee systemen zijn bekeken: metaalcomplexen en metaaldeeltjes op kooldraden. Een belangrijk onderdeel van mijn onderzoek is het vastbinden van het rhodium-antranilzuur metaalcomplex op kooldraden geweest. Een metaalcomplex heeft een aantal voordelen boven kleine metaaldeeltjes. Een complex heeft meestal een beter gedefinieerde structuur en de reactie is vaak beter te sturen met dit soort katalysatoren. Bovendien kan ieder metaalatoom worden gebruikt als katalytisch centrum, terwijl met kleine metaaldeeltjes alleen de oppervlakteatomen meedoen. Het is echter moeilijk om het complex na (vloeistoffase) reactie weer te scheiden van de producten. Een manier om dit probleem op te lossen is om zo'n

complex vast te binden op een drager. Zo hoop je dat het complex zijn voordelige eigenschappen behoudt en gemakkelijk af te scheiden is. Helaas is het meestal niet zo simpel en doen er zich een hoop problemen voor. Doordat het complex vastgebonden wordt veranderen er vaak een heleboel eigenschappen. Een alternatief is om een metaalcomplex op een drager te construeren, terwijl je probeert rekening te houden met de veranderingen die kunnen optreden tijdens het binden op een drager. Deze benadering is toegepast in dit onderzoek.

Voordat het rhodium-antranilzuur complex op kooldraden gebonden kan worden moet je eerst meer informatie verkrijgen over het complex zelf zonder kooldraden. Daarom heb ik het rhodium-antranilzuur complex en het gerelateerde rhodium fenylantranilzuur complex bestudeerd (zie hoofdstuk vier). De structuur van fenylantranilzuur en antranilzuur is te vinden in Figuur 4.1. Beide liganden hebben een carboxylgroep [(HO)C=O] en een aminegroep (HN of H_2N). Uit infrarood metingen blijkt dat deze liganden een interactie met het rhodium atoom hebben via deze groepen. De vibraties van deze groepen veranderen namelijk, wat erop duidt dat er iets aan gebonden is. Bovendien is bij rhodium-fenyl antranilzuur een rhodium-stikstof binding te zien, wat aanduidt dat een binding tussen rhodium en het amine van fenyl antranilzuur gevormd is. Andere technieken wijzen er echter op dat de complexen niet puur zijn. Tijdens de synthese en tijdens katalytische reactie worden kleine rhodium deeltjes gevormd. Deze deeltjes zijn ook actief in de gebruikte testreactie (hydrogenering van cyclohexeen). De resultaten laten vooral zien dat het systeem erg lastig is.

In hoofdstuk vijf beschrijf ik het binden of het immobiliseren van rhodium-antranilzuur op visgraat kooldraden. De eerste stap was oxidatie van de draden (zie Figuur 5.2). De zuurstofgroepen werden vervolgens omgezet in reactievere zuurchloride groepen en antranilzuur werd gebonden aan de draden via deze groepen. Vervolgens werd het rhodium weer aan het antranilzuur gezet. Om beter uit te kunnen leggen wat ik in dit hoofdstuk gedaan heb, zal ik eerst nog twee belangrijke technieken beschrijven.

Met XPS spectroscopie wordt een materiaal bestraald met röntgenstraling. De röntgenstraling slaat elektronen uit de atomen van het materiaal en de hoeveelheid en de energie van deze uitgetreden elektronen wordt gemeten. Alleen de elektronen aan het oppervlak van het materiaal bereiken de detector en je kijkt dus selectief naar het oppervlak. De energie van de elektronen geeft aan naar welk element je kijkt [bijvoorbeeld chloor (Cl_{2p}) of stikstof (N_{1s}), zie Figuur 5.4]. Zie je bijvoorbeeld een piek bij de energie van chloor, dan zit er chloor op het oppervlak van het gemeten materiaal.

Met EXAFS spectroscopie wordt een materiaal ook bestraald met röntgenstraling en worden er elektronen uit de atomen van het materiaal geslagen. Er wordt nu echter gekeken naar de röntgenstraling die door het monster heen komt (vergelijk met IR spectroscopie). Door de energie van de röntgenstraling goed te kiezen worden alleen elektronen uit één element verwijderd (in mijn geval de rhodium atomen). Het elektron dat uit een atoom

treedt heeft een interactie met de omringende atomen. Afhankelijk van de precieze energie van de röntgenstraling kan het elektron door die interactie moeilijker of gemakkelijker uit het atoom treden. Vergelijkbaar met IR spectroscopie wordt er röntgenstraling geabsorbeerd als het elektron uittreedt. Omdat dit afwisselend moeilijker en gemakkelijker gaat meet je een soort slinger. Voorbeelden zijn te vinden in Figuur 5.7A en C. De horizontale as is een energie as en de verticale as geeft de intensiteit weer. De slinger wordt met behulp van een wiskundige (Fourier) transformatie omgezet. Door een model zodanig aan te passen dat deze klopt met de experimenteel gevonden waarden (de data "fitten") kun je informatie krijgen over het soort en het aantal buren rondom de rhodium atomen.

Infrarood opnamen van de verschillende immobilisatiestappen (Figuur 5.3) laten zien dat er na het binden van antranilzuur minder vibraties zijn van zuurstofgroepen, maar wel vibraties van antranilzuur. Dit wijst erop dat het antranilzuur aan de zuurstofgroepen gebonden is. Als antranilzuur aan een zuurstofgroep vastzit, dan zal deze niet meer vibreren bij de oude frequentie. De intensiteit van de infrarood band van de zuurstofgroepen neemt dan af. Met XPS kunnen we het immobilisatieproces ook heel mooi volgen. Geoxideerde draden en draden met antranilzuur eraan bevatten geen chloor (Cl_{2p}), terwijl op de draden met de zuurchlorides en de draden met rhodium-antranilzuur wel chloor waar te nemen is (Figuur 5.4A). Dit is precies wat we verwachten, want zuurchloride groepen bevatten chloor en het rhodium werd erop gebracht als rhodium chloride. Ook verwachten we dat zodra antranilzuur op de draden zit we stikstof (N_{1s}) zien met XPS, omdat antranilzuur een stikstofatoom heeft. Figuur 5.4B laat zien dat ook dit mooi klopt.

De EXAFS analyses van het gebonden rhodium-antranilzuur complex geven het soort atomen rond het rhodium, het aantal buren (N) en de afstand tot het rhodium (R) [zie Tabel 5.4]. Deze resultaten zijn nog vrij abstract. Om die reden zijn de EXAFS resultaten gebruikt om met een speciaal rekenprogramma een model van het gebonden complex te maken. Het resultaat is te zien in Figuur 5.11 en op de voorkant van dit boekje. Alle resultaten samen laten zien dat het gelukt is om het rhodium-antranilzuur complex te binden op de kooldraden.

Het rhodium-antranilzuur complex is helaas niet werkzaam als katalysator. Daarom is geprobeerd om het complex te activeren door een reactie met natriumboorhydride ($NaBH_4$). Het bleek echter dat door deze procedure kleine rhodium metaaldeeltjes op de draden gevormd werden. Deze deeltjes zijn wél erg actief in de vloeistoffase hydrogenering van cyclohexeen. Alhoewel het dus wel gelukt is om actieve metaaldeeltjes te maken, is het niet gelukt om een actief metaalcomplex te maken. Er moet dus nog verder onderzoek gedaan worden naar een betere activeringsprocedure van het gebonden rhodium-antranilzuur complex. Ook kan de procedure van immobiliseren gebruikt worden voor het binden van andere complexen.

In hoofdstuk zes heb ik kleine rhodium metaaldeeltjes op kooldraden gemaakt. Ik heb gekeken naar het effect van oxidatie van de kooldraden op de kwaliteit van de uiteindelijke katalysator en ik heb verschillende synthesetechnieken gebruikt. Bestudering van de katalysatoren met de elektronenmicroscoop (Figuur 6.2) laat zien dat de oxidatie in salpeterzuur/zwavelzuur (HNO_3/H_2SO_4) een noodzaak is om kleine rhodium deeltjes op de kooldraden te krijgen. Dit resultaat is direct gerelateerd aan de resultaten van hoofdstuk drie. Alleen met deze oxidatiemethode worden de draden goed bevochtigd met water. Bij een slechte bevochtiging met water kan het rhodium zich niet goed verdelen over de draden en krijg je grote bonken (nog steeds maar 100 miljoenste millimeter!). Door de juiste synthesetechnieken te gebruiken kunnen extreem kleine rhodium deeltjes op de draden gemaakt worden. Deze deeltjes zijn zo klein dat ze zelfs met elektronenmicroscopie niet meer te zien zijn. Gelukkig hebben we ook nog EXAFS. EXAFS laat zien dat er rondom rhodium atomen een bepaald aantal andere rhodium atomen zitten (zie Tabel 6.3). Bij hele grote rhodium deeltjes heeft een rhodium atoom in het deeltje twaalf buren. Worden de deeltjes kleiner, dan wordt ook het aantal buren minder omdat een steeds grotere fractie van atomen aan het oppervlak van een deeltje zit. Een rhodium atoom aan het oppervlak kan geen twaalf buren om zich heen hebben, want aan één kant van het atoom (boven het oppervlak) zitten helemaal geen andere rhodium atomen. Als bijna alle deeltjes aan het oppervlak zitten heeft een atoom bijvoorbeeld gemiddeld nog maar zes buren. Dus met behulp van de EXAFS resultaten kun je de grootte van de rhodium deeltjes berekenen. Het blijkt dat de deeltjes afmetingen hebben van één tot twee miljoenste millimeter. Met EXAFS is ook de interactie tussen rhodium en koolstofatomen van de draden te zien. Hoewel in dit proefschrift niets meer gedaan is met deze rhodium-koolstof interactie, kun je hiermee informatie winnen over de invloed van de kooldraden op de rhodium deeltjes en zou je uiteindelijk ook kunnen verklaren waarom je verschillende activiteiten en selectiviteiten vindt. De synthesemethoden in hoofdstuk zes beschrijven hoe je zulke kleine deeltjes moet maken.

De rhodium-op-kooldraad katalysatoren zijn ook getest in de vloeistoffase hydrogenering van cyclohexeen. Het blijkt dat de katalysatoren zo actief zijn in deze reactie dat je niet meer snel genoeg waterstof kunt aanvoeren. Ook heb ik gevonden dat de activiteit van de katalysatoren nauwelijks afhangt van de grootte van de rhodium deeltjes. In principe zou je verwachten dat een katalysator met kleinere deeltjes actiever is omdat er meer rhodium atomen aan het oppervlak zitten. Het blijkt dat andere factoren bij vloeistoffase reacties een veel belangrijkere rol spelen. Eén van die factoren is het aan elkaar plakken van de kooldraaddeeltjes zelf in de vloeistof. Hierdoor wordt de katalysator niet meer netjes verdeeld over het reactiemengsel en neemt de activiteit af.

De rode draad door mijn proefschrift is het gebruik van kooldraden als katalysator dragermateriaal. Nadat eerst veel meer kennis vergaard is over het oppervlak, de reactiviteit en de oxidatie van kooldraden, zijn de draden gebruikt als drager voor metaalcomplexen en metaaldeeltjes. Alhoewel de procedure moeilijk is, is het gelukt om een metaalcomplex (rhodium-antranilzuur) te binden aan de kooldraden. Het complex is helaas katalytisch niet actief en verder onderzoek is nodig. Ook zijn kleine metaaldeeltjes op kooldraden gemaakt. Deze synthese was erg succesvol. Zeer kleine rhodium metaaldeeltjes op de draden maakte deze katalysator zeer actief in de vloeistoffase hydrogenering van cyclohexeen.

Dankwoord

Hier is het dan: het meest gelezen onderdeel van het proefschrift (alhoewel ik hoop dat de samenvatting voor leken een goede tweede zal zijn)! Mijn naam staat op de voorkant van dit boekje, maar dat betekent niet dat ik de klus in mijn eentje geklaard heb. Veel mensen hebben, ieder op hun manier, bijgedragen aan de totstandkoming van dit proefschrift. De afgelopen vijf jaar zijn niet de makkelijkste uit mijn leven geweest. Ik wil niet alleen de mensen bedanken die technisch aan dit werk hebben bijgedragen, maar ook de personen die mij bijgestaan hebben in moeilijke tijden.

Beste Diek, vanaf het begin lag onze rolverdeling vast. Dat had goede en minder goede kanten, maar het gaf wel veel duidelijkheid. Ik heb jouw enorme vertrouwen in mijn kunnen, ook als ik daar zelf aan twijfelde, enorm gewaardeerd. Toen het onderzoek minder liep was jij verbaasd daarover, want ik had tot dan toe alles zo fantastisch gedaan! Ik denk dat we door de jaren heen een goede, open samenwerking gehad hebben. Ik heb van jou geleerd hoe ik mijn verhaal moet verkopen aan een breder publiek.

Beste John, in de eerste jaren van mijn onderzoek hebben we minder contact gehad, maar daarna is onze relatie uitgediept. Bedankt voor de uren achter de elektronenmicroscoop, de discussies over mijn werk en de mijmeringen over het verloop van mijn onderzoek. Jij hebt de combinatie van studie en sport altijd erg gewaardeerd. Ik zal niet snel het moment vergeten dat ik je de wering 7 uitlegde en het moment dat jij mij na mijn NCCC-lezing vroeg of de spanning vooraf hetzelfde was als voor een schermwedstrijd!

Beste Jos, jij bent de rots in de branding: altijd aanwezig en, door wat voor storm dan ook, niet van je stuk te krijgen. Jouw rustige natuur en relativerende vermogen heb ik af en toe hard nodig gehad. Jouw persoonlijke benadering en vermogen om mensen een hart onder de riem te steken in crisissituaties is onschatbaar. Veel mensen verbazen zich nog steeds over de enorme kennis die jij paraat hebt over een breed scala aan onderwerpen.

Graag wil ik de studenten die onder mijn begeleiding gewerkt hebben bedanken voor de inzet, de motivatie en de resultaten. Gerbrand, Michel, Martijn en Daphne, bedankt voor het praktische werk. Mathieu, Ron en Lukas, bedankt voor de scripties.

Beste Krijn, soms voelde ik me meer een concurrent dan een medestander in kooldradenland. Toch denk ik dat alle kooldradenmensen een uitstekende

samenwerking gehad hebben. Bedankt voor je grote inzet bij het regelen van een contractverlenging en voor je hulp in het berekenen van de Thiele modulus. Joop, bedankt voor de discussies over de IR spectra. Frank, bedankt voor het wegwijs maken in de geheimen van Cerius^2. Onno, dank voor de hulp met het uitwerken van de XPS data en de discussies daarover. Jeroen en ook Harry, bedankt voor de begeleiding tijdens mijn eerste stapjes in XDAP-land.

Ook wil ik hier alle mensen bedanken die samen met mij EXAFS metingen uigevoerd hebben of die voor mij metingen gedaan hebben: Bob, Dick, Jeroen, Miguel, Jan, Marc, Ad, Marieke, Harry, Michiel, Andrea, Anne, Claudia, Laurens en Moniek. Een speciaal bedankje gaat hier naar Moniek, die mij verving toen het echt niet anders kon. Vierentwintig uur per dag met elkaar optrekken eist een hoge tol van elkaar. We hebben er altijd een goede tijd van weten te maken en ik heb veel goede herinneringen. Ad, ik hoop dat jouw naam nog steeds deuren opent in Grenoble! Jan, hoe lang heb je nou daarboven in de hutch gehangen? Andrea, voorzichtig met het binnenrijden van parkeergarages!

Ook zonder ondersteunend personeel zou het leven een stuk moeilijker geweest zijn. Ad, bedankt voor de hulp met het EXAFS gebeuren. Ad, bedankt voor de XPS metingen. Marjan, bedankt voor de XRD ondersteuning en de foto's. Fred, bedankt voor de TGA metingen en je altijd grote bereidwilligheid om dure chemicaliën voor me aan te schaffen. Jos, bedankt voor de tips over de bouw van mijn opstelling en het stikstoforgel. Mijn Gardena koppelingen zijn altijd een succes tijdens rondleidingen! Ine, Thea, Ans en Monique, bedankt voor de secretariële ondersteuning. Thea, bedankt voor alle financiële en administratieve zaken. Voortaan je deur dichthouden!

Een speciaal woord van dank gaat hier naar John. Helaas kan je mijn promotie niet meer meemaken. Je plotselinge overlijden was een klap voor ons allemaal. John, bedankt voor alle metingen die je voor mij uitgevoerd hebt en voor de computerondersteuning. Belangrijker nog, bedankt voor alle serieuze en gekke discussies die we gehad hebben. Je was een gekke vent, maar daardoor wel het zonnetje van de vakgroep (ook al was het regelmatig wisselend bewolkt!).

Ik wil graag Evert en Gerrit van de instrumentmakerij bedanken voor het werk dat ze voor mij verricht hebben. Gerrit, ik kijk nog steeds met plezier naar de stalen onderkant van mijn roerder, die jij gedraaid hebt, en naar de deurtjes van mijn opstelling. Lou, Viktor en Henk: bedankt voor de elektronische ondersteuning. Graag wil ik Wim, Igno en Wil van de glasblazerij bedanken voor de goede service, het goede werk en de vrolijke benadering van alles. Als ik nog een keer snel wat van jullie nodig heb, zal ik weer een taart meenemen! Ook de Audio-Visuele dienst heb ik aan het werk gehouden. Ingrid, bedankt voor het samenstellen van twee posters; Alois, dank voor de tips betreffende de lay-out van het binnenwerk; Jan, de omslag is erg mooi geworden. Veel dank daarvoor.

Ik wil mijn drie kamergenoten bedanken voor alle uren die we samen doorgebracht hebben. Miguel, I have enjoyed your company very much during the first ten months of my contract, even though we had to share the computer! Without you, I wouldn't know what Dutch bureaucracy is. Marije, enge Neanderthaler, we kennen elkaar nog van onze studententijd. Ik zat al een paar maanden alleen toen bekend werd dat jij bij ons zou beginnen. Iedereen beweerde dat jij bij hen op de kamer zou komen, maar ik wist wel beter! Ons kamergenootschap is dan ook uitgegroeid tot een vriendschap, waarvan ik hoop dat die nog lang voort zal duren. Bedankt voor alle steun en vriendschap. Marjolein, jij bent later bij ons ingetrokken. Dat was even wennen na een aantal jaren met z'n tweeën, maar had ook als voordeel dat we de mooiste AIO-kamer van de vakgroep betrokken. Ik heb het altijd amusant gevonden dat ik op een beta-faculteit twee vrouwen als kamergenoot heb gehad. Ook jij bent een zonnetje en altijd in voor een grapje. Ik geloof niet dat ik je ooit op een slecht humeur heb kunnen betrappen (in tegenstelling tot mezelf!). Bedankt voor de goede sfeer, waardoor er veel gelachen is op de kamer.

Verder wil ik alle AIO's en andere collega's bedanken voor de discussies over het werk, de collegialiteit, de goede sfeer op de vakgroep en de talloze activiteiten naast het werk: BBQ, kerstdiner, LIIT, (vrijdagmiddag)borrels, langlaufen, survival, schaatsen, fietsen, klimmen, verjaardagen, concerten, drinken in de stad enzovoort. Ik hoop veel van jullie nog te zien als ik weg ben.

Lieve mam, bedankt voor alle steun en begrip. We zijn erg hetzelfde. Dat botst soms, maar verbindt ook. Ik heb me altijd door jou gestimuleerd gevoeld. Je stelt jezelf niet vaak op de voorgrond en stelt ook weinig eisen. Wees maar gerust. Ik zal op jouw oude dag jouw rolstoel nog voortduwen!

Lieve pap, jouw beroerte heeft een flinke schaduw over mijn promotieperiode geworpen. Gelukkig zijn we er allebei tot nu toe goed doorheen gekomen. Bedankt voor je liefde en zorg. Je bent een echte trotse vader! Ik wens jou voor de komende tijd vooral rust toe.

Lieve Peter, lieve stief, wat zal ik je missen de zestiende! De dag zal kaler zijn zonder jou. Jij bent voor mij de echte wetenschapper en soms ook de verstrooide prof. Je hebt me gewoon vakliteratuur laten lezen bij de voorbereiding van middelbare school referaten over kannibalisme en objectiviteit in de wetenschap! Het is niet voor niets dat sommige mensen dachten dat ik een kind van jou was. Je hebt een grote invloed op mijn leven gehad en dat zal nog voortduren. Ik hoop echt te leven volgens de ontdekkingen die jij op het laatst nog hebt gedaan: dat uiteindelijk omgang met naasten en geliefden het belangrijkste is wat er is en dat je dingen die je graag wilt doen niet te lang moet uitstellen. Ik zal je nooit vergeten.

Ook de rest van de familie wil ik bedanken voor alle steun en alle goede momenten die ik met ze beleefd heb. Lieve Maurik, we hebben al veel samen beleefd. Ik hoop dat ongeluk niet meer tussen ons in zal staan.

Lieve Piet en Mariet, bij jullie heb ik net zo'n warm nest gevonden als thuis. Ik ben dan ook gelijk opgenomen in de familie. Bedankt daarvoor.

Beste Raymond, onze vriendschap gaat lang terug. Ik zie steeds beter hoe waardevol zo'n vriendschap is. Op nog vele jaren! Bedankt voor alle belangstelling voor mijn vakgebied. Ben benieuwd of je na de Schrödinger vergelijking ook de finesses van EXAFS spectroscopie zult begrijpen!

Alle scherm(st)ers bedankt voor de vele trainingsuren en wedstrijdweekeinden die we samen doorgebracht hebben. Ook hier geldt dat zo intensief met elkaar omgaan de zenuwen soms op de proef stelt. We zijn een goede, hechte groep bij elkaar. Dat moet zo blijven! Schermen is voor mij altijd de ideale uitlaatklep geweest. Er zijn momenten geweest dat dat heel belangrijk was. Bobo Anton, het geregel gaat je niet altijd in de koude kleren zitten. Sjefke, onze tijd in Budapest was bijzonder. Symke, op nog vele uurtjes 's avonds laat in de file! Sjakie, op een behouden terugkomst.

Beste Dick, ik kwam met een huiduitslag, maar al snel ging het over andere dingen. Ik ben veel over mezelf te weten gekomen en heb om leren gaan met situaties die me tot daarvoor in de greep hadden. Bedankt daarvoor!

Lieve Hanneke, natuurlijk zijn de laatste bedankjes gericht aan jouw adres. Ik heb grote bewondering voor jouw onvoorwaardelijke steun en inzet bij crisissituaties. Als het erom spant, komt het beste in je boven. Ik zal nooit vergeten hoe je die uroloog behandelde! Ik heb me vaak afgevraagd of je al die crisissen niet eens zat werd. Gelukkig niet dus. Bedankt voor alles,

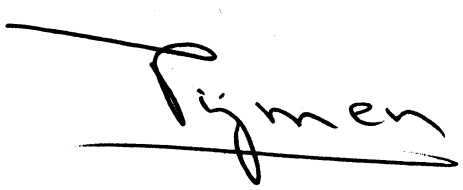

Ik draag dit proefschrift op aan Peter.

List of Publications

R.G. Leliveld, T.G. Ros, A.J. van Dillen, J.W. Geus, and D.C. Koningsberger, Journal of Catalysis **185** (1999), 513
Influence of Si/Al Ratio on Catalytic Performance of (Co)Mo/Saponite Catalysts

T.G. Ros, A.J. van Dillen, J.W. Geus, and D.C. Koningsberger, *ChemPhysChem*, accepted
Surface Structure of Untreated Parallel and Fishbone Carbon Nanofibres: an Infrared Study

T.G. Ros, A.J. van Dillen, J.W. Geus, and D.C. Koningsberger, *Chem. Eur. J.*, accepted
Surface Oxidation of Carbon Nanofibres

T.G. Ros, M.K. van der Lee, A.J. van Dillen, J.W. Geus, and D.C. Koningsberger, *J. Mol. Catal.*, submitted
Rhodium Complexes with (N-phenyl) Anthranilic Acid Ligands as Catalysts for Hydrogenation

T.G. Ros, A.J. van Dillen, J.W. Geus, and D.C. Koningsberger, *Chem. Eur. J.*, submitted
Modification of Carbon Nanofibres for Immobilisation of Metal Complexes. A Case Study with Rhodium-Anthranilic Acid

T.G. Ros, D.E. Keller, A.J. van Dillen, J.W. Geus, and D.C. Koningsberger, *Chem. Eur. J.*, submitted
Preparation and Activity of Small Rhodium Metal Particles on Fishbone Carbon Nanofibres

Curriculum Vitae

Tijmen Ros werd geboren op 29 mei 1972 te Nieuwerkerk aan den IJssel. In september 1984 begon hij aan het voorbereidend wetenschappelijk onderwijs en in juni 1990 behaalde hij het Gymnasium diploma (ongedeeld) aan het Stedelijk Gymnasium te Leiden. In september 1991 ving hij aan met de studie Scheikunde aan de Universiteit Utrecht en hij passeerde het propedeuse examen *met genoegen* in augustus 1992. In november 1996 legde hij het doctoraalexamen *cum laude* af met bijvakken bij de Sectie Natuurwetenschap en Samenleving (Exergy Analyis of an Integrated Steel Plant) en bij "the Institute of Isotopes, Hungarian Academy of Sciences", Budapest, Hongarije (Hydrogenation of Ethylene over a Pt/Si model catalyst) en het hoofdvak bij de Sectie Anorganische Chemie en Katalyse (De invloed van de Si/Al ratio op de ontzwavelingsactiviteit van synthetische kleien - Een studie naar geschikte katalysatoren voor hydrokraken). Vanaf januari 1997 was hij als Onderzoeker in Opleiding (OIO) aan de Sectie Anorganische Chemie en katalyse aan de Universiteit Utrecht verbonden. De verkregen onderzoeksresultaten staan beschreven in dit proefschrift.